Symmetry Breaking, Order-by-Disorder, Fragmentation, and Spin-Liquids in the Magnetic Pyrochlore Lattice with Anisotropic Interactions

by

Daniel Lozano Gómez

A thesis
presented to the University of Waterloo
in fulfillment of the
thesis requirement for the degree of
Doctor of Philosophy
in
Physics

Waterloo, Ontario, Canada, 2023

© Daniel Lozano Gómez 2023

Examining Committee Membership

The following served on the Examining Committee for this thesis. The decision of the Examining Committee is by majority vote.

External Examiner:	Hae-Young Kee Group Professor, Dept. of Physics, University of Toronto
Supervisor:	Michel J. P. Gingras Professor, Dept. of Physics and Astronomy, University of Waterloo
Internal Member:	Anton Burkov Professor, Dept. of Physics and Astronomy, University of Waterloo
Internal Member:	David Hawthorn Professor, Dept. of Physics and Astronomy, University of Waterloo
Internal-External Member:	Marcel Nooijen Professor, Dept. of Chemistry, University of Waterloo

Author's Declaration

This thesis consists of material all of which I authored or co-authored: see Statement of Contributions included in the thesis. This is a true copy of the thesis, including any required final revisions, as accepted by my examiners.

I understand that my thesis may be made electronically available to the public

I understand that my thesis may be made electronically available to the public.

Statement of Contribution

The work presented in this thesis comprehends four independent research projects corresponding to Chapters 4, 5, 6, and 7. Although the results presented in this thesis originates from distinct collaborations, the discussion and analysis presented here was fully written by Daniel Lozano Gómez.

Chapter 4, is based on the manuscript in Ref. [1]. In this chapter, the pseudo-fermion functional renormalization group results were obtained by Vincent Noculak, the high-temperature series expansion results were obtained by Jaan Oitmaa, and the classical low-temperature expansion, linear spin waves, Irrep analysis and Monte Carlo results were obtained by Daniel Lozano Gómez.

The results presented in Chapter 5 are obtained from a collaboration with Alexander Hickey. In this chapter the linear spin waves analysis was performed by Alex Hickey, and the classical low-temperature expansion, Irrep analysis and Monte Carlo by Daniel Lozano Gómez.

All the results and analysis presented in Chapter 6 were solely obtained by Daniel Lozano Gómez.

The results presented in Chapter 7 are obtained from a collaboration with Kristian Chung, where both Kristian Chung and Daniel Lozano Gómez, obtained and verify all the results presented independently.

Two additional research projects [2, 3] are not mentioned or discussed in this thesis as a personal choice of Daniel Lozano Gómez.

Abstract

Within the study of frustrated magnetism, the pyrochlore lattice is deemed a fruitful ground where phenomena such as quantum and thermal order-by-disorder, moment fragmentation, and spin-liquids, both quantum and classical, might be realized. In this thesis, we study a Heisenberg and Dzyaloshisnkii-Moriya nearest-neighbor Hamiltonian in this lattice which presents all the above phenomena, providing a quantitative description through the application of both analytical and numerical approaches. First, we obtain a phase diagram where three long-range ordered phases (two antiferromagnetic and one ferromagnetic), and two spin-liquid points, the well-known classical Coulomb phase and a new spin-liquid, that we dub "order-by-disorder selected spin liquid", are identified. We then proceed to study the order-by-disorder selection in two of the long-range ordered phases (an antiferromagnetic and a ferromagnetic phase) and show that the quantum order-by-disorder selection mechanism in one of these phases is only produced at non-zero temperature, i.e. without zero-temperature quantum order-by-disorder. Then, we study the newly identified spin-liquid and the evolution of its correlation function as a function of temperature. The correlation function of this spin-liquid presents pinch-lines, twofold and fourfold pinch-points at high temperature, whereas at low temperature, these features are replaced by a spin-ice pattern. This effect is a consequence of the order-by-disorder selection of an extensive subset of ground-states (the spin-ice states) within the manifold. Finally, we study the phenomenon of fragmentation, commonly referred to as the observation of both sharp pinch-points and Bragg peaks in the correlation functions of an ordered phase. Specifically, we demonstrate how this effect is a consequence of a Helmholtz-Hodge decomposition of the spin mode excitations in an ordered phase, and is therefore expected to be observed especially for Hamiltonians whose interaction parameters are proximate to a spin-liquid point.

Acknowledgements

The work presented in this thesis is a result of the incredibly fruitful collaborations, and never-ending support that I have received throughout my degree. First and foremost I must acknowledge my advisor Michel J. P. Gingras for supporting me, and creating the environment where my work and appreciation for the theoretical and experimental aspects of frustrated magnetism was able to flourish. I acknowledge my Master's and Bachelor's advisor Neelima G. Kelkar for guiding my first steps into the beautiful and challenging career of a physicist.

I must also acknowledge my close friends who I had the privilege to meet, work with, and learn from. First of all I must acknowledge Kristian Chung with whom I learned most of the physics leading to the results presented in this thesis and became one of my closest collaborators. Alex Hickey, for all the physics and non-physics related conversations which nurture our work and friendship. Darren Pereira, for influencing my work-life balance, and presenting an exemplary commitment to our work, which I still try emulate every day. Itamar Aharony for his unique sense of humor which lighten the mood of every conversation we had. Naman Gupta, with whom I had endless conversations on politics and common cultural grounds. I must also acknowledge some of my friends with whom I share meals, thoughts, and laughter. Wen Jin, Cyrus Cerkauskas, Jennifer Reid, Aritro Mukherjee, and Pablo Millan. Working and befriending each one of you has undoubtedly improved my life in Canada and my experience as a graduate student. I hope that our paths keep on crossing in the future.

Lastly, I want to acknowledge my parents, my sister Tatiana, and my girlfriend Mariana. You all gave me the love, support, and motivation I needed from the very beginning to the end of my degree.

Agradecimientos

El trabajo presentado en esta tesis es el resultado de provechosas colaboraciones y el imparable soporte que he recibido a lo largo de este grado. Primero que todo, debo agradecer a mi supervisor Michel J. P. Gingras por apoyarme y crear el ambiente donde mi trabajo y apreciación por los aspectos teóricos y experimentales de magnetismo frustrado pudieron florecer. Agradezco a la supervisora de mi pregrado y maestría Neelima G. Kelkar por guiarme en los primeros pasos que tome a lo largo de la bella y retadora carrera de un fisíco.

También debó agradecer a mis amigos cercanos que tuve el privilegio de conocer, de trabajar y aprender de. Primero que todo debo agradecer a Kristian Chung con quien aprendí la mayoría de la Física que conllevo a los resultados presentados en esta tesis y quien se combirtió en uno de mis más cercanos colaboradores. Alex Hickey, por todas las conversaciones que tuvimos de Física y otros temas que nutrieron nuestro trabajo y amistad. Darren Pereira, por influenciar mi balance entre vida personal y trabajo como también representar un compromiso ejemplar hacia nuestro trabajo, algo que sigo tratando de emular al día de hoy. Itamar Aharony por su único sentido del humor que aligero el ambiente cada vez que teníamos una conversación. Naman Gupta, con quien tuve interminables conversaciones de política y aspectos culturales similares. También debo agradecer a algunos de mis amigos con quienes pude compartir comidas, pensamientos y risas. Wen Jin, Cyrus Cerkauskas, Jennifer Reid, Aritro Mukherjee y Pablo Millan. Trabajar y volverme amigo de cada uno de ustedes sin lugar a duda ha mejorado mi vida en Canada y mi experiencia como estudiante graduado. Espero que nuestros caminos se sigan cruzando en el futuro próximo.

Finalmente, quiero agradecer a mis papas, a mi hermana Tatiana y a mi novia Mariana. Ustedes me dieron el amor, soporte y motivación que necesite desde el principio hasta el final de mi grado.

Dedication

To the four people and two dogs I love the most: my parents, my sister Tatiana, my girlfriend Mariana, and my two huskies Elvis and Maia.

Table of Contents

Examining Committee ii

Author's Declaration iii

Statement of Contribution iv

Abstract v

Acknowledgements vi

Dedication viii

List of Figures xiv

List of Tables xxii

List of Abbreviations xxiii

1 Introduction 1

1.1 Symmetry Breaking in the Ising Model 2

1.2 Geometric Frustration 5

1.3 The Pyrochlore Lattice 6

1.4 An Overview of the Thesis 9

2 Ising and Heisenberg spins **10**

2.1 From Electrons to Pseudo-Spins . . . 11

2.2 Ising Spins . . . 14

2.2.1 Emergent magnetic charges and fluxes . . . 17

2.2.2 Real Space Ising Spins Configurations . . . 21

2.2.3 Spin-ice in systems beyond the nearest-neighbor model . . . 22

2.3 Three-component Spins . . . 24

2.3.1 Magnetically Ordered Phases in the nearest-neighbor Hamiltonian . 26

2.3.2 Order-by-Disorder . . . 28

2.3.3 Spin-liquids in the pyrochlore lattice . . . 31

2.4 Overview of the Next Chapters . . . 34

3 The Tool Box **36**

3.1 Self-Consistent Gaussian Approximation . . . 36

3.1.1 Application to the Heisenberg Antiferromagnet . . . 39

3.2 Classical Low-Temperature Expansion . . . 41

3.2.1 Application to $\mathbf{Er_2Ti_2O_7}$ . . . 43

3.3 Quantum Linear Spin-Wave Theory . . . 44

3.3.1 Application to $\mathbf{Yb_2Ti_2O_7}$ . . . 48

3.4 Irreducible Representation Analysis . . . 49

3.4.1 General Idea . . . 50

3.4.2 Irreducible Representation of the Tetrahedral Group $\mathbf{T_d}$ . . . 52

3.4.3 Application of Irreducible Representation to the Spin Fluctuations in a Low-Temperature Phase . . . 59

3.5 Iterative Minimization . . . 59

3.6 Classical Monte Carlo . . . 60

4 The Heisenberg and Dzyaloshinskii-Moriya Hamiltonian Phase Diagram 63
4.1 The Heisenberg and and DM Hamiltonian . . . 63
4.2 Irrep Analysis . . . 65
4.3 Monte Carlo Simulations: a First Approach . . . 67
4.4 Order-by-Disorder in the $\mathbf{\Gamma_5}$ phase . . . 69
4.5 Monte Carlo Simulations: the $\mathbf{\Gamma_5}$ Manifold . . . 70
4.6 Quantum Phase Diagram . . . 76
4.6.1 PFFRG and HTSE Results . . . 76
4.6.2 Quantum Order-by-Disorder . . . 78
4.7 Conclusion and Outlook . . . 79

5 Order-by-Disorder in the Colinear Ferromagnet 80
5.1 Accidental $\mathbf{O(3)}$ Symmetry . . . 80
5.2 Quantum Thermal Order-by-Disorder . . . 82
5.3 Classical Thermal Order-by-Disorder . . . 85
5.4 Monte Carlo Analysis . . . 87
5.5 Conclusion and Outlook . . . 94

6 An Order-by-Disorder Selected Spin-Liquid 98
6.1 Irrep Analysis and Interaction Matrix . . . 98
6.2 Anisotropic Features in the Neutron Scattering Structure Factor . . . 100
6.3 Monte Carlo: An Order-by-Disorder-Selected Spin-Liquid . . . 104
6.3.1 The Spin-Ice Phase in the $\mathbf{J_{DM}/J = 2}$ Model . . . 110
6.4 Non-Kramers Spin Systems . . . 112
6.5 Conclusion and Outlook . . . 115

7 Theory of Fragmentation **116**
7.1 The Coulomb Phase in the Heisenberg Antiferromagnet 117
7.2 The Single-Ion Anisotropy Model 120
7.2.1 A Classical Low-Temperature Expansion 122
7.2.2 Effective Low-Energy Theory 127
7.3 The Magnon Bands 130
7.4 Pinch Points in $\mathbf{FeF_3}$ and Proximity to Other Spin-Liquids 134
7.5 Conclusion and Outlook 135

8 General Conclusions and Broad Outlook **136**

References **139**

APPENDICES **155**

A Pyrochlore Lattice Vectors and Local Basis **156**

B Neutron Scattering **159**

C High-Symmetry Paths in the Brillouin Zone **162**

D Classical Low-Temperature Expansion in a Field **164**

E Interaction Parameters Basis **166**

F Linear Spin Wave Theory **168**

G High Temperature Series Expansion **171**

H Dipolar-Octupolar Fragmentation Derivation **179**

I Perturbative Monte Carlo **189**

I.1 High temperature-$J_\perp$ expansion 193

I.2 Magnetization 197

I.3 Structure factor 199

I.4 Application to the XXZ model on the square lattice 201

I.5 Conclusions 204

List of Figures

1.1 $\varepsilon(\boldsymbol{q})$ of the Ising ferromagnetic model on a square lattice shown in a contour plot (left) and a 3D plots (right) where we set $J = 1$. 3

1.2 Free energy $\mathcal{F}$ as. a function of m in Eq. (1.4) plotted for decreasing values of a_i corresponding to different temperatures T_i where we have $a_4 < a_3 < a_2 < a_1$. 4

1.3 Two frustrated units: a triangle (left) and a tetrahedron (right). In both cases, the spins are assumed to be Ising and are constrained to point "up" or "down", where an anti-aligned configuration is preferred for antiferromagnetic interactions. In the tetrahedron the "up" direction refers to the spin pointing towards the center of the tetrahedron and the "down" direction to the spin pointing away from the center of the tetrahedron. In both cases, the blue question marks makes reference to the choice where adding an "up" or "down" spin results in the same energy for the resulting configuration. . 6

1.4 Pyrochlore lattice illustrated from two different perspectives. 7

1.5 Pyrochlore lattice where the up tetrahedra are colored in red and the down tetrahedra are colored in blue. 7

2.1 Local $\{\boldsymbol{x}_i, \boldsymbol{y}_i, \boldsymbol{z}_i\}$ directions for the four sublattices in a single tetrahedron. Here the blue, green, and red arrows correspond to the local $\boldsymbol{x}_i, \boldsymbol{y}_i,$ and $\boldsymbol{z}_i$ directions respectively. 11

2.2 Two-in-two-out state in the Ising spins system on the left and in crystallized water on the right where the red sphere represents an oxygen atom and the blue spheres represent hydrogen atoms. 16

2.3 Energy bands of the adjacency matrix (2.12) shown along high-symmetry paths in the $(hh\ell)$] (a), and in the $(hk0)$ (b) planes, and in 3D in $(hh\ell)$] (c), and in the $(hk0)$ (d) planes. We refer the reader to Appendix C for a description of the symmetry paths used. 18

2.4 Neutron structure factor in the spin-ice phase observed in the $(hh\ell)$ (a) and $(hk0)$ (b) scattering planes. 20

2.5 Smallest closed loop form by Ising spins. The remaining spins are not shown as each can adopt two possible configurations fulfilling the ice rules. 21

2.6 (a) Spin-ice configuration in two adjacent tetrahedra. (b) Excited configuration where the cyan spin has been flipped creating a $Q = -2$ (blue) and a $Q = 2$ (red) magnetic charges in the tetrahedra sharing the spin. 22

2.7 $\boldsymbol{q} = \boldsymbol{0}$ orders in a single up tetrahedron where the red arrows depict the spin and the global $\boldsymbol{x}$, $\boldsymbol{y}$, and $\boldsymbol{z}$ are shown in red, green and blue, respectively. 27

2.8 Canted ferromagnetic $\boldsymbol{q} = \boldsymbol{0}$ configurations resulting from a specific combination of the coplanar antiferromagnetic and the colinear ferromagnetic states. 27

2.9 Cartoon picture for the (a) energy landscape of an exact $U(1)$ degenerate manifold. (b) Energy landscape of an accidental $U(1)$ degenerate manifold. In both figures, the color represents the energy and the minimum energy is marked by the dashed white. 30

2.10 Neutron structure factor for the Heisenberg antiferromagnetic model observed in the $(hh\ell)$ (a) and $(hk0)$ (b) scattering planes. These correlation functions were obtained using a SCGA discussed in Section 3.1 for the lowest temperature shown in Fig. 3.1. 33

3.1 Lagrange multiplier as a function of temperature for the Heisenberg antiferromagnet. The red dashed line marks the value $\lambda_0 = 3/2$. 40

3.2 Entropic weight difference between states in the Γ_5 manifold. Here, the entropic difference is taken with respect to the entropic weight of the ψ_3 states. 44

3.3 Neutron elastic structure factor for $Yb_2Ti_2O_7$ in the $(hh\ell)$ plane. 48

3.4 (a) Rotation axis for the C_2, C_3, and S_4 transformations (b) Reflection plane σ_d. 52

3.5 (a) Spin configurations for the $T_{1\parallel}$ (cyan) and $T_{1\perp}$ (orange) irreps.(b) Spin configurations for the T_{1+} (blue) and T_{1-} (red) irreps. Go to this link for an animation on how the irrep modes evolve as a function of the angle θ. . . . 58

4.1 DM vectors for a single tetrahedron. Here the D_{01}, D_{02}, D_{03}, D_{12}, D_{13} and D_{23} are shown. 64

4.2 IEP as a function of the parametrization angle θ. The dashed lines at $\theta = 135°$ and $\theta = 243°$ mark the points where two or more IEPs intersect. . 66

4.3 Phase diagram obtained from the study of the $\{m_I\}$ order parameters. . . 68

4.4 Order parameters susceptibilities χ_I for the E and the $T_{1\perp}$ irreps measured for $\theta = 250°$ (a) and $\theta = 300°$ (b). 69

4.5 Entropic weight difference $\Delta\mathcal{S}$ as a function of the parametrization angle θ. The inset shows the minimum in $\Delta\mathcal{S}$ centered around $\theta \sim 350°$. 70

4.6 ψ_2 (left) and ψ_3 (right) where the spins (red arrows) point along the local x and y axes for ψ_2 and ψ_3, respectively. 71

4.7 Evolution of the m_E and m_{E6} order parameters as a function of temperature for $\theta = 250°$ (a) and $\theta = 300°$ (b). 72

4.8 Temperature dependent phase diagram for the Γ_5 phase illustrating a selection between the ψ_2 and ψ_3 ordering as a function of θ. 73

4.9 Phase diagram obtained from the study of the $\{m_I\}$ order parameters and the m_{E6} parameter. 74

4.10 Panel (a) illustrates the m_E and m_{E6} parameters measured for $\theta = 300°$. Panels (b), (d) and (f) show 2D polar histograms of $\boldsymbol{m}_{E,\mathrm{av}}$. Panels (c), (e) and (g) show 1D histograms of the angle ϕ where the vertical red lines mark multiples of $\pi/6$. Here, the second row (panels (b) and (c)) corresponds to data taken at T_0, the third row (panels (d) and (e)) corresponds to data taken at T_1, and the fourth row (panels (f) and (g)) corresponds to data taken at T_2. 75

4.11 Classical and quantum phase diagram of the Heisenberg and DM Hamiltonian where the outer most ring shows the selection at $T \to 0$ and the middle ring corresponds to the ordered phase selected at T_c as identified by MC. The inner circle corresponds to the magnetic phases as identified by PFFRG. 77

4.12 Zero-point energy correction difference between the ψ_3 and ψ_2 states, i.e. $\Delta E_0 = E_0(\psi_3) - E_0(\psi_2)$. Inset shows a zoomed version of this difference for $\theta \in [344°, 346°]$. 78

5.1 DM vectors between a site i and its nearest neighbors for a single tetrahedron. Note that the orientation of DM vectors can be associated with an oriented closed loop. 82

5.2 Free energy difference $\Delta\mathcal{F}$ for $\theta = 227°$ (a) and $\theta = 240°$ (b). In this diagrams the orientation with the least minimum energy difference is selected. 83

5.3 Phase diagram constructed using the free energy difference $\Delta\mathcal{F}$ obtained through LSW where $\Delta\mathcal{F} < 0$ indicates a $\langle 111 \rangle$ selection and $\Delta\mathcal{F} > 0$ indicates a $\langle 110 \rangle$ selection. 85

5.4 Entropic weight difference $\Delta\mathcal{S}$ for $\theta \in [135°, 243°)$ (a) and $\theta \in [230°, 243°)$ (b). 86

5.5 Temperature evolution of the M_{42}, M_{44}, and M_6 parameters for $\theta = 235°$ (a), $\theta = 238°$ (b), $\theta = 240°$ (c) obtained using classical MC for a system size $L = 12$. Note that for an isotropic system we would expect these parameters to plateau to the values $M_{42} = 3/4$, $M_{44} = 3/5$ and $M_6 = 9/35$. 89

5.6 Total magnetization density plot as sampled from MC for $\theta = 235°$ (a), $\theta = 238°$ (b), and $\theta = 240°$ (c) for the temperature given in the title of each panel. These distributions were obtained for a system size of $L = 12$ for $\theta = 235°, 238°$ and for $L = 10$ for $\theta = 240°$. 91

5.7 Total magnetization density plot as sampled from MC for $\theta = 239°$ sampled at the temperature indicated in the title. 92

5.8 Total magnetization density plot as sampled from MC for $\theta = 235°$ (a), $\theta = 238°$ (b), and $\theta = 240°$ (c) for a temperature close T_c ($T_c = 0.440,\ 0.335,\ 0.224$ for $\theta = 235°,\ 238°, 240°$, respectively) where the exact value of the temperature is given in the title of each panel. These distributions were obtained for a system size of $L = 12$ for $\theta = 235°, 238°$ and for $L = 10$ for $\theta = 240°$. . 93

5.9 Total magnetization density plot as sampled from MC for $\theta = 240°$ for the temperatures given in the title of each panel. These distributions were obtained for a system size of $L = 10$. 94

5.10 Approximate phase diagram of the ferromagnetic phase with the magnetization orientations identified using through MC. 95

5.11 Specific heat for different values of θ approaching the Γ_5 phase. 96

5.12 Irrep order parameters as a function of temperature for angles θ close to $\theta = 243°$. 97

6.1 Interaction matrix energy bands of the Heisenberg and DM model with $J_{\mathrm{DM}}/J = 2$ plotted along high-symmetry paths in the $(hh\ell)$ (a) and $(hk0)$ (b) planes. We refer the reader to Appendix C for more details of the high-symmetry paths chosen. 99

6.2 Lagrange multiplier λ obtained for the $J_{\mathrm{DM}}/J = 2$ model. 101

6.3 Neutron structure factor for the $J_{\mathrm{DM}}/J = 2$ model in the $(hh\ell)$ (a) and $(hk0)$ (b) planes obtained using a SCGA. 102

6.4 Chain of tetrahedra where each tetrahedron is in a T_1^{xy} (a) and ψ_2 (b) configuration. Note that the two configurations only differ by the flipping of blue spins. 103

6.5 Energy (left) and specific heat (right) obtained through MC for the $J_{\mathrm{DM}}/J = 2$ model. We label the temperature at maximum of the specific heat as T^*. Both functions were obtained for a system size $L = 10$. 105

6.6 Specific heat measured for the $J_{\mathrm{DM}}/J = 2$ model for various systems sizes L. Note that the specific heat bump centered at T^* does not sharpen as L is increased. 105

6.7 Neutron structure factors for the $J_{\mathrm{DM}}/J = 2$ model above (a) and below (b) the temperature T^*. In each panel the left plot corresponds to the $(hh\ell)$ plane and the right plot to the $(hk0)$ plane. These structure factors were obtained for a system size $L = 10$. 107

6.8 P^z_{local} projection as a function of temperature measured through MC for an $L = 10$ system. 108

6.9 Neutron structure factors in the $(hh\ell)$ (left) and $(hk0)$ (right) obtained using IM for a system of size $L = 10$ and $N_{\mathrm{meas}} = 1000$. 109

6.10 Polarized neutron structure factors in the $(hh\ell)$ (left column) and $(hk0)$ (right column) obtained using MC for a system of size $L = 10$. 111

6.11 Average value of the NSF channel in the $(hh\ell)$ plane as a function of temperature. Here the lower three temperatures are below T^*, and the red dashed line marks the value predicted for the flat NSF for the spin-ice phase observed in the nearest-neighbor Ising Hamiltonian [3]. 112

6.12 Classical phase diagram obtained using an irrep analysis. This phase diagram agrees to the one reported by Ref. [4]. Here the lower black dot represents the $J_{\mathrm{DM}}/J = 2$ model and the upper black dot the dual model. . 113

6.13 Neutron structure factors for the dual model below the temperature T^*.The left plot corresponds to the $(hh\ell)$ plane and the right plot to the $(hk0)$ plane. These structure factors were obtained for a system size $L = 10$. 114

7.1 Energy bands of the interaction matrix of the Heisenberg antiferromagnet illustrated in two high-symmetry paths in the $(hh\ell)$ (a) and $(hk0)$ (b). . . 118

7.2 Bands of the Heisenberg antiferromagnetic model colored by the projection P_{Irrot} in a high-symmetry path in the $(hh\ell)$ (upper plot) and $(hk0)$ (lower plot) planes. 120

7.3 Neutron scattering in the $(hh\ell)$ plane obtained through MC simulations for a system size $L = 10$. The temperatures at which these correlation function were obtained are shown in the title of each panel. For both $T < T_c$ and $T \ll T_c$, we have removed the magnetic Bragg peaks to expose the diffuse scattering pattern. 121

7.4 Energy bands of the interaction matrix of the single-ion-anisotropy model in Eq. (7.11) illustrated in two high-symmetry paths in the $(hh\ell)$ (a) and $(hk0)$ (b). 122

7.5 Neutron structure factor in the $(hh\ell)$ (a) and $(hk0)$ (b) planes obtained using a CLTE. These correlation functions were obtained using Eq. (3.13) where the temperature prefactor is not taken into account. 123

7.6 Energy bands of the Hessian along a high-symmetry path in the $(hh\ell)$ plane colored by the irrotational projection P_{Irrot}. 126

7.7 Neutron structure factor in the $(hh\ell)$ (a) and $(hk0)$ (b) obtained using a CLTE considering the contribution of only the two lowest bands. The white arrows in the $(hk0)$ plane illustrate the location of the twofold and fourfold pinch pints. 127

7.8 (a) Magnon bands of the single-ion anisotropy Hamiltonian in a high-symmetry path in the $(hh\ell)$ plane where we have considered $J = 1$ meV and $d = -0.25$ meV. Here we have used a Gaussian function to make the magnon bands wider to mimic what would be observed in an experiment. (b) Energy integrated inelastic neutron scattering obtained from integrating the contribution of the magnon bands shown in panel (a). 131

7.9 Magnon bands of the single-ion anisotropy Hamiltonian in a high-symmetry path in the $(hh\ell)$ plane where we have considered $J = 1$ meV and $d = -0.25$ meV. The coloring of the bands is obtained by using the P_{Irrot} projection where $P_{\text{Irrot}} = 0$ (blue) means that the corresponding mode is fully rotational, $P_{\text{Irrot}} = 1$ (red) means that the corresponding mode is fully irrotational, and $0 < P_{\text{Irrot}} < 1$ means that the corresponding mode has a mixed rotational-irrotational nature. Here the white dashed line represents ω_{cut}. . 132

7.10 Energy integrated inelastic neutron scattering obtained from integrating the contribution of the two lower magnon bands in the $(hh\ell)$ (left) and $(hk0)$ (right) planes. 133

7.11 Energy integrated inelastic neutron scattering obtained from integrating the contribution of the third magnon band in the $(hh\ell)$ (left) and $(hk0)$ (right) planes. These figures present discontinuous and highly varying features (noise) in sections where two magnon bands cross, i.e. energy degeneracy lines in the magnon bands. In other words, these features are numerical artifacts resulting from separating the contribution of the modes at these degeneracy lines. 133

7.12 Magnon bands for the Heisenberg and DM Hamiltonian with $J = 1$meV, $J_{\text{DM}} = 0.02/\text{meV}$ (upper plot). 134

A.1 Pyrochlore lattice for a single FCC unit cell where the FCC vectors $\{\boldsymbol{R}\}$ are illustrated in red and the sublattice vectors $\{\boldsymbol{r}\}$ are shown in blue. Here the size of the box, i.e. the cubic unit cell, is r_c. 158

B.1 An scattered neutron with wave vector $\boldsymbol{q}$ in the $(hh\ell)$ scattering plane where the incident neutron initial polarization axis is $\hat{z}_s \parallel (1\bar{1}0)$, and the local basis defined by the direction of wave vector $\boldsymbol{q}$ and the polarization axis $\hat{z}_s$ is shown. 159

C.1 High-symmetry paths demarked in red in the $(hk0)$ (left) and $(hh\ell)$ (right) planes. The black dots denote the boundary between different Brillouin zones. 162

C.2 3D high-symmetry paths and points illustrated in different two perspectives. 163

I.1 Nearest neighbors diagram for a square lattice. The center site in black is the base site, red sites as the first neighbors, blue sites as the second nearest neighbors, and green sites as the third nearest neighbors. 202

I.2 Energy curves for $J_\perp = -0.5J$. 203

I.3 Moments of the magnetization obtained through PMC and QMC simulations for $J_\perp = -0.07J$ (a) $\langle M^2 \rangle$, (b) $\langle M^4 \rangle$. 203

I.4 Binder ratio obtained by QMC and PMC for $J_\perp = -0.07J$. 204

I.5 Phase diagram for the XXZ model with ferromagnetic interactions obtained through QMC and PMC simulations. 204

List of Tables

3.1 Character table of the group T_d where the numbers represent the value of the character $\chi(g)$ for the block represented by the corresponding irrep. . . 53

C.1 High-symmetry points 163

List of Abbreviations

AIAO	All-in-All-out
CLTE	Classical low-temperature expansion
DM	Dzyaloshinskii-Moriya
FCC	Face-centered cubic
HP	Holstein-Primakoff
IEP	Irrep energy parameter
Irrep	Irreducible representation
LRO	Long-range order
LSW	Linear spin-waves
MC	Monte Carlo
ML	Machine Learning
NSF	Non-spin-flip
ObD	Order-by-Disorder
PC	Palmer-Chalker
PMC	Perturbative Monte Carlo
SCGA	Self-consistent gaussian approximation
SF	Spin-flip

Chapter 1

Introduction

One of the most challenging and interesting concepts to study is collective phenomena. The possibility that the collective behavior of individual constituents differ, and could even realize some type of emergent behavior only observed at large scales has been exemplified in different fields as biology, with the flocks of birds [5], economy, with the behavior of stock markets [6] and, to the preference of the author of this thesis, in physics where multiple examples could be provided. In condensed matter, systems presenting collective phenomena are perhaps one of the most studied as these often exhibit exotic behavior resulting from seemingly simple microscopic principles. In this context, the study of systems where superconductivity, topological insulators, and spin-liquids have been observed or predicted has captivated the physics community in the last decades. In this regard, the study of magnetic systems, where phenomena as symmetry breaking, highly-correlated disorder states, and topological excitations have been observed, may represent an almost ideal platform to study collective behavior.

Magnetism is one of the oldest physical phenomenon known to humanity where historical records indicate that the ancient Greeks and Chinese observed it in iron-rich magnetic stones known as "lodestones". In condensed matter, magnetism is one of the most fundamental phenomenon which often represents an ideal platform to first approach and study collective behavior by studying the Ising model [7] on a square lattice where a symmetry-breaking transition at a temperature T_c to a long-range ordered state is observed. Interestingly, this same model on different lattices may lead to entirely different low-temperature states as a consequence of geometrical frustration. In this chapter, we provide a brief introduction to symmetry-breaking, the Landau theory used to describe it, geometrical frustration, and the pyrochlore lattice.

1.1 Symmetry Breaking in the Ising Model

The Ising model in a square lattice is one of the simplest and most studied physical systems in condensed matter. This model consists on discrete variables located at the vertices of a lattice representing magnetic dipoles, which we call spins, that can take values of ± 1 representing two possible orientations "up" or "down". For the nearest-neighbor ferromagnetic Ising model, the spins interact with each other where being "align" with their nearest-neighbor s is energetically preferred. The Hamiltonian, i.e. energy function, describing such system is given by

$$\mathcal{H} = J \sum_{\langle ij \rangle} \sigma_i^z \sigma_j^z, \tag{1.1}$$

where i and j denote the vertices of the lattice considered, $\sigma_i^z = \pm 1$ denote the spin variable at site i, $\langle ij \rangle$ denotes i and j nearest neighbors, and $J < 0$ for the ferromagnetic case. In the Hamiltonian (1.1) each term can be minimized by "aligning" neighboring spins along the same direction, i.e. $\sigma^z = 1$ or $\sigma^z = -1$ for neighboring spins. At high temperatures, i.e. $T/|J| \gg 1$, a system described by the Ising model is in a paramagnetic phase where the spins take random orientations $\sigma_i^z = \pm 1$. In contrast, for a ferromagnetic J, at low temperatures the spins tend to be aligned effectively minimizing the energy of the system. This model therefore presents a *symmetry breaking* transition at a temperature $T_c \sim J$ from a paramagnetic phase to a ferromagnetic phase.

The spin configuration which minimizes the energy associated with the Hamiltonian (1.1) can be identified by performing a Fourier transformation of the spin variables into the reciprocal space basis

$$\sigma^z(\boldsymbol{q}) = \frac{1}{\sqrt{N}} \sum_{\boldsymbol{i}} \sigma_i^z e^{i \boldsymbol{r}_i \cdot \boldsymbol{q}}, \tag{1.2}$$

where $\boldsymbol{r}_i$ is the location of the spin i, N is the number of spins in the system, and $\boldsymbol{q}$ are the reciprocal space vectors. Applying the inverse of this transformation to the Hamiltonian (1.1) on a square lattice yields the diagonal reciprocal space Hamiltonian

$$\begin{aligned} \mathcal{H} &= \sum_{\boldsymbol{q}} \left(\frac{J}{2} \sum_{\boldsymbol{\delta}} \cos\left(\boldsymbol{q} \cdot \boldsymbol{\delta}\right) \right) \left| \sigma^z(\boldsymbol{q}) \right|^2 \\ &= \sum_{\boldsymbol{q}} \varepsilon(\boldsymbol{q}) \left| \sigma^z(\boldsymbol{q}) \right|^2 \end{aligned} \tag{1.3}$$

where $\boldsymbol{\delta}$ represents the nearest-neighbor translation vectors. For the square lattice we have $\varepsilon(\boldsymbol{q}) = J(\cos(q_x r_c) + \cos(q_y r_c))$ where r_c is the nearest neighbor distance, see Fig. 1.1. The

eigen mode $\sigma^z(\boldsymbol{q})$ which minimizes the energy function $\varepsilon(\boldsymbol{q})$ is expected to dominate the low-temperature physics and therefore identify the corresponding low-temperature configuration. For the ferromagnetic case we therefore expect the $\boldsymbol{q} = \boldsymbol{0}$ state which in real space translates to having all spins up or down.

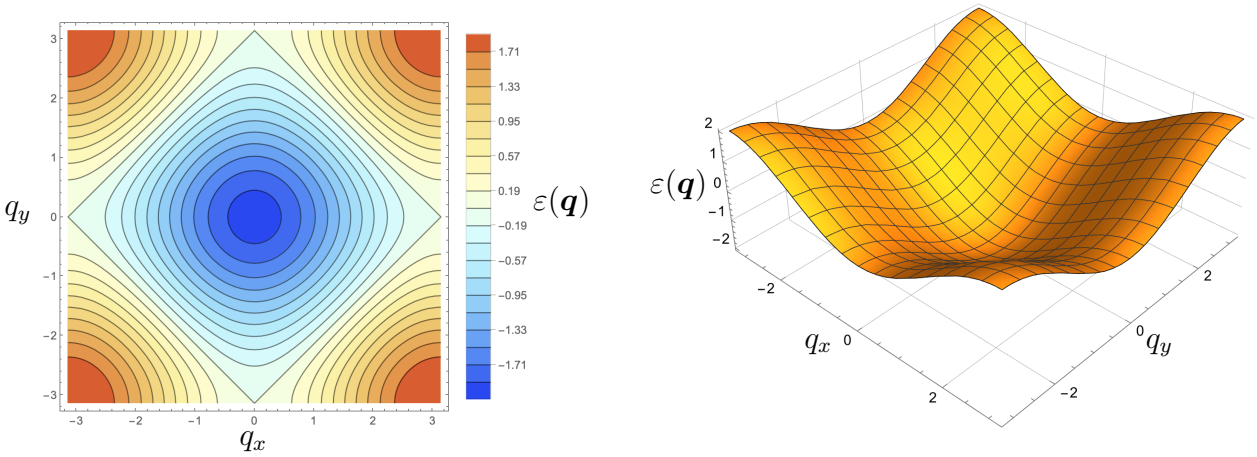


Figure 1.1: $\varepsilon(\boldsymbol{q})$ of the Ising ferromagnetic model on a square lattice shown in a contour plot (left) and a 3D plots (right) where we set $J = 1$.

The transition between the high-temperature disorder state and the low-temperature ordered state at T_c can be described by a Landau theory where an *order parameter* m can be used to signal the transition from the disordered phase, where $m = 0$, to the ordered phase where m acquires a finite value. This theory takes as its starting assumption that the free energy $\mathcal{F}$ of the system is a smooth function of the order parameter m. Close to the phase transition at T_c we may approximate the free energy function by considering symmetry-allowed powers of the order parameter m. For the ferromagnetic Ising model, the order parameter m is the total magnetic moment, $m = \frac{1}{N}\sum_i \sigma_i^z$, and the free energy theory is constraint to be invariant under the flipping the signs of all spins. This constraint results in the landau free energy theory

$$\mathcal{F} \quad = \quad \mathcal{F}_0 + am^2 + bm^4 + O(m^6), \tag{1.4}$$

where a and b are temperature dependent parameters and $\mathcal{F}_0$ is a constant that we may set to zero. The values of a and b can be deducted by minimizing the free energy with respect to m, this is

$$\frac{\delta \mathcal{F}}{\delta m} = 2am + 4bm^3 = 0 \rightarrow m(a + 2bm^2) = 0 \tag{1.5}$$

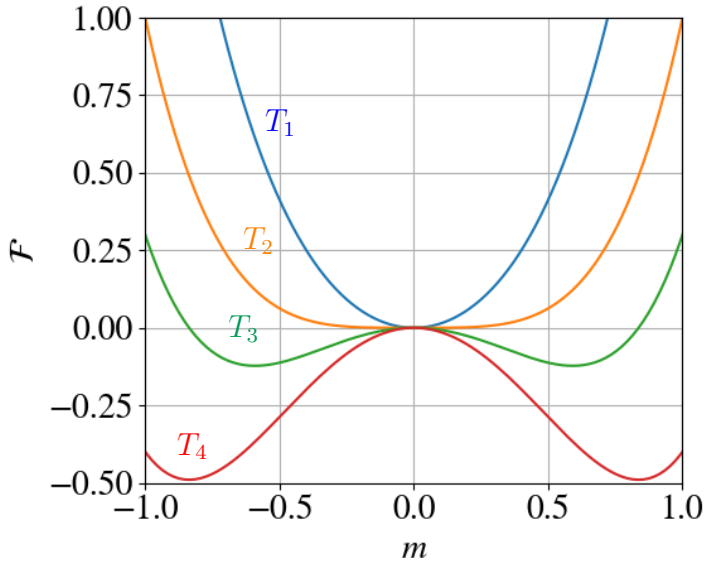


Figure 1.2: Free energy $\mathcal{F}$ as. a function of m in Eq. (1.4) plotted for decreasing values of a_i corresponding to different temperatures T_i where we have $a_4 < a_3 < a_2 < a_1$.

Above T_c, we have $m = 0$ and therefore $a, b > 0$. In contrast, below T_c, m acquires a finite value, $m = \sqrt{-a/(2b)}$, which can be solved by considering $a = a_0 \frac{T-T_c}{T}$ and $b = b_0$ where a_0 and b_0 are positive constants. Fig. 1.2 shows the free energy as a function of the order parameter m for various values of a. In this figure, $a_1 > 0$ corresponds to a temperature above T_c ($T_1 > T_0$), $a_2 = 0$ corresponds to T_c ($T_2 = T_c$), and $a_3, a_4 < 0$ for temperatures below Tc ($T_c > T_3 > T_4$). This analysis therefore predicts the evolution of the order parameter below T_c to be

$$m = \sqrt{\frac{a_0(T_c - T)}{2b_0 T}}. \tag{1.6}$$

Although an exact solution of the Ising model in a square lattice shows that $m \propto \left(\frac{T_c-T}{T}\right)^{1/8}$ [8], the Landau formalism is an excellent starting point when describing a disorder to order transition. Moreover, we note that this formalism is exactly the same for an Ising ferromagnetic model in any other 2D lattice, as are the triangular, honeycomb, kagomé, lattices, and lattices in 3D and higher dimensions.

An equivalent behavior would have been obtained for the antiferromagnetic Ising model on a square lattice where the order parameter would now be the staggered magnetization,

i.e. $m = \sum_{i\in A} \sigma_i^z - \sum_{i\in B} \sigma_i^z$ where A and B represent a partition of the sites of the square lattice such that every A site only has B site nearest-neighbors and vise-versa. For the antiferromagnetic model on the square lattice, the energy $\varepsilon(\boldsymbol{q}) = J(\cos(q_x r_c)+\cos(q_y r_c))$ in Eq. (1.3) would now be minimized at $\boldsymbol{q} = [\pi/r_c, \pi/r_c]$ which translates in a Néel state where the spins in the A sites point up (down) while the spins in the B sites point down (up), therefore minimizing the energy associated with every pairwise set of neighbors $\sigma_i^z\sigma_j^z = -1$[1]. A Landau free energy analysis for the antiferromagnetic Ising model on a square lattice would then result in the same predictions as for the ferromagnetic model for the evolution of the order parameter. However, and in contrast to the ferromagnetic case, this description cannot be extended to all other 2D lattices [9] nor 3D lattices [10]. This is for example the case of the kagomé and pyrochlore lattices where *geometric frustration* may prevent the system from ordering at low temperatures, resulting in far more interesting low-temperature configurations, and another expression of collective behavior. In fact, an analysis of the energy bands $\varepsilon(\boldsymbol{q})$ for these lattices identifies an *extensive* number of $\boldsymbol{q}$ points at which this function acquires its minimum value and therefore preventing the system from adopting a single configuration describing the low-temperature state.

1.2 Geometric Frustration

In magnetism, geometric frustration refers to the conflicting interactions resulting from the position of the interacting magnetic particles which prevents every pairwise interaction to be minimized. For the nearest-neighbor Ising antiferromagnet, geometric frustration in a lattice can be seen whenever the spins share a set of nearest neighbors[2]. Such scenario is fulfilled for lattices constructed by frustrated units where all the spins are nearest neighbors. The smallest and simplest example of a frustrated unit is a triangle with which we can construct the triangular [9] and kagomé [11] lattices in 2D, and the face-centered cubic (FCC) [12], pyrochlore [13], hyper-kagomé [14] and trillium [15] lattices in 3D. Since the Ising antiferromagnetic interaction is minimized by "anti-aligning" nearest-neighbors, all the pairwise interaction in a frustrated unit cannot be minimized simultaneously which can result in extensively degenerate ground state manifolds and therefore exotic low-temperature physics, see Fig. 1.3[3].

[1] Another way of thinking about this is to simply flip the $\varepsilon(\boldsymbol{q})$ function shown in Fig. 1.1 where now the minimum is at $\boldsymbol{q} = [\pi/r_c, \pi/r_c]$.

[2] This could be easily remembered by the phrase "My neighbor's neighbor is my neighbor".

[3] As a side note, this is somewhat similar to the Greek tragedy where an unstoppable force meets an unmovable object. In other words, the system is faced with a decision of where to make the spin point in a frustrated unit where both outcomes are equally good and bad at the same time.

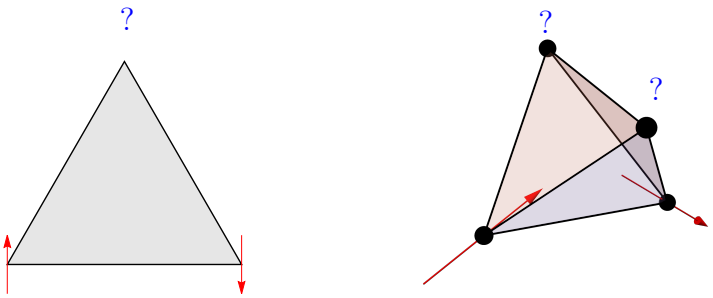


Figure 1.3: Two frustrated units: a triangle (left) and a tetrahedron (right). In both cases, the spins are assumed to be Ising and are constrained to point "up" or "down", where an anti-aligned configuration is preferred for antiferromagnetic interactions. In the tetrahedron the "up" direction refers to the spin pointing towards the center of the tetrahedron and the "down" direction to the spin pointing away from the center of the tetrahedron. In both cases, the blue question marks makes reference to the choice where adding an "up" or "down" spin results in the same energy for the resulting configuration.

Although we have focused our discussion on the Ising model, geometric frustration is not limited to such interactions or spins. In fact, magnetic systems with other spin degrees of freedom and interactions in a geometrically frustrated lattice may also display exotic collective behavior. Perhaps some of the most influential work pointing out how frustration in magnetism could lead to exotic new behavior at low temperatures was authored by Phil Anderson [16, 17]. In his work, Anderson highlighted how the combination of frustration and low spin values could lead to a spin-liquid phase [18], a highly-disordered yet highly-correlated state. The possibility of such state sparked an increasing interest in the study of geometrically frustrated systems. The work presented in this thesis is focused in the study of the pyrochlore lattice.

1.3 The Pyrochlore Lattice

The word pyrochlore comes from greek *pyro-* ($\pi\upsilon\rho$) *-chlore* ($\chi\lambda\omega\rho o\zeta$) meaning *green fire* as a direct reference to the color the first occurrence of a material described by this lattice structure turned when ignited. The magnetic pyrochlore lattice is a network of corner-sharing tetrahedra where the spin degrees of freedom are located at the corners of each tetrahedron, see Fig. 1.4, whose symmetry group, and therefore the allowed lattice transformations, are given by the $Fd3m$ space group. In this corner-sharing network, the tetrahedra can be

labeled as "up" or "down" tetrahedra[4], see Fig. 1.5. An alternative way of visualizing this lattice is to consider face-centered cubic lattice with a sublattice structure of four sites forming the up tetrahedra, where the 0^{th} sublattices are located at every face-centered cubic vector. For a more detailed presentation of the lattice positioning of the spins we refer the reader to Appendix A.

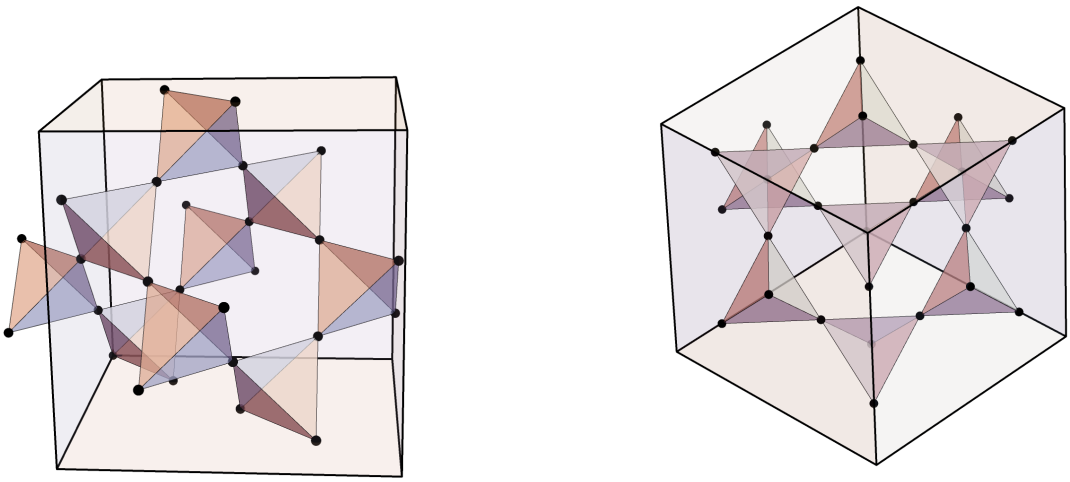


Figure 1.4: Pyrochlore lattice illustrated from two different perspectives.

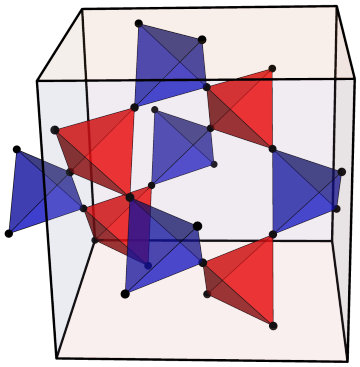


Figure 1.5: Pyrochlore lattice where the up tetrahedra are colored in red and the down tetrahedra are colored in blue.

[4]This labeling therefore implies that each up tetrahedron share its corners with the adjacent down tetrahedra

During the last few decades the pyrochlore lattice has received increasing attention partly as a consequence of the many compounds that have been synthesized realizing this structure [19–21], this includes the increasing number of pyrochlore oxides of the form $A_2B_2O_7$ compounds [19, 20, 22, 23], where A is a $4f$ rare-earth magnetic ion, and the AB_2X_4 spinel compounds [19, 24], where B is a $3d-5d$ magnetic ion. At low temperatures, the electronic structure of the magnetic ions in these compounds is often found in a ground state doublet which allows the description of the low-temperature physics by pseudo-spin 1/2 operators interacting via an effective Hamiltonian [23]. The competing interactions on this lattice may result in exotic phenomena such as order-by-disorder selection [25], the magnon Hall-effect [26], magnetic moment fragmentation [27], and the realization of spin-liquids in both classical [28] and quantum [29] models. In fact, the pyrochlore lattice is well known for hosting a classical spin-liquid dubbed spin-ice [13, 28] realized in the compounds $Ho_2Ti_2O_7$ [30] and $Dy_2Ti_2O_7$ [31], and more recently a promising quantum spin-liquid candidate in the magnetic compound $Ce_2Zr_2O_7$ [29]. The liquid-like correlations in these compounds result in the observation of sharp anisotropic features in their correlation functions, signaling the strong correlations observed in these phases. In this regard, the search of such exotic phases has been greatly benefited by the study of unpolarized neutron scattering (Eq. (1.7)) which provides a measurement of the spin-spin correlations $\chi^{\alpha\gamma}_{ab}(\boldsymbol{q})$ of a compound

$$S_{\perp}(\mathbf{q}) = \sum_{\alpha\gamma}\sum_{ab} \underbrace{\left(\delta_{\alpha\beta} - \frac{q_\alpha q_\gamma}{\boldsymbol{q}^2}\right)}_{\text{Neutron Projector}} \chi^{\alpha\gamma}_{ab}(\boldsymbol{q}), \tag{1.7}$$

$$\chi^{\alpha\gamma}_{ab} = \int_{-\infty}^{\infty} dt\ e^{i\omega t}\langle \mu^{\alpha}_{a}(\boldsymbol{q},0)\mu^{\gamma}_{b}(-\boldsymbol{q},t)\rangle, \tag{1.8}$$

$$\mu^{\alpha}_{a}(\boldsymbol{q},t) = \frac{1}{\sqrt{N}}\sum_{i}\mu^{\alpha}_{ia}(t)e^{i\boldsymbol{r}_{ia}\cdot\boldsymbol{q}}, \tag{1.9}$$

where μ^{α}_{ia} refers to the α component magnetic moment $\boldsymbol{\mu}_{ia}$ at the FCC site i and sublattice a [32], and the neutron projector factor filters the perpendicular components of the moments $\boldsymbol{\mu}$[5]. Additional information from the study of neutron scattering, and therefore the correlation function, can be obtained by considering the *polarized* neutron scattering which decomposes the neutron scattering into the non-spin-flip (NSF) and the spin-flip

[5]This filtering is a simple consequence of the divergence-free condition in the magnetic fields $\nabla\cdot\boldsymbol{B}$, which in reciprocal space translates in $\boldsymbol{q}\cdot\boldsymbol{B}=0$, where $\boldsymbol{B}$ is a magnetic field and which for spin models is produced by the magnetic moments at each point of the lattice.

(SF) channels

$$S_{\perp}^{\mathrm{NSF}}(\mathbf{q}) = \sum_{ab}\sum_{\alpha,\beta}\left(z_s^{\alpha} z_s^{\beta}\right)\chi_{ab}^{\alpha,\gamma}(\boldsymbol{q}), \tag{1.10}$$

$$S_{\perp}^{\mathrm{SF}}(\mathbf{q}) = S_{\perp}(\mathbf{q}) - S_{\perp}^{\mathrm{NSF}}(\mathbf{q}), \tag{1.11}$$

where z_s is the scattering vector along which the neutrons are initially polarized. We refer the reader to Appendix B for more details regarding these functions and Appendix C for details in the reciprocal space high-symmetry planes and paths used to study the neutron structure factor in this work.

1.4 An Overview of the Thesis

In this thesis, we study symmetry-breaking, order-by-disorder, Fragmentation, and the realization of a novel spin-liquid phase in the pyrochlore lattice. Although our results are mainly focused on the Heisenberg and Dzyaloshinskii-Moriya model, the tools and analysis presented in this thesis can be extended and used to study other magnetic Hamiltonian in the pyrochlore lattice.

In Chapter 2, we present a brief overview of how the magnetic Hamiltonians in pyrochlore lattice are obtained, discuss some of the allowed nearest-neighbor interactions when considering Ising and Heisenberg spin degrees of freedom, and give a first introduction to the collective magnetic phenomena studied in this thesis. Chapter 3 is dedicated to present the analytical and numerical techniques we have used and developed to perform our analysis. This chapter also provides examples of the application of some of these approaches. In Chapters 4 and 5, we present a quantum and classical phase diagram for the Heisenberg and Dzyaloshinskii-Moriya Hamiltonian and expose the order-by-disorder selection present in some of the identified phases. In Chapter 6, we study an instance of the Heisenberg and Dzyaloshinskii-Moriya model where a novel spin-liquid phase is identified separated by a crossover at a temperature T^* to a spin-ice spin-liquid phase. We argue that an order-by-disorder mechanism might be responsible for the distinct spin-liquid phases above and below T^*. In Chapter 7, we study how a magnetically ordered phase in the vicinity of a spin-liquid phase can present remnant correlations indicative of the proximity to the spin-liquid. We mainly focus on ordered phases proximate to the Coulomb spin-liquid, but expect that our results can be generalized to other spin-liquids. Lastly, in Chapter 8, we provide a summary and conclusion of the work presented in this thesis.

Chapter 2

Ising and Heisenberg spins

In this chapter, an overview of the origin of the pseudo-spin degrees of freedom and the magnetic Hamiltonians consisting of nearest-neighbor interactions between the pseudo-spins in the pyrochlore lattice is presented. These Hamiltonians descent from the different symmetry allowed interactions between the pseudo-spin at each site of the pyrochlore lattice which can be related to a magnetic moment $\boldsymbol{\mu}_i$ at site i

$$\boldsymbol{\mu}_i = -\mu_{\mathrm{B}} \left[g_z \boldsymbol{z}_i \hat{S}_i^z + g_{\pm} (\boldsymbol{x}_i \hat{S}_i^x + \boldsymbol{y}_i \hat{S}_i^y) \right], \tag{2.1}$$

where $\{\boldsymbol{x}_i, \boldsymbol{y}_i, \boldsymbol{z}_i\}$ define the *local* basis at site i with $\boldsymbol{z}_i$ is oriented along the local [111] direction, $\boldsymbol{y}_i$ along the C_2 axis[1], $\boldsymbol{x}_i = \boldsymbol{y}_i \times \boldsymbol{z}_i$, and $\{\hat{S}_i^x, \hat{S}_i^y, \hat{S}_i^z\}$ are the effective pseudo-spin operators at site i, see Fig. 2.1.

After motivating the use of the pseudo-spin degrees of freedom, we present the possible nearest-neighbor magnetic Hamiltonians in the pyrochlore lattice where the magnetic moments are Ising or Heisenberg-like. First, systems with Ising spins are presented where special attention is provided to the antiferromagnetic nearest-neighbor model whose ground state is described by the so-called *spin-ice* states. Then, for Heisenberg spins, a general overview of the allowed nearest-neighbor interactions, the $\boldsymbol{q} = 0$ ground state configurations, and some of the possible exotic ground states are provided.

[1] This is $(1\bar{1}1)$ for the 0^{th} sublattice.

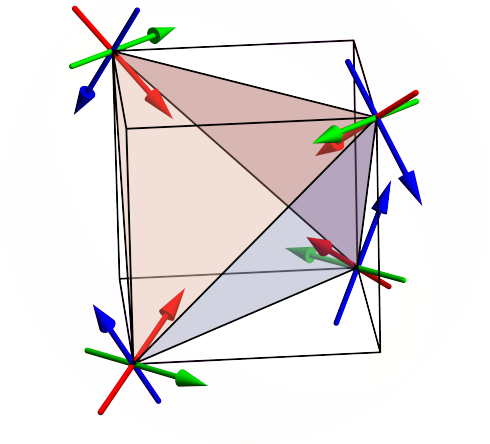


Figure 2.1: Local $\{\boldsymbol{x}_i, \boldsymbol{y}_i, \boldsymbol{z}_i\}$ directions for the four sublattices in a single tetrahedron. Here the blue, green, and red arrows correspond to the local $\boldsymbol{x}_i, \boldsymbol{y}_i$, and $\boldsymbol{z}_i$ directions respectively.

2.1 From Electrons to Pseudo-Spins

Since most of the magnetic compounds relevant for the analysis and discussion in this thesis are composed of rare-earth elements, the brief overview of the pseudo-spin degrees of freedom presented here is focused on the magnetic Hamiltonians relevant to these rare-earth based magnets. In particular, the work presented in this thesis is mostly applied to compounds of the form $A_2B_2O_7$, where A is a trivalent magnetic rare-earth ion, B is a non-magnetic transition metal, and O are oxygen atoms. In these compounds, the A and B ions arrange in two interpenetrating pyrochlore lattices. For a more detailed discussion, we refer the reader to [23, 33, 34].

The 4f electrons in a rare-earth ion can be considered to be well isolated from electrons in other ions due to the the radial dependence of its wave function. This observation can be translated into a hierarchy of energies where single-ion physics dominates over two-ion exchange. In other words, single-ion physics must first be considered towards the derivation of an effective model. For a single rare-earth ion, the 4f electrons are subject to Coulomb interactions, spin-orbit coupling, and a crystal field produced by the environment of the ion, where the first two interactions dominate over the crystal field. The many-body ground state can be found by first minimizing the Coulomb and spin-orbit coupling interactions by applying Hund's rules [33] resulting on a set of many-body states with a definite total

angular momentum J[2] and a degeneracy of $(2J+1)$ for the ground state, i.e. $|J, m_J\rangle$. Next, the application of the crystal field splits the $(2J+1)$ many-body states. In particular, we are interested in systems where the crystal field ground state is describe by a doublet we label $|\pm\rangle$, which is a linear combination of total angular momentum states $|J, m_J\rangle$. In fact, the realization of this ground state doublet represents a key ingredient in the derivation of an effective pseudo-spin model: the effective model is obtained by projecting the full Hamiltonian into its ground state doublet subspace [23]. A ground state doublet can be realized in two ways depending on the number of 4f electrons in the ion[3]. For ions with an odd number of electrons, and hence a half-integer total angular momentum J, Kramers' theorem [35] implies that all the resulting crystal field states are doubly degenerate[4] which in turn yields a doublet as the ground state. On the other hand, for ions with an even number of electrons the two-fold degeneracy in the ground state must be imposed by the crystal symmetry.

The gap produced between the crystal field ground state and the first excited state is considerably higher than the energy of the two-ion interactions [36–38][5]. Consequently, at temperatures well below the gap energy, we can restrict the analysis to the ground state, assuming that the crystal field excited states are unpopulated, and then consider the effect of the two-ion exchange. This procedure yields an effective low-temperature Hilbert space in each ion consisting of only two states (the double $|\pm\rangle$), which can be effectively described in terms of a pseudo-spin 1/2 system using the operators

$$\hat{S}^z \equiv \frac{1}{2}\left(|+\rangle\langle+| - |-\rangle\langle-|\right), \quad \hat{S}^+ \equiv |+\rangle\langle-|, \quad \hat{S}^- \equiv |-\rangle\langle+|. \tag{2.2}$$

Note that the resulting pseudo-spin operators are *not* required to transform as an angular momentum operator, as one would naively expect for a simple spin 1/2 system [39]. This disparity stems from the definition of the pseudo-spin operators in Eq. (2.2), where the raising and lowering operators connecting the two ground states $|\pm\rangle$ may be composed by more than one angular momentum operator $\hat{J}^{\pm}$. This seemingly simple difference results

[2] As the spin-orbit coupling dominates over the crystal field interactions, the total angular momentum J is a good quantum number. Note that this is not the case when dealing with magnetic ions where the valence electrons are located in other orbitals, for example the d electrons.

[3] Note that this sole observation classifies the rare-earth elements according to the number of unpaired electrons in the 4f orbital

[4] Kramers' theorem relates the two distinct states by unitary transformation which relies on the total angular momentum J. If the angular momentum is a half-integer the two states are guaranteed to be different.

[5] This is usually around $10 - 100\text{K} \sim 1 - 10\text{meV}$, whereas the as two-ion interactions are around $0.01 - 0.5\text{meV}$

in entirely different magnetic behavior where the pseudo-spin operators may transform as magnetic dipoles, quadrupoles, or octupoles [23], where the magnetic moment $\boldsymbol{\mu}_i$ in Eq. (2.1) is only carried by those components which transform as dipoles. The pseudo-spin operators can then be assembled to find the symmetry-allowed bilinear exchange interactions. Depending on how these operators transform, we can broadly identify three distinct types of allowed Hamiltonians which can be sub-classified as Kramers or non-Kramers. More specifically, these three cases are usually referred to as the effective spin-1/2 (Kramers), non-Kramers, and dipolar-octupolar Hamiltonians (Kramers).

The effective spin-1/2 (Kramers) Hamiltonian has all pseudo-spin operators transforming as magnetic dipoles yielding

$$\begin{aligned}\mathcal{H} = \sum_{\langle ij \rangle} \Big[J_{zz} \hat{S}_i^z \hat{S}_j^z \;\; - \;\; & J_{\pm} \left(\hat{S}_i^+ \hat{S}_j^- + \hat{S}_i^- \hat{S}_j^+ \right) + J_{\pm\pm} \left(\gamma_{ij} \hat{S}_i^+ \hat{S}_j^+ + \text{h.c.} \right) \\ & + \;\; J_{z\pm} \left(\zeta_{ij} \hat{S}_i^z (\hat{S}_j^+ + \hat{S}_j^-) + \text{h.c.} \right) \Big],\end{aligned} \tag{2.3}$$

where h.c. stands for hermitian conjugate, and $\gamma_{ij} = -\zeta_{ij}^*$ is a bond-dependent phase factor [23], and $\{J_{zz}, J_{\pm}, J_{\pm\pm}, J_{z\pm}\}$ label the possible coupling interactions between the pseudo-spin operators[6]. For this effective spin-1/2 system, the magnetic moment $\boldsymbol{\mu}_i$ in Eq. (2.1) is not constrained to have a non-zero value of $g_{\pm}$[7] and therefore can realize strong Ising ($g_z \gg g_{\pm}$), strong XY ($g_{\pm} \gg g_z$), and Heisenberg ($g_z = g_{\pm} \neq 0$) magnetic moments. This model is of special relevance for the results presented in this thesis and is further discussed in the rest of the chapter.

The non-Krammers Hamiltonian has the $\hat{S}^z$ operator transforming as a magnetic dipole whereas the $\hat{S}^{\pm}$ operators transform as a quadrupole. The essential difference between these two operators is that the quadrupole degrees of freedom are time-reversal even whereas the dipolar degrees of freedom are time-reversal odd. This difference forbids a mixing term between these degrees of freedom yielding the non-Kramers Hamiltonian

$$\mathcal{H} = \sum_{\langle ij \rangle} \left[J_{zz} \hat{S}_i^z \hat{S}_j^z - J_{\pm} \left(\hat{S}_i^+ \hat{S}_j^- + \hat{S}_i^- \hat{S}_j^+ \right) + J_{\pm\pm} \left(\gamma_{ij} \hat{S}_i^+ \hat{S}_j^+ + \text{h.c.} \right) \right]. \tag{2.4}$$

Note that when comparing the effective spin 1/2 Hamiltonian in Eq. (2.3) with the non-Kramers Hamiltonian Eq. (2.4), the only apparent difference is that the latter[8] does not

[6]Note that since the construction of the pseudo-spin operators is mostly based on symmetry, these operators are defined in the *local* sublattice basis as this is the basis.

[7]All of its components transform as dipoles and hence each one of these contributes to the magnetic moment.

[8]This ignores the fact that the pseudo-spins are dipolar in Eq. (2.3) and octupolar in Eq. (2.4).

have a coupling $J_{z\pm}$. This difference is of crucial importance and will be discussed again in the next subsection and in Chapter 6.

The other possible magnetic Hamiltonian is known as the dipolar-octupolar (Kramers) Hamiltonian where the $\hat{S}^x, \hat{S}^z$ operators transform as a dipole whereas the $\hat{S}^y$ operator transforms as an octupole[9]. Altogether, the effective Hamiltonian for this system yields

$$\mathcal{H} = \sum_{\langle ij \rangle} \left[J_{xx} \hat{S}_i^x \hat{S}_j^x + J_{yy} \hat{S}_i^y \hat{S}_j^y + J_{zz} \hat{S}_i^z \hat{S}_j^z + J_{xz} \left(\hat{S}_i^x \hat{S}_j^z + \hat{S}_i^z \hat{S}_j^x \right) + \right], \tag{2.5}$$

where $J_{xx} = 2(J_{\pm\pm} - J_{\pm})$, $J_{yy} = 2(J_{\pm\pm} + J_{\pm})$, and $J_{xz} = 2J_{z\pm}$[10] [23]. Note the application of a rotation around the local y axis, which effectively mixes the x and z components, results in an effective Hamiltonian which does not have a J_{xz} coupling. Although the effective Hamiltonian, now described by an XYZ model, is simpler, one has to account that now both the x and z components carry a dipolar moment.

Having provided a brief overview of some of the magnetic Hamiltonians that may be realized on the pyrochlore lattice, in the next sections, we consider the classical spin Hamiltonians and present some of the possible Ising and Heisenberg Hamiltonians and some of the different low-temperature phases that these realize.

2.2 Ising Spins

As stated in Chapter 1, the simplest spin Hamiltonian on the pyrochlore lattice is the nearest-neighbors Ising model

$$\mathcal{H} = J \sum_{\langle ij \rangle} \sigma_i^z \sigma_j^z = \frac{J}{2} \sum_{\boxtimes} \left(\sum_{i \in \boxtimes} \sigma_i^z \right)^2 + \text{constant}, \tag{2.6}$$

where $\boxtimes$ refers to a single tetrahedron in the lattice, and the Ising spins are constrained to point either into ($\sigma^z = +1$ for up tetrahedron) or away ($\sigma^z = -1$ for up tetrahedron) of

[9] Note that the $\hat{S}^x$ operator is a mix of both dipole and octupole degrees of freedom, this mixed combination presented in the x operator allows coupling with the z degree of freedom but not with the y [40].

[10] Note that if we had chosen to write the Hamiltonian in terms of the $\{J_{zz}, J_{\pm}, J_{\pm\pm}, J_{z\pm}\}$ interactions the bond-dependent phase factors would not be present as a consequence of how the octupolar degrees of freedom transform.

the center of the tetrahedron[11]. This model is realized for the exchange coupling constants $\{J_{zz}, J_{\pm}, J_{\pm\pm}, J_{z\pm}\} = \{J, 0, 0, 0\}$. For the ferromagnetic case where $J < 0$, the energy is minimized by maximizing the magnitude of the Ising moment for every tetrahedron. This condition is accomplished by making every spin to point in or out of every up tetrahedron, this amounts to having all spins pointing along (or against) their local $\boldsymbol{z}$ direction as shown in Fig. 2.1. In other words,

$$\sum_{i\in\boxtimes} \sigma_i^z = \pm 4. \tag{2.7}$$

Fulfilling this condition leads to a long-range ordered configuration known as the all-in-all-out state. This long-range ordered state will be further discussed when introducing the Heisenberg models and the possible long-range ordered configurations. On the other hand, for the antiferromagnetic Ising model where $J > 0$, minimizing the Hamiltonian (2.6) requires the net moment in each tetrahedron to vanish, i.e.

$$\sum_{i\in\boxtimes} \sigma_i^z = 0. \tag{2.8}$$

For a single tetrahedron, out of the $2^4 = 16$ states, this constraint is fulfilled by 6 configurations, the two-in-two-out states, where two spins point into and two spins point away from the center of a tetrahedron. The sole fulfillment of this constraint, in addition to the fact that different two-in-two-out configurations share some of the spin orientations[12], leads to an extensively degenerate ground state manifold, i.e. a ground state manifold where the number of states increases exponentially as a function of the system size. The states in this manifold are referred to as the *spin-ice* states where the inspiration for this name originates from the way water freezes into ice: a similar two-in-two-out constraint is found in water ice where the molecules freeze into a configuration where the oxygen atoms are located on diamond lattice sites[13] while the hydrogen atoms are constrained to lie between the oxygen atoms. The oxygen atoms in this configuration, therefore, have two hydrogen atoms which are closer and two which are further[14]. The equivalence between the spin-ice configurations and water ice is obtained by associating the spin orientation pointing into (away from) a tetrahedron center to a hydrogen atom being close to (further from) the oxygen at the center of the tetrahedron, see Fig. 2.2.

[11] This is along their local z direction

[12] This condition is crucial as it allows for the construction of different states by tilling the lattice with the different 6 two-in-two-out configurations.

[13] The diamond lattice is the parent line graph of the pyrochlore lattice where the diamond lattice sites can be associated to the centers of the tetrahedra in the pyrochlore lattice.

[14] This is simply a consequence of building the crystal structure with water molecules.

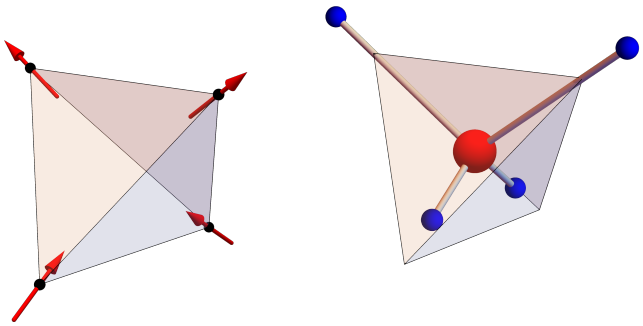


Figure 2.2: Two-in-two-out state in the Ising spins system on the left and in crystallized water on the right where the red sphere represents an oxygen atom and the blue spheres represent hydrogen atoms.

The entropy for water ice, and other crystal structures with randomness in their atomic arrangement, was studied by Linus Pauling [41]. To elucidate this extensive degeneracy for the spin system, and following Pauling's arguments for water ice, we can consider the fraction of states that fulfill the constraint in Eq. (2.8) in a single tetrahedron, times the number of possible states in the system. In other words,

$$W_N = \left(\frac{6}{16}\right)^{N/2} 2^N = \left(\frac{3}{2}\right)^{N/2}, \tag{2.9}$$

where N is the number of spins in the system, and $N/2$ is the number of tetrahedra. The entropy associated with this ground state manifold is therefore

$$\mathcal{S} = k_{\mathrm{B}} \ln W_N = \frac{N k_{\mathrm{B}}}{2} \ln\left(\frac{3}{2}\right), \tag{2.10}$$

which is referred to as the Pauling entropy. The extensive degeneracy of the ground state manifold prevents the system from undergoing a transition to a symmetry-broken state, therefore remaining paramagnetic all the way down to $T = 0$, realizing a classical *spin-liquid* phase. The spins in this paramagnetic state are strongly correlated as these are constrained by Eq. (2.8) which, at low temperatures, lead to algebraic correlations between the spins. Moreover, this system realizes an emergent magnetic theory described by magnetic charges Q and magnetic fluxes $\boldsymbol{B}$ [13, 28, 42, 43]. At low temperatures, the magnetic charges are suppressed and the fluxes fulfill the condition $\nabla \cdot \boldsymbol{B} = 0$, i.e. the fluxes become divergent-free or *irrotational*. The emergence theory of fluxes and the resulting the algebraic correlation between these inspired the name of this paramagnetic

spin-liquid phase as a *Coulomb* phase. Below, a brief description of how this emergent theory is obtained is provided and then a real space description of the spin configurations composing this phase is provided.

2.2.1 Emergent magnetic charges and fluxes

The emergence of magnetic fluxes and charges was first formally demonstrated by Conlon and Chalker [13, 42] where the spin degrees of freedom are mapped onto magnetic charge and fluxes. Then, by producing a long-wavelength expansion at low temperatures, an emergent Gauss' law on the fluxes exposes the divergence-free constraint which results in the algebraic correlations between the spins.

Before making the above statements more precise, some general remarks on the Hamiltonian (2.6) are provided. This Hamiltonian can be rewritten in the following way

$$\mathcal{H} = J \sum_{\langle ij \rangle} \sigma_i^z \sigma_j^z = \frac{J}{2} \sum_{ij} \sigma_i^z \mathcal{A}_{ij} \sigma_j^z, \tag{2.11}$$

where $\mathcal{A}_{ij}$ is the pyrochlore lattice nearest-neighbor adjacency matrix, where its matrix elements are 1, i.e. $\mathcal{A}_{ij} = 1$, if the i and j sites are nearest neighbors, and 0 otherwise. In reciprocal space, this matrix consists of a block-diagonal form composed of 4×4 blocks labeled by the sublattice indices a and b

$$\mathcal{A}_{a,b}(\mathbf{q}) = 2 \begin{pmatrix} 1 & \cos\left(\frac{q_x+q_y}{4}\right) & \cos\left(\frac{q_x+q_z}{4}\right) & \cos\left(\frac{q_y+q_z}{4}\right) \\ \cos\left(\frac{q_x+q_y}{4}\right) & 1 & \cos\left(\frac{q_y-q_z}{4}\right) & \cos\left(\frac{q_x-q_z}{4}\right) \\ \cos\left(\frac{q_x+q_z}{4}\right) & \cos\left(\frac{q_y-q_z}{4}\right) & 1 & \cos\left(\frac{q_x-q_y}{4}\right) \\ \cos\left(\frac{q_y+q_z}{4}\right) & \cos\left(\frac{q_x-q_z}{4}\right) & \cos\left(\frac{q_x-q_y}{4}\right) & 1 \end{pmatrix}, \tag{2.12}$$

where we have assumed the cubit unit cell size $a = 1$ for simplicity, see Appendix A. The diagonalization of the adjacency matrix in reciprocal space reveals two degenerate low-energy flat bands, reflecting the extensive degeneracy of the ground state configurations, and two dispersive bands. The eigenvalues $\{\varepsilon(\boldsymbol{q})\}$ of the adjacency matrix, illustrated in Fig. 2.3, are

$$\begin{aligned} \varepsilon_{0,1} &= 0, \\ \varepsilon_{2,3} &= \frac{1}{2}\left(4 \pm \sqrt{2}\sqrt{2 + c_{x,y} + c_{x,-y} + c_{x,z} + c_{x,-z} + c_{z,y} + c_{z,-y}}\right), \end{aligned} \tag{2.13}$$

where for short-hand notation we have used $c_{\alpha,\gamma} \equiv \cos\left(\frac{q_\alpha - q_\gamma}{2}\right)$. Although only the two lowest energy bands are *completely* degenerate, there is a degeneracy between the two

lowest bands and the third band at $\boldsymbol{q} = 0$. Close to this point the first dispersive band disperses as $\boldsymbol{q}^2$ whereas the second dispersive band disperses as $4 - \frac{1}{16}\boldsymbol{q}^2$.

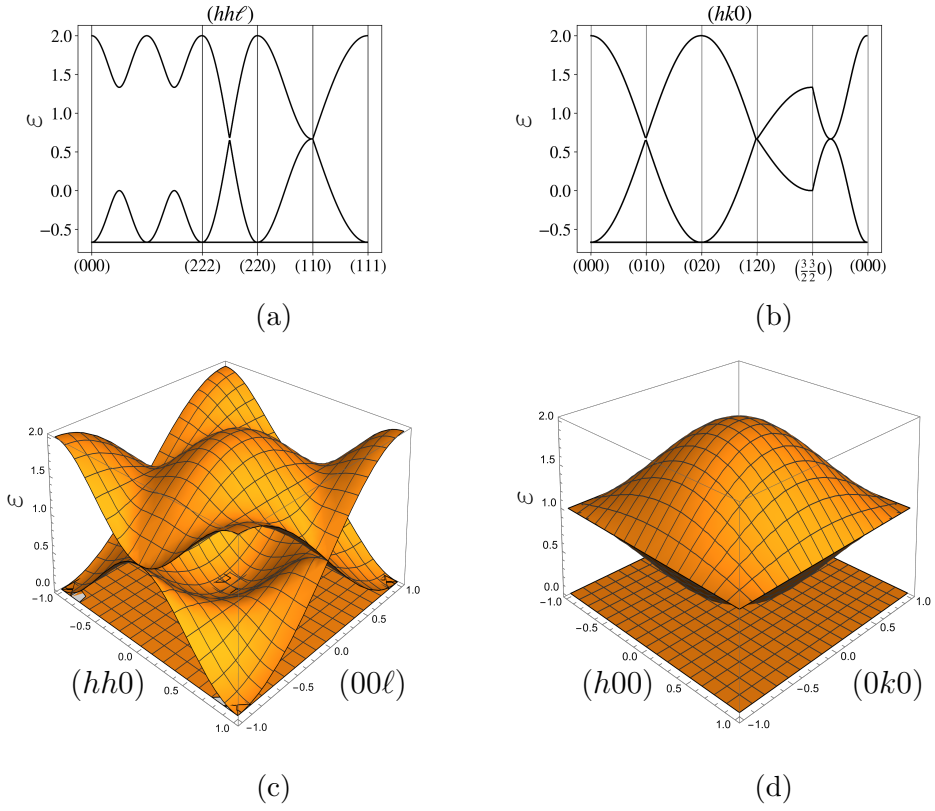


Figure 2.3: Energy bands of the adjacency matrix (2.12) shown along high-symmetry paths in the $(hh\ell)$] (a), and in the $(hk0)$ (b) planes, and in 3D in $(hh\ell)$] (c), and in the $(hk0)$ (d) planes. We refer the reader to Appendix C for a description of the symmetry paths used.

The physical interpretation of these energy bands can be exposed by mapping the Hamiltonian (2.6) from spins to charges and fluxes through the transformation

$$\begin{pmatrix} Q \\ B_x \\ B_y \\ B_z \end{pmatrix} = \frac{1}{2} \begin{pmatrix} 1 & 1 & 1 & 1 \\ 1 & -1 & -1 & 1 \\ 1 & -1 & 1 & -1 \\ 1 & 1 & -1 & -1 \end{pmatrix} \begin{pmatrix} \sigma_0^z \\ \sigma_1^z \\ \sigma_2^z \\ \sigma_3^z \end{pmatrix}, \tag{2.14}$$

or equivalently

$$Q = \frac{1}{2}\sum_a \sigma_a^z, \tag{2.15}$$

$$B^\alpha = \frac{\sqrt{3}}{2}\sum_a \hat{z}_a^\alpha \sigma_a^z, \tag{2.16}$$

where $\hat{z}_a$ is the local z direction of sublattice a, see Appendix A. A direct comparison between the above equations and Eq. (2.8) translates into the suppression of magnetic charges at low temperatures since the Hamiltonian (2.6) transforms to

$$\mathcal{H} = J\sum_{\langle ij\rangle}\sigma_i^z\sigma_j^z = 2J\sum_{\boxtimes}\left(Q_{\boxtimes}\right)^2 + \text{constant}, \tag{2.17}$$

therefore clarifying that at low temperatures the system fulfills the condition $Q_{\boxtimes} = 0$ for all tetrahedra. To obtain the low-temperature theory of this model, we can first consider the long-wavelength expansion of the adjacency matrix (2.12) yielding

$$\mathcal{A}_{a,b}(\mathbf{q}) = 2\delta_{a,b} - \begin{pmatrix} 0 & \left(\frac{q_x+q_y}{4}\right)^2 & \left(\frac{q_x+q_z}{4}\right)^2 & \left(\frac{q_y+q_z}{4}\right)^2 \\ \left(\frac{q_x+q_y}{4}\right)^2 & 0 & \left(\frac{q_y-q_z}{4}\right)^2 & \left(\frac{q_x-q_z}{4}\right)^2 \\ \left(\frac{q_x+q_z}{4}\right)^2 & \left(\frac{q_y-q_z}{4}\right)^2 & 0 & \left(\frac{q_x-q_y}{4}\right)^2 \\ \left(\frac{q_y+q_z}{4}\right)^2 & \left(\frac{q_x-q_z}{4}\right)^2 & \left(\frac{q_x-q_y}{4}\right)^2 & 0 \end{pmatrix} + O(\boldsymbol{q}^4), \tag{2.18}$$

where δ_{ab} is a Dirac delta. Next, introducing the transformation in Eq. (2.14) to the Hamiltonian (2.6), yields the effective low-temperature Hamiltonian

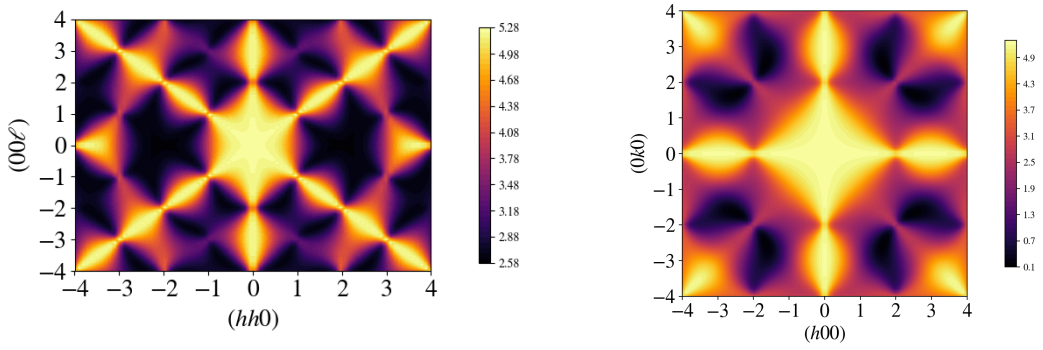
$$\mathcal{H} = J\sum_{\boldsymbol{q}} |\boldsymbol{q}\cdot\boldsymbol{B}(\boldsymbol{q})|^2 + O(\boldsymbol{q}^4), \tag{2.19}$$

where the magnetic charge terms have been suppressed[15]. Minimizing the effective low-temperature Hamiltonian (2.19) requires the fluxes to become transverse to $\boldsymbol{q}$, i.e. $\boldsymbol{q}\cdot\boldsymbol{B}(\boldsymbol{q}) = 0$. In real space, the expression $\boldsymbol{q}\cdot\boldsymbol{B}(\boldsymbol{q}) = 0$ translates into the divergence-free constraint $\nabla\cdot\boldsymbol{B} = 0$, therefore, elucidating the origin of the rotational nature of the fluxes $\boldsymbol{B}$. The configurations fulfilling this constraint are those described by the two degenerate low energy flat bands, illustrated in Fig. 2.3[16]. In these states, the spin-spin

[15] In practice, instead of suppressing the magnetic charges these can be integrated out which results in a redefinition of the fluxes without changing the overall result.

[16] To obtain a real space picture we can use the definition of the divergence operator in a lattice which corresponds to the sum of the bonds degrees of freedom connecting to a site. Therefore, for a flux defined on a diamond lattice site, the divergence corresponds to the sum of the spin in the tetrahedron assigned to that site.

correlation, $\langle \sigma_i^z \sigma_j^z \rangle$, are dipolar[17] [44–46] which in reciprocal space translate into highly anisotropic features known as *pinch points*, these features are shown in Fig. 2.4 for the neutron structure factor $S_\perp(\boldsymbol{q})$, see Appendix B.



(a) (b)

Figure 2.4: Neutron structure factor in the spin-ice phase observed in the $(hh\ell)$ (a) and $(hk0)$ (b) scattering planes.

Upon increasing temperature, the constraint (2.8) may be violated which translates into a thermal population of the upper bands of the adjacency matrix, and thus realizing higher energy spin configurations. These configurations might be states which violate the divergence-free constraint, i.e. $\boldsymbol{q} \cdot \boldsymbol{B}(\boldsymbol{q}) \neq 0$, and also states where the magnetic charges have not been suppressed, i.e. $Q \neq 0$. In fact, breaking the divergent-free constraint results in an energy cost proportional to $\boldsymbol{q}^2$, see Eq.(2.19), given by the first excited band whereas the inclusion of charges results in a constant shift (plus a decreasing energy cost $-\frac{1}{16}\boldsymbol{q}^2$) given by the second excited band, see Eq. (2.17)[18]. The inclusion of these higher energy configuration results into an increasing pinch point width[19] which will be discussed in further detail in Sec. 3.1. Following this identification, spin configurations fulfilling the constraint (2.8) are referred to as *rotational* configurations, while those violating this condition as *irrotational* configurations. In the following section, a real-space description of these configurations is provided.

[17]This comes from the fact that the divergence free constraint results in dipolar correlations between the fluxes which is then inherited by the spin variables [3, 44].

[18]Note that for a single tetrahedron a charge can acquire the values of 0, ±2 and ±4.

[19]Click on the corresponding scattering plane, $(hh\ell)$] or $(hk0)$, for an animation on how the pinch point width changes as the temperature is lowered.

2.2.2 Real Space Ising Spins Configurations

To construct a spin-ice configuration in the pyrochlore lattice one has to follow the *ice rules* [13, 28, 47] where every tetrahedron must be in a two-in-two-out configuration. Although there are many configurations which can be constructed by the implementation of these rules, a common trait can be found between these states: these configurations are described by oriented *closed loops* of spins [48, 49] on the pyrochlore lattice where the segments of a loop are composed by two spins, one going in and one going out of a tetrahedron, see Fig. 2.5 for an example on the smallest possible loop[20]. In a system with periodic boundary conditions, the closed loops can wrap around the system[21] effectively generating topological sectors defined by the number of times a loop wraps around the system. Each topological sector can be characterized by the total flux $\boldsymbol{B}$ a spin configuration in the lattice has.

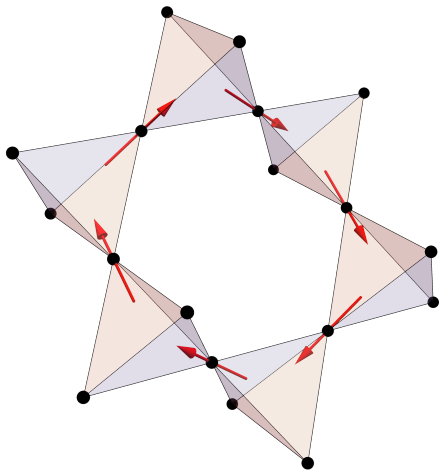


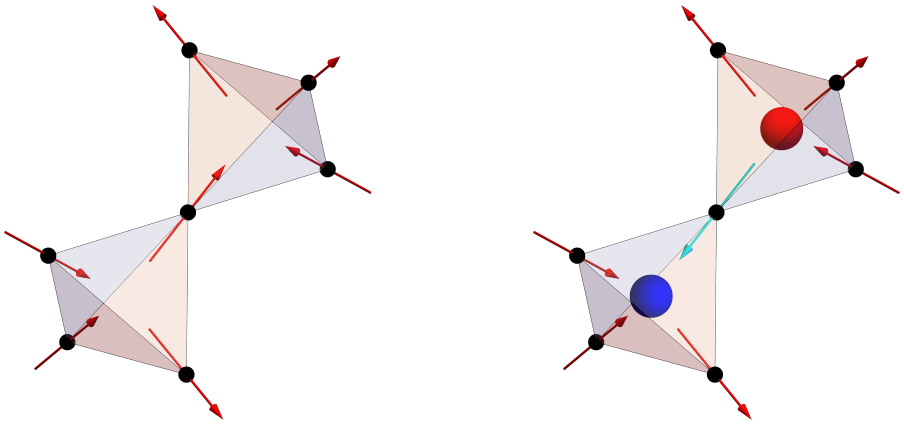
Figure 2.5: Smallest closed loop form by Ising spins. The remaining spins are not shown as each can adopt two possible configurations fulfilling the ice rules.

Higher energy configurations can be constructed starting from spin-ice configurations by performing single spin-flips, and therefore breaking the ice rule, see Fig. 2.6. Interestingly, a single spin-flip generates two magnetic charges, one $Q = 1$ and one $Q = -1$ charge

[20] Interestingly, it has been shown that the probability of two spins to be on the same loop plateaus to a constant value [50]

[21] In other words crossing a periodic boundary an odd number of times before closing the loop.

in the adjacent tetrahedra which share the flipped spin, see Fig. 2.6 (b), see Eq. (2.15). The generation of these two magnetic excitations by a *single* spin-flip is referred to as *fractionalization* [51]. For the nearest-neighbor antiferromagnetic model, the two generated charges can move freely in the lattice with no extra energy cost and are only destroyed when meeting on the same tetrahedron. These charges define the end-points of a string of spins, such strings have been dubbed *Dirac strings* and have been broadly studied in this system [52, 53].



(a) (b)

Figure 2.6: (a) Spin-ice configuration in two adjacent tetrahedra. (b) Excited configuration where the cyan spin has been flipped creating a $Q = -2$ (blue) and a $Q = 2$ (red) magnetic charges in the tetrahedra sharing the spin.

2.2.3 Spin-ice in systems beyond the nearest-neighbor model

Other allowed Ising spin interactions in the pyrochlore lattice include the further-nearest-neighbor interactions and dipolar interactions. The inclusion of these further neighbor interactions may still stabilize a spin-ice phase. For example, consider the inclusion of second nearest-neighbor (J_2), and third-a nearest-neighbors (J_{3a}) interactions, the so-called *extended spin-ice* model where phases such as *spin slush* [54] as well as spin-ice can be observed

$$\mathcal{H}_{\text{ESI}} = J \sum_{\langle ij \rangle} \sigma_i^z \sigma_j^z + J_2 \sum_{\langle ij \rangle_2} \sigma_i^z \sigma_j^z + J_{3a} \sum_{\langle ij \rangle_{3a}} \sigma_i^z \sigma_j^z, \tag{2.20}$$

where $\langle ij \rangle_2$ and $\langle ij \rangle_{3a}$ denote pairs of second and third-a nearest neighbors. In this model, for the case $J' = J_2 = J_{3a}$ the spin-ice phase is realized for $-1/2 \leq J'/J \leq 1/4$. In this

case, the observation of the spin-ice manifold is directly related to the interaction matrix of the Hamiltonian which, for the case $J_2 = J_{3a}$ can be taken to be a polynomial of the adjacency matrix $\mathcal{A}$ [3, 55]. Consequently, the eigenvectors of $\mathcal{A}$ remain eigenvectors of the full interaction matrix. In particular, for the case $-1/2 \leq J'/J \leq 1/4$, the low-energy eigenvectors of extended spin-ice are the *same* as those for the regular nearest-neighbor model, preserving the same ground state manifold and therefore realizing a low-temperature spin-ice phase.

When including dipolar interactions, the Ising Hamiltonian takes the form

$$\mathcal{H}_{\text{dip}} = J \sum_{\langle ij \rangle} \sigma_i^z \sigma_j^z + \frac{D}{2} \sum_{i,j} \frac{\boldsymbol{z}_i \cdot \boldsymbol{z}_j - 3(\boldsymbol{z}_i \cdot \boldsymbol{r}_{ij})(\boldsymbol{r}_{ij} \cdot \boldsymbol{z}_j)}{(r_{ij}/r_{\text{nn}})^3} \sigma_i^z \sigma_j^z, \tag{2.21}$$

where $\boldsymbol{z}_i$ is the local [111] direction of site i, $\boldsymbol{r}_{ij}$ is the separation vectors between site i and site j, and r_{nn} is the nearest-neighbor distance. Interestingly, for $(J + 5D)/3 > 0$ this model stabilizes a finite temperature spin-ice phase[22] before collapsing into an ordered phase at low temperatures [48]. It is worth noting that the pyrochlore compounds $Ho_2Ti_2O_7$ and $Dy_2Ti_2O_7$ are accurately described by this model where both compounds fulfill the condition $(J + 5D)/3 > 0$[23] therefore realizing a spin-ice phase [47]. In fact, it has been shown that pinch point features, as those shown in Fig. 2.4, are observed in the neutron structure factor for $Ho_2Ti_2O_7$ [30, 32]. Naturally, one may wonder what other interactions can be included which preserve, or mildly modify, the realization of a low-temperature spin-ice phase. In particular, this may include the introduction of off-diagonal interaction terms, this is $\{J_{zz}, J_{\pm}, J_{\pm\pm}, J_{z\pm}\} \neq \{J, 0, 0, 0\}$, which are of especially relevant in terms of material realization. The inclusion of these off-diagonal couplings has been studied from both a quantum and classical perspective.

From a quantum perspective, the inclusion of a small $J_{\pm}$ to the Hamiltonian (2.6) was considered by Ref. [56] resulting in the realization of a $U(1)$ spin-liquid with gapless "photon"[24] excitations. The inclusion of additional couplings has been extensively studied using a gauge mean-field theory [57, 58] and projective symmetry group approaches [59] resulting in the prediction of other spin-liquid phases and quadrupolar magnetic orders.

[22] This approximation is obtained by simply separating Hamiltonian (2.21) into the nearest-neighbors Hamiltonian and a Hamiltonian containing all the longer-range interactions. This procedure yields the nearest-neighbor interaction parameter $(J + 5D)/3$ and consequently it is expected that the condition $(J + 5D)/3 > 0$ realizes a spin-ice phase. A more accurate condition was found by classical Monte Carlo resulting in $(J + 4.53D)/3$ [47].

[23] As well as the stronger condition given by classical Monte Carlo [47].

[24] This is an excitation that disperses $\propto \boldsymbol{q}$.

Going beyond these analytical approximations often requires the application of numerical techniques such as quantum Monte Carlo [60], High-Temperature Series Expansion [61, 62], numerical linked-cluster analysis expansion [63, 64], pseudo-fermion functional renormalization group [65–67] and pseudo-majorana functional renormalization group [68], and recently the application of tensorial network approaches such as density-matrix renormalization group (DMRG) [69]. All of the above techniques however have, however, their own limitations depending on system size, the temperature range where these can be applied, or even thermodynamic quantities that can be studied such as high order in the spin correlation functions. Alternatively, the inclusion of these interactions can be studied from a classical perspective to complement, or even guide, the quantum treatment. In the next section, we present a general overview of the classical treatment for the case $\{J_{zz}, J_{\pm}, J_{\pm\pm}, J_{z\pm}\} \neq \{J, 0, 0, 0\}$.

2.3 Three-component Spins

Although when studying Heisenberg systems we can start by considering the effective spin 1/2 Hamiltonian in Eq. (2.3) with the interaction parameters in the local basis $\{J_{zz}, J_{\pm}, J_{\pm\pm}, J_{z\pm}\}$, here we use a different set of interactions parameters in the *global* basis[25] $\{J, j_{\text{Isi}}, J_{\text{Pd}}, J_{\text{DM}}\}$ which directly refer to the physical origin of the exchange interactions between the spins [70, 71], we refer to this basis as the global physical interaction basis. For the details on how these interaction parameters are related to each other we refer the reader to Appendix E. Note however, that using the basis $\{J_{zz}, J_{\pm}, J_{\pm\pm}, J_{z\pm}\}$ clearly identifies if the Hamiltonian studied is the effective spin-1/2 or the non-Kramers Hamiltonian by simply considering the case when $J_{z\pm} = 0$. For the basis global basis, the distinction between the two Hamiltonians can be clarified by mapping the global couplings $\{J, J_{\text{Isi}}, J_{\text{Pd}}, J_{\text{DM}}\}$ onto the local couplings $\{J_{zz}, J_{\pm}, J_{\pm\pm}, J_{z\pm}\}$.

[25] In other words where the spin components are defined along the global cartesian directions.

In terms of the global basis interaction parameters, the effective spin Hamiltonian is

$$\begin{aligned}
\mathcal{H} &= \mathcal{H}_{\text{Heis}} + \mathcal{H}_{\text{Ising}} + \mathcal{H}_{\text{Pd}} + \mathcal{H}_{\text{DM}} && (2.22)\\
\mathcal{H}_{\text{Heis}} &= J \sum_{\langle ij \rangle} \boldsymbol{S}_i \cdot \boldsymbol{S}_j && (2.23)\\
\mathcal{H}_{\text{Ising}} &= J_{\text{Isi}} \sum_{\langle ij \rangle} (\boldsymbol{S}_i \cdot \boldsymbol{z}_i)(\boldsymbol{S}_j \cdot \boldsymbol{z}_j) && (2.24)\\
\mathcal{H}_{\text{Pd}} &= J_{\text{Pd}} \sum_{\langle ij \rangle} (\boldsymbol{S}_i \cdot \boldsymbol{r}_{ij})(\boldsymbol{r}_{ij} \cdot \boldsymbol{S}_j) && (2.25)\\
\mathcal{H}_{\text{DM}} &= J_{\text{DM}} \sum_{\langle ij \rangle} \boldsymbol{D}_{ij} \cdot (\boldsymbol{S}_i \times \boldsymbol{S}_j) && (2.26)
\end{aligned}$$

where $\boldsymbol{z}_i$ is the local z direction of site i, $\boldsymbol{r}_{ij}$ are the normalized nearest-neighbor separation vectors between sites i and j, and $\boldsymbol{D}_{ij}$ are the allowed Dzyaloshinskii-Moriya (DM) vectors [72, 73] whose description and derivation are provided further in Chapter 4. The above bilinear spin interaction terms are known as the Heisenberg (2.23), Ising (2.24)[26], pseudo-dipolar (2.25)[27], and Dzyaloshinskii-Moriya (DM) (2.26). Note that for $S > 1/2$, another symmetry-allowed interaction is the single-ion anisotropy

$$\mathcal{H}_{\text{SIA}} = d \sum_i (\boldsymbol{S}_i \cdot \boldsymbol{z}_i)^2 , \qquad (2.27)$$

which favors (disfavors) the orientation of the spins along their local z direction for $d < 0$ ($d > 0$)[28]. This term is of special relevance in Chapter 7, where it will be discussed in further detail.

Starting from the Hamiltonian (2.22) with the addition of the single-ion anisotropy in Eq. (2.27), we can now study the possible low-temperature phases realized in pyrochlore systems, these being magnetically ordered or disordered phases.

[26] Here we use this name to refer to the interaction between the local z degrees of freedom of the spins.

[27] Note that this term originates from considering dipolar interactions, see Eq. (2.21), up to first nearest-neighbors.

[28] for $S = 1/2$ this term is just a constant shift in the energy.

2.3.1 Magnetically Ordered Phases in the nearest-neighbor Hamiltonian

As a consequence of the corner-sharing structure of the pyrochlore lattice, the nearest-neighbor Hamiltonian (2.22) can be expressed as

$$\mathcal{H} = \sum_{\boxtimes} \mathcal{H}_{\boxtimes} \tag{2.28}$$

where $\boxtimes$ denotes single tetrahedron, and the sum includes both up and down tetrahedra. Yan *et al.* [74] showed that for this model the possible (classical) long-range ordered (LRO) phases can be found by identifying a spin configuration which minimizes the energy in a *single* up (or down)[29] tetrahedron[30]. The minimum energy spin configuration it then replicated for all up (or down) tetrahedra in the lattice. The possible resulting states, labeled as $\boldsymbol{q} = \mathbf{0}$ orders, are the all-in-all-out (AIAO) [75], the coplanar antiferromagnet [73, 76], the colinear ferromagnet [77–81], the Palmer-Chalker (PC) [82–85], the ψ_2 [61, 86–88], and the ψ_3 states [89, 90], shown in Fig. 2.7. Before continuing it is important to mention that, depending on the couplings $\{J, j_{\text{Isi}}, J_{\text{Pd}}, J_{\text{DM}}\}$, and specially when $j_{\text{Isi}} \neq 0$ and $J_{\text{Pd}} \neq 0$, the minimum energy configuration may be described by a combination of the colinear ferromagnet and coplanar antiferromagnet states resulting on a two possible *canted* ferromagnetic states [70, 70, 91–95], see Fig. 2.8 for a possible combination of the colinear and coplanar states which we label the Ice and ferromagnetic xy states for reasons which will become clear in chapter 3. The properties of these $\boldsymbol{q} = 0$ ground states, and the precise combination between the colinear ferromagnet and coplanar antiferromagnet states are derived by studying the transformations under which a single tetrahedron is invariant, i.e. the transformation of the tetrahedral group T_d. We delay this analysis to Chapter 3 where the precise spin configurations, the energy as a function of the interaction parameters $\{J, j_{\text{Isi}}, J_{\text{Pd}}, J_{\text{DM}}\}$ associated to each $\boldsymbol{q} = 0$ state, and further symmetry analysis of T_d group is presented.

The identification of a LRO phase through this relatively simple, yet powerful, minimum energy configuration in a single tetrahedron has shown to be remarkably accurate when predicting the low-temperature ground state configurations for a plethora of compounds described by the Hamiltonian (2.22) [70, 77, 82, 87, 89]. Perhaps more interesting is the case when the energy analysis of the $\boldsymbol{q} = 0$ states identifies a degeneracy between

[29] In other words minimizing $\mathcal{H}_{\boxtimes}$.

[30] The choice of considering the up or down tetrahedra does not change the end result as these two are related by a C_2 symmetry which is demonstrated by Ref. [74].

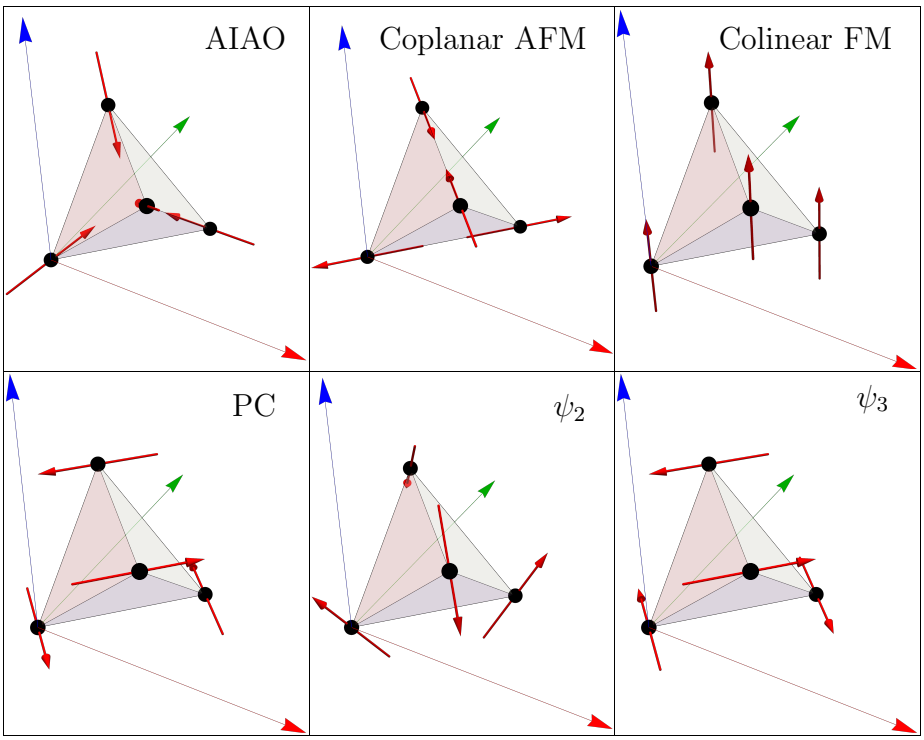


Figure 2.7: $\boldsymbol{q} = \boldsymbol{0}$ orders in a single up tetrahedron where the red arrows depict the spin and the global $\boldsymbol{x}$, $\boldsymbol{y}$, and $\boldsymbol{z}$ are shown in red, green and blue, respectively.

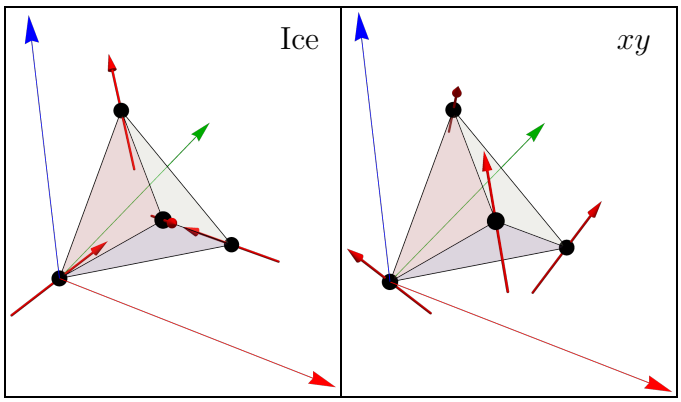


Figure 2.8: Canted ferromagnetic $\boldsymbol{q} = \boldsymbol{0}$ configurations resulting from a specific combination of the coplanar antiferromagnetic and the colinear ferromagnetic states.

two or more configuration. This degeneracy can be understood as a competition of different orders which may lead to two possible outcomes: either temperature or quantum fluctuations select one of the energy-degenerate states leading to a low-temperature LRO phase, a phenomenon dubbed *Order-by-Disorder* [25], or the competition is so strong that the system completely avoids LRO and instead realizes a magnetically disordered phase down to $T = 0$, i.e. a spin-liquid phase. These two cases are discussed in the following sections.

2.3.2 Order-by-Disorder

The term order-by-disorder (ObD) was coined by Villain *et al.* [25] when studying the "domino model": an Ising model on a rectangular lattice where two types of ions are considered and the interactions between these are type-dependent. In his work, Villain showed that this model exhibits LRO at low temperatures but not at $T = 0$. Interestingly, Villain demonstrated that the addition of quenched random impurities[31] could restore LRO thus demonstrating the first realization of an unexpected effect where the introduction of disorder may lead to an ordered configuration.

In magnetism, ObD is usually observed in systems where different energy degenerate spin configurations are not related by a global symmetry. Using these states, we may identify an equal energy manifold formed by spin configurations resulting from a normalized linear combination of the energy-degenerate states. The states in this manifold are related by an *accidental* symmetry[32] parametrizing the equal energy manifold [96]. Crucially, this transformation *does not* leave the Hamiltonian invariant and therefore is referred to as an accidental symmetry. In practice, ObD is usually understood as the quantum or thermal selection of a set of configurations from the energy-degenerate manifold where the selected states present lower energy fluctuations at $T = 0$ thus minimizing the total internal energy in the quantum case, or higher entropic fluctuations at finite temperatures thus minimizing the free energy, $F = E - TS$. The exact quantitative argument behind this selection mechanism for both the $T = 0$ and the $T > 0$ case is presented in Chapter 3.

A simple example of the accidental degeneracy and the ObD selection is provided by the *compass* model in a square lattice [97, 98] where the Hamiltonian is given by

$$\mathcal{H} = \sum_{\boldsymbol{r}} \left(J_x S^x_{\boldsymbol{r}} S^x_{\boldsymbol{r}+\boldsymbol{e}^x} + J_y S^y_{\boldsymbol{r}} S^y_{\boldsymbol{r}+\boldsymbol{e}^y} \right), \tag{2.29}$$

[31] This is by selecting a set of sites in the lattice and making this non-interacting and thus non-magnetic.

[32] This term is usually used to refer to a transformation with which the states in the equal energy manifold can be obtained.

where $\boldsymbol{r}$ is the lattice site position and $\boldsymbol{e}^{\alpha}$ is the displacement vectors along the α direction. For the case $J_x = J_y = J < 0$ the ground state is a ferromagnet where all spins point along the same in-plane direction, therefore having a $U(1)$ symmetry[33] on the ground state manifold related to the total magnetization orientation of the state. However, this $U(1)$ symmetry is *accidental* as it is not a symmetry of the Hamiltonian. In fact, a careful study of the spin configurations would show that the states where all the spins are oriented along the Cartesian $\boldsymbol{x}$ or $\boldsymbol{y}$ directions possess lower quantum energy fluctuations resulting in lower total energy and therefore the selection of these states.

The accidental symmetry manifold and the dependence of the fluctuations about a given spin configuration can be understood by the cartoon shown in Fig. 2.9(a) and (b). In this figure, the Cartesian axis would represent some parameters in configuration space where every point represents a different spin configuration. The color in these figures represents the energy associated with the corresponding configurations, where the white dashed line marks the lowest energy in the configuration space landscape. Clearly, Fig. 2.9(a) has an exact $U(1)$ symmetry and therefore all points along the white dashed line are equivalent as well as the energy fluctuations around these. In other words, the energy fluctuations along both, the radial (perpendicular to the dashed line) and angular direction (along the dashed line), are equivalent for *all* configurations in the dashed line. It is however clear that the energy landscape in Fig. 2.9(b) does not present a $U(1)$ degeneracy although it *appears* to if we only focus on the white dashed line[34], but rather a C_4[35] degeneracy. In fact, the radial energy fluctuations for the states in the white dashed line are "softer" at points along the axis, i.e. at angles $n\pi/2$ with n being an integer. Fig. 2.9(b) can be therefore understood as a cartoon picture of the energy landscape of what would be observed for the compass model.

Quantitatively, the energy for the fully polarized states for the compass model as a function of the rotation angle θ is given by [97]

$$E_{\rm GS} = -JS^2N + \frac{1}{2}\sum_{\boldsymbol{q}} 4JS\sqrt{1-\cos^2\theta\cos(\boldsymbol{q}\cdot\mathbf{e}^x) - \sin^2\theta\cos(\boldsymbol{q}\cdot\mathbf{e}^y)}, \tag{2.30}$$

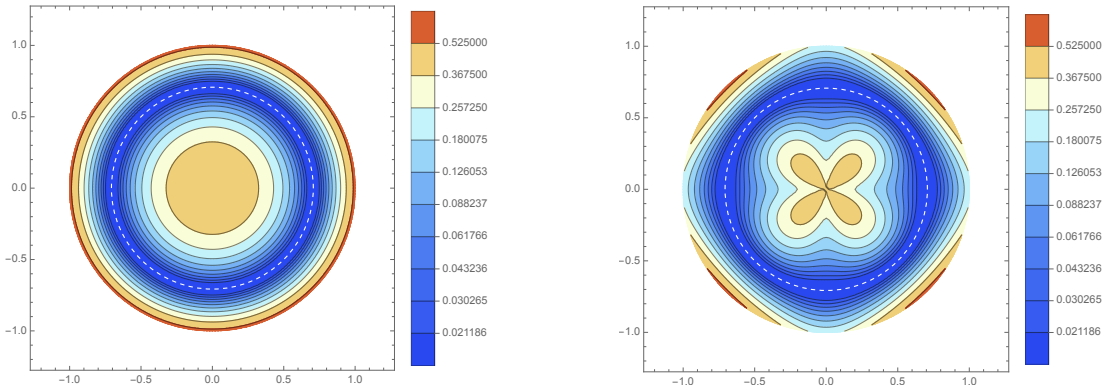
where S is the spin length and N is the number of sites in the square lattice. The energy (2.30) is composed of two terms: the first is the classical ground state energy of a polarized configuration, and the second term is associated with the quantum corrections provided by the excitations about the state[36]. The equivalence of the first term for *all*

[33] A simple rotational symmetry around the $\boldsymbol{z}$ direction.

[34] This apparent degeneracy is what we refer to as the accidental degeneracy.

[35] this is a rotation by $\pi/2$ about the z axis

[36] This second term is the zero-point energy correction and is further discussed in Section 3.3.



(a) (b)

Figure 2.9: Cartoon picture for the (a) energy landscape of an exact $U(1)$ degenerate manifold. (b) Energy landscape of an accidental $U(1)$ degenerate manifold. In both figures, the color represents the energy and the minimum energy is marked by the dashed white.

orientations[37] clearly demonstrates the accidental symmetry observed in the system. On the other hand, the excitations about the selected configuration present an anisotropy with a C_4 symmetry. The energy (2.30) is therefore minimized whenever $\theta = n\pi/2$ where n is an integer, elucidating the selection of the configurations where all spins point along the x or y directions.

The observation of accidental symmetries and the ObD selection are not uncommon in frustrated magnetism [73, 74, 86, 99, 100]. Typically, it is expected that quantizing the Hamiltonian will lift the accidental symmetry of the ground state due to an additional contribution from quantum fluctuations about the ground state [99]. In fact, for a bilinear Hamiltonian in the pyrochlore lattice, the ψ_2 and ψ_3 configurations are bound to have the same classical ground state energy [71, 74, 89][38]. The degeneracy between these two configurations gives rise to the accidental $U(1)$ symmetry and therefore an energy-degenerate manifold known as the Γ_5 manifold [23, 71, 74]. The selection of either configuration is therefore a consequence of ObD where the exact mechanism can be either thermal, quantum or a combination of both. Note however that the quantum and thermal ObD mechanism might promote *different* configurations. Consequently, upon ordering, a system might select a given spin configuration at T_c, for example ψ_2, while at low temperatures

[37] This means that the term is not a function of the angle θ.

[38] This argument does not take into account a possible crystal field interaction term which may differentiate these two configurations.

the system *reorients* itself onto another configuration, for example ψ_3. Interestingly, this temperature-dependent selection has not been pervasively discussed in the literature where some studies only provide predictions at $T = 0$ naively assuming that the selected state is conserved upon increasing temperature. These effects are further studied in Chapters 4 and 5.

Although an ObD selection may suggest that an ordered phase can always be accessible when energy degeneracy is present, there are cases where the competition between the different orders is so strong that the system remains disordered down to $T = 0$ producing a disorder yet highly correlated phase, i.e a spin-liquid. This is for example the case for spin-ice. In the next section, we present one of the best known spin-liquids realized in the pyrochlore lattice with nearest-neighbor interactions.

2.3.3 Spin-liquids in the pyrochlore lattice

The avoidance of a LRO phase is related to strong competition between different orders which persist to the lowest temperatures. For the pyrochlore lattice with nearest-neighbor interactions, the possible competing orders are the $\boldsymbol{q} = 0$ states presented in Subsection 2.3.1 possessing the lowest classical energy for a given set of parameters $\{J, J_{\text{Isi}}, J_{\text{Pd}}, J_{\text{DM}}\}$. Therefore, a spin-liquid phase in the general bilinear magnetic Hamiltonian (2.22) might be realized for interaction parameters where two or more of the $\boldsymbol{q} = 0$ orders are degenerate in energy.

The Heisenberg Antiferromagnet

One of the best known examples of a spin-liquid in a pyrochlore system with Heisenberg degrees of freedom is presented by the antiferromagnetic Heisenberg model (2.23). This Hamiltonian, in direct analogy to the Ising Hamiltonian in Eq. (2.6), may be written as

$$\mathcal{H}_{\text{Heis}} = \frac{J}{2} \sum_{\boxtimes} \left(\sum_{i \in \boxtimes} \boldsymbol{S}_i \right)^2 + \text{constant}. \tag{2.31}$$

From the above equation, it is clear that the ground state configurations are those which have no net-magnetization in every tetrahedra. In terms of the $\boldsymbol{q} = 0$ states, this is translated into a competition between the antiferromagnetic states AIAO, coplanar antiferromagnet, PC, ψ_2, and ψ_3, shown in Fig. 2.7. Interestingly, this model presents a similar emergent field theory as the one realized by spin-ice where the ground state configurations

obey a divergence-free constraint. To make this connection clear, we can express the Hamiltonian (2.31) in terms of the adjacency matrix $\mathcal{A}_{ij}$ and the isotropic spin interaction matrix $J_{\text{Iso}}^{\alpha\gamma} = \delta_{\alpha\gamma} J$,

$$\begin{aligned}
\mathcal{H}_{\text{Heis}} &= \sum_{\langle ij \rangle} \sum_{\alpha\gamma} S_i^{\alpha} \mathcal{A}_{ij} J_{\text{Iso}}^{\alpha\gamma} S_j^{\beta} \\
&= \sum_{\langle ij \rangle} \boldsymbol{S}_i^T \left(\mathcal{A}_{ij} \otimes J_{\text{Iso}} \right) \boldsymbol{S}_j \\
&= J \sum_{\langle ij \rangle} \boldsymbol{S}_i^T \left(\mathcal{A}_{ij} \otimes \mathbb{1}_{3\times 3} \right) \boldsymbol{S}_j .
\end{aligned} \tag{2.32}$$

where $\mathbb{1}_{3\times 3}$ is the identity matrix for the spin components. Given the spin interactions are isotropic, the interaction matrix for this Hamiltonian is equivalent to the one found for the Ising system with the only difference that now each band is threefold degenerate steaming from isotropic interactions. In fact, a direct comparison between Eq. (2.32) and Eq. (2.11) shows that this Hamiltonian can be simply understood as three copies of the Ising model. Therefore, we can consider a basis transformation similar to the one in Eq. (2.15) and Eq. (2.16) where now a charge and a set of fluxes is defined for *every* spin component α

$$Q^{\alpha} = \frac{1}{2} \sum_{a} S_a^{\alpha}, \tag{2.33}$$

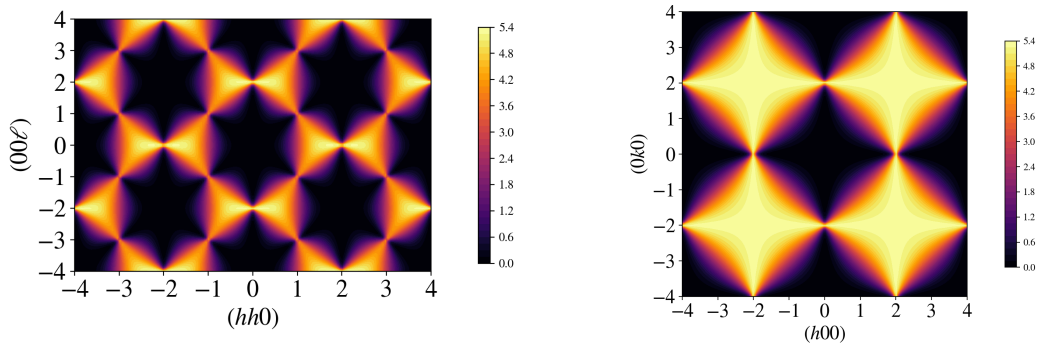
$$\boldsymbol{B}^{\alpha} = \frac{\sqrt{3}}{2} \sum_{a} \boldsymbol{z}_a \, S_a^{\alpha}. \tag{2.34}$$

In this case, the charges Q^{α} are related to the total magnetization components, which vanishes for the ground state configurations. A long-wavelength expansion equivalent to the one presented in Subsection 2.2.1 results in the effective long wavelength Hamiltonian

$$\mathcal{H} = J \sum_{\boldsymbol{q}} \sum_{\alpha} |\boldsymbol{q} \cdot \boldsymbol{B}^{\alpha}(\boldsymbol{q})|^2 + O(\boldsymbol{q}^4), \tag{2.35}$$

and consequently, in an emergent Gauss' law $\nabla \cdot \boldsymbol{B}^{\alpha} = 0$ for the set of fluxes defined for each spin component. The neutron structure factor correlation function in reciprocal space at low temperatures, i.e. where the divergence-free condition is enforced, is shown in Fig. 2.10 for the $(hh\ell)$] and $(hk0)$ scattering planes[39]. Note that, similar to what was shown for spin-ice in Fig. 2.4, pinch point features are observed signaling the rotational nature of the low-temperature modes and therefore the algebraic correlations between spins in the low-temperature phase, i.e. forming a Coulomb phase.

[39]Click on the corresponding scattering plane, $(hh\ell)$] or $(hk0)$, for an animation on how the pinch point width changes as the temperature is lowered.



(a) (b)

Figure 2.10: Neutron structure factor for the Heisenberg antiferromagnetic model observed in the $(hh\ell)$ (a) and $(hk0)$ (b) scattering planes. These correlation functions were obtained using a SCGA discussed in Section 3.1 for the lowest temperature shown in Fig. 3.1.

Although the condition for the Heisenberg antiferromagnet and spin-ice seem to be equivalent, a small precision is needed. In spin-ice, the divergence-free condition relates to a zero total Ising magnetic moment along the local z direction in each tetrahedron, see Eq. (2.8). For a single tetrahedron this condition is fulfilled by the two-in-two-out states which have a non-zero magnetization, see Fig. 2.6(a). On the other hand, for the Heisenberg antiferromagnet, the divergence-free condition relates to a zero total magnetization in each tetrahedron, i.e. each tetrahedron must be in an antiferromagnetic configuration. A simple way of making this difference clear is to consider a Heisenberg ferromagnet (2.23) with an addition single-ion-anisotropy term (2.27). If we now take the limit $d \to -\infty$ the spins are now constraint to lie along the local z direction and we can therefore take $\boldsymbol{S}_i = \boldsymbol{z}_i \sigma_i$. Since $\boldsymbol{z}_i \cdot \boldsymbol{z}_j = -1/3$ for $i \neq j$, the resulting model yields is an Ising antiferromagnet[40]. This minor clarification is used in Chapters 6 and 7 when discussing the realization of a spin-ice phase in a system of Heisenberg spins.

The observation of pinch points in the Heisenberg antiferromagnet has been extensively studied [42, 43, 46, 101] and has motivated the search of compounds which exhibit these features in the reciprocal space correlation functions [29, 75, 102–106]. In particular, recent work on the compound $Ce_2Zr_2O_7$, a dipolar-octupolar magnet which remains disorder down to the lowest temperatures studied, yields pinch point features in its correlation

[40] With an additional multiplicative factor of 1/3.

function [29].

Spin-liquids in other degenerate manifolds

As stated at the beginning of this section, the avoidance of LRO can be accomplished when multiple magnetic orders compete such that LRO, and a possible ObD is avoided. This observation alone provides us with a recipe, or at least an indication where other possible spin-liquids may be realized. This is for example the case of the *pinch-line-singularity* [107], the *rank-2* $U(1)$ [108], the pseudo-Heisenberg antiferromagnet [4] spin-liquids. In the pinch-line-singularity spin-liquid (an effective spin 1/2 system) the PC, a splayed ferromagnet, ψ_2 and ψ_3 orders compete. In the rank-2 $U(1)$ spin-liquid (an effective spin 1/2 system) the coplanar antiferromagnet, the ψ_2 and ψ_3 orders compete[41]. Lastly, for the pseudo-Heisenberg antiferromagnet (a non-Kramers system) the PC, the T_1^{xy} splayed ferromagnet, and spin-ice compete. In all of the above case, the low-temperature phase may be described by an emergent rank-2 field theory constructed upon the competing orders and is further discussed in Chapter 3.

2.4 Overview of the Next Chapters

In the last few sections, the different low-temperature magnetic phases, including magnetic LRO and spin-liquids, were discussed. Special attention was brought upon models where multiple magnetic orders compete leading to the observation of either an ObD-selected magnetic order or a spin-liquid phase. Finding a model that presents this competition might require fine-tuning in the interaction parameters $\{J, j_{\text{Isi}}, J_{\text{Pd}}, J_{\text{DM}}, d\}$, i.e. a specific set of values for these, as is the case for the spin-liquids presented in the last section. Nevertheless, there are certain spin models in the pyrochlore lattice which are localized at phase boundaries for a range of the interaction parameters considered. This is precisely the case of the Heisenberg and DM Hamiltonian

$$\mathcal{H} \;=\; J\sum_{\langle ij\rangle}\boldsymbol{S}_i\cdot\boldsymbol{S}_j + J_{\text{DM}}\sum_{\langle ij\rangle}\boldsymbol{D}_{ij}\cdot(\boldsymbol{S}_i\times\boldsymbol{S}_j), \tag{2.36}$$

[41] This spin-liquid is realized in the breathing pyrochlore [109] with a Heisenberg and DM interactions Hamiltonian. Crucially, J_{DM} vanishes in the down (or the up) tetrahedra. As a consequence, in the up (or down) tetrahedra the ψ_2, ψ_3, and coplanar states are degenerate in energy. On the other hand, in the down (or up) tetrahedra *all* the antiferromagnetic $\boldsymbol{q}=0$ orders are degenerate in energy. The mixed degeneracy between different tetrahedra prevents the formation of a LRO by an ObD effect as would be expected for a uniform J_{DM} interaction as is discussed in Chapter 4.

where, for a set of parameters, this model resides at the boundary between a splayed ferromagnet and a Γ_5 phase [110]. This model is of special relevance for compounds where d orbital electrons are responsible for the magnetic behavior, as it was noted that the Heisenberg exchange and the DM interactions are the leading magnetic interactions [37]. This is for example the case of $Lu_2V_2O_7$ [26], $Y_2V_2O_7$ [81], FeF_3 [75], and $NaCaNiF_4$ [111][42]. This model has been explored for certain range of the interaction parameters J and J_{DM}; however, a complete study of this Hamiltonian is yet to be done [26, 73, 75, 76, 112].

In this thesis, we present a detail exploration of the Heisenberg and DM Hamiltonian and the phases observed for *all* possible values of the interaction parameters J and J_{DM}. In Chapter 4, we present a phase diagram obtained for the classical and quantum system where one ferromagnetic phase and two antiferromagnetic phases are identified. In Chapter 5, we study the phenomenon of ObD in the ferromagnetic phase where certain magnetization orientations are chosen. We further demonstrate that the selection for the quantum case is *purely* thermal, uncovering a novel route towards the realization of ObD. In Chapter 6, we study a point in the phase diagram presented in Chapter 4 where no magnetic order is observed effectively realizing a novel spin-liquid phase. Interestingly, at this point in parameter space, the spin system exhibits a bump in the specific heat at a temperature T^*, signaling a rapid crossover from a high-temperature spin-liquid to a low-temperature spin-liquid. We argue that this is entropic in nature and provide evidence of this. Lastly, in Chapter 7, we explore the possible observation of liquid-like correlations in ordered phase for systems whose interaction parameters are proximate to a spin-liquid phase.

[42]The model describing this compound also considers other types of interactions, however, the leading interactions are the Heisenberg and DM.

Chapter 3

The Tool Box

This chapter presents an overview of the analytical and numerical methods used throughout this thesis. These methods are both analytical and numerical in nature. We first present the analytical methods: the self-consistent gaussian approximation, classical low-temperature expansion, quantum linear spin-wave theory, and the irreducible representation analysis of the tetrahedral group T_d. In order to demonstrate the application of this analytical approaches we provide a brief example of how these can be applied at the end of each section. Next, the numerical methods used are presented, these being classical Monte Carlo and iterative minimization.

3.1 Self-Consistent Gaussian Approximation

The self-consistent gaussian approximation (SCGA) [42, 104] is a classical approximation where the hard-spin constraint, i.e. having spins which *individually* fulfill the spin length constraint, is replaced by a soft-spin constraint where the spin length constraint is preserved in *average*. In other words, for a n-component spin the spin length constraint

$$\sum_{\alpha}^{n} (S^{\alpha})^2 = |\boldsymbol{S}|^2 = S^2,$$

is replaced by the thermodynamic average condition

$$\langle |\boldsymbol{S}|^2 \rangle = S^2.$$

This condition can be realized by the introduction of a Lagrange multiplier imposing such average constraint at all temperatures. The introduction of this approximation in the spin-length constraint results in a quadratic theory, i.e. Gaussian theory, which can be solved exactly and from which quantities as the correlation functions can be computed. Since this approximation has been widely used in the study of spin-liquids [42, 44, 104], we apply it in Chapter 6 to study the neutron structure factor of a spin-liquid.

To illustrate how this approximation works for the pyrochlore lattice, we start by considering a general spin Hamiltonian with quadratic interactions

$$\mathcal{H} = \frac{1}{2}\sum_{ia,jb}\sum_{\alpha,\gamma} J^{\alpha,\gamma}_{ia,jb} S^{\alpha}_{ia} S^{\gamma}_{jb}, \tag{3.1}$$

where the sub-indices i and j refer to the primitive FCC vectors $\boldsymbol{R}$, the sub-indices a and b to the sublattice structure, and the super-indices α and γ to the components of the spins, we refer the reader to Appendix A for more details in this convention. The classical partition function associated with this Hamiltonian yields

$$\mathcal{Z} \;=\; \int \prod_{i}^{N} d\boldsymbol{S}\; \delta\left(|\boldsymbol{S}_i| - S^2\right) \exp\left[-\frac{\beta}{2}\sum_{ia,jb}\sum_{\alpha,\gamma} J^{\alpha,\gamma}_{ia,jb} S^{\alpha}_{ia} S^{\gamma}_{jb}\right],$$

where the delta function is introduced to impose the spin length. This constraint can be further carried as a part of the action in the Hamiltonian by expressing the delta function as an integral over an auxiliary field φ

$$\begin{aligned}
\mathcal{Z} \;&=\; \int \prod d\boldsymbol{S} d\varphi \;\exp\left[-i\sum_{ia}\frac{\varphi_{ia}}{2}(\boldsymbol{S}^T_{ia}\boldsymbol{S}_{ia} - S^2)\right] \exp\left[-\frac{\beta}{2}\sum_{ia,jb}\sum_{\alpha,\gamma} J^{\alpha,\gamma}_{ia,jb} S^{\alpha}_{ia} S^{\gamma}_{jb}\right] \\
&=\; \int \prod d\boldsymbol{S} d\varphi \;\exp\left[-\frac{1}{2}\sum_{ia,jb}\boldsymbol{S}^T_{ia}\left(\beta J_{ia,jb} + i\varphi_{ia}\delta_{ia,jb}\right)\boldsymbol{S}_{jb} + iS^2\sum_{ia}\frac{\varphi_{ia}}{2}\right].
\end{aligned} \tag{3.2}$$

Note that introducing the field φ_{ia} results in an effective interaction matrix $M_{ia,ib} = (\beta J_{ia,jb} + i\varphi_{ia}\delta_{ia,jb})$ from which the spin-spin correlation function can be identified, $G_{ia,ib} = (M_{ia,ib})^{-1}$, see Appendix B. The introduction of these fields yields a quadratic action in the spin variables which can be integrated out. To do so, we use the Gaussian d-dimensional integral

$$I = \int d^d x \exp\left[-\frac{1}{2}\boldsymbol{x}^T A \boldsymbol{x}\right] = \left(\frac{(2\pi)^d}{\det(A)}\right)^{\frac{1}{2}}.$$

where A is a $(d \times d)$ matrix and x an d-dimensional vectors. Applying the above identity the following expression is obtained

$$\begin{aligned}
\mathcal{Z} &= \int \mathcal{D}\varphi \left(\frac{(2\pi)^N}{\det(M)} \right)^{1/2} \exp\left[\frac{iS^2}{2} \sum_{ia} \varphi_{ia} \right], \\
&= (2\pi)^{N/2} \int \mathcal{D}\varphi \exp\left[\frac{S^2}{2} \sum_{ia,\alpha} (i\varphi_{ia}) - \frac{1}{2} \ln\det M \right], \\
&= (2\pi)^{N/2} \int \mathcal{D}\varphi \exp\left[\frac{S^2}{2} \mathrm{Tr}(i\varphi) - \frac{1}{2} \mathrm{Tr} \ln M \right], \\
&= (2\pi)^{N/2} \int \mathcal{D}\varphi \exp\left[\frac{1}{2} \mathrm{Tr}\left(S^2 i\varphi - \ln M \right) \right],
\end{aligned}$$

where, by translational symmetry, the φ fields are taken to be equal over all sites of the lattice and an isotropic to correctly represent the nature of the spins' components [1], and N is the number of spins. For isotropic interactions, the above equations obtain a factor of n in the term $\ln M$ and can therefore be evaluated exactly in the limit $n \to \infty$. Alternatively, for the case where n is finite, a saddle point approximation can be taken yielding the constraint

$$\begin{aligned}
\frac{\partial}{\partial \varphi_j} \mathrm{Tr}\left(S^2 i\varphi - \ln(\beta J + i\varphi) \right) &= 0, \\
\sum_{\alpha} (\beta J + i\varphi)^{-1}_{jj,\alpha\alpha} &= S^2.
\end{aligned}$$

This equation can be further solved in reciprocal space by taking the Fourier transform of the matrix $M = \beta J + i\varphi$ and assuming that $i\varphi = \lambda$ is real[2] yielding

$$\frac{1}{N} \sum_{\boldsymbol{q},m} (\beta \epsilon_m(\boldsymbol{q}) + \lambda)^{-1} = S^2, \tag{3.3}$$

where $\epsilon_m(\boldsymbol{q})$ are the eigenvalues of the interaction matrix $J(\boldsymbol{q})$. To impose this constraint it is customary to shift the eigenvalues $\epsilon_m(\boldsymbol{q})$ such that the minimum eigenvalue is 0, i.e. $\epsilon_{\min}(\boldsymbol{q}) = 0$. This shift is produced to avoid the possibility of having a vanishing

[1] Each spin is considered to be equivalent and related by a C_3 symmetry in the global frame.

[2] This condition by itself appears to be quite confusing as the auxiliary fields φ were introduced from the definition of a delta function; however, recasting these fields amounts to imposing a probability distribution on the spin length described by a gaussian probability centered at S^2, see Eq. (3.2). This is also the reason why one refers to λ as a Lagrange multiplier.

denominator on the left-hand side of the above equation and amounts to shifting the value of λ by $\beta\epsilon_{\min}$. This seemingly subtle change associates λ with the inverse of the thermal occupation number of the lowest energy mode of the effective interaction matrix M [3].

In practice, when applying the SCGA the auxiliary field λ is first computed self-consistently and then used to compute other quantities of interest. In particular, this approach provides the following expression for the correlation function structure factor

$$\chi_{ab}^{\alpha\gamma} = \langle S_a^\alpha(\boldsymbol{q}) S_b^\gamma(-\boldsymbol{q})\rangle = \sum_{\boldsymbol{q}} (\beta J_{ab}^{\alpha\gamma}(\boldsymbol{q}) + \lambda)^{-1}, \tag{3.4}$$

which can be easily identified from Eq. (3.2).

Although the SCGA has demonstrated great success when describing a variety of pyrochlore magnets [42, 44, 104] one should be vigilant as there might be some effects that might not be captured by this approach. In particular, it has been noted that this approximation fails to capture the phenomenon of order-by-disorder [46] which is typically produced by higher-order terms in a free-energy description[3].

3.1.1 Application to the Heisenberg Antiferromagnet

To demonstrate how the SCGA can be implemented, we apply this approximation to the Heisenberg antiferromagnetic Hamiltonian (2.23). The interaction matrix for this Hamiltonian has 6 degenerate low energy bands, and 6 dispersive bands as discussed in Subsection 2.3.3. Using this interaction matrix, we may compute self-consistently the Lagrange multiplier λ in Eq. (3.3) as a function of temperature, see Fig. 3.1. Note that at low temperatures, the value of λ *plateaus* to a constant value. For a Hamiltonian with low-energy flat bands, this value reflects the ratio of low-energy flat bands to the total number of bands (12 for the Heisenberg model) times 3.

To be more precise, and assuming $S = 1$ for simplicity, consider Eq. (3.3) and assume that there are N_f number of degenerate low-energy flat bands, this is flat bands with $\epsilon_m(\boldsymbol{q}) = 0$. Therefore, at $T \to 0$ ($\beta \to \infty$) the expression in Eq. (3.3) reduces to the sum

[3] An example of a higher order term is discussed in Chapter 4 for the Γ_5 phase where a sixth order term in the order parameter, i.e. $O(m^6)$, is the first term in a free-energy expansion which differentiates between the ψ_2 and ψ_3 orders.

over the flat bands, indexed by $m\prime$,

$$\begin{aligned} \frac{1}{N}\sum_{\boldsymbol{q},m\prime}\lambda_0^{-1} &= 1, \\ \frac{N_f N_{\mathrm{FCC}}}{4N_{\mathrm{FCC}}}\lambda_0^{-1} &= 1, \\ \lambda_0 &= 3\left(\frac{N_f}{12}\right), \end{aligned} \tag{3.5}$$

where the sum $\sum_{\boldsymbol{q}} 1$ reduces to the number of $\boldsymbol{q}$ points, i.e. the number of FCC points N_{FCC}. Note that by an equivalent argument when, $T \to \infty$ ($\beta \to 0$), λ plateaus to 3 as now the sum in Eq. (3.5) is instead taken over all bands[4]. For the Heisenberg antiferromagnet as $T \to \infty$, $\lambda \to 3/2$, i.e. the number of degenerate low-energy bands is $N_f = 6$.

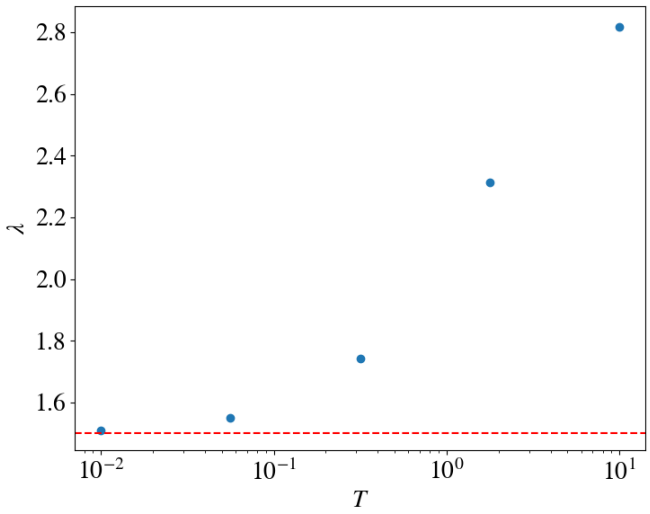


Figure 3.1: Lagrange multiplier as a function of temperature for the Heisenberg antiferromagnet. The red dashed line marks the value $\lambda_0 = 3/2$.

The values of λ can then be used to compute the correlation function of the spin, and

[4]In Eq.(3.3) taking $\beta \to 0$ amounts to having an equal contribution from all bands of $\frac{1}{\lambda}$. Although we could naively say that this would be equivalent to $N_f = 12$, to be completely precise, this is not the case as the starting point for Eq. (3.5) is taking $\beta \to \infty$ which for the high-temperature limit is now $\beta \to 0$ such that *all* bands equally contribute.

in particular the neutron structure factor. These are shown in Fig. 2.10 for the $(hh\ell)$ and $(hk0)$ scattering planes.

3.2 Classical Low-Temperature Expansion

As a magnetic system orders at low temperatures in a long-range ordered configuration, one might be interested in studying the fluctuations of the spins about the ordered configuration. These fluctuations can be used to study the dynamics of the system (the magnon bands), thermal entropic selection, and correlation functions in the ordered phase. To study these fluctuations at low temperatures in a classical system we consider the general quadratic spin Hamiltonian in Eq. (3.1), and assume that the spin components are described in a frame where the $\hat{z}$ axis is the *ordering* direction. In other words,

$$\boldsymbol{S} = \left(\delta n^x, \delta n^y, \sqrt{S^2 - (\delta n^x)^2 - (\delta n^y)^2}\right) \simeq \left(\delta n^x, \delta n^y, S\left(1 - \frac{(\delta n^x)^2}{2S^2} - \frac{(\delta n^y)^2}{2S^2}\right)\right),$$

where it is assumed that the system presents small fluctuations δn^α about the ordering orientation, where α labels the perpendicular directions to the spin ordering direction with $|\delta n^\alpha| \ll S$. In general, the ordered configuration does not have all spins pointing along the same direction; therefore, a sub-index labeling the spins composing the repeating ordered structure is required. For the case of the pyrochlore lattice with nearest-neighbor interactions, we can safely assume that the ordered configuration can be described by a single tetrahedron[5]. Therefore, for a general long-range ordered configuration, the spin variables are expressed as

$$\boldsymbol{S}_a = \left(\delta n_a^x, \delta n_a^y, \left(S - \frac{(\delta n_a^x)^2}{2S} - \frac{(\delta n_a^y)^2}{2S}\right)\right), \tag{3.6}$$

where a labels the sublattice in a single tetrahedron. Introducing the above expression into the Hamiltonian in Eq. (3.1) expressed in the *rotated* basis yields[6]

$$\mathcal{H} \;=\; \mathcal{H}^{(0)} + \mathcal{H}^{(2)} + O(\delta n^3), \tag{3.7}$$

[5] As discussed in the Chapter 2, the nearest-neighbor Hamiltonian for the pyrochlore lattice, the ordered configurations are always $\boldsymbol{q} = 0$ orders, i.e. in a single tetrahedron.

[6] Note that there is no first-order term as it is assumed that the ordered configuration chosen is a true ground state. In fact, the requirement of having a vanishing linear term is also fulfilled by states which describe saddle points in the energy function. This condition can be then used to study meta-stable states and was used by Ref. [113] in the context of linear spin wave theory.

where the zeroth order term is associated with the classical ground state energy of the ordered configuration,

$$\mathcal{H}^{(0)} = \frac{S^2}{2}\sum_{ia,jb} J^{zz}_{ia,jb}, \tag{3.8}$$

and the second-order term is an effective quadratic Hamiltonian for the fluctuating components of the spins

$$\begin{aligned}\mathcal{H}^{(2)} &= \frac{1}{2}\sum_{ia,jb}\sum_{\alpha,\gamma}\left(\delta n^{\alpha}_{ia} J^{\alpha\gamma}_{ia,jb}\delta n^{\gamma}_{jb}\right) - \frac{1}{4}\sum_{ia,jb}\sum_{\alpha,\gamma}\left[(\delta n^{\alpha}_{ia})^2 J^{zz}_{ia,jb} + J^{zz}_{ia,jb}(\delta n^{\gamma}_{jb})^2\right], \\ &= \frac{1}{2}\sum_{ia,jb}\sum_{\alpha,\gamma}\left(\delta n^{\alpha}_{ia} J^{\alpha\gamma}_{ia,jb}\delta n^{\gamma}_{jb}\right) - \frac{1}{2}\sum_{ia,jb}\sum_{\alpha}(\delta n^{\alpha}_{ia})^2 J^{zz}_{ia,jb}. \end{aligned} \tag{3.9}$$

The effective Hamiltonian in Eq. (3.9) can be further simplified in reciprocal space, resulting in

$$\begin{aligned}\mathcal{H}^{(2)} &= \frac{1}{2}\sum_{a,b}\sum_{\alpha,\gamma}\sum_{\boldsymbol{q}}\delta n^{\alpha}_{a}(-\boldsymbol{q})\left(J^{\alpha,\gamma}_{a,b}(\boldsymbol{q}) - \delta_{a,b}\delta_{\alpha,\gamma}\sum_{m} J^{zz}_{a,m}(0)\right)\delta n^{\gamma}_{b}(\boldsymbol{q}), \\ &= \frac{1}{2}\sum_{a,b}\sum_{\alpha,\gamma}\sum_{\boldsymbol{q}}\delta n^{\alpha}_{a}(-\boldsymbol{q}) H^{\alpha,\gamma}_{a,b}(\boldsymbol{q})\delta n^{\gamma}_{b}(\boldsymbol{q}). \end{aligned} \tag{3.10}$$

where $\alpha, \gamma \in \{x, y\}$ represent the *local* xy coordinates, and the matrix $H^{\alpha,\gamma}_{a,b}$ is commonly referred to as the Hessian [90]. The Hamiltonian in Eq. (3.10) can be diagonalized under an orthogonal transformation U

$$\sum_{a,b}\sum_{\alpha,\gamma}(U^{\dagger})^{\alpha}_{n,a} H^{\alpha,\gamma}_{a,b} U^{\gamma}_{m,b} = \varepsilon_n \delta_{n,m},$$

where $\{\varepsilon_n\}$ are the eigenvalues of the Hessian. The effective quadratic Hamiltonian in Eq. (3.7) defines a partition function for the fluctuating components

$$\begin{aligned}\mathcal{Z} &= e^{-\beta\mathcal{H}^{(0)}}\int\prod_{a,\alpha}(\mathcal{D}\ \delta n^{\alpha}_{a})\exp\left\{-\frac{\beta}{2}\sum_{a,b}\sum_{\alpha,\gamma}\sum_{\boldsymbol{q}}\delta n^{\alpha}_{a}(-\boldsymbol{q})H^{\alpha,\gamma}_{a,b}(\boldsymbol{q})\delta n^{\gamma}_{b}(\boldsymbol{q})\right\} \\ &= e^{-\beta\mathcal{H}^{(0)}}\int\prod_{a,\alpha}(\mathcal{D}\ \delta n^{\alpha}_{a})\exp\left\{-\frac{\beta}{2}\sum_{n}\sum_{\boldsymbol{q}}\varepsilon_n(\boldsymbol{q})\delta v_n(-\boldsymbol{q})\delta v_n(\boldsymbol{q})\right\}, \end{aligned} \tag{3.11}$$

where $\{\delta v_n(\boldsymbol{q})\}$ are the eight eigen modes of the Hessian $H^{\alpha,\gamma}_{a,b}(\boldsymbol{q})$. Note that the above equation implies that the average occupation of the eigen modes of the Hessian $\{\delta v_n\}$ is inversely proportional to the corresponding eigenvalue

$$\langle |\delta v_n|^2 \rangle = T/\varepsilon_n(\boldsymbol{q}). \tag{3.12}$$

From Eq. (3.11) the correlation function of the fluctuating components yields

$$\begin{aligned} \langle \delta n^\alpha_a(-\boldsymbol{q}) \delta n^\gamma_b(\boldsymbol{q}) \rangle &= T \left(H^{\alpha,\beta}_{a,b}(\boldsymbol{q}) \right)^{-1} \\ &= T \sum_n \frac{U^\alpha_{na}(-\boldsymbol{q}) U^\gamma_{nb}(\boldsymbol{q})}{\varepsilon_n(\boldsymbol{q})}. \end{aligned} \tag{3.13}$$

The Eq. (3.13) is the correlation function in the *local* basis; therefore, to obtain the correlation function in the global basis the fluctuating components must be rotated back into the global frame

$$\chi^{\alpha\gamma}_{ab} = \sum_{\mu,\nu} (R^{\alpha,\mu}_a)^T R^{\gamma,\nu}_b \langle \delta n^\mu_a(-\boldsymbol{q}) \delta n^\nu_b(\boldsymbol{q}) \rangle \,, \tag{3.14}$$

where R_a is the rotation matrix from the global frame into the local $\boldsymbol{z}_a$ ordering direction. Furthermore, the partition function in Eq. (3.11) can be exactly evaluated to study the evolution of the free energy, and therefore the entropy, as a function of the ordered configuration [74, 90]

$$\mathcal{F} = \mathcal{H}^{(0)} - NT \ln T + \frac{T}{2} \sum_{\boldsymbol{q}} \ln \det \left(H(\boldsymbol{q}) \right). \tag{3.15}$$

The above expression can be used to study the free energy associated with a given ordering configuration. Consequently, for Hamiltonians where the classical ground-state manifold has an accidental symmetry, Eq. (3.15) can be used to study the thermal entropic selection towards a configuration in the classical ground state manifold.

3.2.1 Application to $Er_2Ti_2O_7$

To demonstrate how the thermal ObD selection can be exposed through Eq. (3.15), we study the entropic weight associate to a ground state configuration ψ

$$-\frac{\partial \mathcal{F}}{\partial T} = \mathcal{S}(\psi) = N(\ln T + 1) - \frac{T}{2} \sum_{\boldsymbol{q}} \ln \left(\det H(\boldsymbol{q}) \right). \tag{3.16}$$

For example, we consider the effective spin 1/2 compound $Er_2Ti_2O_7$ [61, 86, 88], whose interaction parameters identify the Γ_5 manifold as the ground state manifold with an accidental $U(1)$ degeneracy, see Subsection 3.4.2. The states in this manifold can be parameterized by a linear combination of the ψ_2 and ψ_3 spin configurations. In other words, the spins of a single tetrahedron configuration in the Γ_5 manifold can be written as

$$\boldsymbol{S}_a^{\Gamma_5}(\theta_{\Gamma_5}) = \cos(\theta_{\Gamma_5})\boldsymbol{S}_a^{\psi_3} + \sin(\theta_{\Gamma_5})\boldsymbol{S}_a^{\psi_2}, \tag{3.17}$$

where $\boldsymbol{S}_a^{\psi_3}$ and $\boldsymbol{S}_a^{\psi_2}$ denote the spin orientations on sublattice a in each of the respective two types spin configurations, and θ_{Γ_5} is an angle parameterize the Γ_5 manifold [1]. We can then define the entropic weight difference as $\Delta\mathcal{S}(\theta_{\Gamma_5}) = \mathcal{S}(\theta_{\Gamma_5}) - \mathcal{S}(0)$ where the state with the most entropic weight is expected to be selected at $T = 0^+$. Using the parameters in Ref. [74] for $Er_2Ti_2O_7$, we compute the quantity $\Delta\mathcal{S}(\theta_{\Gamma_5})$ illustrated in Fig. 3.2. Note that the maximum of this function is located at $\theta_{\Gamma_5} = 30°, 90°$. These angles are associated with the ψ_2 configuration and the entropic weight predicts that at low temperatures this configuration is selected [74].

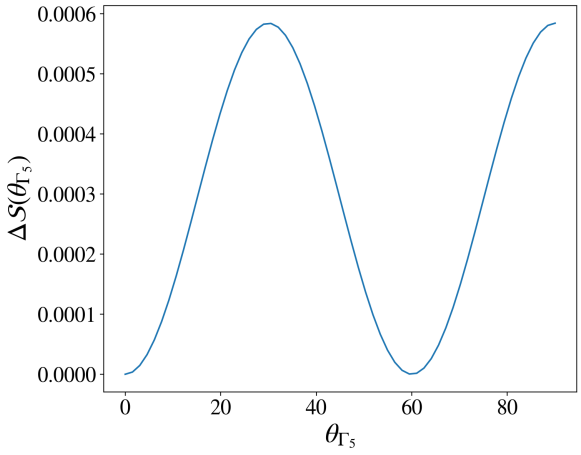


Figure 3.2: Entropic weight difference between states in the Γ_5 manifold. Here, the entropic difference is taken with respect to the entropic weight of the ψ_3 states.

3.3 Quantum Linear Spin-Wave Theory

In the previous section, the classical spin fluctuations about a ground state configurations were studied. Alternatively, we could have started by considering the *quantum* fluctua-

tions instead. This analysis is produced by recasting the spin operators in the classical ground state ordering frame into bosonic operators through the Holstein-Primakoff (HP) transformation [70, 74, 90, 110]

$$\begin{aligned}\hat{S}^z_{ia} &= S - \hat{c}^\dagger_{ia}\hat{c}_{ia},\\ \hat{S}^+_{ia} &= S^x_{ia} + iS^y_{ia} = (2S - \hat{c}^\dagger_{ia}\hat{c}_{ia})^{1/2}\hat{c}_{ia},\\ \hat{S}^-_{ia} &= S^x_{ia} - iS^y_{ia} = \hat{c}^\dagger_{ia}(2S - \hat{c}^\dagger_{ia}\hat{c}_{ia})^{1/2},\end{aligned}$$

where $[\hat{c}_{ia}, \hat{c}^\dagger_{jb}] = \delta_{ia,jb}$. Here, it is assumed that the proliferation of the HP bosons *lower* the spin value along the ordering direction, therefore producing an excitation. At low temperatures, the system is assumed to have small fluctuations about the classical ground state configuration which allows us to assume that the number of HP bosons is small compared to S, i.e. $\hat{c}^\dagger_{ia}\hat{c}_{ia}/S \ll 1$. Applying this approximation to the spin operators yields

$$\begin{aligned}\hat{S}^+_{ia} &\simeq \sqrt{2S}\hat{c}_{ia},\\ \hat{S}^-_{ia} &\simeq \sqrt{2S}\hat{c}^\dagger_{ia},\end{aligned}$$

or in terms of the *local* spin components

$$\begin{aligned}\hat{S}^z_{ia} &= S - \hat{c}^\dagger_{ia}\hat{c}_{ia},\\ \hat{S}^x_{ia} &= \sqrt{\frac{S}{2}}(\hat{c}_{ia} + \hat{c}^\dagger_{ia}) + O(\hat{n}_{ia}/S^{1/2}),\\ \hat{S}^y_{ia} &= -i\sqrt{\frac{S}{2}}(\hat{c}_{ia} - \hat{c}^\dagger_{ia}) + O(\hat{n}_{ia}/S^{1/2}).\end{aligned} \tag{3.18}$$

Introducing the spin operators in terms of the HP bosons in the bilinear Hamiltonian in Eq. (3.1) written in the local ground state basis results in the following Hamiltonian [7]

$$\begin{aligned}\mathcal{H} &= \sum_{a,b}\frac{S(S+1)}{2}J^{zz}_{a,b}(\boldsymbol{q}=0) + \frac{S}{2}\sum_{\boldsymbol{q}}X^\dagger(\boldsymbol{q})\begin{pmatrix}A(\boldsymbol{q}) & B(\boldsymbol{q})\\ B^*(-\boldsymbol{q}) & A^*(-\boldsymbol{q})\end{pmatrix}X(\boldsymbol{q})\\ &= \sum_{a,b}\frac{S(S+1)}{2}J^{zz}_{a,b}(\boldsymbol{q}=0) + \frac{S}{2}\sum_{\boldsymbol{q}}X^\dagger(\boldsymbol{q})H_{LSW}X(\boldsymbol{q}),\end{aligned} \tag{3.19}$$

[7] Note that the constant term in Eq. (3.19) in comparison to Eq. (3.8) has a factor of $(1 + \frac{1}{S})$. This factor is taken to be a small quantum correction which vanishes when $S \to \infty$.

where

$$
\begin{aligned}
A_{ab}(\boldsymbol{q}) &= \frac{1}{2}\left[J^{xx}_{a,b}(\boldsymbol{q}) + J^{yy}_{a,b}(\boldsymbol{q}) - i\left(J^{xy}_{a,b}(\boldsymbol{q}) - J^{yx}_{a,b}(\boldsymbol{q})\right)\right] - \delta_{a,b}\sum_{\ell} J^{zz}_{a,\ell}(\boldsymbol{q}=0)\\
A^{*}_{ab}(-\boldsymbol{q}) &= \frac{1}{2}\left[J^{xx}_{a,b}(\boldsymbol{q}) + J^{yy}_{a,b}(\boldsymbol{q}) + i\left(J^{xy}_{a,b}(\boldsymbol{q}) - J^{yx}_{a,b}(\boldsymbol{q})\right)\right] - \delta_{a,b}\sum_{\ell} J^{zz}_{a,\ell}(\boldsymbol{q}=0)\\
B^{*}_{ab}(-\boldsymbol{q}) &= \frac{1}{2}\left[J^{xx}_{a,b}(\boldsymbol{q}) - J^{yy}_{a,b}(\boldsymbol{q}) - i\left(J^{xy}_{a,b}(\boldsymbol{q}) + J^{yx}_{a,b}(\boldsymbol{q})\right)\right]\\
B_{ab}(\boldsymbol{q}) &= \frac{1}{2}\left[J^{xx}_{a,b}(\boldsymbol{q}) - J^{yy}_{a,b}(\boldsymbol{q}) + i\left(J^{xy}_{a,b}(\boldsymbol{q}) + J^{yx}_{a,b}(\boldsymbol{q})\right)\right]\\
X(\boldsymbol{q}) &= \begin{pmatrix}\hat{c}_0(\boldsymbol{q}) & \hat{c}_1(\boldsymbol{q}) & \hat{c}_2(\boldsymbol{q}) & \hat{c}_3(\boldsymbol{q}) & \hat{c}^{\dagger}_0(-\boldsymbol{q}) & \hat{c}^{\dagger}_1(-\boldsymbol{q}) & \hat{c}^{\dagger}_2(-\boldsymbol{q}) & \hat{c}^{\dagger}_3(-\boldsymbol{q})\end{pmatrix}^{T}.
\end{aligned}
$$

The above Hamiltonian describes the fluctuating components around the ordering ground state, the magnon excitations. Since the resulting expression is quadratic, the eigen modes defining the excitations of resulting system can be exactly studied. To do so, a Bogoliubov transformation preserving the bosonic commutation relations is applied [70, 74, 110]. In other words, given the commutation relation on $X(\boldsymbol{q})$,

$$\left[X_i(\boldsymbol{q}), X^{\dagger}_j(\boldsymbol{q}')\right] = \sigma_{ij}\delta_{\boldsymbol{q},\boldsymbol{q}'},$$

where

$$\sigma = \begin{pmatrix} 1_{4\times 4} & 0_{4\times 4} \\ 0_{4\times 4} & -1_{4\times 4}\end{pmatrix},$$

we define a Bogoliubov transformation U such that

$$X(\boldsymbol{q}) = UY(\boldsymbol{q}),$$

where

$$Y(\boldsymbol{q}) = \begin{pmatrix}\hat{d}_0(\boldsymbol{q}) & \hat{d}_1(\boldsymbol{q}) & \hat{d}_2(\boldsymbol{q}) & \hat{d}_3(\boldsymbol{q}) & \hat{d}^{\dagger}_0(-\boldsymbol{q}) & \hat{d}^{\dagger}_1(-\boldsymbol{q}) & \hat{d}^{\dagger}_2(-\boldsymbol{q}) & \hat{d}^{\dagger}_3(-\boldsymbol{q})\end{pmatrix}^{T},$$

resulting in the bosonic commutation relations of $Y(\boldsymbol{q})$ operators

$$\left[Y_i(\boldsymbol{q}), Y^{\dagger}_j(\boldsymbol{q}')\right] = \sigma_{ij}\delta_{\boldsymbol{q},\boldsymbol{q}'}.$$

By applying this transformation into the quadratic Hamiltonian, and ignoring the constant term, we obtain the quadratic bosonic Hamiltonian[8]

$$\begin{aligned}\mathcal{H}^{(2)} &= \frac{S}{2}\sum_{\boldsymbol{q}} Y^{\dagger}(\boldsymbol{q})U^{\dagger}H_{LSW}UY(\boldsymbol{q}) \\ &= \frac{S}{2}\sum_{\boldsymbol{q}} Y^{\dagger}(\boldsymbol{q})\sigma U^{-1}\sigma H_{LSW}UY(\boldsymbol{q}) \\ &= \frac{S}{2}\sum_{\boldsymbol{q}} Y^{\dagger}(\boldsymbol{q})\sigma D_{LSW}Y(\boldsymbol{q}),\end{aligned}$$

where D_{LSW} is diagonal[9]. Using the commutation relation of the Bogoliubov bosons and the occupation number operator, the above Hamiltonian can be written as a simple quantum harmonic oscillator Hamiltonian

$$\mathcal{H}^{(2)} = S\sum_{\boldsymbol{q}}\sum_{a}\omega_a(\boldsymbol{q})\left[\hat{n}_a(\boldsymbol{q})+\frac{1}{2}\right], \tag{3.20}$$

where $\{\omega_a(\boldsymbol{q})\}$ are the magnon energies and $\{n_a(\boldsymbol{q})\}$ is the corresponding occupation number. The magnon energies define the allowed energy and momentum values at which an excitation can be produced. These excitations can be experimentally observed in the inelastic neutron scattering in an ordered phase [70, 74, 90], and can be described using the HP bosons by the expression

$$\begin{aligned}S(\boldsymbol{q},\omega) &= \sum_{a,b}\sum_{\alpha,\beta}\sum_{\gamma,\phi}\underbrace{\left(\delta_{\alpha,\beta}-\frac{q_\alpha q_\beta}{\boldsymbol{q}^2}\right)}_{\text{projection factor}}R_a^{\alpha,\gamma}R_b^{\beta,\phi}\langle\hat{S}_a^{\gamma}(-\boldsymbol{q},-\omega)\hat{S}_b^{\phi}(\boldsymbol{q},\omega)\rangle, \\ &= \frac{S}{2}\sum_{\alpha,\beta}\left(\delta_{\alpha,\beta}-\frac{q_\alpha q_\beta}{\boldsymbol{q}^2}\right)\sum_{a}\left[n_{\mathrm{BE}}(\epsilon_a)\delta(\omega-\epsilon_a)\tilde{\boldsymbol{M}}_{a,a}^{\alpha,\beta}+(1+n_{\mathrm{BE}}(\epsilon_a))\delta(\omega-\epsilon_a)\tilde{\boldsymbol{M}}_{a+s,a+s}^{\alpha,\beta}\right],\end{aligned} \tag{3.21}$$

where the projection factor accounts for the perpendicular components of the scattered neutrons, n_{BE} is the Bose-Einstein distribution, and the matrix $\tilde{\boldsymbol{M}}$ is defined as

$$\tilde{\boldsymbol{M}}^{\alpha,\beta} = \sigma U^{-1}\sigma\boldsymbol{M}^{\alpha,\beta}U$$

[8]Here the identity $U^{-1}=\sigma U^{\dagger}\sigma$ is used which is easily derived from the bosonic commutation relations.

[9]Note that the Bogoliubov transformation defines the eigenvectors of the matrix σH_{LSW} *instead* of the matrix H_{LSW}.

with

$$M_{a,b}^{\alpha,\beta} = \sum_{\gamma,\phi} I_\gamma I_\phi \begin{pmatrix} p_\gamma R_a^{\alpha,\gamma} R_b^{\beta,\phi} & p_\gamma p_\phi R_a^{\alpha,\gamma} R_b^{\beta,\phi} \\ R_a^{\alpha,\gamma} R_b^{\beta,\phi} & p_\phi R_a^{\alpha,\gamma} R_b^{\beta,\phi}, \end{pmatrix} \tag{3.22}$$

where $I_x = 1$, $I_y = -i$, $p_x = 1$ and $p_y = -1$. For a full derivation of the above expression, the reader is referred to Appendix F.

3.3.1 Application to $Yb_2Ti_2O_7$

The Eq. (3.21) can be used to study magnon modes observed in the inelastic neutron scattering of an ordered phase. This expression can be used to study the energy-integrated neutron structure factor in the ordered phase resulting from the magnon excitations by integrating Eq. (3.21) over *all* energies

$$S(\boldsymbol{q}) = \int_0^\infty S(\boldsymbol{q}, \omega) d\omega. \tag{3.23}$$

The resulting expression is the diffuse scattering that would be observed *beneath* the magnetic Bragg peaks in the elastic neutron scattering.

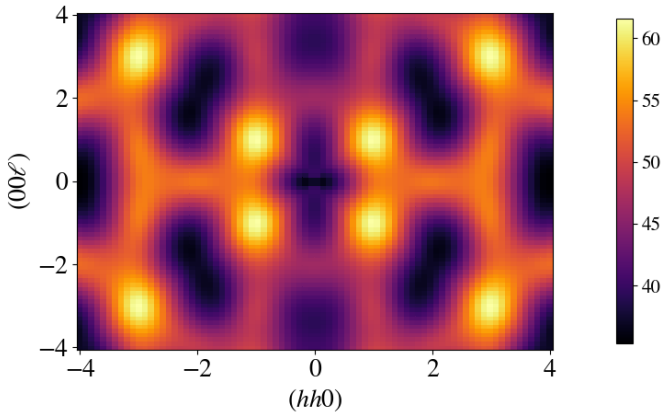


Figure 3.3: Neutron elastic structure factor for $Yb_2Ti_2O_7$ in the $(hh\ell)$ plane.

As an example, consider the effective spin 1/2 compound $Yb_2Ti_2O_7$, and take the interaction parameters identified by Ref. [70]. The elastic neutron structure factor at $T \to 0$

for this compound is calculated using Eq. (3.23) and illustrated in Fig. 3.3. For this compound, rods along the [111] direction in the neutron scattering structure factor have attracted considerable attention in the last few years [70, 93–95], which were believed to be related to pinch point features [114] and latter associated as being an artifact from the neutron projector [92, 115]. Ref. [116] noted that the rod features would disappear in the ordered phase as the temperature is lowered. This observation agrees with the prediction shown in Fig. 3.3 as this structure factor was taken for $T \to 0$. However, the rods of scattering along the [111] direction can be *recovered* by increasing the temperature in Eq. (3.23) (not shown) which in turn corresponds to increasing the magnon population. Interestingly, if the structure factor is obtained through a classical low-temperature expansion in Eq. (3.13) with the corresponding neutron projector, the rods of scattering are obtained and are *not* predicted to vanish as $T \to 0$ as the temperature in this expression simply consists of a multiplicative factor which only modifies the intensity of the pattern but not its modulation.

3.4 Irreducible Representation Analysis

The irreducible representation (irrep) analysis is based on the study of a symmetry group and how this can be decomposed into independent subspaces. Since we are interested in the study of a Hamiltonian $\mathcal{H}$ defined on a lattice, and the lattice itself has a symmetry group $\mathcal{G}$, the identification of the eigen modes of the Hamiltonian can be done by studying those of the group $\mathcal{G}$ instead. This is simply a property of the invariance of $\mathcal{H}$ under the a symmetry transformations $g \in \mathcal{G}$,

$$g\mathcal{H}g^{-1} = \mathcal{H}, \tag{3.24}$$

or equivalently $[g, \mathcal{H}] = 0$. For the pyrochlore lattice with nearest-neighbor interactions, this analysis was carried by Yan *et al.* [74] for the tetrahedral group T_d. This study was inspired by the observation that the Hamiltonian of the pyrochlore lattice with *only* nearest-neighbor interactions can be expressed as the sum of Hamiltonians in each tetrahedron, see Eq. (2.28). Therefore, the irrep analysis of the T_d identifies the eigen modes of a single tetrahedron which in turn represent the possible $\boldsymbol{q} = 0$ modes discussed in Subsection 2.3.1. Here, we present the general ideas describing this decomposition by first discussing how an irrep analysis would be produced for a group $\mathcal{G}$ and then apply these to T_d.

3.4.1 General Idea

In order to find a decomposition of the group $\mathcal{G}$, we first have to find a representation in which this symmetry group can be partitioned into a direct sum of independent subspaces. To this end, we first have to study the structure of the group and the different types of transformations defined in this group, i.e. different types of rotations and reflections. To do so, one can classify the objects of the group in different equivalence classes [117] defined by the conjugation operation over an element $f_1 \in \mathcal{G}$ by another element $g \in \mathcal{G}$

$$g f_1 g^{-1}. \tag{3.25}$$

Then, two elements of the group f_1 and f_2 belong to the same equivalence class if and only if

$$g f_1 g^{-1} = f_2. \tag{3.26}$$

for some element $g \in \mathcal{G}$. In other words, a group $\mathcal{G}$ can be partitioned into different sets, called the equivalence classes, where elements of a particular set are related by the transformation Eq. (3.26). A consequence of this classification into equivalence classes is that group elements that act similarly will end up in the same equivalence class. For example, all lattice reflections belong to the same equivalence class[10].

To depart from the abstract representation of the group $\mathcal{G}$, we can study its matrix representation Γ instead[11]. This representation preserves *all* the properties of the equivalence classes and the algebra[12] of the elements of the group. However, the choice of the matrix representation is not unique as one can produce a similarity transformation that defines a different but equivalent basis Γ'. Therefore, to describe the matrix representation Γ, a property invariant under a similarity transformation must be used. The trace of the matrix representation possess this property and as such is called the *character* of the representation

$$\chi(g) = \mathrm{Tr}\left[\Gamma(g)\right] = \mathrm{Tr}\left[\Gamma'(g)\right]. \tag{3.27}$$

Now suppose that there exist some representation Γ where the matrices of the operators are found to be *block diagonal* such that any operation performed can be taken as the operation over distinct subspaces. If this is the case, in principle we could describe the

[10] Given that the similarity transformation Eq. (3.26) does not change the equivalence class of an object, this operation defines closed orbits (this refers to the sequence of elements resulting from an operation repeated multiple times which is bound to be repeated in a finite group) where, potentially, all members of the equivalence class are connected by this operation.

[11] For example, the identity transformation $\mathcal{E}$ is then represent by a identity matrix $\mathbb{1}$.

[12] This means the operations and group products defined.

group as a direct sum of distinct subspaces which do not overlap under any symmetry transformation. In other words, one could partition the symmetry group $\mathcal{G}$ as

$$\mathcal{G} = \mathcal{G}_0 \oplus \mathcal{G}_1 \oplus + \cdots .$$

This construction implies a relation between the character of the transformation in the group $\mathcal{G}$ and the character in the corresponding subspaces $\mathcal{G}_i$

$$\chi(g) = \sum_i \chi_i(g). \tag{3.28}$$

Moreover, imagine that the subspace $\mathcal{G}_i$ is observed h_i times in this representation. Then, the character can be written as

$$\chi(g) = \sum_i h_i \chi_i(g). \tag{3.29}$$

The above equation for the character of the element g has been produced by assuming that a block diagonal representation could be obtained. In principle, one could try to keep on repeating this process where each block would be further block-diagonalized. However, since the groups considered are finite[13], this procedure always comes to an end. In fact, when no further decomposition can be produced, the representation found is said to be *irreducible*; hence, the name irreducible representation. After finding the irreducible representation of the group $\mathcal{G}$, we may want to know how many subspaces are found following this procedure, see Eq. (3.28). Fortunately, the number of subspaces is exactly the same number as the number of equivalence classes described above [117].

To apply this formalism to a given system, two theorems [33, 117], or rather the equations given by those, are used:

$$\mathcal{N}\delta_{ij} = \sum_g \chi_i^*(g)\chi_j(g), \tag{3.30}$$

and

$$h_j = \frac{1}{\mathcal{N}} = \sum_g \chi_j(g)\chi(g), \tag{3.31}$$

where $\mathcal{N}$ is the number of elements found in the group $\mathcal{G}$. A compact way of presenting all the information of this construction is illustrated in the character table $\chi(g)$ of the different irreducible representations where the subspaces and equivalence classes are listed

[13] These being the symmetry groups on a finite lattice.

along with the characters in each of the corresponding subspaces. In the next subsection we consider the irreducible representation of the group T_d, present its character table, and discuss the eigen modes found for the single tetrahedron Hamiltonian $\mathcal{H}^{\boxtimes}$ in Eq. (2.28) which correspond to the $\boldsymbol{q} = 0$ configurations.

3.4.2 Irreducible Representation of the Tetrahedral Group $\mathbf{T_d}$

The tetrahedral group T_d is composed by the symmetry operations that transform a single tetrahedron into itself. The possible transformations are the identity ($\mathcal{E}$), a rotation by $2\pi/3$ about (111) axis (C_3), a rotation by π about the Cartesian axis (C_2), a rotation by $\pi/2$ about a Cartesian axis followed by a reflection from the perpendicular plane defined by this axis (S_4), and a reflection defined by a plane which cuts the tetrahedron in half (σ_d)[14]. In Fig. 3.4, an example of some of the rotation axis as well as one of the reflection planes are illustrated.

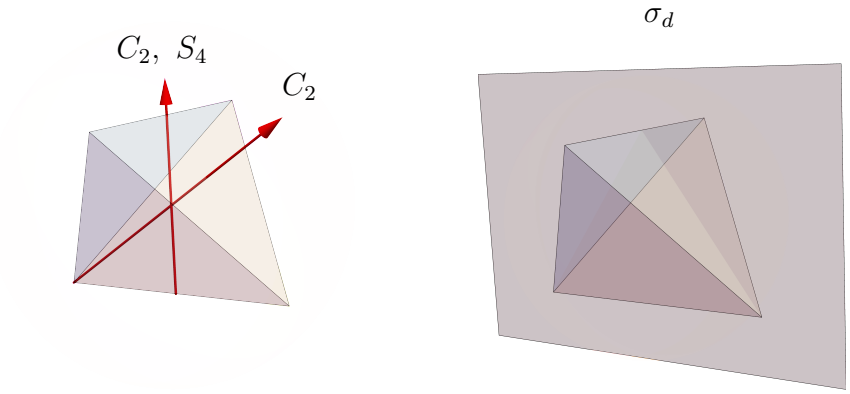


Figure 3.4: (a) Rotation axis for the C_2, C_3, and S_4 transformations (b) Reflection plane σ_d.

The character table for the group T_d is given in Table 3.1 [118] where, in the top row, the different equivalence classes are listed[15], and in the first column, the irreps are provided. Note that the dimension of each subspace is provided by the trace (or character) of the identity operator in the first column. It is customary to name the different resulting

[14]The total number of elements for this group is 24 which coincides with size of the permutation group of four elements as $4! = 24$

[15]Here the number beside each corresponds to the number of elements in each equivalence class

	$\mathcal{E}$	8 C_3	3 C_2	6 S_4	6 σ_d
A_1	1	1	1	1	1
A_2	1	1	1	-1	-1
E	2	-1	2	0	0
T_1	3	0	-1	1	-1
T_2	3	0	-1	-1	1

Table 3.1: Character table of the group T_d where the numbers represent the value of the character $\chi(g)$ for the block represented by the corresponding irrep.

subspaces by the dimensionality that these span. All one-dimensional representations are labeled with the letter A, two-dimensional representations by the letter E, and three-dimensional representations by the letter T. With the character table, and Eq. (3.29), we find that the group T_d can be partitioned in the following way[16]

$$T_d = A_2 \oplus E \oplus T_1 \oplus T_1 \oplus T_2 \tag{3.32}$$

where two copies of the T_1 irrep are identified, this double appearance of the T_1 irrep is further discussed below. The resulting subspaces are characterized by a basis that transforms according to the character table. For example, consider the one-dimensional A_2 representation. As the basis of this representation is one-dimensional, the character is simply a multiplicative factor which transform the basis of the representation. Therefore, the basis of this space is invariant under the C_3 and C_2 rotations whereas it changes sign under the action of S_4 and σ_d. In terms of the spin components, a natural choice for this basis is to take the spins pointing along their local $\boldsymbol{z}$ direction, i.e. the AIAO configuration in Fig. 2.7, as this configuration is invariant under C_3 and C_2 transformations. Furthermore, a reflection will take the basis vector into its inverse additive since spins are axial vectors and this transformation is equivalent to producing rotation by π around the vector normal to the reflecting plane[17]. This demonstrates that the AIAO configuration is indeed the basis of the A_2 irrep.

Clearly, the case of a one-dimensional representation is the simplest as the characters in this representation are the transformations themselves. For all other non-one-dimensional irreps we would have to consider the action of the symmetry operations on the basis vectors

[16] This decomposition is obtained as $\dim(T_d) = 12 = 1+2+3+3+3 = \dim(A_2)+\dim(E)+\dim(T_1)+\dim(T_1)+\dim(T_2)$ where each number correspond to the dimensionality of the corresponding irrep subspace.

[17] For example, if we produce a reflection along the (110) directions, then all vectors will simply be rotted by π around the vector $(1\bar{1}0)$, producing an overall negative sign.

corresponding to each subspace. Therefore, the characters of the symmetry operations shown in Tab. 3.1 are the trace of these transformations in the subspace span by the basis. Although this calculation can be performed, the identification of the other irrep modes can be done by instead considering the $\boldsymbol{q} = 0$ orders presented in Subsection 2.3.1. In fact, since the irreps basis are spin configurations that transform within the subspace defined by their corresponding irrep, it should not be surprising that these configurations coincide with the $\boldsymbol{q} = 0$ orders as these are the eigen modes of a single tetrahedron Hamiltonian[18]. In the irreducible presentation terminology, the AIAO corresponds to the A_2 irrep, the ψ_2 and ψ_3 correspond to the E irrep, the PC states correspond to the T_2 irrep, and the coplanar antiferromagnet and colinear ferromagnet states correspond to the T_1 irreps. Since both coplanar antiferromagnet and colinear ferromagnet states belong to the T_1 irrep, we label $T_{1\perp}$ the irrep corresponding to the coplanar antiferromagnet and $T_{1\parallel}$ the irrep corresponding to the colinear ferromagnet. Moreover, note that the ψ_2 and ψ_3 spin configurations belong to the *same* irrep E, and therefore the same eigen mode of $\mathcal{H}^{\boxtimes}$. This observation clarifies why the two configurations are energy-degenerate as previously stated in Subsection 2.3.1.

Taking the spins in the global frame, the irrep modes, $\boldsymbol{m}_I^{\boxtimes}$ for the I^{th} irrep, corresponding to the spin configurations in a single tetrahedron illustrated in Fig. 2.7 are

$$m_{A_2}^{\boxtimes} = \frac{1}{2\sqrt{3}} \sum_a (\boldsymbol{z}_a \cdot \boldsymbol{S}_a), \tag{3.33}$$

$$\boldsymbol{m}_{E}^{\boxtimes} = \frac{1}{2} \sum_a \begin{pmatrix} \frac{1}{\sqrt{6}} \boldsymbol{x}_a \cdot \boldsymbol{S}_a \\ \frac{1}{\sqrt{2}} \boldsymbol{y}_a \cdot \boldsymbol{S}_a \end{pmatrix}, \tag{3.34}$$

$$\boldsymbol{m}_{T_{1\parallel}}^{\boxtimes} = \frac{1}{2} \sum_a \begin{pmatrix} S_a^x \\ S_a^y \\ S_a^z \end{pmatrix}, \tag{3.35}$$

$$\boldsymbol{m}_{T_{1\perp}}^{\boxtimes} = \frac{1}{2\sqrt{2}} \sum_a \begin{pmatrix} z_a^x \boldsymbol{v}_a^{yz} \cdot \boldsymbol{S}_a \\ z_a^y \boldsymbol{v}_a^{xz} \cdot \boldsymbol{S}_a^y \\ z_a^z \boldsymbol{v}_a^{xy} \cdot \boldsymbol{S}_a^z \end{pmatrix}, \tag{3.36}$$

$$\boldsymbol{m}_{T_2^{\boxtimes}} = \frac{1}{2\sqrt{2}} \sum_a \begin{pmatrix} (\boldsymbol{z}_a \times \boldsymbol{S}_a)^x \\ (\boldsymbol{z}_a \times \boldsymbol{S}_a)^y \\ (\boldsymbol{z}_a \times \boldsymbol{S}_a)^z \end{pmatrix}, \tag{3.37}$$

where z_a^α is the α component of the local $\boldsymbol{z}_a$ direction of the a^{th} sublattice, and $\boldsymbol{v}_a^{\alpha\beta}$ are the normalized bond vectors attached to a sublattice site a belonging to an up-tetrahedron and which lie on the cubic α-γ plane defined as

[18] As $[g, \mathcal{H}] = 0$ for $g \in T_d$ these are also eigen modes in T_d. In other words, the eigen modes of $\mathcal{H}$ coincide with the irrep modes.

$$
\begin{aligned}
\boldsymbol{v}_0^{xy} &= -\boldsymbol{v}_1^{xy} = \frac{1}{\sqrt{2}}\begin{pmatrix}1\\1\\0\end{pmatrix}, \qquad \boldsymbol{v}_2^{xy} = -\boldsymbol{v}_2^{xy} = \frac{1}{\sqrt{2}}\begin{pmatrix}-1\\1\\0\end{pmatrix}, \\
\boldsymbol{v}_0^{xz} &= -\boldsymbol{v}_2^{xz} = \frac{1}{\sqrt{2}}\begin{pmatrix}1\\0\\1\end{pmatrix}, \qquad \boldsymbol{v}_1^{xz} = -\boldsymbol{v}_3^{xz} = \frac{1}{\sqrt{2}}\begin{pmatrix}1\\0\\-1\end{pmatrix}, \\
\boldsymbol{v}_0^{yz} &= -\boldsymbol{v}_3^{yz} = \frac{1}{\sqrt{2}}\begin{pmatrix}0\\1\\1\end{pmatrix}, \qquad \boldsymbol{v}_1^{yz} = -\boldsymbol{v}_2^{yz} = \frac{1}{\sqrt{2}}\begin{pmatrix}0\\-1\\1\end{pmatrix}.
\end{aligned}
$$

The Diagonalized Single Tetrahedron Hamiltonian $\mathcal{H}^{\boxtimes}$

The irrep modes $\{\boldsymbol{m}_I^{\boxtimes}\}$ can be used to re-express the Hamiltonian in a single tetrahedron $\mathcal{H}^{\boxtimes}$ in its diagonal basis. To this end, we first have to express $\mathcal{H}^{\boxtimes}$ as a 12-dimensional matrix and then used the irrep modes $\{\boldsymbol{m}_I^{\boxtimes}\}$ to diagonalize it. Although this procedure can be done in the global physical interaction parameter basis $\{J, J_{\text{Ising}}, J_{\text{Pd}}, J_{\text{DM}}, d\}$, it is instead useful to work in a basis which reflects the symmetries of a single tetrahedron. Following Ref. [74], this basis is constructed by considering the general bilinear exchange Hamiltonian (3.1) and studying the effect of the bond exchange matrix $J_{a,b}^{\alpha\gamma}$ between two sites in a single tetrahedron, $\{J_1, J_2, J_3, J_4, d\}$[19]. For example, the exchange matrix in an up tetrahedron between the sublattices 0 and 1 is

$$
J_{0,1} = \begin{pmatrix} J_1 & J_3 & -J_4 \\ J_3 & J_1 & -J_4 \\ J_4 & J_4 & J_2 \end{pmatrix}, \tag{3.38}
$$

where the resulting couplings are related to the global physical interaction parameter basis $\{J, J_{\text{Ising}}, J_{\text{Pd}}, J_{\text{DM}}\}$ in the following way

$$
\begin{aligned}
J &= J_1 - J_3, && (3.39)\\
J_{\text{Ising}} &= -3J_1 + 3J_2 + 3J_3, && (3.40)\\
J_{\text{Pd}} &= -2J_1 + 2J_2 + 4J_3, && (3.41)\\
J_{\text{DM}} &= -J_1 + J_2 + J_3 + J_4, && (3.42)
\end{aligned}
$$

[19] Note that for both descriptions the single-ion-anisotropy term is unchanged.

or equivalently

$$J_1 = J - \frac{1}{3}J_{\text{Ising}} + \frac{1}{2}J_{\text{Pd}}, \tag{3.43}$$

$$J_2 = J + \frac{1}{3}J_{\text{Ising}}, \tag{3.44}$$

$$J_3 = -\frac{1}{3}J_{\text{Ising}} + \frac{1}{2}J_{\text{Pd}}, \tag{3.45}$$

$$J_4 = -\frac{1}{3}J_{\text{Ising}} + J_{\text{DM}}. \tag{3.46}$$

The other exchange matrices $J_{a,b}$ can be obtained by performing the symmetry transformations in T_d. For example, the $J_{0,3}$ matrix can be obtained by performing a C_3 rotation about the (111) axis, i.e. $J_{0,3} = \Gamma(C_3)J_{0,1}\Gamma(C_3)^T$. Lastly and for completeness, we provide the local interaction matrix $J_{a,a}$ which only contains the single-ion anisotropy interactions. These matrices are obtained by considering the matrix resulting from the operation $\boldsymbol{z}_a\boldsymbol{z}_a^T$[20]. For example, for the 0^{th} sublattice the $J_{0,0}$ matrix is

$$J_{0,0} = \frac{d}{3}\begin{pmatrix} 1 & 1 & 1 \\ 1 & 1 & 1 \\ 1 & 1 & 1 \end{pmatrix}. \tag{3.47}$$

In terms of the irrep modes $\{\boldsymbol{m}_I^{\boxtimes}\}$, we now can write the single tetrahedron Hamiltonian as

$$\begin{aligned}\mathcal{H}^{\boxtimes} = \frac{1}{2}\Big[&a_{A_2}(m_{A_2}^{\boxtimes})^2 + a_E(\mathbf{m}_E^{\boxtimes})^2 + a_{T_2}(\mathbf{m}_{T_2}^{\boxtimes})^2 \\ &+a_{T_{1,\parallel}}(\mathbf{m}_{T_{1\parallel}}^{\boxtimes})^2 + a_{T_{1,\perp}}(\mathbf{m}_{T_{1\perp}}^{\boxtimes})^2 + a_{T_{1,\text{mix}}}\mathbf{m}_{T_{1\parallel}}^{\boxtimes}\cdot\mathbf{m}_{T_{1\perp}}^{\boxtimes}\Big].\end{aligned} \tag{3.48}$$

where a_I is the irrep energy parameter (IEP), i.e. the energy cost of the spin configuration corresponding to the I^{th} irrep. In terms of the parameter basis $\{J_1, J_2, J_3, J_4, d\}$, these

[20]This is simply a way to rewrite the single-ion-anisotropy term $(\boldsymbol{S}_a\cdot\boldsymbol{z}_a)^2 = \boldsymbol{S}_a^T(\boldsymbol{z}_a\boldsymbol{z}_a^T)\boldsymbol{S}_a$.

IEPs take the form

$$a_{A_2} = -2J_1 + J_2 - 2J_3 - 4J_4 + d \tag{3.49}$$
$$a_{E} = -2J_1 + J_2 + J_3 + 2J_4 \tag{3.50}$$
$$a_{T_2} = -J_2 + J_3 - 2J_4 \tag{3.51}$$
$$a_{T_{1\parallel}} = 2J_1 + J_2 + \frac{d}{3} \tag{3.52}$$
$$a_{T_{1\perp}} = -J_2 - J_3 + 2J_4 + \frac{2d}{3} \tag{3.53}$$
$$a_{T_{1,\text{mix}}} = -\frac{\sqrt{2}}{3}(3J_3 + d). \tag{3.54}$$

Note that in Eq. (3.48) there is a term that mixes the two identified T_1 irreps, i.e. the coplanar antiferromagnet and the colinear ferromagnet configurations. This mixing is possible as both irreps transform in the same symmetry subspace T_1. To avoid this complication we may define a *new* irrep basis for the T_1 irreps such that the mixing term is avoided. The rotated basis for the T_1 irreps is defined as

$$\boldsymbol{m}^{\boxtimes}_{T_1+} = \cos\theta\ \boldsymbol{m}^{\boxtimes}_{T_1\parallel} + \sin\theta\ \boldsymbol{m}^{\boxtimes}_{T_1\perp} \tag{3.55}$$
$$\boldsymbol{m}^{\boxtimes}_{T_1-} = \sin\theta\ \boldsymbol{m}^{\boxtimes}_{T_1\parallel} - \cos\theta\ \boldsymbol{m}^{\boxtimes}_{T_1\perp} \tag{3.56}$$

where the rotation angle, also refer to as the *splayed* angle is given by

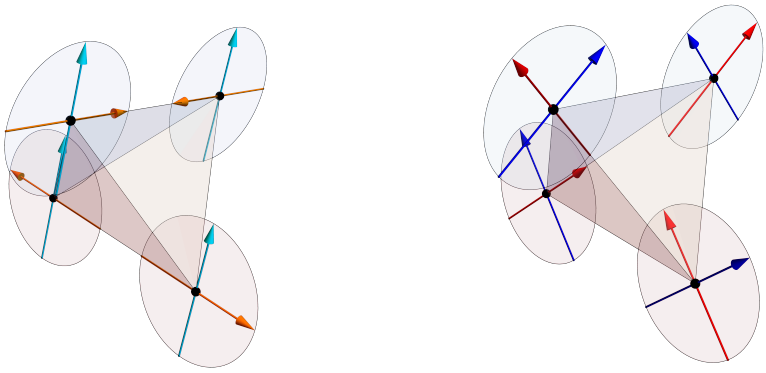
$$\theta = \arctan\left(\frac{\sqrt{8}(d + 3J_3)}{6J_1 + 6J_2 + 3J_3 - 6J_4 - d}\right). \tag{3.57}$$

Fig. 3.5 illustrates the irrep modes for the T_1 irreps before producing a rotation in Fig. 3.5(a) and after producing a rotation in Fig. 3.5(b) by $\theta = \pi/4$. In this figure, the disks in each sublattice show the rotation of the spins. The resulting states are the so-called splayed ferromagnetic states shown in Fig. 2.8.

The rotation to the $\{\boldsymbol{m}^{\boxtimes}_{T_1\pm}\}$ in Eqs. (3.55) basis diagonalizes Eq. (3.48) identifying the new IEPs

$$a_{T_1-} = \frac{1}{2}(a_{T_1\parallel} + a_{T_1\perp} - \sqrt{a^2_{T_1,\text{mix}} + (a_{T_1\parallel} - a_{T_1\perp})^2} \tag{3.58}$$
$$a_{T_1+} = \frac{1}{2}(a_{T_1\parallel} + a_{T_1\perp} + \sqrt{a^2_{T_1,\text{mix}} + (a_{T_1\parallel} - a_{T_1\perp})^2}. \tag{3.59}$$

Note that the Ice (xy) configuration shown in Fig. 2.8 is a particular combination of the $T_{1\perp}$ and $T_{1\parallel}$ irreps configurations where the spins lie on the local $\boldsymbol{z}$ direction (local xy



(a) (b)

Figure 3.5: (a) Spin configurations for the $T_{1\parallel}$ (cyan) and $T_{1\perp}$ (orange) irreps.(b) Spin configurations for the T_{1+} (blue) and T_{1-} (red) irreps. Go to this link for an animation on how the irrep modes evolve as a function of the angle θ.

plane) for the Ice (xy) configuration. From here on, when the Ice and xy configurations are used, we refer to the corresponding irreps as T_1^{Ice} and T_1^{xy} respectively.

The irrep basis of $\mathcal{H}^{\boxtimes}$ can then be used to predict the $\boldsymbol{q} = 0$ ground state of the system by considering which of the irreps has the minimum IEP a_I. This procedure was carried by Yan *et al.* [74] where they identified the possible $\boldsymbol{q} = 0$ phases for the set of parameters $\{J_1, J_2, J_3, 0\}$ with $J_3 < 0$ and by Benton [119] for another set of parameters. Note however, that when two irreps or configurations have the same IEP, i.e. these are degenerate in energy, the irrep analysis is not capable of predicting what the state of the system will be. As discussed in Section 2, this degeneracy leads to two possible outcomes: an ObD-selected phase or a spin-liquid phase. In particular, when the a_E is the minimum IEP and since the ψ_2 and ψ_3 configurations are both represented by the E irrep, the irrep analysis cannot predict which of the two describes the ground state of the system. The selection in these cases is via an ObD mechanism which can be studied through a classical low-temperature expansion or linear spin wave theory.

Additionally, since the irrep analysis identifies the $\boldsymbol{q} = 0$ modes of the system, it represents a good starting point to perform a long-wavelength approximation, i.e. when $\boldsymbol{q} \to 0$ [4, 107, 108]. This approach is used in Chapter 7.

3.4.3 Application of Irreducible Representation to the Spin Fluctuations in a Low-Temperature Phase

The irrep analysis is not limited to studying the prediction of an ordered phase. This approach can also be used to describe the fluctuations about an ordered phase which, up to quadratic order, can be obtained from the classical low-temperature expansion. In other words, the Hessian H in Eq. (3.10) and therefore the fluctuating components of the spins can be studied and described through an irrep decomposition.

As an example consider an AIAO ground state (A_2) as the $\boldsymbol{q} = 0$ configuration. We may construct the Hessian by projecting out the components of the other irreps whose spins are along the ordering direction and adding a diagonal shift related to the weight of the ground state irrep, i.e. the IEP. Since the spins in the AIAO configuration lie in their local z direction, all irreps which are uniquely composed by spins along these directions are projected out, i.e. the A_2 and the T_1^{Ice} irreps. We are left with the $\{T_E, T_2, T_1^{xy}\}$. Therefore, the Hessian can be obtained by considering

$$\begin{aligned} H &= (\mathbb{I} - \mathbb{P}_{A_2})\mathcal{H}(\mathbb{I} - \mathbb{P}_{A_2})^T + \text{constant shift} \\ &\propto c_E\mathbb{P}_E + c_{T_2}\mathbb{P}_{T_2} + c_{T_{1,\text{Planar}}}\mathbb{P}_{T_{1,\text{Planar}}}, \end{aligned} \tag{3.60}$$

where the coefficient c_I is defined by the weight $(a_I - a_{A_2})$, the $\mathbb{P}_I$ are the projections onto the corresponding irrep subspaces and, the constant shift is associated with the ground state energy of the AIAO state.

3.5 Iterative Minimization

An alternative approach towards studying the ground state configurations, the correlation functions, and other thermodynamic quantities of a system, is to appeal to numerical methods capable of accessing these quantities. Iterative minimization is a numerical method that identifies spin configurations that classically minimize the energy of a system given by its Hamiltonian

$$\mathcal{H} = -\sum_i \boldsymbol{h}_i \cdot \boldsymbol{S}_i, \tag{3.61}$$

where $\boldsymbol{h}_i$ is the molecular field at site i.

The procedure followed by this numerical approach can be summarized in the following way: first, a spin configuration is constructed by first considering a system with randomly

oriented spins. Then, for a randomly selected spin on the system $\boldsymbol{S}_i$, its molecular field $\boldsymbol{h}_i$ is calculated. The spin $\boldsymbol{S}_i$ is then oriented along its molecular field $\boldsymbol{h}_i$ effectively lowering the energy of the system. This process is repeated an N number of times where N is the number of spins in the system. We call these N updates a sweep of the system. The spin reorientation is carried until the energy between subsequent sweeps is less than a threshold ΔE_{cut}. The configuration resulting from the last sweep is then stored in memory. This process is then repeated an N_{meas} number of times, each starting from a different randomly oriented spin configuration. The stored N_{meas} spin configurations are then used to compute any quantities of interest.

For the general bilinear Hamiltonian in Eq. (2.22) the molecular field is defined as

$$\boldsymbol{h}_i = -\frac{1}{2}\sum_{j@i}\left[J\boldsymbol{S}_j + J_{\text{DM}}(\boldsymbol{S}_j \times \boldsymbol{D}_{ij}) + J_{\text{Pd}}\boldsymbol{r}_{ij}(\boldsymbol{S}_j \cdot \boldsymbol{r}_{ij}) + J_{\text{Ising}}\boldsymbol{z}_i(\boldsymbol{S}_j \cdot \boldsymbol{z}_j)\right], \tag{3.62}$$

where $j@i$ refers to all the sites j which are nearest neighbors to the site i, the factor $1/2$ is added to avoid over-counting in Eq. (3.61), and the DM interaction term is obtained by using the triple product rule in the DM term. For a given set of parameters $\{J, J_{\text{Ising}}, J_{\text{Pd}}, J_{\text{DM}}\}$, iterative minimization uniformly explores the complete ground state manifold of the system. This method however *does not* include any temperature dependence and is therefore blind to any temperature-related effects, such as thermal ObD.

3.6 Classical Monte Carlo

Classical Monte Carlo (MC) represents one of the most powerful numerical tools when studying classical spin systems. In this section, we only provide a brief overview of the general ideas behind this approach and focus on the spin updates used to produce the results presented in this thesis. For a more detail discussion we refer the reader to [120–123].

Consider the case where we are interested in numerically studying a system of continuous degrees of freedom $\{\phi\}$ with a Hamiltonian $\mathcal{H}[\phi]$. A thermodynamic quantity $\langle p\rangle$ is formally defined as

$$\langle p\rangle = \frac{1}{\mathcal{Z}}\int \mathcal{D}\phi\; p[\phi]\; e^{-\beta\mathcal{H}[\phi]}, \tag{3.63}$$

where $\mathcal{D}\phi = \prod_i d\phi_i$, the Boltzmann weight is $e^{-\beta\mathcal{H}[\phi]}$, and $\mathcal{Z} = \int \mathcal{D}\phi\, e^{-\beta\mathcal{H}[\phi]}$ is the partition function. If we are interested in numerically measuring this quantity, strictly speaking, we

would have to compute the quantity $p[\phi]$ for every possible configuration of the continuous degrees of freedom $\{\phi\}$ and then average these values weighed by the corresponding Boltzmann factor. Since performing this exact measurement is virtually impossible when the system size is increased, we can instead focus on measuring this quantity over a subset of configurations which are more likely to be accessed by the system. In other words, we focus on configurations with a higher Boltzmann weight. The idea of measuring a quantity over the most likely configurations is often referred to as *importance sampling* and is the central concept behind the measurements obtained through MC.

In order to measure a thermodynamic quantity at a temperature T using MC, we first have to identify the configurations which are most likely to be accessed at this temperature. The identification of these configurations is performed in the following way: starting from a configuration $\{\phi_n\}$ we propose an update and with some probability accept the update resulting in the configuration $\{\phi_{n+1}\}$. In this process, the updates proposed must be *ergodic*, i.e. capable of accessing any configuration on the system given sufficient time. The type of updates used play a crucial role in MC as these may significantly improve the statistics of the thermodynamic quantities measured[21]. For the spin systems studied in this thesis we use three types of updates: a Gaussian update [120], over-relaxation [87, 124], and valley average [125].

The Gaussian update consists in updating a spin $\boldsymbol{S}_i$ by considering a deviation from its original orientation by a normalized random vector $\boldsymbol{v}$. This deviation updates the spin at site i in the following way $\boldsymbol{S}_i \to (\boldsymbol{S}_i + \epsilon\boldsymbol{v})/|\boldsymbol{S}_i + \epsilon\boldsymbol{v}|$, where ϵ is a parameter which is varied as a function of temperature such that the updates are accepted 50% of the time, this is having a 50% acceptance rate. The Gaussian update is accepted with a probability proportional to the ratio of the Boltzmann factors of the original and proposed, i.e. configuration $e^{\beta\Delta E}$ where ΔE is the difference in energy between both configurations. This move is ergodic as any spin orientation may be accessible by the random shift $\epsilon\boldsymbol{v}$.

The over-relaxation updated is based on the molecular field at site i in Eq. (3.62). The spin at this site can be expressed as $\boldsymbol{S}_i = \boldsymbol{S}_i^{\parallel} + \boldsymbol{S}_i^{\perp}$ where $\boldsymbol{S}_i^{\parallel}$ ($\boldsymbol{S}_i^{\perp}$) is the component of the spin $\boldsymbol{S}_i$ which is parallel (perpendicular) to $\boldsymbol{h}_i$ defined as

$$\boldsymbol{S}_i^{\parallel} = \frac{(\boldsymbol{S}_i \cdot \boldsymbol{h}_i)}{|\boldsymbol{h}_i|^2}\boldsymbol{h}_i, \tag{3.64}$$

$$\boldsymbol{S}_i^{\perp} = \left(\boldsymbol{S}_i - \frac{(\boldsymbol{S}_i \cdot \boldsymbol{h}_i)}{|\boldsymbol{h}_i|^2}\boldsymbol{h}_i\right). \tag{3.65}$$

[21] This is because some update may be capable of accessing more configurations which possess the same Boltzmann weight compared to others which cannot. This is for example the case of the loop move for a spin-ice system [48].

The over-relaxation update consists on *flipping* the perpendicular component of the spin

$$\boldsymbol{S}_i = \boldsymbol{S}_i^{\parallel} + \boldsymbol{S}_i^{\perp} \rightarrow \boldsymbol{S}_i^{\parallel} - \boldsymbol{S}_i^{\perp}. \tag{3.66}$$

Clearly, this update does not produce any energy change in the system and it is, therefore, *always* accepted[22]. However, the over-relaxation update alone is not ergodic (configurations with a different $\boldsymbol{S}_i^{\parallel}$ cannot be reached with this update) and it is therefore supplemented with an additional update which is ergodic[23]. This update is especially useful when studying energy-degenerate manifolds as the Γ_5 manifold discussed in Section 2.3.1 as was noted by Ref [87].

Lastly, the valley average consists on performing N_{sim} independent MC simulations and then averaging the thermodynamic quantities measured over the N_{sim} simulations. This average is of especial relevance in glassy systems [125] where the system can get frozen in a spin configuration.

The classical MC method discussed here describes the spins in the system as normalized classical three dimensional vectors. The introduction of quantum effects would then require to perform a quantum version of this method, i.e. a quantum Monte Carlo. Unfortunately, this method is often limited by the infamous sign problem therefore limiting its application to high-temperatures. There is however a proposal of adding quantum fluctuations [126, 127] in a perturbative way by a method dubbed perturbative Monte Carlo. In Appendix I we illustrate how this method can be applied to an XXZ model on a square lattice.

[22] The ratio of the Boltzmann weights between the original and updated configuration is always 1.
[23] In the systems we study, we use over-relaxation supplemented with the Gaussian update.

Chapter 4

The Heisenberg and Dzyaloshinskii-Moriya Hamiltonian Phase Diagram

In this section we present a detail study of the Heisenberg and Dzyaloshinskii-Moriya (DM) model in the pyrochlore lattice, two of the possible symmetry-allowed interaction in the pyrochlore lattice as previously discussed in Chapter 2. These interactions are of special relevance for pyrochlore magnets with $3d$-$5d$ transition metal elements as it is expected for the DM term to be the leading interaction following the Heisenberg exchange [37, 75, 80]. To produce a full study of this Hamiltonian, we first apply an irrep analysis effectively predicting which $\boldsymbol{q} = \boldsymbol{0}$ orders can be realized. To go beyond this analysis, we apply classical Monte Carlo (MC), classical low-temperature expansion (CLTE), and linear spin wave theory (LSW). Since the results presented in this chapter are presented and discussed in detail in Ref. [1], here we simply present a brief overview of the results which is especially useful for the upcoming chapters.

4.1 The Heisenberg and and DM Hamiltonian

The Heisenberg and DM Hamiltonian in the pyrochlore lattice is given by

$$\mathcal{H} = J \sum_{\langle ij \rangle} \boldsymbol{S}_i \cdot \boldsymbol{S}_j + J_{\mathrm{DM}} \sum_{\langle ij \rangle} \boldsymbol{D}_{ij} \cdot (\boldsymbol{S}_i \times \boldsymbol{S}_j), \tag{4.1}$$

where the DM vectors $\boldsymbol{D}_{ij}$ can be obtained by following the Moriya rules [72, 128, 129]. Following these set of rules results in the six DM vectors corresponding to the six bonds found in a tetrahedron, namely,

$$\boldsymbol{D}_{01} = (-1,1,0), \quad \boldsymbol{D}_{02} = (1,0,-1), \quad \boldsymbol{D}_{03} = (0,-1,1), \tag{4.2}$$

$$\boldsymbol{D}_{12} = (0,1,1), \quad \boldsymbol{D}_{13} = (-1,0,-1), \quad \boldsymbol{D}_{23} = (1,1,0), \tag{4.3}$$

we refer the reader to Appendix A for the sublattice structure and its labeling. All other DM vectors can be obtained by noting that $\boldsymbol{D}_{ij} = -\boldsymbol{D}_{ji}$[1]. Following Refs. [26, 73, 76], we refer to the above set of vectors $\{\boldsymbol{D}_{ij}\}$ as *direct* DM vectors and their inverse additive $\{-\boldsymbol{D}_{ij}\}$ as *indirect* DM vectors. Fig. 4.1 illustrates some of the direct DM vectors in a single tetrahedron.

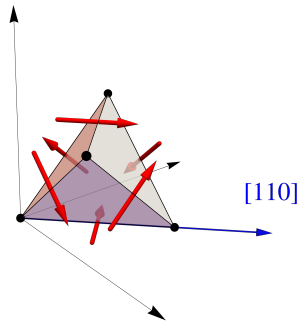


Figure 4.1: DM vectors for a single tetrahedron. Here the D_{01}, D_{02}, D_{03}, D_{12}, D_{13} and D_{23} are shown.

With the above definition for the DM vectors in place, we are now ready to study the Hamiltonian (4.1) for any choice of interaction parameters $\{J, J_{\mathrm{DM}}\}$. To this end we adopt the parametrization

$$J = \cos\theta \quad J_{\mathrm{DM}} = \sin\theta, \tag{4.4}$$

which gives us access to all possible ratios of the interaction parameters J and J_{DM}. Moreover, since $J^2 + J_{\mathrm{DM}}^2 = 1$ we take all energy scales in this section to be measured in units of $\sqrt{J^2 + J_{\mathrm{DM}}^2} = 1$. In what follows, we keep the definition of the DM vectors provided in Eq. (4.2) and (4.3) fixed and instead consider the sign change of the J_{DM} parameter. Therefore, we refer to $J_{\mathrm{DM}} > 0$ as a *direct* DM interaction and $J_{\mathrm{DM}} < 0$ as a *indirect* DM interaction.

[1]This property can be easily seen as the Hamiltonian (4.1) is invariant under $i \longleftrightarrow j$. Since the cross product is antisymmetric under this transformation the DM vectors must also be antisymmetric.

4.2 Irrep Analysis

A first approximation to identify a phase diagram of the Hamiltonian (4.1) can be performed by applying an irrep analysis and studying the evolution of the IEPs $\{a_{A_2}, a_E, a_{T_1+}, a_{T_1-}, a_{T_2}\}$ as a function of temperature, see Subsection 3.4.2. In general, producing this analysis would first requires us to identify the correct combination of the T_1 irreps which diagonalize the Hamiltonian and for which $a_{T_1,\text{mix}}$ vanishes. Fortunately, from the expression for $a_{T_1,\text{mix}}$ in Eq. (3.54) we have that

$$a_{T_1,\text{mix}} = -\frac{\sqrt{2}}{3}(-J_{\text{Ising}} + \frac{3}{2}J_{\text{Pd}} + d), \tag{4.5}$$

which vanishes for the Hamiltonian (4.1) as it does not have an Ising, pseudo-dipolar or single-ion anisotropy interactions. Therefore, the T_1 irrep modes that diagonalize the single-tetrahedron Hamiltonian $\mathcal{H}^{\boxtimes}$ with only Heisenberg and DM interactions correspond to the colinear ferromagnet ($T_{1\parallel}$) and the coplanar antiferromagnet ($T_{1\perp}$) spin configurations as shown in Fig. 2.7. Following this identification, we can use the corresponding IEPs and express them in terms of the interaction parameters J and J_{DM} yielding

$$\begin{aligned}
a_{A_2} &= -J - 4J_{\text{DM}}, && (4.6)\\
a_E &= -J + 2J_{\text{DM}}, && (4.7)\\
a_{T_2} &= -J - 2J_{\text{DM}}, && (4.8)\\
a_{T_{1\parallel}} &= 3J, && (4.9)\\
a_{T_{1\perp}} &= -J + 2J_{\text{DM}}, && (4.10)
\end{aligned}$$

or in terms of the parametrization in Eq. (4.4)

$$\begin{aligned}
a_{A_2} &= -\cos(\theta) - 4\sin(\theta), && (4.11)\\
a_E &= -\cos(\theta) + 2\sin(\theta), && (4.12)\\
a_{T_2} &= -\cos(\theta) - 2\sin(\theta), && (4.13)\\
a_{T_\parallel} &= 3\cos(\theta), && (4.14)\\
a_{T_{1\perp}} &= -\cos(\theta) + 2\sin(\theta). && (4.15)
\end{aligned}$$

Note that for this model $a_E = a_{T_{1\perp}}$ for all angles $\theta \in [0, 360°)$. The dependence of these parameters as a function of the parametrization angle is shown in Fig. 4.2. According to the irrep analysis, the lowest energy irrep (the one with the smallest IEP) is expected to describe the classical $\boldsymbol{q} = \boldsymbol{0}$ ground state. From Fig. 4.2 we can identify three regimes: two where a single irrep configuration has the lowest energy IEP, and one where two irrep

configurations share the lowest energy IEP. In other words, the irrep analysis predicts that the A_2 irrep (AIAO order), and the $T_{1\parallel}$ irrep (colinear ferromagnet order) describe the classical ground state for $\theta \in (0°, 135°)$ and $\theta \in (135°, 243°)$ respectively. On the other hand, for $\theta \in (243°, 360°)$ the irrep analysis is inconclusive as it identifies the E and the $T_{1\perp}$ irreps as the minimum energy configurations. This observation aligns with what was reported by Ref. [110] where a set of interaction parameters for the Hamiltonian (4.1) locates this spin model at a phase boundary[2].

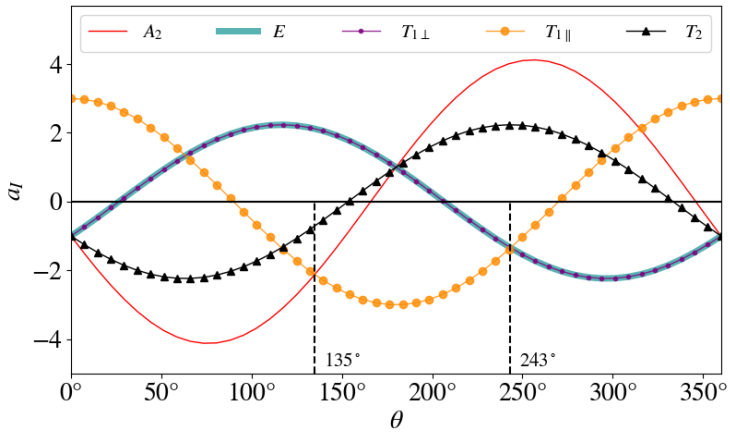


Figure 4.2: IEP as a function of the parametrization angle θ. The dashed lines at $\theta = 135°$ and $\theta = 243°$ mark the points where two or more IEPs intersect.

Although the irrep analysis identifies two competing irreps for $\theta \in (243°, 360°)$, as discussed in Chapter 2, this does not equate to avoiding the realization of an ordered phase at low temperatures as ObD might select one of the competing orders. As a consequence of the energy degeneracy of the two irreps for $\theta \in (243°, 360°)$ the classical ground state manifold is then composed by two continuous manifold: the Γ_5 manifold and the *coplanar* manifold. The Γ_5 manifold is composed by spin configurations resulting from a combination of the ψ_2 and ψ_3 states, whereas the coplanar manifold is composed by spin configuration resulting from a combination of the ψ_3 and $T_{1\perp}$ states where the spins in both irreps lie in the *same* Cartesian plane. The spin configurations in these manifold can take the form

$$\boldsymbol{S}_a^{\Gamma_5}(\phi) = \cos(\phi)\boldsymbol{S}_a^{\psi_3} + \sin(\phi)\boldsymbol{S}_a^{\psi_2}, \tag{4.16}$$

$$\boldsymbol{S}_a^{\text{coplanar}}(\gamma) = \cos(\gamma)\boldsymbol{S}_a^{\psi_3} + \sin(\gamma)\boldsymbol{S}_a^{T_{1\perp}}, \tag{4.17}$$

[2]Click on the link for an animation of the phase diagram where the red dot marks the location of the Heisenberg and DM model, the x axis is $J_{z\pm}/J_{\pm}$, the y axis is $J_{\pm\pm}/J_{\pm}$, and the phase diagram is evolved as a function of $J_{zz}/J_{\pm}$. In this diagram, the yellow phase is a splayed ferromagnet, the blue is a Γ_5 phase, and the gray phase is a PC phase.

where $\boldsymbol{S}_a^I$ is the a sublattice spin corresponding to the I^{th} irrep[3]. In the above equations, ϕ and γ can be thought as angles describing a rotation about the local z axis and the Cartesian axis perpendicular to the plane where the spins reside, respectively. Although the realization of this manifold was noted by [73, 76], its decomposition into the E and $T_{1\perp}$ irreps was not clarified. Although the degeneracy between the E and the $T_{1\perp}$ irrep can not be equated to avoiding an ordered phase, at high temperatures this degeneracy does imply that the susceptibilities associated with both orders should follow the same behavior, i.e. $\lim_{T\to\infty}\chi_E = \lim_{T\to\infty}\chi_{T_{1\perp}}$. This statement follows form a Landau theory where the coefficient of the quadratic term in the expansion of the free energy in terms of the irrep modes is proportional to $(3T + a_I)$ where T is the temperature [130, 131]. The high-temperature susceptibility for the irrep modes is therefore proportional to $(3T + a_I)^{-1}$, which results in equivalent susceptibilities for energy degenerate irreps at these temperatures and is further studied below.

4.3 Monte Carlo Simulations: a First Approach

To go beyond the irrep analysis, we apply classical MC simulations where we consider the interaction parameters $\{J, J_{\text{DM}}\}$ in terms of the parametrization in Eq. (4.4). To study the realization of a $\boldsymbol{q} = \boldsymbol{0}$ magnetically ordered phase corresponding to the irrep modes we study the irrep order parameters $\{\boldsymbol{m}_I^{\boxtimes}\}$, defined in Subsection 3.4.2, averaged over all tetrahedra

$$\boldsymbol{m}_{I,\text{av}} \equiv \frac{4}{N}\sum_{\boxtimes}\boldsymbol{m}_I^{\boxtimes}, \tag{4.18}$$

and study the evolution of its thermal average over the configurations sampled through MC as a function of temperature

$$m_I \equiv \langle|\boldsymbol{m}_{I,\text{av}}|\rangle, \tag{4.19}$$

where $\langle\cdots\rangle$ refers to thermal averaging. In an ordered phase described by the I^{th} irrep, the corresponding thermal averaged order parameter m_I plateaus to 1 at low temperatures whereas all other order parameters vanish.

MC simulations is performed for a system of $N = 4\times L^3$ spins with $L = 10$ and averaged between $20-100$ independent MC runs. We refer the reader to Ref. [1] for a more details of the MC simulations. The study of these order parameters as a function of the parametrization angle θ reveals a phase diagram where three ordered phases are identified,

[3]For an animation of the $\boldsymbol{q} = \boldsymbol{0}$ spin configurations found in these manifold go to Γ_5 or coplanar.

see Fig. 4.3. In agreement with the irrep analysis, for $\theta \in (0°, 135°)$ and $\theta \in [135°, 243°)$ an AIAO and colinear ferromagnetic phases are respectively observed[4]. In contrast to what was predicted by the irrep analysis, for $\theta \in (243°, 360°)$ a Γ_5 ordered is observed. Moreover, our MC simulations detected two points where no $\boldsymbol{q} = \boldsymbol{0}$ ordered phases were detected. One of these points is the Heisenberg antiferromagnetic point, i.e. $J_{\mathrm{DM}} = 0$ ($\theta = 0$), which was discussed in Subsection 2.3.3. The other point however corresponds to the value of θ for which $J_{\mathrm{DM}}/J = 2$ and where the $T_{1\perp}$, $T_{1\parallel}$, and the E irreps share the same IEP, see Fig. 4.2. A more in-depth study and analysis of this point is performed in Chapter 6.

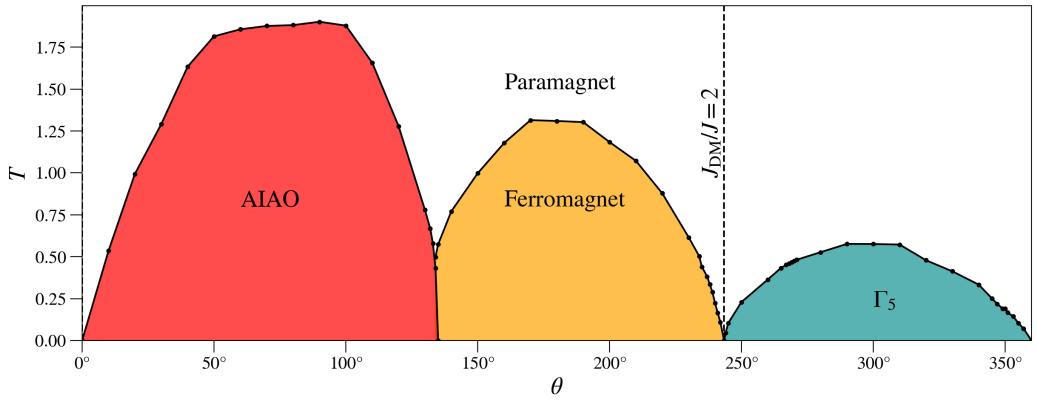


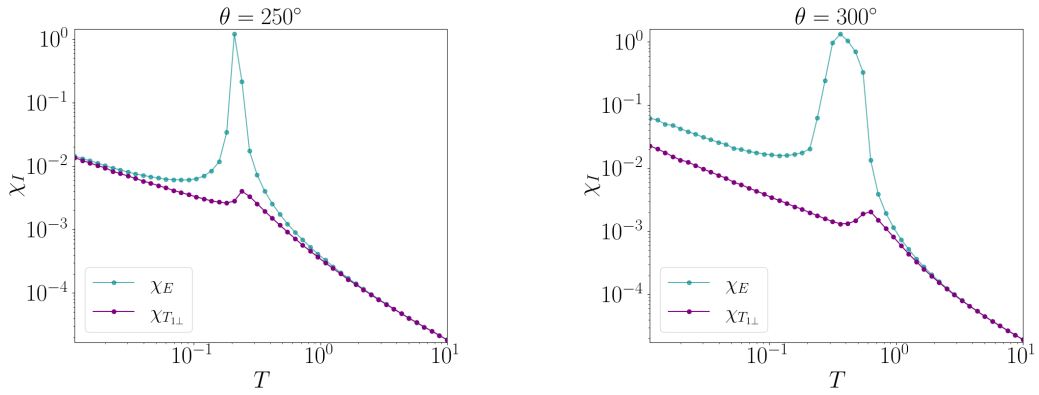
Figure 4.3: Phase diagram obtained from the study of the $\{m_I\}$ order parameters.

As previously stated, our MC simulations detect Γ_5 order corresponding to the E irrep and showed no signal of a $T_{1\perp}$ phase, however, and as stated in the previous section, the competition between the E and the $T_{1\perp}$ modes can be exposed at high temperatures by studying the evolution of the susceptibilities associated with each irrep. We therefore define the order parameter susceptibility (using the standard form used in MC simulations of finite-size classical three-component spin systems [132]) as

$$\chi_I = \frac{\langle \boldsymbol{m}_{I,\mathrm{av}}^2 \rangle - \langle |\boldsymbol{m}_{I,\mathrm{av}}| \rangle^2}{T} \tag{4.20}$$

for $I \in \{E, T_{1\perp}\}$. The susceptibility for both irreps is shown in Fig. 4.4(a) and (b) for $\theta = 250°$ and $\theta = 300°$ respectively. A similar behavior was observed for all other parametrization angles $\theta \in (243°, 360°)$. As expected, at high temperatures the susceptibility for both irreps agree at high temperatures only deviating from each other when approaching the critical temperature T_c.

[4]Note that MC identified the colinear ferromagnet as the $\boldsymbol{q} = \boldsymbol{0}$ ground state at $\theta = 135°$.



(a) (b)

Figure 4.4: Order parameters susceptibilities χ_I for the E and the $T_{1\perp}$ irreps measured for $\theta = 250°$ (a) and $\theta = 300°$ (b).

After identifying the different order phases in terms of the thermally averaged irrep modes $\{m_I\}$, we can now focus on the region where the Γ_5 manifold is identified as the ordered phase. As discussed in Chapter 2, this manifold comes from an accidental $U(1)$ degeneracy and therefore an ObD mechanism is expected to select either the ψ_2 or the ψ_3 states. In the next section, this selection is studied through a CLTE for the low-temperature regime before returning to the MC analysis to study what the selection is at all other temperatures. It is worth noting that the selection of the ψ_3 order at low temperatures for the Hamiltonian (4.1) with an antiferromagnetic Heisenberg interaction and an indirect DM coupling was first observed by Ref. [73]. This study however was limited to a finite range of ratios between the two interaction couplings and did not make any claims of the possibility of an intermediate phase.

4.4 Order-by-Disorder in the Γ_5 phase

To study the ObD selection for $\theta \in (243°, 360°)$ we first apply a CLTE and study the entropic weight associated with the ψ_2 and ψ_3 in Eq. (3.16), see Subsection 3.2.1. According to this approximation, at low temperatures the ordered configuration with the highest entropic weight is expected to be selected. Consequently, we study the difference of this quantity between the two orders, i.e. $\Delta\mathcal{S} = \mathcal{S}(\psi_3) - \mathcal{S}(\psi_2)$. According to this definition, if $\Delta\mathcal{S} > 0$ a ψ_3 order is entropically preferred while for $\Delta\mathcal{S} < 0$ a ψ_2 order is preferred.

As shown in Fig. 4.5, $\Delta\mathcal{S}$ is found to be positive in the low-temperature limit, i.e.

$T = 0^+$, for *all* values of the parametrization angle θ where the Γ_5 phase is identified. In other words, at low temperatures, the ψ_3 order is expected to be selected by a thermal ObD mechanism. Moreover, note that the $\Delta\mathcal{S}$ shows a minimum value around $\theta \sim 350°$ which can be interpreted as a stronger competition between ψ_2 and ψ_3 orders at this angle, see inset in Fig. 4.5.

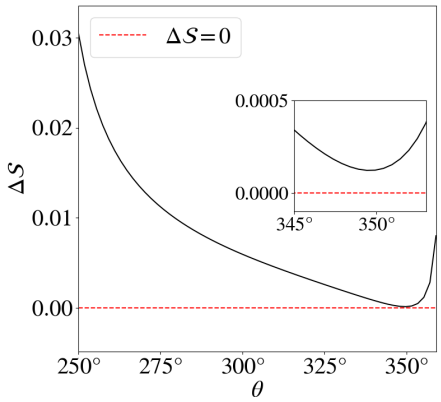


Figure 4.5: Entropic weight difference $\Delta\mathcal{S}$ as a function of the parametrization angle θ. The inset shows the minimum in $\Delta\mathcal{S}$ centered around $\theta \sim 350°$.

Although the CLTE predicts a selection of the ψ_3 order at low temperatures, this does not mean that the ψ_3 order is selected at T_c. Studying this selection with a CLTE would require to go beyond the quadratic theory presented in Subsection 3.2. We leave this analysis for future work and return to the MC analysis to study the ObD selection in the Γ_5 manifold at all temperatures below T_c in the next section.

4.5 Monte Carlo Simulations: the Γ_5 Manifold

In Section 4.3, the thermal average order parameters $\{m_I\}$ were used to identify the onset of a $\boldsymbol{q} = \boldsymbol{0}$ ordered phase. For $\theta \in (243°, 360°)$ the m_E order parameter was found to saturate to 1 at low temperatures, signaling a Γ_5 ordered phase. This parameter however does not differentiate between ψ_2 or ψ_3 orders[5] and therefore another quantity is needed to expose the ObD selection. Therefore, following Refs. [86, 87, 112, 133], we study the

[5]This is because we are measuring the magnitude of the E irrep mode which would evolve in the same way for both orders.

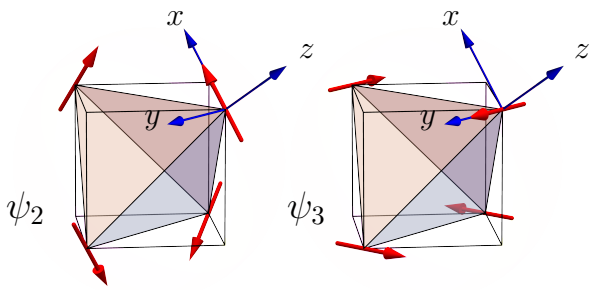


Figure 4.6: ψ_2 (left) and ψ_3 (right) where the spins (red arrows) point along the local x and y axes for ψ_2 and ψ_3, respectively.

parameter m_{E6} defined as

$$m_{E6} = \langle |\boldsymbol{m}_{E,\mathrm{av}}| \cos(6\phi) \rangle \tag{4.21}$$

where $\langle \cdots \rangle$ denotes thermal average, $\phi = \arctan\left(m^y_{E,\mathrm{av}}/m^x_{E,\mathrm{av}}\right)$, and $\boldsymbol{m}_{E,\mathrm{av}} = (m^x_{E,\mathrm{av}}, m^y_{E,\mathrm{av}})$ defined as

$$m^x_{E,\mathrm{av}} = \frac{1}{N}\sum_i \boldsymbol{x}_i \cdot \boldsymbol{S}_i \tag{4.22}$$

$$m^y_{E,\mathrm{av}} = \frac{1}{N}\sum_i \boldsymbol{y}_i \cdot \boldsymbol{S}_i \tag{4.23}$$

where $\boldsymbol{x}_i$ and $\boldsymbol{y}_i$ are the *local* xy basis of the spin $\boldsymbol{S}_i$ at site i, see Subsection 3.4.2 and Appendix A. Note that ψ_2 states can be associated with the spins pointing along the local x direction whereas the ψ_3 are associated with the spins pointing along the local y direction, see Fig. 4.6. Consequently, in the Eq. (4.21), the angle ϕ refers to the Γ_5 angle in Eq. (4.16) where, $\phi = n\pi/3$ corresponds to a ψ_3 order, whereas $\phi = n\pi/3 + \pi/6$ corresponds to a ψ_2 order for $n \in 0, 1, 2, 3, 4, 5$ [86, 133]. Therefore, the parameters m_{E6} is expected to become positive for ψ_2 order and negative for ψ_3 order; however, this quantity should merely be viewed as a *proxy* of these orders as we further discuss at the end of this chapter.

The origin of the m_{E6} parameter and the reason why this parameter is well suited to differentiate between the ψ_2 and ψ_3 orders stems from the first anisotropic term in a Landau theory where the order parameter is given by the E irrep mode. Ref. [71] constructed such theory by considering a complex order parameter $m_{xy} = \sqrt{m_x^2 + m_y^2}\exp(i\phi)$ where m_x and m_y are related to the onsite magnetization in the local xy planes and ϕ is the Γ_5 angle in Eq. (4.16). Using this quantity, and including the local z order parameter m_z, Ref. [71] found that the first anisotropic term in the m_x and m_y components in the Landau free energy corresponds to

$$\delta\mathcal{F} = 2\eta_6 |m_{xy}|^6 \cos(6\phi), \tag{4.24}$$

where η_6 is a temperature dependent parameter whose sign determines which order configuration is expected to be selected, for $\eta_6 < 0$ a ψ_2 order is selected and for $\eta_6 > 0$ a ψ_3 order is selected. In terms of the irrep modes, m_{xy} corresponds to the magnitude of $\boldsymbol{m}_{E,\mathrm{av}}$ whereas m_α corresponds to the α component of $\boldsymbol{m}_{E,\mathrm{av}}$ in Eq. (4.22) and (4.23).

Before presenting the m_{E6} parameter temperature evolution as measured via MC simulations, an important clarification must be made about this thermodynamic quantity and the limitations encompassing it. Refs. [71, 86, 133] noted that this sixth order term in the free energy is *dangerously* irrelevant. This means that while the evolution of this term does not affect the critical properties of the system, it plays a *crucial* role in the ObD selection at $T \leq T_c$ [71]. Additionally, this means that there is an emergent length-scale $\Lambda(T)$ associated to this anisotropy [133]. Consequently, the ObD selection only takes place for system sizes bigger than this length-scale. Therefore, we study the temperature evolution of the m_E and m_{E6} parameters for three different system sizes $L = 8, 10, 12$ and illustrate these in Fig. 4.7 for two set of interaction parameters corresponding to the parametrization angle $\theta = 250°$ and $\theta = 300°$.

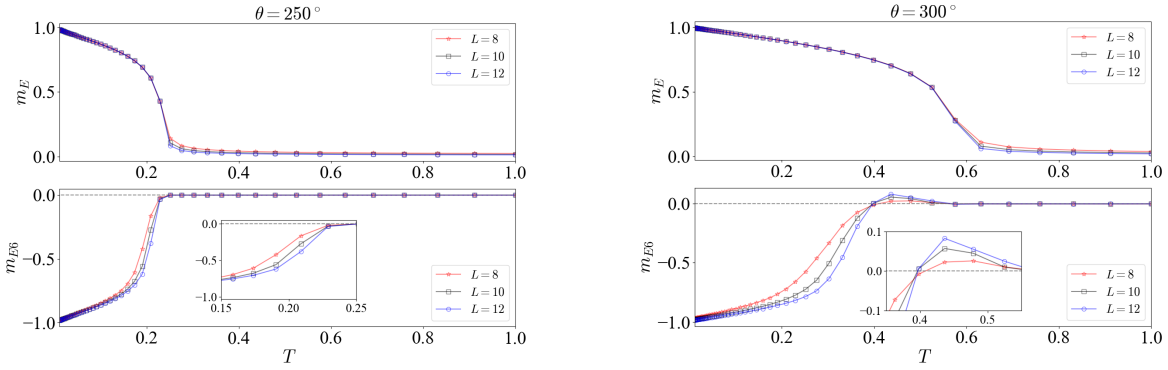


Figure 4.7: Evolution of the m_E and m_{E6} order parameters as a function of temperature for $\theta = 250°$ (a) and $\theta = 300°$ (b).

For both angles, the m_E order parameter increases and plateaus to 1 at low temperatures. On the other hand, the evolution of the m_{E6} parameter is fundamentally different for $\theta = 250°$ and $\theta = 300°$. For $\theta = 250°$, the m_{E6} parameter becomes negative just below T_c and keeps on increasing its magnitude to low temperatures. In contrast, for $\theta = 300°$, the m_{E6} parameter first becomes positive below T_c and only changes sign to a temperature we label T_{Γ_5}. As was mentioned before, and following Refs. [86, 112, 133], the negative

sign of the m_{E6} parameter would lead us to identify a ψ_3 order below T_c and all the way down to $T \to 0$ for the angle $\theta = 250°$. In contrast, for $\theta = 300°$ an intermediate ψ_2 phase is identified from T_c to T_{Γ_5} which is then replaced by a ψ_3 phase which prevails all the way down to $T \to 0$. The value of T_{Γ_5} is identified with the change of sign of the m_{E6} order parameter measured for system sizes $L = 10, 12$ which crosses at this temperature [112], see inset of Fig. 4.7(b). Note that when increasing the system size used in the MC simulations, the value of the m_{E6} increases, see inset in Figs. 4.7(a) and (b). This increment in the value of the m_{E6} is presumably related to the emergent length-scale $\Lambda(T)$, i.e. ObD selection produced by the sixth order term in the free energy becomes more prevalent for increasing system size [86, 112, 133, 134].

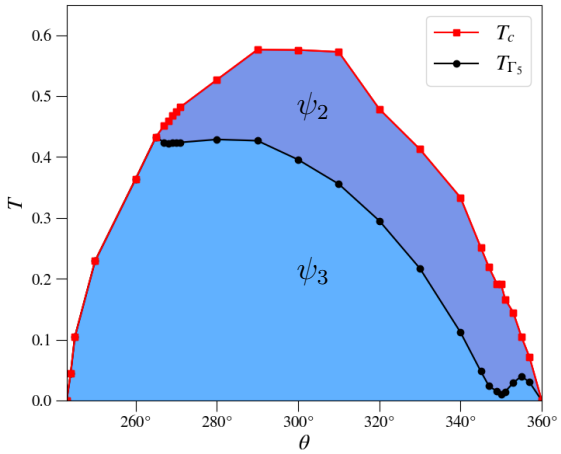


Figure 4.8: Temperature dependent phase diagram for the Γ_5 phase illustrating a selection between the ψ_2 and ψ_3 ordering as a function of θ.

Performing a similar analysis on the sign of the m_{E6} parameter and identification of the corresponding ψ_2 and ψ_3 orders on angles $\theta \in (243°, 360°)$ lets us construct the phase diagram shown in Fig. 4.8. The m_{E6} analysis identifies two regions: one for $\theta \in (243°, 265°)$ where a *single* transition is observed into a ψ_3 order, and a second region for $\theta \in (265°, 360°)$ where an intermediate ψ_2 phase is detected at high temperatures followed by a transition into a ψ_3 phase at T_{Γ_5}. Interestingly, a drop in the value of T_{Γ_5} is observed for $\theta \sim 350°$. This drop in T_{Γ_5} can be understood in terms of the CLTE entropic weight difference shown in Fig. 4.5 which presents a minimum around the same value of θ and implies stronger competition between the two phases. Such strong competition could be interpreted as a suppression of the transition between the two orders. In fact, note that as $\Delta\mathcal{S}$ decreases in Fig. 4.5 when approaching $\theta \sim 350°$, T_{Γ_5} drops as seen in Fig. 4.8.

Although similar results were reported by Ref. [112], that work only considered values of up to $J_{\rm DM}/J \sim 1.5$. Here, by implementing the parametrization in Eq. (4.4), we are able to identify the phase diagram for *all* possible ratios of $J_{\rm DM}/J$. The classical phase diagram of the magnetic phases including the inner structure in the Γ_5 phase is shown in Fig. 4.3.

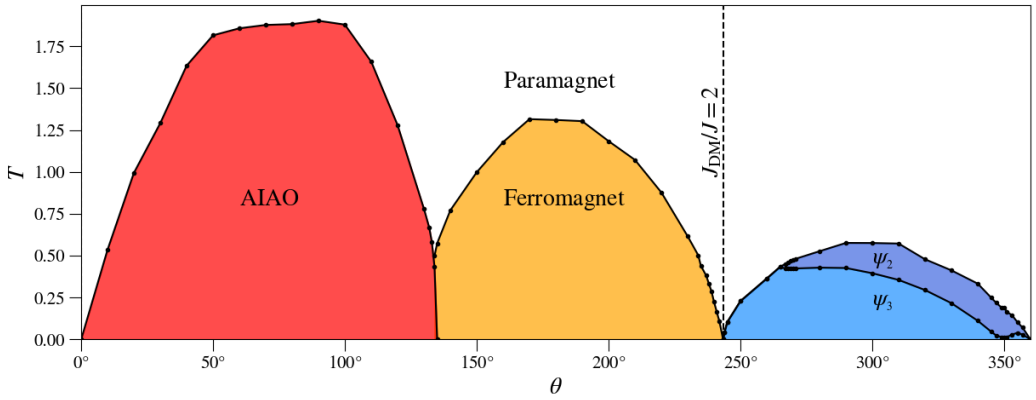


Figure 4.9: Phase diagram obtained from the study of the $\{m_I\}$ order parameters and the m_{E6} parameter.

Before continuing with the quantum version of this phase diagram, a word of caution is needed. According to Ref. [71], the transition between the ψ_2 and ψ_3 orders in the Γ_5 phase should either be a *single* first order transition or *two continuous* second order transitions. The first scenario would imply a discontinuity in the m_{E6} parameter, whereas the second scenario would imply an intermediate phase between the ψ_2 and ψ_3 order. Our MC analysis does not present a discontinuity in the these quantities. To explore the possibility of an intermediate phase, we study the distribution of the angle ϕ obtained by averaging 100 independent MC simulations and show these distributions for $\theta = 300°$ at three temperatures, one below T_c and above T_{Γ_5}, one at approximately T_{Γ_5}, and one below T_{Γ_5}[6].

Fig. 4.10 illustrates the 2D and 1D histograms for the Γ_5 angle ϕ for the temperatures marked by black dashed lines in panel (a) where the m_E and m_{E6} order parameters are illustrated. As can be seen, for T_0, both the 1D and 2D histograms show wide peaks at $n\pi/3$ with $n \in \{0, 1, 2, 3, 4, 5\}$, which according to the sign of m_{E6} is identified as a ψ_2 order.

[6]For $\theta = 300°$ we used for the three temperatures $T_0 = 0.461$, $T_1 = 0.395$, $T_2 = 0.249$, where all temperatures are in units of $\sqrt{J^2 + J_{\rm DM}{}^2} = 1$.

At T_1, both the 1D and 2D histograms show an almost featureless distribution where all angles ϕ in the Γ_5 phases are sampled with a comparable frequency. Lastly, for T_2, both the 1D and 2D histograms show sharp peaks at $n\pi/3 + \pi/6$ with $n \in \{0, 1, 2, 3, 4, 5\}$, at this temperature a ψ_3 order is identified. An intermediate phase would be indicated by peaks in the distribution of ϕ at positions which are not related to a ψ_2 or a ψ_3 order.

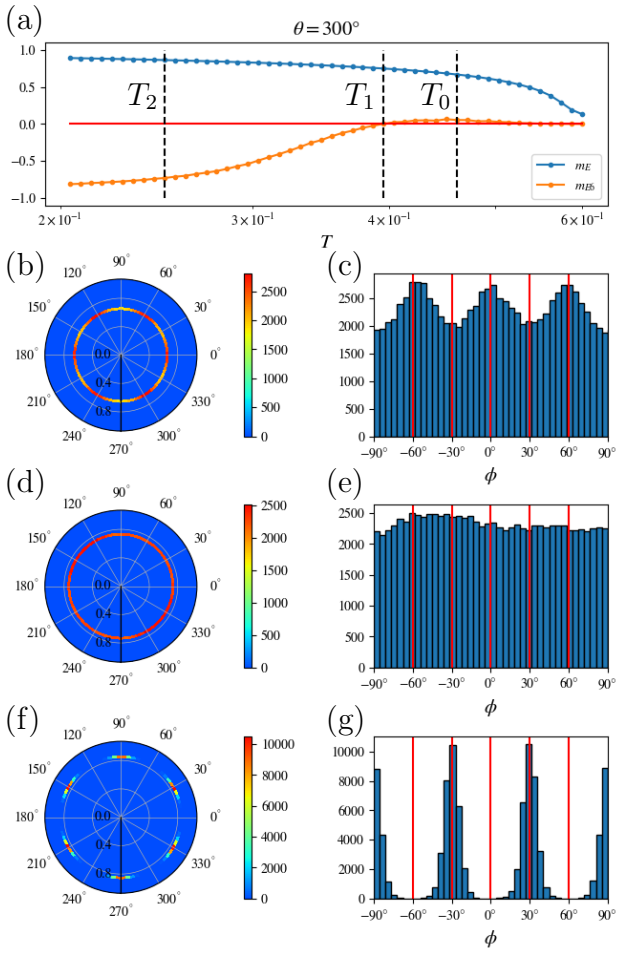


Figure 4.10: Panel (a) illustrates the m_E and m_{E6} parameters measured for $\theta = 300°$. Panels (b), (d) and (f) show 2D polar histograms of $\boldsymbol{m}_{E,\mathrm{av}}$. Panels (c), (e) and (g) show 1D histograms of the angle ϕ where the vertical red lines mark multiples of $\pi/6$. Here, the second row (panels (b) and (c)) corresponds to data taken at T_0, the third row (panels (d) and (e)) corresponds to data taken at T_1, and the fourth row (panels (f) and (g)) corresponds to data taken at T_2.

We do not find any evidence of an intermediate phase which does not allow us to identify the nature of the transition between the low-temperature ψ_3 phase and the high-temperature ψ_2 phase as a second order phase transition. An equivalent observation was performed in Ref. [133] when studying a similar system in the pyrochlore lattice which also shows a high-temperature ψ_2 phase followed by a low-temperature ψ_3 phase. The failure in identifying the order of the transition might be related to the emergent length-scale $\Lambda(T)$ associated with the dangerously irrelevant term in the free energy. Moreover, note that for T_0 in Fig. 4.10 the ϕ distribution reveals that the MC is sampling configurations from *all* angles across the Γ_5 manifold although the distribution is clearly peaked at angles associated to the ψ_2 state. In a true ψ_2 ordered phase we would expect the peaks of the ϕ distributions at T_0 to look like the peaks observed for the distributions at T_2. Presumably, as the system size is increased, the ϕ distributions would become sharper and consequently the value of m_{E6} would increase, see Fig. 4.7. The system size limitation observed in the ϕ distributions is the reason why we take the sign of the m_{E6} parameter as a *proxy* of the ordered configuration [1]. Addressing this complication would require the study of bigger system sizes and we therefore leave this study for future work.

4.6 Quantum Phase Diagram

To study the phase diagram in the quantum model we apply three methods: pseudo-fermion functional renormalization group (PFFRG), a high-temperature series expansion (HTSE), and LSW theory. In this section, we focus in the results provided by the LSW theory and only present the results from PFFRG and HTSE. The detail description and analysis of both PFFRG and HTSE can be found in Ref. [1]. The identified classical and quantum phase diagrams are summarized in the angular phase diagram in Fig. 4.11.

4.6.1 PFFRG and HTSE Results

In general, the phases found in the quantum case by PFFRG at $T = 0$ are consistent with those identified in the classical picture: there are three magnetically ordered phases, and two spin-liquid phases. The magnetic phases are identified to be the AIAO for $\theta \in (10°, 135.75°)$, colinear ferromagnet for $\theta \in (135.75°, 229°)$, and the Γ_5 phase for $\theta \in (243°, 338°)$. On the other hand, the two spin-liquid phases are found around $\theta = 0°$ and another close to $\theta \sim 243°$ where the $J_{\mathrm{DM}}/J = 2$ classical spin-liquid is identified. Interestingly, the two spin-liquid phases are found to be stable for a wider range of angles

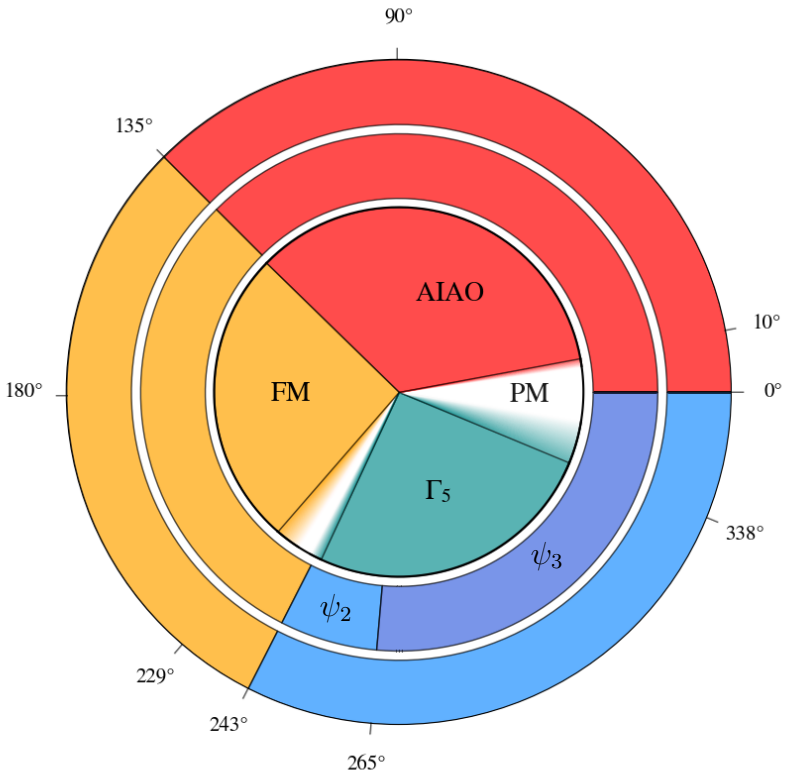


Figure 4.11: Classical and quantum phase diagram of the Heisenberg and DM Hamiltonian where the outer most ring shows the selection at $T \to 0$ and the middle ring corresponds to the ordered phase selected at T_c as identified by MC. The inner circle corresponds to the magnetic phases as identified by PFFRG.

than what is observed in the classical case. Unfortunately, the current PFFRG implementation does not allow for an identification of the ObD selected phase in the Γ_5 phase as this method can only study two point correlators whereas the ObD selection is driven by a sixth order correlation function [86], see Section 4.5.

To study the selected orders at T_c, we applied a HTSE and study the sixth order cumulants [61]. This analysis identified a similar ψ_2/ψ_3 selection as what was identified by MC: for $\theta < 260°$ a ψ_3 phase is identified and for most angles $\theta > 260°$ a ψ_2 is identified. For $\theta = 310°,\ 320°$ the HTSE was inconclusive finding that different Padé approximants

of the series predicts different orders. For a more detailed discussion of these results, we refer the reader to Ref. [1], and Appendix G where the HTSE for χ_I is calculated up to order β^2 for the E and $T_{1\perp}$ irreps, see Eq. (4.20).

4.6.2 Quantum Order-by-Disorder

To study the quantum ObD selected states at $T \to 0$ and supplement the quantum phase diagram identified through PFFRG, we study the zero-point energy correction to the classical energy about the ψ_2 and ψ_3 states. This correction is related to the zero-point motion, i.e. at $T = 0$, of the magnon energies given by Eq. (3.20), namely

$$E_0(\psi) = \frac{S}{2} \sum_{\boldsymbol{q}} \sum_{a} \omega_a(\boldsymbol{q}), \tag{4.25}$$

where the state with the *lowest* energy correction is expected to be selected as $T \to 0$. Consequently, we study the difference in this correction between the ψ_3 and ψ_2 states, i.e. $\Delta E_0 = E_0(\psi_3) - E_0(\psi_2)$, as a function of the parametrization angle θ, see Fig. 4.12.

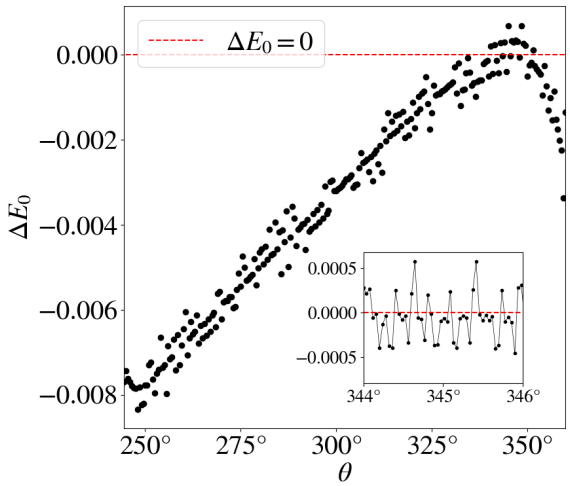


Figure 4.12: Zero-point energy correction difference between the ψ_3 and ψ_2 states, i.e. $\Delta E_0 = E_0(\psi_3) - E_0(\psi_2)$. Inset shows a zoomed version of this difference for $\theta \in [344°, 346°]$.

As can be seen, for most angles, $\Delta E_0 < 0$ signaling a ψ_3 selection. Interestingly, and in contrast to the classical case, for $\theta \in [344°, 352°]$ ΔE_0 oscillates between $\Delta E_0 < 0$ and

$\Delta E_0 > 0$ which translates in an oscillating selection between the ψ_2 and ψ_3 orders[7]. These oscillations can be understood by considering the expression for ΔE_0 as a function of the local exchange interaction parameters derived by Ref. [110]

$$\Delta E_0 \sim J_\pm \Big[c_3 \left(\frac{J_{\pm\pm}}{J_\pm} \right)^3 + c_2 \left(\frac{J_{\pm\pm} J_{z\pm}}{J_\pm^2} \right)^2 + c_1 \left(\frac{J_{\pm\pm} J_{z\pm}^4}{J_\pm^5} \right) + c_0 \left(\frac{J_{z\pm}}{J_\pm} \right)^6 \Big], \tag{4.26}$$

where the coefficients c_i are dimensionless functions of $J_{zz}/J_\pm$. In the above equation, the local interaction parameters are combinations of trigonometric functions resulting from the parametrization in Eq. (4.4) and therefore the oscillations observed in Fig. 4.12[8]. Moreover, we believe that this phenomenon is related to the observation of a thin regime in the local interaction parameters $\{J_{zz}, J_\pm, J_{\pm\pm}, J_{z,\pm}\}$ phase diagram where ψ_2 order is selected [110]: the parametrization chosen oscillates in the phase boundary progressively approaching the Heisenberg point while crossing through the ψ_2/ψ_3 phases identified by Ref. [110] which results in the oscillations observed. Quantitatively demonstrating this would require to identify the 3D phase diagram and we therefore leave this for future work.

4.7 Conclusion and Outlook

In this section we have identified the magnetic phase diagram for the Heisenberg and DM Hamiltonian in both the classical and quantum model. In both cases, three $\boldsymbol{q} = \boldsymbol{0}$ ordered phases, two antiferromagnetic phases (AIAO and Γ_5 phases) and one ferromagnetic phase (colinear ferromagnet phase), and two spin-liquid phases are identified (the Heisenberg antiferromagnet and the $J_{\mathrm{DM}}/J = 2$ spin-liquid). Moreover, an ObD selection is observed in the Γ_5 phase where a ψ_3 phase was identified for $\theta \in (243°, 265°)$ at all temperatures, whereas for $\theta \in [265°, 360°)$ an intermediate ψ_2 phase is identified followed by a low-temperature ψ_3 phase. Since the interest in the Heisenberg and DM Hamiltonian originated from the exact degeneracy between two symmetry breaking phases, our work motivates the study of other magnetic systems living in phase boundaries which may present fruitful ground on the identification of new exotic phenomena. Moreover, our results can be used to spearhead the search for models in the interaction parameter space which may realize similar types of spin-liquids and even to motivate the search of these in other geometries.

[7] We have verified the origin of these oscillations by implementing different integration techniques (Riemann integration, MC integration, and a Python integration function), as well as the numerical study of this quantity using a CLTE which *all* resulted in the same oscillations.

[8] The local interaction parameters in terms of the parametrization Eq. (4.4) take the form $J_{zz} = -\frac{1}{3}(\cos(\theta) + 4\sin(\theta))$, $J_\pm = \frac{1}{6}(\cos(\theta) - 2\sin(\theta))$, $J_{\pm\pm} = \frac{1}{3}(\cos(\theta) + \sin(\theta))$ and $J_{z\pm} = \frac{1}{3\sqrt{2}}(2\cos(\theta) - \sin(\theta))$.

Chapter 5

Order-by-Disorder in the Colinear Ferromagnet

In Chapter 4, the magnetic phases realized for the Heisenberg and DM Hamiltonian were identified and studied. In particular, we focused on the antiferromagnetic Γ_5 phase where the ground state manifold possesses an accidental $U(1)$ symmetry, which in turn leads us to study the effect of quantum and thermal ObD in this phase. Similar ObD effects have been widely studied for other pyrochlore Hamiltonians where the ground state configuration is a Γ_5 state [73, 74, 86, 87, 89, 110, 112]. In contrast, much less attention has been given to the onset of these phenomena for colinear ferromagnetic phases in the pyrochlore lattice where an *accidental* $O(3)$ symmetry is associated with the ferromagnetic states, and therefore the ground state manifold. The ObD selection in colinear ferromagnetic phases has been studied for other lattices and interactions [135–137] where a selection of the magnetization orientation has been observed. In this chapters we study the quantum and thermal ObD phenomenon in the ferromagnetic phases using LSW for the quantum model, and CLTE and MC for the classical model.

5.1 Accidental O(3) Symmetry

Starting from the Heisenberg and DM Hamiltonian as defined in Chapter 4

$$\mathcal{H} = J \sum_{\langle ij \rangle} \boldsymbol{S}_i \cdot \boldsymbol{S}_j + J_{\mathrm{DM}} \sum_{\langle ij \rangle} \boldsymbol{D}_{ij} \cdot (\boldsymbol{S}_i \times \boldsymbol{S}_j), \tag{5.1}$$

where we now consider a set of interactions parameters $\{J, J_{\rm DM}\} = \{\cos\theta, \sin\theta\}$ such that the low temperature phase is a colinear ferromagnetic phase, see Fig. 4.11 in Chapter 4. Additionally, all the energy related quantities presented in this chapter are measured in units of $\sqrt{J^2 + J_{\rm DM}^2}$, as was done in that chapter. As was previously discussed in Chapter 4, this model realizes a $\boldsymbol{q} = \boldsymbol{0}$ colinear ferromagnetic state for $\theta \in [135°, 243°)$ for the classical model and $\theta \in [135°, 229°)$ for the quantum model, as illustrated in Fig. 4.11. In the absence of the DM interaction, i.e. $J_{\rm DM} = 0$, the Hamiltonian in Eq. (5.1) is a ferromagnetic Heisenberg model with an exact global $O(3)$ symmetry[1]. When $J_{\rm DM} \neq 0$, the anisotropy introduced by the DM interaction reduces the symmetry group from $O(3)$ to the tetrahedral group T_d [74, 118], a subgroup of $O(3)$ [33, 117].

Despite the anisotropy induced by the DM interaction, the ground state manifold *retains* a global $O(3)$ symmetry in both the classical *and* quantum models. In the classical case, the irrep modes of the $T_{1\|}$ correspond to configurations where the spins are polarized along the global Cartesian axis. A polarized configuration in an arbitrary direction can be obtained by a linear combination of the irrep modes preserving the classical energy of the polarized configuration. This linear configuration between different ferromagnetic states is equivalent to the combination given in Eq. (4.16) for the Γ_5 phase where instead of the ψ_2/ψ_3, states we use colinear configurations along different axis. In the quantum case, the accidental $O(3)$ symmetry in the ground state manifold is retained as a consequence of the chirality of the DM vectors for a single site in a tetrahedron,

$$\sum_{\substack{j\neq i \\ i,j\in\boxtimes}} \boldsymbol{D}_{ij} = 0, \tag{5.2}$$

which geometrically translates into a chirality associated to the DM vectors of a site i in a single tetrahedron as shown in Fig. 5.1.

To illustrate how the chirality of the DM vectors results in the accidental symmetry of the quantum ground state manifold, consider a fully polarized product state, i.e. colinear ferromagnetic state, oriented along the global magnetization direction $\hat{\boldsymbol{m}}$

$$|\Psi_0(\hat{\boldsymbol{m}})\rangle = \bigotimes_{i=1}^{N} \left|\uparrow_i^{\hat{\boldsymbol{m}}}\right\rangle. \tag{5.3}$$

Clearly, the above state is an eigenstate of the Heisenberg Hamiltonian (2.23), as we have $\mathcal{H}_{\rm Heis}\,|\Psi_0(\hat{\boldsymbol{m}})\rangle = -3JNS^2\,|\Psi_0(\hat{\boldsymbol{m}})\rangle$ independent of the magnetization axis, reflecting the

[1] In other words, an $O(3)$ rotation operator $U_{\rm Rot}$ commutes with the Hamiltonian, $[\mathcal{H}, U_{\rm Rot}] = 0$.

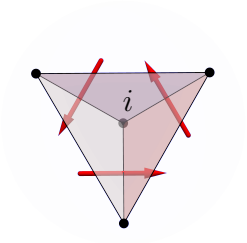


Figure 5.1: DM vectors between a site i and its nearest neighbors for a single tetrahedron. Note that the orientation of DM vectors can be associated with an oriented closed loop.

fact that Eq. (2.23) is fully O(3) symmetric. Furthermore, an application of the DM Hamiltonian (2.26) to this state yields

$$\mathcal{H}_{\mathrm{DM}} \left|\Psi_0(\hat{\boldsymbol{m}})\right\rangle = iJ_{\mathrm{DM}} S \sum_{i\in\boxtimes} \underbrace{\left(\sum_{\substack{j\neq i \\ i,j\in\boxtimes}} d_{ij}^{+} \right)}_{=0} S_i^{-} \left|\Psi_0(\hat{\boldsymbol{m}})\right\rangle = 0, \tag{5.4}$$

where $d_{ij}^{+} \equiv \boldsymbol{D}_{ij} \cdot (\boldsymbol{u} + i\boldsymbol{v})$, where $\boldsymbol{u}$ and $\boldsymbol{v}$ label the perpendicular directions to the $\hat{\boldsymbol{m}}$ polarization. Therefore, the energy associated with the state $|\Psi_0(\hat{\boldsymbol{m}})\rangle$ is the Heisenberg exchange energy. Consequently, from Eq. (5.2) and Eq. (5.4), all the colinear ferromagnetic states preserve the Heisenberg energy which results in the accidental symmetry in the quantum model. It is worth noting that the preservation of the $O(3)$ symmetry of the colinear ferromagnet ground manifold is generally not expected as the introduction of anisotropic interactions usually results in orientation dependent energy contributions which lift the degeneracy. In the next section we study the effects of temperature in the selection of a magnetization orientation for the quantum case.

5.2 Quantum Thermal Order-by-Disorder

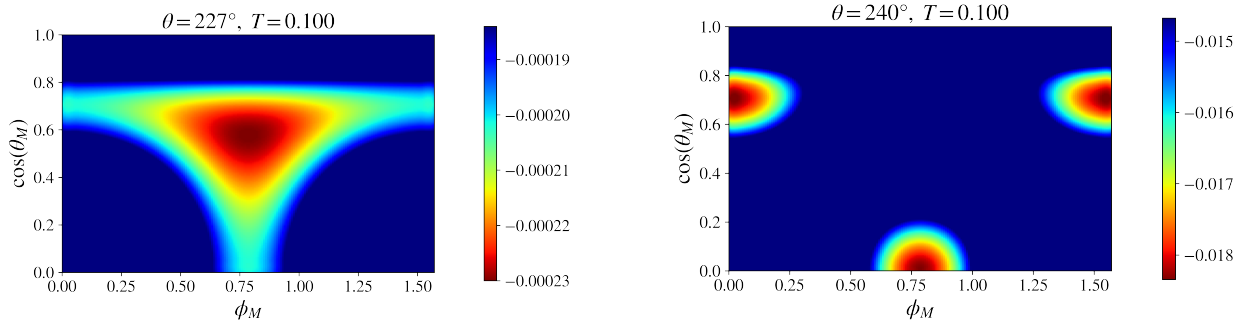
Typically, it is expected that quantizing the Hamiltonian in Eq. (5.1) would lift the accidental symmetry of the ground state due to the additional contribution from the zero-point energy correction [110], a mechanism commonly referred to as quantum ObD [100, 110, 125]. Interestingly, since the colinear ferromagnetic states are exact eigenstates of the Hamiltonian in Eq. (5.1) the degeneracy over *all* magnetization orientations is preserved even after

considering the zero-point energy corrections[2]. While this observation is strictly valid in the limit $T = 0$, we would expect the accidental $O(3)$ symmetry to be lifted by thermal effects involving anisotropic energy fluctuations at $T \neq 0$. In other words, we may study the *thermal quantum ObD* mechanism where the selection is produced by the way the energy fluctuations about a ground state configuration are populated.

Within a LSW theory, the energy fluctuations are described by the magnons and the allowed energies of these fluctuations by the magnon bands, see Section 3.3. To study how the anisotropy of these fluctuations and the way these are populated result in a thermal quantum ObD selection, we compute the free energy difference [100] associated to the magnon excitations about different magnetization orientations $\hat{\boldsymbol{n}}$ and $\hat{\boldsymbol{m}}$

$$\Delta\mathcal{F} = \mathcal{F}^{(\hat{\boldsymbol{m}})} - \mathcal{F}^{(\hat{\boldsymbol{n}})} = T \sum_{\boldsymbol{q}} \sum_{a} \ln \left(\frac{1 - e^{-\omega_a^{(\hat{\boldsymbol{m}})}(\boldsymbol{q})/T}}{1 - e^{-\omega_a^{(\hat{\boldsymbol{n}})}(\boldsymbol{q})/T}} \right), \tag{5.5}$$

where $\{\omega_a^{(\hat{\boldsymbol{m}})}(\boldsymbol{q})\}$ are the magnon energies associated to the colinear ferromagnet orientated along the $\hat{\boldsymbol{m}}$ direction, we have taken $k_{\mathrm{B}} = 1$, and the values shown are in units of $\sqrt{J^2 + J_{\mathrm{DM}}^2}$. From the above expression, it is clear that the temperature dependence of the free energy difference relies on how the magnon bands are populated. Therefore, if we identify an orientation $\hat{\boldsymbol{m}}$ such that $\Delta\mathcal{F} \leq 0$ for all other orientations $\{\hat{\boldsymbol{n}}\}$, then $\hat{\boldsymbol{m}}$ is identified as the preferred orientation.[3]



(a) (b)

Figure 5.2: Free energy difference $\Delta\mathcal{F}$ for $\theta = 227°$ (a) and $\theta = 240°$ (b). In this diagrams the orientation with the least minimum energy difference is selected.

[2]This was also verified numerically for different orientations.

[3]Since the magnon spectrum changes depending on the orientation of the total magnetization (not shown), it is therefore expected that the free energy difference will identify a preferred orientation.

We have computed the free energy difference $\Delta\mathcal{F}$ in Eq. (5.5), for $\hat{\boldsymbol{n}} = \langle 001 \rangle$ and $\hat{\boldsymbol{m}} = [\cos(\phi_M)\sin(\theta_M), \sin(\phi_M)\sin(\theta_M), \cos(\theta_M)]$ in the first octant[4]. Within this analysis, the orientation with the most negative free energy at a temperature T is expected to be selected. Although the PFFRG results presented in Chapter 4 predict a disordered phase for $\theta \in [229°, 243°]$, we apply the free energy analysis for $\theta \in [135°, 243°)$ and postpone the discussion of the disordered phase to the end of the chapter. Fig. 5.2 shows $\Delta\mathcal{F}$ for $\theta = 227°$ in panel (a) and $\theta = 240°$ in panel (b) at $T = 0.1$. In these plots, the minimum in $\Delta\mathcal{F}$ is found at $\cos(\theta_M) = 1/\sqrt{3}$, and $\phi = \pi/4$ and $\cos(\theta_M) = 0$ and $\phi = 0$[5] corresponding to the $\langle 111 \rangle$ and $\langle 110 \rangle$ orientations, respectively.

Producing a similar analysis at low temperatures (i.e. $T \to 0$) for $\theta \in [135°, 243°)$ identifies two regions in parameter space: one for $\theta < 239°$ and another for $\theta > 239°$ where the $\langle 111 \rangle$ and $\langle 110 \rangle$ orientations are respectively selected. As illustrated in Chapter 4, the ObD selection at $T \to 0$ does not have to agree with the selection produced at higher temperatures. Therefore, using the same free energy difference calculation, we identify the ObD magnetization orientation selection as a function of temperature T/T_c as shown in Fig. 4.8. In this figure, the values of T_c used are obtained from the MC simulations presented in Chapter 4, see Fig. 4.3. Our analysis identifies a phase diagram where either the $\langle 111 \rangle$ or $\langle 110 \rangle$ orientations are selected.

The phase diagram in Fig. 5.3 shows the difference $\Delta\mathcal{F}$ between the $\langle 111 \rangle$ and $\langle 110 \rangle$ orientations where positive values indicate a $\langle 110 \rangle$ selection and the negative values indicate a $\langle 111 \rangle$ selection. This phase diagram shows *re-entrance* [82] of the $\langle 110 \rangle$ orientation, i.e. a regime where an intermediate $\langle 110 \rangle$ phase is observed between a high and low temperature the $\langle 111 \rangle$ phase. The $\langle 110 \rangle$ phase is first detected at low temperatures for $\theta \sim 239°$ reaching $\theta \sim 229°$ as temperature is increased around $T/T_c \sim 0.2$ and then decreasing upon increasing temperature up to $\theta \sim 236°$. Consequently, for $\theta \in [229°, 236°)$, a $\langle 111 \rangle$ orientation is predicted at low temperatures followed by an *intermediate* $\langle 110 \rangle$ orientation, and finally $\langle 111 \rangle$ orientation at high temperatures. For $\theta < 229°$ our analysis predicts a selection of the $\langle 111 \rangle$ orientation for all temperatures although the free-energy difference decreases its magnitude, and therefore the selection weakens, as $\theta \to 180°$. This decreasing free energy difference is expected from approaching the Heisenberg limit which has an exact $O(3)$ symmetry. This decreasing effect in the free energy difference is also seen as T approaches 0. This effect is however expected, as for $T \to 0$ the free energy starts to approach the limit where it is solely described by the zero-point energy correction which, as previously discussed, is the equivalent for all colinear ferromagnetic states.

[4] In Cartesian coordinates this is for $x, y, z > 0$.

[5] The other points are related by C_3 rotations.

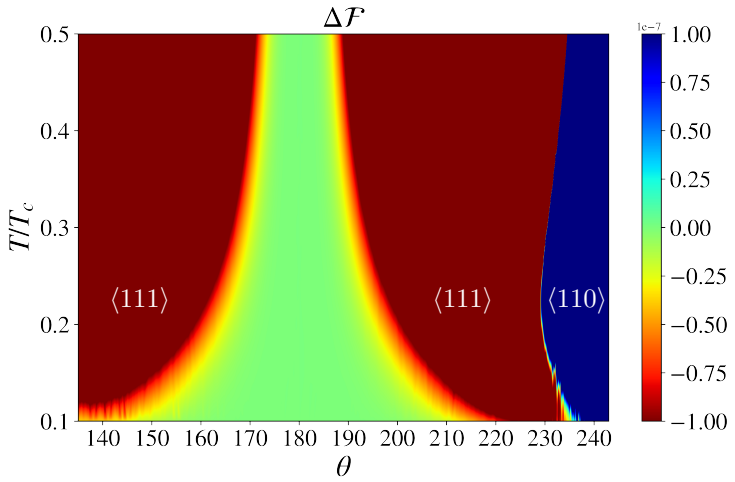
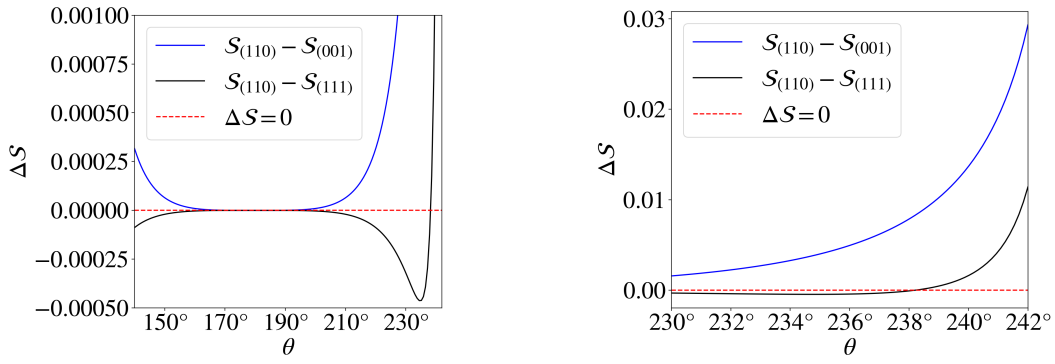


Figure 5.3: Phase diagram constructed using the free energy difference $\Delta\mathcal{F}$ obtained through LSW where $\Delta\mathcal{F} < 0$ indicates a $\langle 111\rangle$ selection and $\Delta\mathcal{F} > 0$ indicates a $\langle 110\rangle$ selection.

Note that the selection towards an orientation is expected to be rather weak, as the free energy difference $\Delta\mathcal{F} \sim O(10^{-7})$, and only increases when approaching a phase boundary. In fact, comparing the free energy scale in the ferromagnetic phase to the zero-point energy difference $\Delta E_0 \sim O(10^{-4})$ in the Γ_5 discussed in Chapter 4 would imply an entropic selection by an energy quantity which is three orders of magnitude smaller. This observation naturally raises the question on whether a selection of a given magnetization orientation can be observed or if this effect will only take place at low temperatures which could in principle be inaccessible experimentally or even numerically.

5.3 Classical Thermal Order-by-Disorder

To assess the classical thermal ObD selection at low temperatures in the colinear ferromagnetic phase, we study the entropic weight difference between distinct magnetization orientations, $\Delta\mathcal{S}$. The entropic weight selection presented in this section is analogous to the one performed in Section 4.4 for the Γ_5 phase, and as such we only present the results. Figure 5.4 shows the entropic weight difference $\Delta\mathcal{S}$ between the $\langle 110\rangle$ and $\langle 001\rangle$, and between the $\langle 110\rangle$ and $\langle 111\rangle$ orientations. In these figures, the configuration with the highest entropic weight is expected to be selected at low temperatures, see Subsection 3.2.1.



(a) (b)

Figure 5.4: Entropic weight difference $\Delta\mathcal{S}$ for $\theta \in [135°, 243°)$ (a) and $\theta \in [230°, 243°)$ (b).

From Fig. 5.4, and in agreement with the LSW analysis, we found that the $\langle 001\rangle$ orientation is not favored for any angle $\theta \in [135°, 243°)$, i.e. $\mathcal{S}_{\langle 001\rangle}$ is always smaller than $\mathcal{S}_{\langle 111\rangle}$ and $\mathcal{S}_{\langle 110\rangle}$. We illustrate this by showing $\mathcal{S}_{\langle 110\rangle} - \mathcal{S}_{\langle 001\rangle}$ in Fig. 5.4(a) and (b)[6]. Additionally, this analysis identifies two regions in parameter space where different orientations are favored at low temperatures: one for $\theta \in (135°, 238°)$ and another for $\theta \in (238°, 243°)$ where the $\langle 111\rangle$ and $\langle 110\rangle$ orientations are selected respectively, see Fig. 5.4(b). The identification of these phases is similar to what is predicted by LSW for low temperatures where the two regions are $\theta \in (135°, 239°)$ and $\theta \in (239°, 243°)$ for $\langle 111\rangle$ and $\langle 110\rangle$ orientations respectively. Moreover, as in the LSW analysis, the ObD selection becomes stronger upon approaching a phase boundary. Unfortunately, and in contrast to what is predicted by LSW, the entropic weight derived in Section 3.2 is *incapable* of identifying a reorientation of the total magnetization as a function of temperature since the temperature only enters as an overall prefactor, see Eq. (3.15). Going beyond this analysis would require considering higher order terms in the CLTE.

Comparing the magnitude of the entropic weight difference for the colinear ferromagnetic state [$\Delta\mathcal{S} \sim O(10^{-4})$] with what was found in Chapter 4 for the Γ_5 phase [$\Delta\mathcal{S} \sim O(10^{-2})$] yields similar results to the comparison made for the quantum ObD selection: the selection is predicted to be two orders of magnitude *weaker* in the ferromagnetic phase than in the antiferromagnetic phase[7]. However, both LSW and CLTE are limited to $T \ll T_c$ and therefore a method capable of going beyond this limit is needed. With this in mind, we now turn to diagnose the possibility of a selection in the magnetization

[6] A similar behavior is found for $\mathcal{S}_{\langle 111\rangle} - \mathcal{S}_{\langle 001\rangle}$ and we therefore omit the presentation of these curves.
[7] This argument excludes the selection in the ferromagnetic phase close to the Γ_5 boundary.

orientations using classical MC.

5.4 Monte Carlo Analysis

The conclusions drawn from the LSW and CLTE analysis are restricted to low temperatures [33, 74]. As such, methods capable of studying the *full* thermal evolution of the ordered phase and the selection in the magnetization orientation are needed in both the classical and quantum case. For the classical case, we apply a classical MC analysis for a system of $N = 4 \times L^3$ spins with $L = 10, 12$ with the update algorithms discussed in Section 3.6 where we have used $N_{\text{sim}} = 100$ and roughly $N_{\text{meas}} \sim 10^5$.

Clearly, the colinear ferromagnet order parameter, i.e. the $m_{T_{1\parallel}}$ irrep, cannot differentiate between different orientations in the total magnetization vector as it only probes the magnitude of the total magnetization. A similar scenario was encountered in the Γ_5 phase where the distinction of the ψ_2 and ψ_3 phases is performed by analyzing the evolution of the m_{E6} parameter instead of the m_E irrep. The reason why the m_{E6} parameter can be used[8] originates from the Landau free energy where this parameter is the first anisotropic term which differentiates the states in the Γ_5 manifold. In that case, the sign of this parameter was used as a proxy to determine whether a ψ_2 or a ψ_3 order is preferred. Following the same ideas we now consider a Landau free energy for the colinear ferromagnetic phase where the order parameters are given by the components of the total magnetization $\boldsymbol{M}$

$$\mathcal{F} = a|\boldsymbol{m}|^2 + K_1^{(1)}(m_x^2 m_y^2 + m_y^2 m_z^2 + m_z^2 m_x^2) + K_1^{(2)}(m_x^4 + m_y^4 + m_z^4) + K_2(m_x^2 m_y^2 m_z^2) + \cdots, \quad (5.6)$$

where

$$m_\alpha \;=\; \frac{1}{N}\sum_i S_i^\alpha. \quad (5.7)$$

In this expansion, the terms with the a, $K_1^{(1)}$, $K_1^{(2)}$, and K_2 constants are the first anisotropic terms in the free energy expansion [136–138][9] which we referred to as the cubic (anisotropy) parameters. In analogy to the Γ_5 manifold m_{E6} parameter, we study

[8] Recall the discussion in Chapter 4 where this parameter is used as a *proxy* to differentiate the two Γ_5 orders.

[9] For simplicity, here we have ignored other possible sixth order terms in the theory. In principle we could use the higher order terms too, but, as is further discussed below, the identification of the orientation is performed by studying other quantities.

the thermal average of the quantities

$$M_{42} = 3\left\langle m_x^2 m_y^2 + m_y^2 m_z^2 + m_z^2 m_x^2 \right\rangle, \tag{5.8}$$

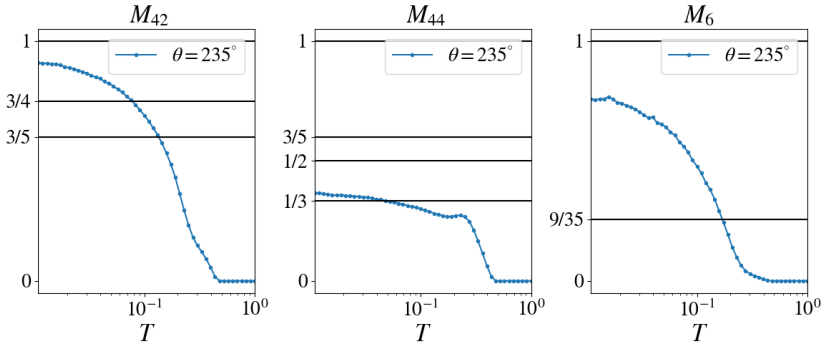
$$M_{44} = \left\langle m_x^4 + m_y^4 + m_z^4 \right\rangle, \tag{5.9}$$

$$M_6 = 27\left\langle m_x^2 m_y^2 m_z^2 \right\rangle, \tag{5.10}$$

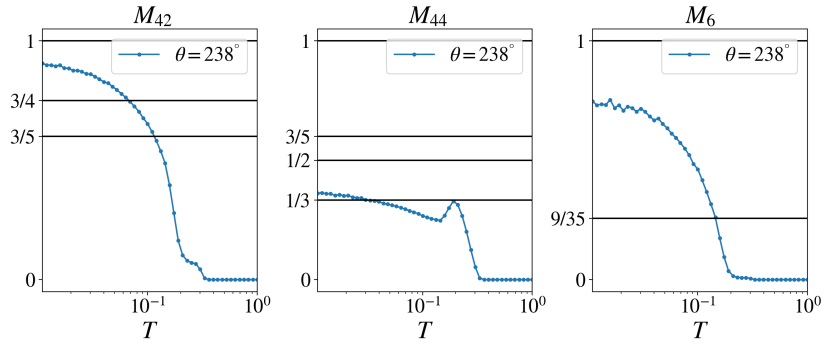
to assess the possibility of a preferred orientation of the total magnetization vector $\boldsymbol{M}$. For fully isotropic systems, the cubic parameters should plateau to the values $M_{42} = 3/4$, $M_{44} = 3/5$ and $M_6 = 9/35$ simultaneously[10]. On the contrary, when a specific orientation for the total magnetization is selected, the values of these thermodynamic quantities differ from those in the isotropic case. For example, these parameters acquire the values $\{M_{42}, M_{44}, M_6\} = \{0, 1, 0\}$, $\{3/4, 1/2, 0\}$, $\{1, 1/3, 1\}$, when the total magnetization vector is oriented along the $\langle 001\rangle$, $\langle 110\rangle$, and $\langle 111\rangle$ directions, respectively. We primarily focus on these orientations as these correspond to high symmetry orientations allowed by cubic symmetry and are also what is predicted to be observed by both LSW and CLTE.

Following the analysis obtained from the CLTE, we present results for three different angles $\theta = 235°,\ 238°,\ 240°$. These angles correspond to regions where the CLTE identified a $\langle 111\rangle$ and $\langle 110\rangle$ ordering for $\theta = 235°$ and $\theta = 240°$, respectively, while $\theta = 238°$ corresponds to the angle where the CLTE analysis does not identify a preferred magnetization orientation between the $\langle 111\rangle$ and $\langle 110\rangle$ orientations, see Fig. 5.4(b). Fig. 5.5 illustrates the evolution of the cubic parameters M_{42}, M_{44}, and M_6 as a function of temperatures obtained for $L = 12$. In these figures, the horizontal lines mark the values that are expected for an isotropic system and those expected for the $\langle 001\rangle$, $\langle 110\rangle$ and $\langle 111\rangle$ orientations. For $\theta = 235°$, the M_{42} and M_6 parameters seem to increase smoothly as the temperature is lowered whereas the M_{44} parameter shows a small decrease in its slope right below the value $M_{44} = 1/3$. Similarly, for $\theta = 238°,\ 240°$ the cubic parameters M_{42} presents a slight change in the slope of the function whereas the M_{44} develops a small bump in a region right below the critical temperature T_c. This behavior, i.e. the change in the slope of the cubic parameter, is more pronounced in the M_6 parameter for $\theta = 240°$ where the function shows a broad bump before starting to decrease. The change in the slope for the cubic parameters may signal a reorientation of the magnetization vector. Furthermore, the oscillations in the cubic parameters at low temperatures are presumably associated with poor statistics which can in principle be improved by running more simulations and measuring more configurations, i.e. increasing N_{meas} and N_{sim}, see Section 3.6.

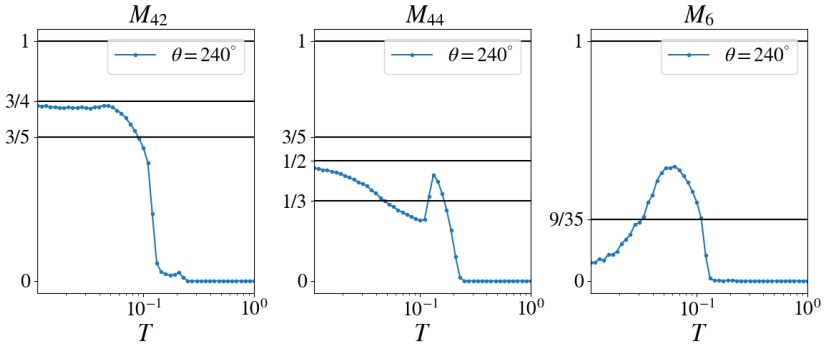
[10]These values are obtained by integrating the associated quantity while considering an equal probability for all orientations. For example, for the M_{44} parameter we obtain $M_{44} = \frac{3}{4\pi}\int (s_x^4 + s_y^4 + s_z^4)\sin(\theta) d\theta d\phi = \frac{3}{5}$ where the components of the spin are taken in spherical coordinates.



(a)



(b)



(c)

Figure 5.5: Temperature evolution of the M_{42}, M_{44}, and M_6 parameters for $\theta = 235°$ (a), $\theta = 238°$ (b), $\theta = 240°$ (c) obtained using classical MC for a system size $L = 12$. Note that for an isotropic system we would expect these parameters to plateau to the values $M_{42} = 3/4$, $M_{44} = 3/5$ and $M_6 = 9/35$.

As can be seen in Fig. 5.5, none of the cubic parameters plateaus to the isotropic case at low temperatures. Additionally, the values of these parameters at low temperature do not agree to what would be expected for the $\langle 001 \rangle$, $\langle 111 \rangle$, or $\langle 110 \rangle$ orientations[11]. This disagreement can be related to the weak selection predicted by the CLTE. In other words, there could be a slight preference for the system to fluctuate around orientations which are favored by the entropic weight, however, given that this effect is small, the system would still able to "explore" other orientations[12]. This would then explain why the values of cubic parameters do not plateau to those related to the $\langle 001 \rangle$, $\langle 110 \rangle$, or $\langle 111 \rangle$ orientations but instead to intermediate values. In fact, for $\theta < 235°$ we observed a similar but more subtle evolution of the cubic parameters to what was observed for $\theta = 235°$ where the deviation from the isotropic values decreases as $\theta \to 180°$[13]. This observation is inline to what is predicted by the CLTE where the entropic weight difference decreases as $\theta \to 180°$, see Fig. 5.4(a). To further study the preferred magnetization orientations and the possibility of the system to "explore" other orientations below we study the distribution of the total magnetization orientation sampled through MC in the first octant for $\theta = 235°,\ 238°,\ 240°$ at a temperature T. First, we focus on the low temperature distribution to compare our findings to what is predicted by the CLTE and then explore the possibility of a reorientation in the magnetization vector at higher temperatures.

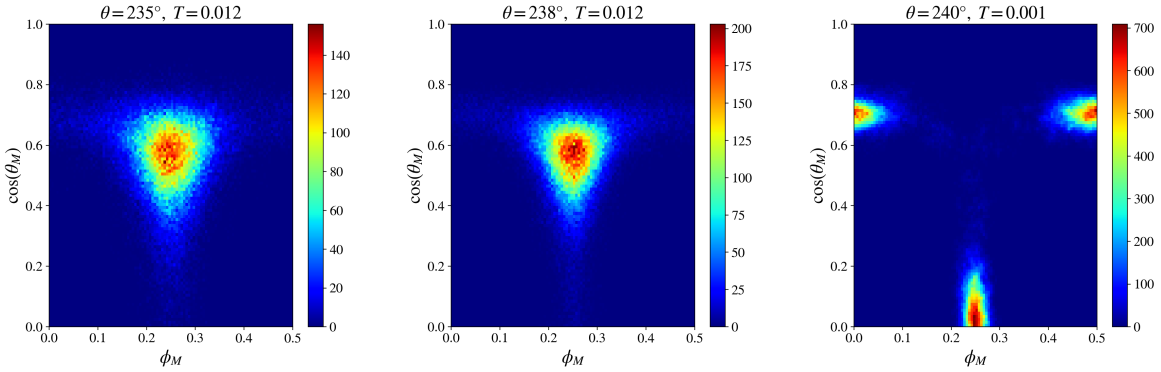
Fig. 5.6 shows the density plots of the magnetization orientation as a function of the azimuth angle ϕ_M and polar angle θ_M at a temperature $T \ll T_c$ for $\theta = 235°,\ 238°,\ 240°$ sampled from MC. The color in these plots indicates the number of configurations that are sampled at the respective orientation, consequently this plots can be understood as a probability distribution of the magnetization orientation at a temperature T[14]. For $\theta = 235°,\ 238°$ the pattern of these distribution is similar to what is predicted for the free energy difference by LSW as shown in Fig. 5.2(a) where a $\langle 111 \rangle$ order is detected. Similarly, the pattern for $\theta = 240°$ agrees to the one obtained for a $\langle 110 \rangle$ orientation for the free energy as shown in Fig. 5.2(b). It is worth noting that the density distribution for these angles is quite scattered, only showing an increase in the number of samples at locations corresponding to the $\langle 111 \rangle$ and $\langle 110 \rangle$ orientations. This observation supports the idea that the system *is* able to explore other magnetization orientations at low temperatures although it "spends" more time in those predicted by the CLTE analysis. Following these

[11] It is worth stating that the deviation of the parameters from the isotropic values increases with the system size L which might be an indication of an emergent length-scale $\Lambda(T)$ similar to the one discussed in Chapter 4.

[12] This is similar to what happened with the m_{E6} parameter and the distribution of the Γ_5 angle ϕ.

[13] This means that while the cubic parameters do not plateau to the isotropic values, the deviation from these is smaller.

[14] This plots are similar to the ϕ distributions shown in Chapter 4.



(a) (b) (c)

Figure 5.6: Total magnetization density plot as sampled from MC for $\theta = 235°$ (a), $\theta = 238°$ (b), and $\theta = 240°$ (c) for the temperature given in the title of each panel. These distributions were obtained for a system size of $L = 12$ for $\theta = 235°, 238°$ and for $L = 10$ for $\theta = 240°$.

observations, we label $\theta = 235°, 238°$ as $\langle 111 \rangle$ phases at low temperatures and $\theta = 240°$ as a $\langle 110 \rangle$ phase at low temperatures. Similar results to those shown for $\theta = 235°$ were obtained for $\theta < 235°$ although the distribution for these angles was found to be broader. This is in turn consistent with the decreasing entropic weight obtained from the CLTE, and the decreasing deviation at low temperatures of the cubic parameters from the isotropic values. Interestingly, the CLTE predicts that at $\theta \simeq 238°$ no selection between the $\langle 111 \rangle$ and $\langle 110 \rangle$ orders is produced. Although this effect is not observed for $\theta = 238°$, it is somewhat observed for $\theta = 239°$ where the density plots of the magnetization orientation shows a high concentration of points at locations corresponding to the $\langle 111 \rangle$ and $\langle 110 \rangle$ orientations, see Fig. 5.7. Altogether, the low-temperature distribution of the magnetization lets us conclude that the predictions obtained from CLTE correctly represent what is observed in the MC simulations.

Having clarified the selection on the magnetization orientation at low temperatures, we now focus on the selection at temperatures near T_c and at intermediate temperatures. Fig. 5.8 shows the magnetization orientation distribution for $\theta = 235°,\ 238°,\ 240°$ at higher temperatures near T_c. For all the indicated angles the distribution at high temperatures now shows a concentration of points at $\phi_M = 0, \pi$ and $\cos(\theta_M) = 0$, and at a broad line covering all angles ϕ_M with $\cos(\theta_M) = 1$. Interestingly, this pattern corresponds to a $\langle 001 \rangle$ and all the other Cartesian axis vectors implying a selection of these orientations at high temperatures. This pattern is however lost for $\theta < 227°$ and is replaced by one

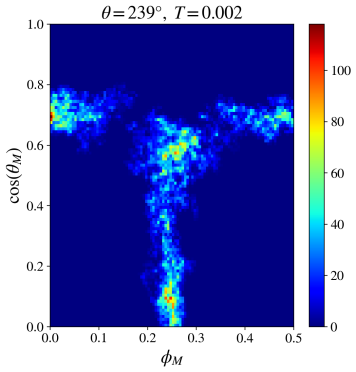
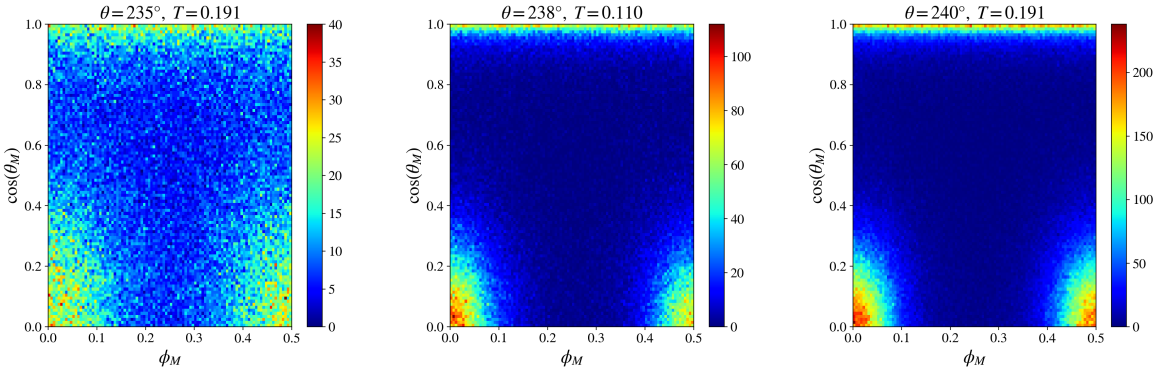


Figure 5.7: Total magnetization density plot as sampled from MC for $\theta = 239°$ sampled at the temperature indicated in the title.

consistent with a $\langle 111 \rangle$ orientation. In other words, for $\theta > 227°$ a $\langle 001 \rangle$ selection seems to occur just below T_c. The selection towards the $\langle 001 \rangle$ or $\langle 111 \rangle$ cubic axis close to T_c is expected from an renormalization group perspective as the cubic symmetry sets in at the critical temperature eliminating the accidental $O(3)$ symmetry [139][15]. The $\langle 001 \rangle$ selection is presumably related to the evolution of the cubic parameters right below T_c shown in Fig. 5.5 where a small but abrupt change was observed in the evolution of these parameters. Note that the selection close to the critical temperature is not captured by LSW or CLTE as these approximations assume small fluctuations about the ordered spin configurations only valid for $T \ll T_c$. Going beyond these low temperatures approximations would require other analytical approaches capable of studying the free energy fluctuations close to T_c [140].

The observation of different patterns in the magnetization orientation distribution at high and low temperatures can be taken as a smoking gun proof of the reorientation of the total magnetization vector for $\theta > 227°$. This however does not mean that no other orientation can be favored at intermediate temperatures. In fact, LSW predicts a reorientation from the $\langle 110 \rangle$ to the $\langle 111 \rangle$ orientation as temperature is increased for $\theta > 239°$ at low and intermediate temperatures, see Fig. 5.3. We therefore study the evolution of the distribution of the magnetization orientation for $\theta > 239°$. Fig. 5.9 shows the evolution of the magnetization distribution for $\theta = 240°$ at three temperatures: one for

[15]From a renormalization group perspective, for a second order phase transition only these two orders can set it and the free energy theory would not have the sixth order cubic parameters as these become irrelevant. This selection however changes when the transition becomes first order and the cubic parameters now enter the theory.

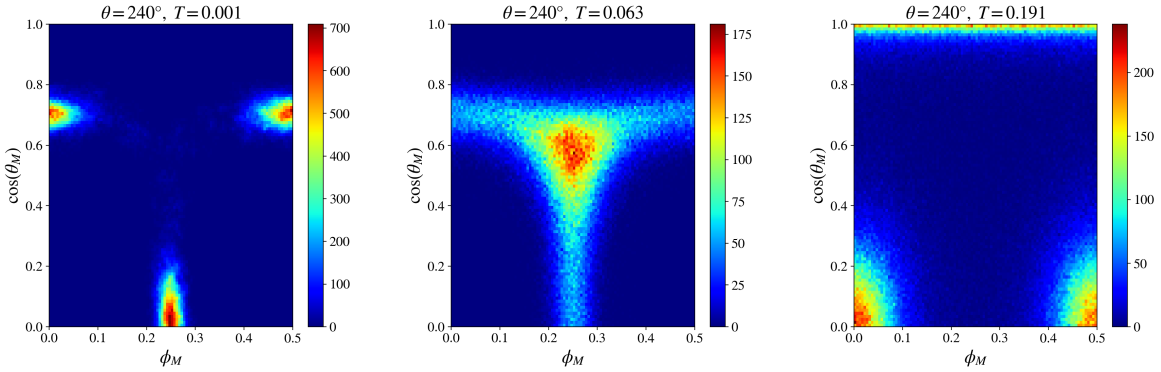


(a) (b) (c)

Figure 5.8: Total magnetization density plot as sampled from MC for $\theta = 235°$ (a), $\theta = 238°$ (b), and $\theta = 240°$ (c) for a temperature close T_c ($T_c = 0.440,\ 0.335,\ 0.224$ for $\theta = 235°,\ 238°, 240°$, respectively) where the exact value of the temperature is given in the title of each panel. These distributions were obtained for a system size of $L = 12$ for $\theta = 235°, 238°$ and for $L = 10$ for $\theta = 240°$.

$T < T_c$, one for an intermediate temperature below T_c, and one just below T_c. As identified before, the patterns of distributions at high and low temperatures for $\theta = 240°$ correspond to a preference for the $\langle 001 \rangle$ and $\langle 110 \rangle$ orientations, respectively. However, the pattern for intermediate temperatures corresponds to a preference for the $\langle 111 \rangle$ orientation although this pattern is more scattered than those observed at low temperatures in Fig. 5.6. Similar results were obtained for $\theta > 240°$.

Altogether, the temperature evolution of the magnetization orientation distribution for $\theta > 240°$ implies that the magnetization vector undergoes *two* re-orientations as the temperature is lowered. On the other hand, for $227° < \theta < 240°$ one re-orientation is observed while for $\theta < 227°$ a preference for the $\langle 111 \rangle$ orientation is observed for *all* temperatures below T_c. We summarize these results in an approximate phase diagram in Fig. 5.10 where the yellow region corresponds to a preference for the $\langle 111 \rangle$ orientation, the purple region corresponds to a preference for the $\langle 001 \rangle$ orientation, and the green region corresponds to a preference for the $\langle 110 \rangle$ orientation in the colinear ferromagnetic phase.



(a) (b) (c)

Figure 5.9: Total magnetization density plot as sampled from MC for $\theta = 240°$ for the temperatures given in the title of each panel. These distributions were obtained for a system size of $L = 10$.

5.5 Conclusion and Outlook

In general terms, the preferred orientation predicted for the total magnetization vector in the classical and quantum models agree: at low temperatures for $\theta < 239°$ a $\langle 111 \rangle$ orientation is preferred whereas for $\theta > 239°$ a $\langle 110 \rangle$ orientation is preferred. Additionally, both the classical and quantum models present a reorientation of the total magnetization vector from the $\langle 110 \rangle$ to the $\langle 111 \rangle$ for $\theta > 240°$. In contrast, the re-entrance of the $\langle 111 \rangle$ orientation for the quantum case predicted by LSW as θ is decreased is not captured by our MC analysis.

The analysis presented for the quantum model ignores the paramagnetic region identified by PFFRG in Chapter 4. In fact, PFFRG does not find a magnetically ordered state for $\theta \in [229°, 243°]$ which also corresponds to the region in space where LSW identifies a $\langle 110 \rangle$ orientation at intermediate temperatures. Interestingly, a relation between low temperature competition and "high" temperature behavior was presented and studied by Ref. [82] where re-entrance of a Palmer-Chalker (PC) phase was observed. In this case, $\theta = 229°$ corresponds to the boundary found by PFFRG where no order is found at $T \to 0$ (the low temperature behavior), and the smallest angle at which LSW predicts a $\langle 110 \rangle$ orientation at $T/T_c \sim 0.2$ (the high temperature behavior). The relation between these two observation, i.e. the avoidance of LRO and the re-entrance of the $\langle 110 \rangle$ phase, deserves further attention.

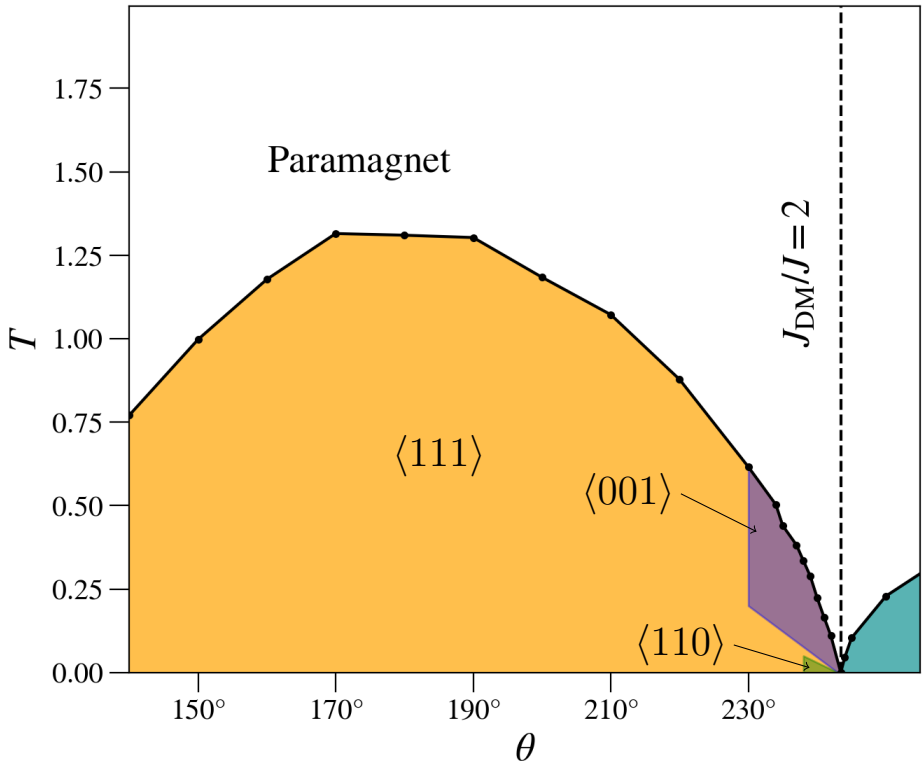


Figure 5.10: Approximate phase diagram of the ferromagnetic phase with the magnetization orientations identified using through MC.

The avoidance of a magnetically ordered phase predicted by PFFRG might imply an instability of the ferromagnetic phase for $\theta \in [229°, 243°]$ which is not captured by our LSW theory. A possible route to capture the instability of the ferromagnetic phase found by PFFRG is using spin-wave theory while considering higher order terms [141]. The introduction of these effects was considered by Ref. [141] where it was found that the magnon-magnon interactions would result in a *breakdown* of a ferromagnetic ordered phase in a region close to the classical phase boundary with a Γ_5 phase. Incidentally, the phase boundary studied by Ref. [141] presents strong competition between the ferromagnetic and antiferromagnetic modes which has been related to the proximity to a classical spin-liquid phase [142], the pinch-line-singularity spin-liquid [107]. Such competition and instability of the ferromagnetic phase could in principle be realized for the Heisenberg and DM Hamiltonian when approaching the J_{DM}/J point for the quantum case as was already hinted by PFFRG.

Although the instability of the colinear ferromagnetic phase is not present in the classical

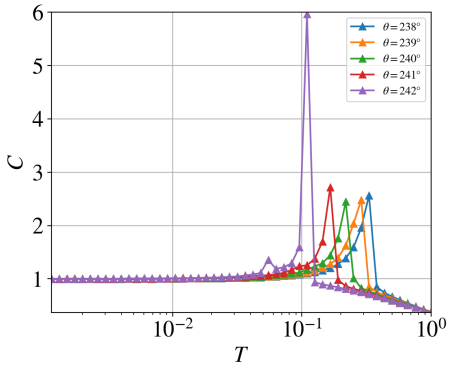


Figure 5.11: Specific heat for different values of θ approaching the Γ_5 phase.

case as our MC simulations identity a magnetically ordered phase, this does not mean that the classical system is immune to the competition related to the proximity to a spin-liquid. In fact, as $\theta \to 243°$ the ordered transition into the colinear ferromagnetic phase starts to become first ordered as shown in Fig. 5.11. Moreover, for $\theta = 242°$ the specific heat develops two peaks: a strong peak associated to the symmetry breaking transition at T_c and a weak peak at $\tilde{T} < T_c$. The origin of this secondary peak at $\tilde{T}$ might be related to an increasing phase competition as our MC simulations detect a region just below T_c where the $m_{T_1\perp}$ parameter acquires a non-zero value and vanishes at $T = \tilde{T}$, see Fig. 5.12. In the next chapter we study the $J_{\rm DM}/J = 2$ model and the paramagnetic phase it realizes.

The ObD selection in this chapter assumed a colinear ferromagnet as the low-temperature ground state configuration. In terms of the irreps, this ground state is obtained by enforcing that the $a_{T_1,\rm mix}$ in Eq. (4.5) vanishes, which is clearly satisfy by the Heisenberg and DM model. There are however other Hamiltonians which can satisfy this constraint although such models can be regarded as fine-tuned. Although in general grounds we expect that those alternative models also present a classical and quantum ObD selection, a zero-point energy correction could already show a preference towards certain magnetic orientations. This correction is expected as the quantum ground state manifold degeneracy may not survive the addition of any other non-DM interaction terms. This observation portrays the ObD selection presented in this chapter as a novel realization of a quantum ObD selection where the selection is *purely* thermal.

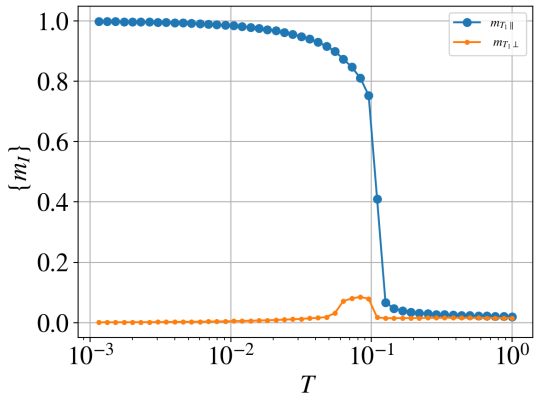


Figure 5.12: Irrep order parameters as a function of temperature for angles θ close to $\theta = 243°$.

Chapter 6

An Order-by-Disorder Selected Spin-Liquid

In the previous chapters we studied the Heisenberg and DM model and characterize its magnetically ordered phases. In Chapter 4, we identified a point in the interaction parameter space where no magnetic order was found both in the classical and the quantum model. This point corresponds to $J_{\rm DM}/J = 2$ with $J < 0$ and $J_{\rm DM} < 0$, and is located in the boundary between an antiferromagnetic Γ_5 phase and a colinear ferromagnetic phase. Additionally, in Chapter 5 we hinted that the cascade of re-orientations in the ferromagnetic phase may be related to the proximity to this point. In the present chapter, we study the Heisenberg and DM Hamiltonian for $J_{\rm DM}/J = 2$ point using a self-consistent gaussian approximation (SCGA), iterative minimization (IM), and classical Monte Carlo (MC). We discuss the competition which ultimately results in the avoidance of LRO and hint at the possibility of an ObD effect selecting an extensive set of configurations within the ground state manifold. In this chapter, we use the magnitude of the Heisenberg interaction J as energy scale for all the energy related quantities presented.

6.1 Irrep Analysis and Interaction Matrix

In Chapter 4, we considered the Heisenberg and DM Hamiltonian

$$\mathcal{H} \;=\; -J\sum_{\langle ij\rangle} \boldsymbol{S}_i\cdot\boldsymbol{S}_j + J_{\rm DM}\sum_{\langle ij\rangle}\boldsymbol{D}_{ij}\cdot(\boldsymbol{S}_i\times\boldsymbol{S}_j), \tag{6.1}$$

and performed an irrep analysis which identified the $\boldsymbol{q} = \mathbf{0}$ states which minimize the energy in a single tetrahedron for a set of interaction parameters $\{J, J_{\mathrm{DM}}\}$ parameterized by Eq. (4.4). In terms of the parametrization in Eq. (4.4), the irrep analysis finds that three irreps, $T_{1\parallel}$, the E, and the $T_{1\perp}$, have the *same* minimum energy, see Fig. 4.2 at $\theta = 243°$. These irreps correspond to the colinear ferromagnet ($T_{1\parallel}$), the Γ_5 (E), and the coplanar ($T_{1\perp}$) $\boldsymbol{q} = \mathbf{0}$ states, see Fig. 2.7. Moreover, note that the energy degeneracy between two T_1 irreps allows us to choose *any* two T_1 irrep modes when describing the theory[1]. In particular, we use the T_1^{Ice} and T_1^{xy} irreps (see Fig. 2.8) such that the low-energy irreps can be separated into the irreps with the *local* xy degrees of freedom, the E and the T_1^{xy} irreps, and the irrep with the *local* z degrees of freedom, the T_1^{Ice}. The separation of the degrees of the irreps in these two categories is especially relevant for $J = 1$, $J_{\mathrm{DM}} = -2$ as the $J_{z\pm}$ coupling *vanishes* signifying that this model describes a non-Kramers system where the local xy degrees of freedom do not interact with the local z degrees of freedom[2], see Section 2.1. In what follows, we refer to the Heisenberg and DM interaction model with $J_{\mathrm{DM}} = -2J$ and a ferromagnetic Heisenberg interaction as the $J_{\mathrm{DM}}/J = 2$ model for short-hand notation[3].

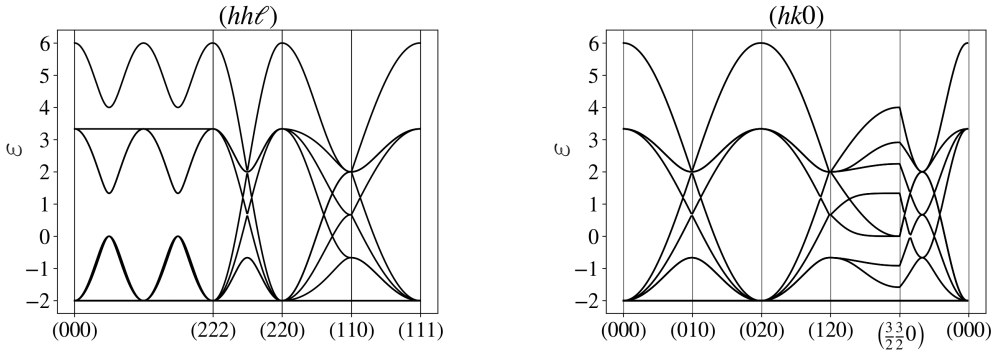


Figure 6.1: Interaction matrix energy bands of the Heisenberg and DM model with $J_{\mathrm{DM}}/J = 2$ plotted along high-symmetry paths in the $(hh\ell)$ (a) and $(hk0)$ (b) planes. We refer the reader to Appendix C for more details of the high-symmetry paths chosen.

As seen in Chapter 4, a MC study does not find any signal of a magnetically ordered

[1]Since the two T_1 irreps are degenerate, any linearly independent basis of composed by these two irreps is a valid irrep mode for this model.

[2]As a consequence, an effective theory of this Hamiltonian should not mix the local z and local xy irreps.

[3]This naming is used to follow the results in Chapters 4 and 5 where the parametrization (4.4) is used.

phase which can be taken as the possible realization of a strongly correlated paramagnet, i.e. a spin-liquid. A similar scenario is found for the pure Heisenberg antiferromagnet ($\{J, J_{\mathrm{DM}}\} = \{J, 0\}$, $J > 0$ in Eq. (6.1).) where the A_2, E, $T_{1\perp}$, and T_2 irreps are energy degenerate [74], see Fig. 4.2 for $\theta = 0°$. The degeneracy of these modes is reflected in the bands of the Heisenberg antiferromagnet interaction matrix which present six degenerate low-energy flat bands and therefore an extensively degenerate ground state manifold. The extensive degeneracy of the ground state manifold of the Heisenberg antiferromagnet model ultimately results in the avoidance of LRO and a classical spin-liquid [43, 74, 101]. In Subsection 2.3.3, we showed how this model showcases an emergent divergent-free constraint [43, 143] which translates in the observation of twofold pinch point features in the Fourier space correlation functions, see Fig. 2.10. As in the Heisenberg antiferromagnet, the $J_{\mathrm{DM}}/J = 2$ model has four low-energy flat bands in the spectrum of its interaction matrix, see Fig. 6.1, which presumably results in the avoidance or LRO. As a first approximation to study the $J_{\mathrm{DM}}/J = 2$ model, we perform a SCGA to study the evolution of the Lagrange multiplier λ and the correlations functions as a function of temperature.

6.2 Anisotropic Features in the Neutron Scattering Structure Factor

The similarity between the Heisenberg antiferromagnet and the $J_{\mathrm{DM}}/J = 2$ model suggests that the methods used for the description of the Heisenberg antiferromagnet can also be used to analyze the $J_{\mathrm{DM}}/J = 2$ model. We therefore use the SCGA, a method widely used when studying spin-liquids [3, 42, 104], to study the evolution of the Lagrange multiplier λ and the neutron structure factor of the $J_{\mathrm{DM}}/J = 2$ model. Figure 6.2 shows the evolution of the Lagrange multiplier λ as a function of temperature. As can be seen, the Lagrange multiplier plateaus to 1 at low temperatures.

As discussed in Subsection 3.1.1, this value should be expected as it reflects the fraction of degenerate low-energy flat bands: for four low energy flat bands, λ should go to $\lambda_0 = 3\left(\frac{4}{12}\right) = 1$. Using the values identified for λ we can now compute the neutron structure factor

$$S^{\perp}(\boldsymbol{q}) = \sum_{\alpha,\gamma}\sum_{\boldsymbol{q}}\left(\delta^{\alpha\gamma} - \frac{q^{\alpha}q^{\gamma}}{|\boldsymbol{q}|^2}\right)\left(\beta J_{ab}^{\alpha\gamma}(\boldsymbol{q}) + \lambda\right)^{-1}, \tag{6.2}$$

where β is the inverse temperature and $J_{ab}^{\alpha\gamma}$ is the interaction matrix of the $J_{\mathrm{DM}}/J = 2$ model. We refer the reader to Section 3.1 for more details in the derivation of the above expression. Although in principle the quadrupolar degrees of freedom would not

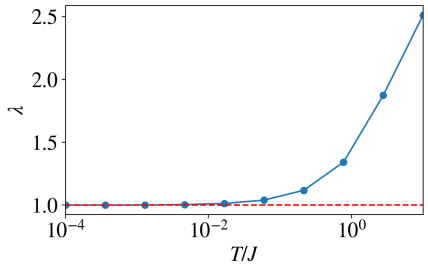


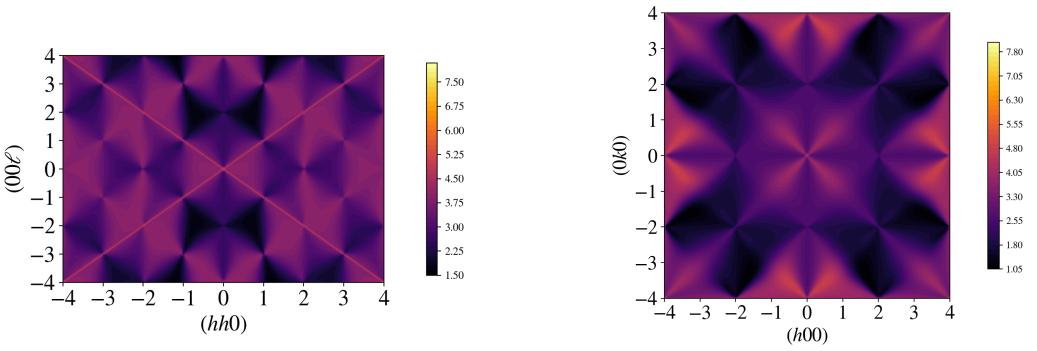
Figure 6.2: Lagrange multiplier λ obtained for the $J_{\rm DM}/J = 2$ model.

be observed in an experiment for the values of $\boldsymbol{q}$ considered[4], here we present the *full* neutron structure factor where both local xy and z degrees of freedom are included in the calculation. The full neutron structure factor in the $(hh\ell)$ and $(hk0)$ scattering planes is shown in Fig. 6.3(a) and (b) respectively for the lowest temperature used in Fig. 6.2[5]. The resulting correlation functions show a multitude of anisotropic features: in the $(hh\ell)$ plane in Fig. 6.3(a) twofold pinch points (at the points $(hh\ell) = [220], [222], [002]$ and other symmetry related points) and a continuous line of scattering intensity along the [111] direction is observed. On the other hand, the neutron scattering in the $(hk0)$ plane in Fig. 6.3(b) shows *fourfold* pinch points at $(hk0) = [000]$. It is worthwhile noting that if we had only considered the local z degrees of freedom, a spin-ice neutron structure factor is observed with roughly the same temperature dependence as the one obtained for the nearest-neighbor Ising antiferromagnet.

Similar anisotropic features, i.e. the continuous line of scattering, and the twofold and fourfold pinch points, have been previously observed in other spin-liquids: in Ref. [107] twofold pinch points and a continuous line of scattering was observed while in Ref. [108] twofold and fourfold pinch points where observed. The observation of all of these anisotropic features has been related to *emergent* field theories where the twofold pinch points describes an emergent divergent-free constraint in vector fields [143], while the fourfold pinch points and the continuous line of scattering have been related to emergent rank-2 theories [107, 108]. Interestingly, the observation of fourfold pinch points has also been related to the realization of *fractons* as line-like excitations which are confined to move in a single direction [145–147].

[4]Effectively, this would equate in modifying the expression in Eq. (6.2) such that only the local z degrees of freedom are considered [144].

[5]Click on the respective scattering plane for an animation of the evolution of the neutron structure factor as a function of temperature, $(hh\ell)$ or $(hk0)$.



(a) $(hh\ell)$ plane (b) $(hk0)$ plane

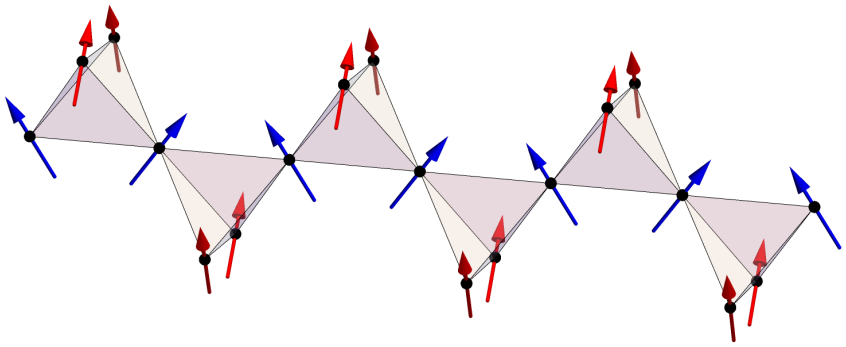
Figure 6.3: Neutron structure factor for the $J_{\rm DM}/J = 2$ model in the $(hh\ell)$ (a) and $(hk0)$ (b) planes obtained using a SCGA.

Although we currently do not have a long-wavelength theory at hand, we can assess the possibility of fracton excitations in this model. To do so, we first have to consider which are the possible ground state configurations allowed of the $J_{\rm DM}/J = 2$ model. The construction of these configurations can be performed by employing the so-called *lego-brick* rules introduced in Ref. [74] where the low-energy irrep modes can be used to tile the pyrochlore lattice. The low-energy irreps for $J_{\rm DM}/J = 2$ model are the $T_1^{\rm Ice}$, T_1^{xy}, and the E (i.e. ψ_2 and ψ_3) irreps, see Fig. 2.7 and Fig. 2.8 for the spin configurations associated with these irreps.

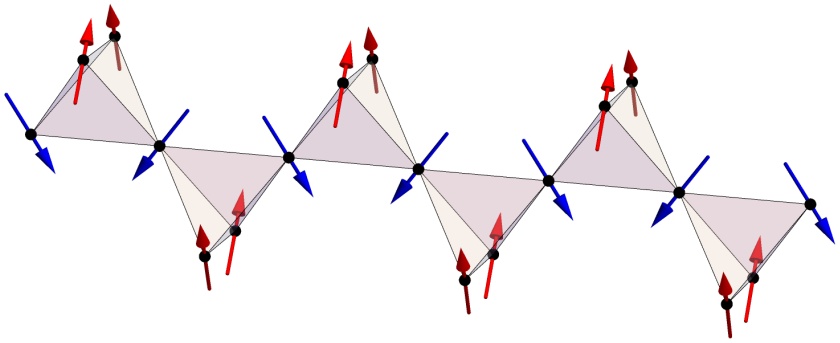
First, we can consider the $\boldsymbol{q} = 0$ ground state configurations. Clearly, these are constructed by considering all the up tetrahedra in the same configuration, i.e. a T_1^{xy}, E, or a $T_1^{\rm Ice}$ irrep mode. Additionally, using combinations of these irreps, other $\boldsymbol{q} = 0$ spin configuration can be constructed where now the spins in a single tetrahedron are described by a combination of irreps similar to the one given in Eq. (4.17) described in Chapter 4. In terms of the $\boldsymbol{q} \neq 0$ modes, the use of the $T_1^{\rm Ice}$ irrep implies that all the spin-ice states[6] are valid ground state configurations for the $J_{\rm DM}/J = 2$ model. Interestingly, we can also construct non-$\boldsymbol{q} = \boldsymbol{0}$ states where the spins in each tetrahedra are described by the T_1^{xy} or the E irrep mode. The construction of these states is as follows: consider a $\boldsymbol{q} = \boldsymbol{0}$ state where all tetrahedra are described by a T_1^{xy} irrep and focus on an infinite *chain* of tetrahedra, see Fig. 6.4(a). Note that flipping all the spins along the chain[7], i.e. the blue

[6] This takes into account $\boldsymbol{q} = 0$ and non-$\boldsymbol{q} = 0$ states.

[7] In other words $\boldsymbol{S}_i \to -\boldsymbol{S}_i$.



(a) T_1^{xy}



(b) ψ_2

Figure 6.4: Chain of tetrahedra where each tetrahedron is in a T_1^{xy} (a) and ψ_2 (b) configuration. Note that the two configurations only differ by the flipping of blue spins.

spins in Fig. 6.4(a), has the effect of swapping the T_1^{xy} spin configuration for the ψ_2 spin configuration, see Fig. 6.4(b). The same chain-flipping procedure can be applied to other chains in the system such that the spins in the each tetrahedra always end up in a ψ_2 or T_1^{xy} configuration[8]. This construction leads to a sub-extensive set of possible states given by all possible combinations of the selected flipped spin chains[9].

The appearance of fracton excitation in this system is related to the chain-flipping construction: in order to avoid any excitations the chain of spins cannot have end-points

[8]Note that this is *not* possible for the ψ_3 in the $J_{\mathrm{DM}}/J = 2$ model.

[9]For example, starting from a $\boldsymbol{q} = \boldsymbol{0}$ T_1^{xy} (ψ_2), we would have to choose two chains out of the $O(L^2)$ chains to flip. This means that there are $(L^2)(L^2-1)/2$ possible states that we can generate. From the above statement, it is easy to see that the number of xy states that can be obtained starting from a single $\boldsymbol{q} = 0$ configuration would be given by $\sum_n^{2L^2} \binom{2L^2}{n} = 2^{2L^2}$.

since the tetrahedra at these end-points would have spin configurations which are not described by the E, T_1^{xy}, or T_1^{Ice} irreps, or a combination of these. Once a chain has two end-points the energy cost of such excitation is *independent* of the length of the chain as long as the end-points remain in the *same* chain of spins where only two tetrahedra are affected[10]. This implies that once a finite chain is generated, the end-points of this chain can freely move in the 1-dimensional path described by the chain. We believe that the end-points of these chain are the fractons which are presumably related to the observation of the fourfold pinch points in the neutron scattering correlation function, see Fig. 6.3(b). Moreover, note that in this construction we have only used the xy irreps. Since the xy degrees of freedom are quadrupolar, the fracton excitations identified are quadrupolar as well. As previously mentioned, to make this argument more precise, an effective long wavelength low-temperature theory should be developed. The construction of such theory is left for future work.

6.3 Monte Carlo: An Order-by-Disorder-Selected Spin-Liquid

After having used the SCGA to study the neutron structure factor for the $J_{\text{DM}}/J = 2$ model, we now apply classical MC to study how these correlation functions evolve as a function of temperature, and check if these agree with what is predicted by SCGA. For the $J_{\text{DM}}/J = 2$ model we considered a system of $N = 4 \times L^3$ spins with $L = 10$, averaged the quantities measured in 500 independent MC simulations, and used $N_{\text{meas}} \sim 10^5$, see Section 3.6. The energy per spin and the specific heat measured with MC are shown in Fig. 6.5. As can be seen in Fig. 6.5, the energy of the $J_{\text{DM}}/J = 2$ model evolves smoothly down to the lowest temperatures where it plateaus to the value $E/J = -3$, as expected from the irrep analysis (see Eq. (3.49)-(3.54)). On the other hand, the specific heat $C = dE/dT$ develops a small bump at $T^*/J \sim 10^{-2}$. Interestingly, a similar bump in the specific heat is seen in spin-ice [48] signaling the thermal depletion of the population of magnetic monopoles, see Section 2.2. Note that at low temperatures, the value of the specific heat plateaus to $C \sim 7/8 = 0.875$ and not 1 as expected from the equipartition theorem, see for example Fig. 5.11. Following [43, 148], the low temperature value of the specific heat implies that the low-energy fluctuations in the ground state result in an effective theory where quadratic and quartic modes are obtained. We have studied the evolution of the specific heat as a function of temperature and systems size, shown in Fig. 6.6, to discard

[10] For another chain would create an additional defect, i.e. three defects instead of two in a single chain.

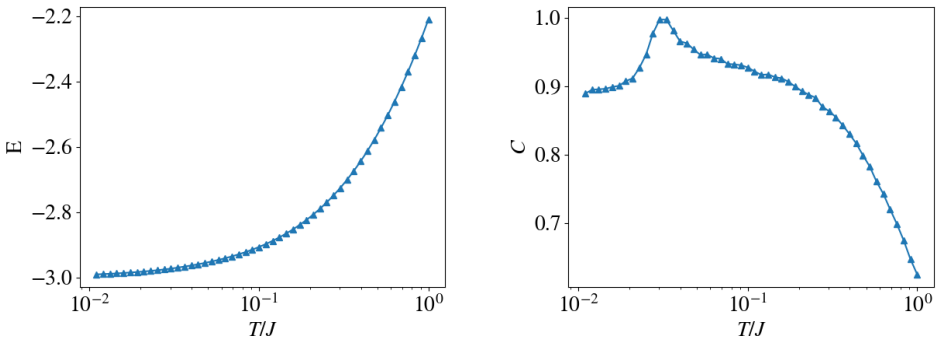


Figure 6.5: Energy (left) and specific heat (right) obtained through MC for the $J_{\mathrm{DM}}/J = 2$ model. We label the temperature at maximum of the specific heat as T^*. Both functions were obtained for a system size $L = 10$.

the possibility that this bump would signal a first order transition in the thermodynamic limit.

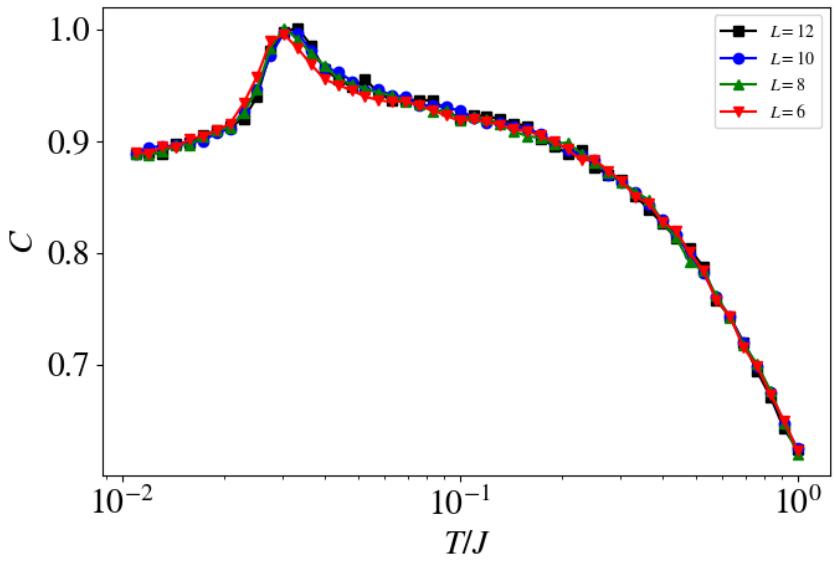


Figure 6.6: Specific heat measured for the $J_{\mathrm{DM}}/J = 2$ model for various systems sizes L. Note that the specific heat bump centered at T^* does not sharpen as L is increased.

To gain some insights on what the bump in the specific heat signals, we study the full[11] neutron structure factors for the $(hh\ell)$ and $(hk0)$ planes obtained through MC for two temperatures, one above and one below T^*. Additionally, we compare these structure factors with the ones obtained using SCGA in Fig. 6.3. Figure 6.7(a) shows the neutron structure factor for both scattering planes at a temperature above T^*. For this temperature, we find a good agreement between these results from MC and the ones predicted by SCGA in Fig. 6.3. The only noticeable difference between the two figures is the high intensity at $\boldsymbol{q} = \boldsymbol{0}$ observed in MC. However, this feature can be obtained by the SCGA when increasing the temperature[12]. In contrast, and perhaps more interesting, the structure factors obtained by MC *below* T^* are radically different to what is observed *above* T^*, see Fig. 6.7(a) and (b): the structure factor below T^* no longer exhibits the continuous intensity lines observed in the $(hh\ell)$ plane nor the fourfold pinch points in the $(hk0)$ plane. Instead, this structure factor only exhibits twofold pinch points. Remarkably, the neutron structure factor in Fig. 6.7(b) resembles the structure factor that found for spin-ice at low temperatures, see Fig. 2.4. This similarity is somewhat unexpected as the Ising nearest-neighbor antiferromagnetic Hamiltonian discussed in Section 2.2 considers Ising spins whereas the $J_{\mathrm{DM}}/J = 2$ model considers Heisenberg spins. However, the irrep analysis identified T_1^{Ice} as one of the low-energy modes where all the spins are constrained to their local z degrees of freedom, similar to the Ising case. The observation of a spin-ice structure factor would then point to the possibility of having the spins in every tetrahedra in a two-in-two-out configuration, i.e. a T_1^{Ice} configuration. In other words, as the temperature is lowered we might expect the spins to adopt a T_1^{Ice} configuration in all tetrahedra.

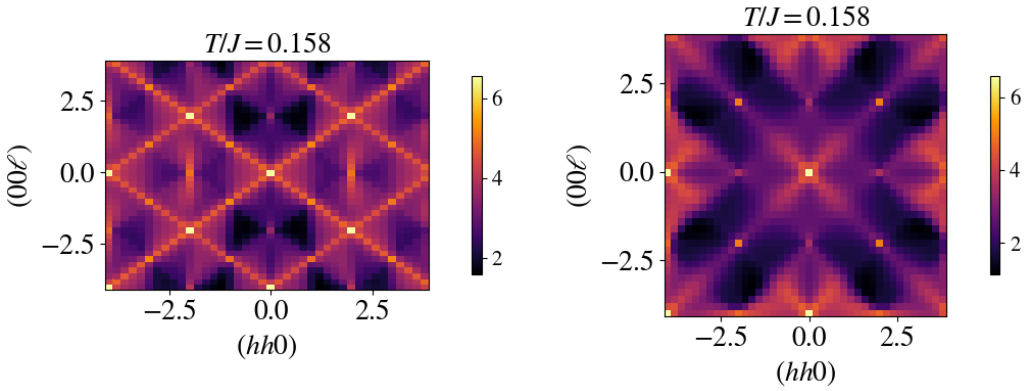
Naively, to study the onset of a spin-ice phase, we can take the same approach as in Chapters 4 and 5 where we study the onset of an irrep mode by studying the m_I parameter where I denotes the corresponding irrep, see Eq. (4.19). These parameters however assume a $\boldsymbol{q} = \boldsymbol{0}$ configuration. Since the spin-ice states are generally not $\boldsymbol{q} = \boldsymbol{0}$ configurations[13] the $m_{T_1^{\mathrm{Ice}}}$ parameter is not well suited to signal such a phase. Instead, to explore wheter the spins are adopting a T_1^{Ice} configuration, we study their projection onto their local z axis

$$P^z_{\mathrm{local}} = \left\langle \frac{1}{N} \sum_i \left(\boldsymbol{z}_i \cdot \boldsymbol{S}_i \right)^2 \right\rangle . \tag{6.3}$$

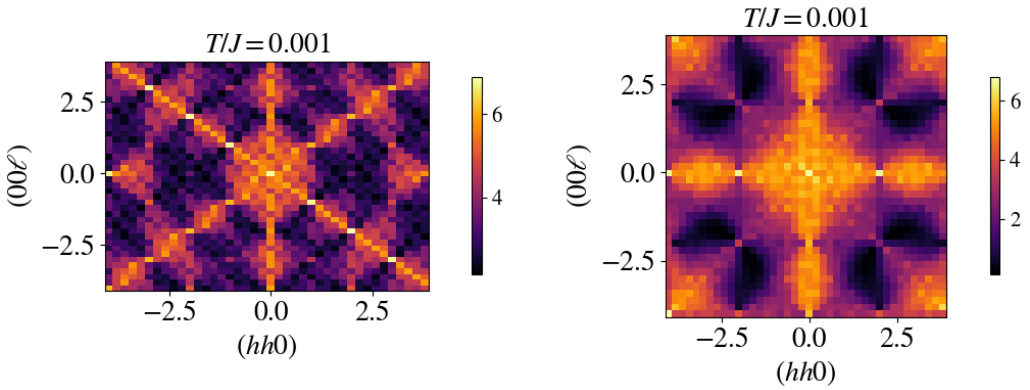
[11] Recall that this means that we are taking into account all spin degrees of freedom when computing these correlation functions.

[12] Check $(hh\ell)$ for the evolution of the neutron structure factor as predicted by the SCGA. Here the high intensity at $\boldsymbol{q} = \boldsymbol{0}$ is observed.

[13] The only $\boldsymbol{q} = \boldsymbol{0}$ spin-ice states are the ones which replicate the same two-in-two-out configuration through the lattice.



(a) $T > T^*$



(b) $T < T^*$

Figure 6.7: Neutron structure factors for the $J_{\mathrm{DM}}/J = 2$ model above (a) and below (b) the temperature T^*. In each panel the left plot corresponds to the $(hh\ell)$ plane and the right plot to the $(hk0)$ plane. These structure factors were obtained for a system size $L = 10$.

In terms of the irreps, this projection measures the "amount" of A_2 and T_1^{Ice} configurations. However, since the A_2 irrep (i.e. AIAO) has a higher energy than the T_1^{Ice} configurations (see Fig. 4.2 at $\theta = 243°$) and at low temperatures, the spins avoid these high energy modes[14], the projection in Eq. (6.3) can thus be taken as a measure of the T_1^{Ice} configurations only.

Figure 6.8 shows the temperature evolution of the P^z_{local}. At high temperatures, this

[14]We have additionally check that the m_{A_2} parameter vanishes as the temperature is progressively lowered (not shown).

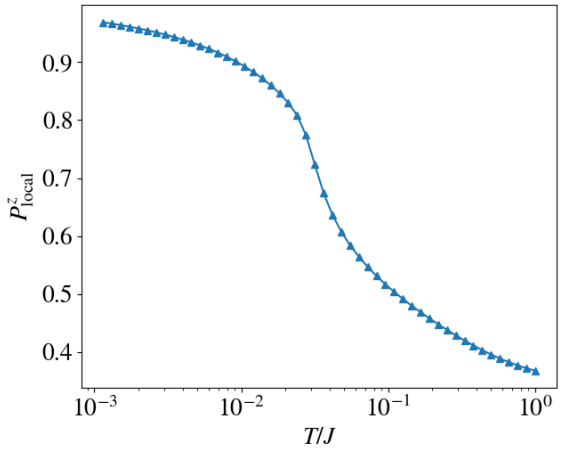


Figure 6.8: P^z_{local} projection as a function of temperature measured through MC for an $L = 10$ system.

projection acquires an approximate value of $P^z_{\text{local}} \sim 1/3$ as expected for a fully paramagnetic system where the spins are free to fluctuate in all directions. As the temperature is decreased, the P^z_{local} projection rapidly increases around $T \sim T^*$ and plateaus to 1 as $T \to 0$. The evolution of P^z_{local} suggests that the low temperature phase below T^* is in fact a spin-ice phase. Interestingly, this phase *is not* predicted by the irrep analysis or SCGA. Therefore, we may ask what is exact mechanism which causes the selection of the spin-ice states. Alternatively, since the irrep analysis and the SCGA do not predict this phase, we may ask what are the approximations leading to their failure. A common feature of both approaches is that both the irrep analysis and SCGA are somewhat build to only describe the quadratic modes of the spins. For example, in Chapter 3, we mentioned that the SCGA is not well suited to capture ObD which typically considers higher order terms in a free-energy description, see Chapters 4 and 5 for the discussion of the m_{E6} and cubic parameters. A similar scenario is realized for the irrep analysis which only identifies the modes used in a quadratic Landau theory. Therefore, the failure of these two methods at low temperatures suggests that there are higher order terms in the free-energy theory affecting the MC simulations and resulting in the selection of the spin-ice manifold. Since the selection of the ground state configuration produced by the higher order terms in the free-energy theory in Chapters 4 and 5 is entropic, we may inquire whether the selection of the ice states may have an entropic origin. In fact, when describing the possible ground state configurations, we stated that the spin-ice manifold is *extensively degenerate*. The extensive degeneracy of the spin-ice states might be associated with an increasing entropy

resulting in the selection of these states. To assess this, we could perform a CLTE to measure the entropic weight associated to different ground state configurations, similar to what was done in Chapters 4 and 5 for the E and the colinear ferromagnet states. This calculation would then yield a higher entropic weight for the spin-ice states over all other configurations in the ground state manifold. However, the exact calculation and implementation of this calculation goes beyond the scope of this thesis and will be performed in future work.

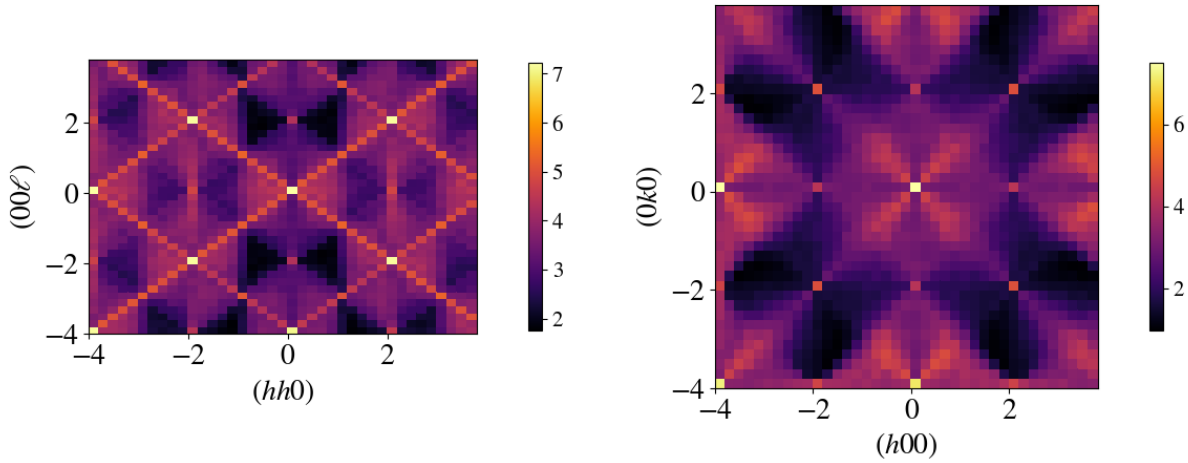


Figure 6.9: Neutron structure factors in the $(hh\ell)$ (left) and $(hk0)$ (right) obtained using IM for a system of size $L = 10$ and $N_{\text{meas}} = 1000$.

Even though with the current state of the methods used in this thesis we cannot produce a direct measurement of entropy $\mathcal{S}$, and consequently the free energy $\mathcal{F} = E - T\mathcal{S}$, we can produce an indirect proof of this selection by considering how the structure factor would look like for $T = 0$[15]. In other words, if the selection of the spin-ice states has an entropic origin, a method which explicitly excludes these effects could in principle shed some light on what the selection mechanism is. We therefore apply iterative minimization (IM) to this model and study the neutron structure factors obtained for the $(hh\ell)$ and $(hk0)$ scattering planes, see Fig. 6.9. Remarkably, the $T = 0$ predictions obtained with IM agree with what is seen in MC *above* T^*, and therefore what was predicted by the SCGA, see Fig. 6.3 and Fig. 6.7. The disagreement between MC and IM at low temperatures alludes to an entropic mechanism, similar to ObD, as the culprit behind the selection of the spin-ice states. In

[15] A possible way of studying the evolution of the entropy would be to use the Lee-Kosterlitz method[149].

other words, the spin-ice spin-liquid in the $J_{\mathrm{DM}}/J = 2$ model can be understood as an order-by-disorder-selected spin-liquid. In the next subsection, we study the spin-ice phase observed in this model and contrast the thermodynamic quantities measured in this phase with those obtained for a spin-ice phase in an Ising system.

6.3.1 The Spin-Ice Phase in the $J_{\mathrm{DM}}/J = 2$ Model

Although the neutron structure factor and the evolution of the projection P^z_{local} seem to point to the realization of a spin-ice phase similar to what is observed in an Ising system, we need to be cautious when comparing the physics observed in both models. For instance, the specific heat C in the spin-ice phase of the Ising model goes to zero [48] whereas in the $J_{\mathrm{DM}}/J = 2$ model it goes to a constant as previously pointed out, see Fig. 6.5. This difference originates from the nature of the spin degrees of freedom: in the $J_{\mathrm{DM}}/J = 2$ model these are Heisenberg spins and not Ising. Despite this fundamental difference, we could ask what other thermodynamic quantities might be similar for these two models. Given that the neutron structure factor of both models seem to agree, a natural starting point for this question is what *other* correlation functions of the $J_{\mathrm{DM}}/J = 2$ model may display a similar pattern to the one observed for an Ising system. Answering this question is of fundamental interest as the unique features observed in other correlation function may guide us in the identification of an effective model realized at low temperatures for the $J_{\mathrm{DM}}/J = 2$ model. For example, the polarized neutron scattering for the spin-ice phase for the nearest-neighbor Ising model is radically different to the one observed the dipolar spin-ice: in the first, the non-spin-flip channel is featureless whereas in the second a strong modulation can be seen [3, 30]. We therefore compute the neutron structure factor non-spin-flip (NSF) channel, defined as

$$S^{\mathrm{NSF}}(\boldsymbol{q}) = \sum_{\alpha,\gamma} \sum_{a,b} \left(S^{\alpha}_{a}(-\boldsymbol{q}) S^{\gamma}_{b}(\boldsymbol{q})\right) \left(\hat{z}^{\alpha}_{s} \hat{z}^{\gamma}_{s}\right), \tag{6.4}$$

and the spin-flip (SF) channel, defined as $S^{\perp}(\boldsymbol{q}) - S^{\mathrm{NSF}}(\boldsymbol{q})$, referring the reader to Appendix B for more details about these correlation functions. In Fig. 6.10, we illustrate the polarized neutron structure factors for the the $J_{\mathrm{DM}}/J = 2$ model below T^*.

In both scattering planes, the SF channel display the typical pinch point features observed in the spin-ice phase [3]. On the other hand, in the NSF channel of the $(hk0)$ plane twofold pinch points can be observed while the $(hh\ell)$ plane seems to have a slight modulation. This modulation however may be related to the thermalization procedure performed in the MC simulations therefore limiting the analysis that we can perform. Our statistics

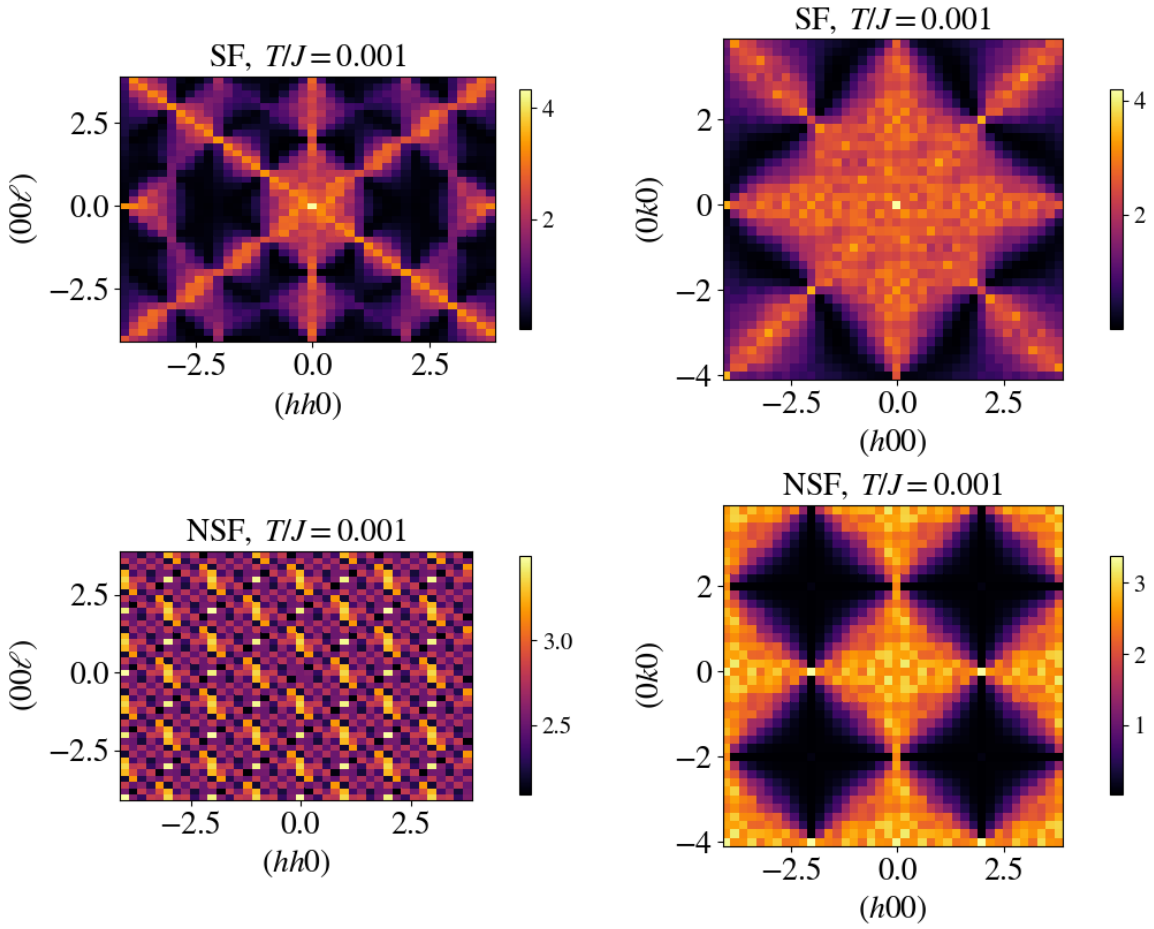


Figure 6.10: Polarized neutron structure factors in the $(hh\ell)$ (left column) and $(hk0)$ (right column) obtained using MC for a system of size $L = 10$.

however allow us to study the average value of the NSF in the $(hh\ell)$ plane, $\langle S^{\mathrm{NSF}}\rangle_{\boldsymbol{q}}$[16], and its behavior as a function of temperature, see Fig. 6.11. As can be seen, at low temperatures, the average plateaus to the value $\langle S^{\mathrm{NSF}}\rangle_{\boldsymbol{q}} = 8/3 \sim 2.66$. This value corresponds to what is predicted for the featureless NSF realized in the nearest-neighbor Ising model at low temperatures [3]. Although this observation suggests that the effective model at low temperatures is the nearest-neighbor antiferromagnetic Ising model, further investigation is needed to provide a more robust identification. Improving the current statistics and

[16]This is simply an uniform average of the intensity of all the $\boldsymbol{q}$ values measured.

thermalization may require the development of a different update algorithm suited to access different spin-ice configurations efficiently in a Heisenberg system [150–152]. Although we have not implemented such loop-like algorithm yet, we have slightly avoided this issue by increasing the number of independent MC simulations used in the implementation of the valley average method discussed in Section 3.6.

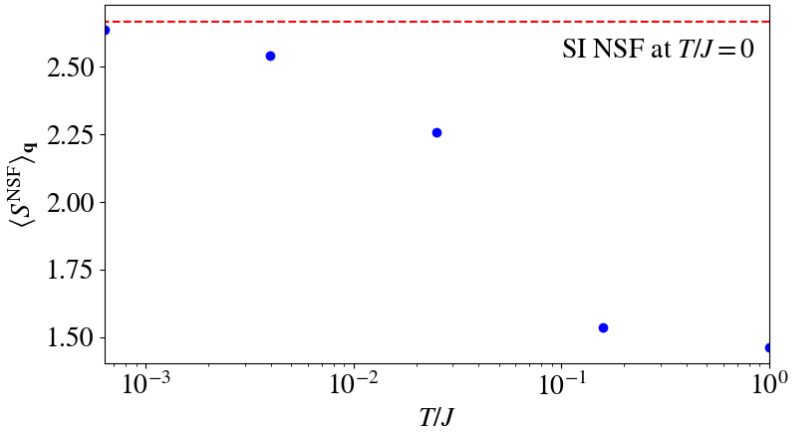


Figure 6.11: Average value of the NSF channel in the $(hh\ell)$ plane as a function of temperature. Here the lower three temperatures are below T^*, and the red dashed line marks the value predicted for the flat NSF for the spin-ice phase observed in the nearest-neighbor Ising Hamiltonian [3].

6.4 Non-Kramers Spin Systems

At the beginning of this chapter we mentioned that in terms of the local interaction parameters $\{J_{zz}, J_{\pm}, J_{\pm\pm}, J_{z\pm}\}$ the $J_{\mathrm{DM}}/J = 2$ model has a zero $J_{z\pm}$ coupling[17] which effectively identifies this Hamiltonian as a non-Kramers Hamiltonian, see Section 2.1. The non-Kramers Hamiltonian has been extensively studied by both quantum and classical methods where four phases have been identified: three of which are quadrupolar and one dipolar [4, 60, 153–155]. Classically, in terms of the irreps, the quadrupolar phases are

[17] Assuming $J = 1$ and $J_{\mathrm{DM}} = -2$ in the Hamiltonain (6.1) leads to the local interaction couplings $\{J_{zz}, J_{\pm}, J_{\pm\pm}, J_{z\pm}\} = \{3, 1/2, -1, 0\}$, or equivalently $\{J_{zz}/J_{zz}, J_{\pm}/J_{zz}, J_{\pm\pm}/J_{zz}, J_{z\pm}J_{zz}\} = \{1, 1/6, -1/3, 0\}$.

described by the E, T_2, and T_1^{xy} spin configurations while the dipolar phase is described by the T_1^{Ice}, see Fig. 6.12. In this diagram, the only $\boldsymbol{q} \neq 0$ predicted phase is the yellow phase which denotes a spin-ice phase.

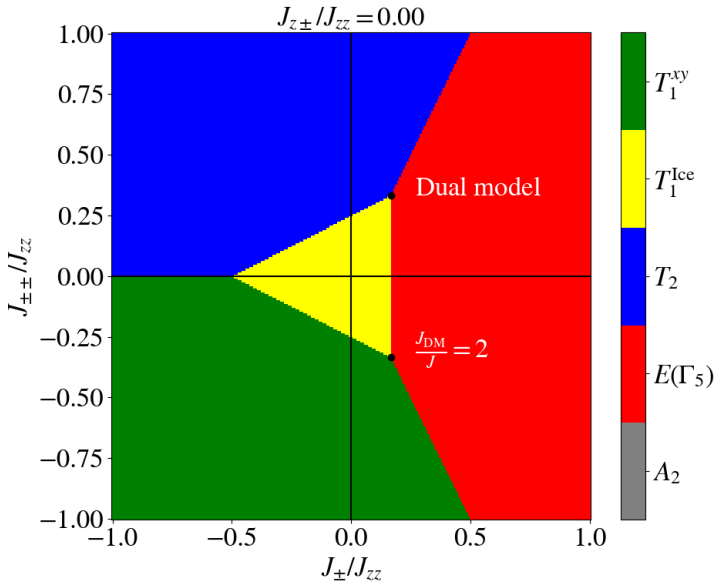


Figure 6.12: Classical phase diagram obtained using an irrep analysis. This phase diagram agrees to the one reported by Ref. [4]. Here the lower black dot represents the $J_{\text{DM}}/J = 2$ model and the upper black dot the dual model.

Incidentally, in the phase diagram in Fig. 6.12 the $J_{\text{DM}}/J = 2$ model falls at a point where three phases meet: the T_1^{xy},the E, and the T_1^{Ice}. We may therefore ask which other points in this phase diagram may correspond to systems where strong competition results in the avoidance of a magnetically ordered phase at low temperatures and possibly the identification of novel spin-liquids as the one identified for the $J_{\text{DM}}/J = 2$ model. A natural starting pointing in the search for such model are the two other points where three phases meet, i.e. the corners of the yellow phase in Fig. 6.12. In fact, the left-most point for which $J_{\pm\pm} = 0$ was studied by Ref. [4] labeling this point as a pseudo-Heisenberg antiferromagnetic phase. The reasoning behind this name is that this model can be transformed into a Heisenberg antiferromagnet by a local rotation in the xy degrees of freedom [4]. In contrast, the model for the interaction parameters in the upper corner of the yellow region has not been characterized. The Hamiltonian described by this point however is *dual* to the $J_{\text{DM}}/J = 2$ model and may be obtained by the transformation in the pseudo-spin operators $\hat{S}_i^{\pm} \to \pm i\hat{S}_i^{\pm}$. In terms of the spin components this transformation translates

into a local rotation in the xy degrees of freedom, which effectively changes the sign of the $J_{\pm\pm}$ coupling. In terms of the irreps, this rotation has the effect of swapping the T_1^{xy} irrep by the T_2 irrep, and the components of the E irrep, i.e. $\psi_2 \leftrightarrow \psi_3$[18]. This point, which we label as a dual model to the $J_{\rm DM}/J = 2$ model, should have an equivalent thermodynamic behavior to the $J_{\rm DM}/J = 2$[19] model therefore exhibiting the same thermodynamic results as the one presented in Fig. 6.5, which we have checked using MC (not shown). However, other quantities as the neutron structure factors in a given scattering plane may change as the low energy modes of the model change under the local transformation. At low temperatures below T^*, the dual model also presents a spin-ice phase with the same structure factors as observed for the $J_{\rm DM}/J = 2$ model in Fig. 6.7(b). However, the neutron structure factor of the dual model *above* T^* does not agree with the one obtained for the $J_{\rm DM}/J = 2$ model, see Fig. 6.13.

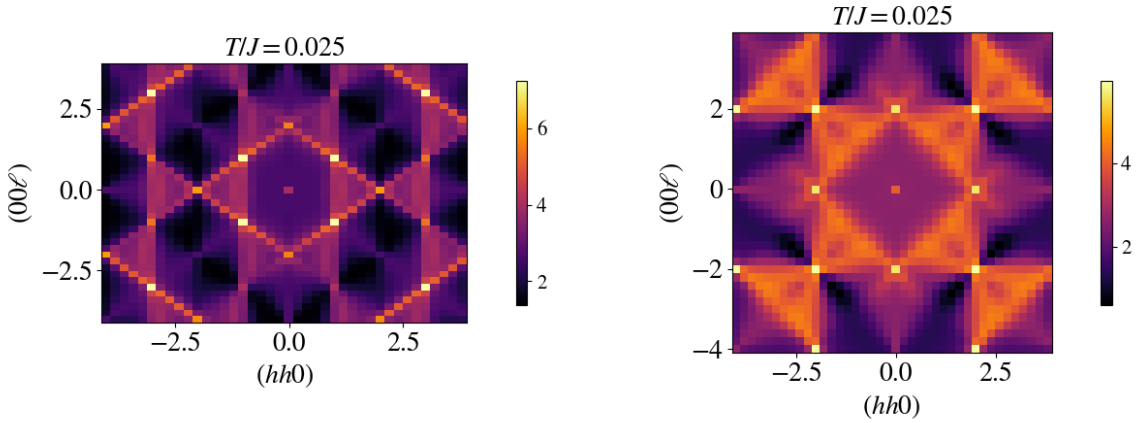


Figure 6.13: Neutron structure factors for the dual model below the temperature T^*.The left plot corresponds to the $(hh\ell)$ plane and the right plot to the $(hk0)$ plane. These structure factors were obtained for a system size $L = 10$.

The similarity at low temperature and disagreement at high temperatures can be understood by the local transformation $\hat{S}_i^{\pm} \to \pm i\hat{S}_i^{\pm}$: since only the local xy degrees of freedom are affected, the structure factor below T^* should be the same as it is generated by spin-ice

[18]This symmetry is observed in the phase diagram in Fig. 6.12 which only swaps the PC phase with the T_1^{xy} phase.

[19]For the dual model, the low-energy irreps are the E, $T_1^{\rm Ice}$, and T_2. Consequently, the ground state configurations constructed for this model with the chain-flipping argument are now build using ψ_3 and PC configurations instead of ψ_2 and T_1^{xy} configurations as shown in Fig. 6.4.

configurations with *only* local z components whereas the structure factor above T^* differs as xy configurations also contribute.

6.5 Conclusion and Outlook

In this chapter, we have studied the $J_{\mathrm{DM}}/J = 2$ model where no magnetic ordered phase is detected down to the lowest temperatures considered. To characterize this phase we applied a variety of analytical and numerical techniques which allowed us to identify a crossover temperature T^* which separates two distinct spin-liquid phases. The correlation function for both spin-liquids were studied, finding that above T^*, anisotropic features such as continuous intensity lines, twofold and fourfold pinch points are observed. In contrast, the spin-liquid below T^* only exhibits twofold pinch points. The similarity between the correlation function of the spin-liquid below T^* with the one observed for a spin-ice system lead us to identify this phase as a spin-ice spin-liquid. Our results suggest that the low temperature spin-ice spin-liquid is selected by an entropic mechanism. To confirm this statement, a study of the entropic weight associated with the spin-ice states will have to be performed. Additionally, the development of a loop algorithm for Heisenberg spin models to improve the statistics obtained in our current MC implementation may shed light in the low-temperature physics of this model and the possibility of an effective low-temperature model. Although the results presented in this chapter only make reference to the classical case, quantum simulations done with PFFRG performed by the group of Johannes Reuther[20] seem to also indicate a spin-liquid phase for interaction parameters close to the ones used in this chapter. The characterization of the novel spin-liquid realized in the $J_{\mathrm{DM}}/J = 2$ model increases the interest in non-Kramers pyrochlores where other novel low-temperature phases may be realized. Our work therefore motivates further analysis of non-Kramers magnetic pyrochlores, their phase diagram, and the anisotropic features observed in their neutron scattering correlation functions [155–160].

[20] Reuther's group webpage.

Chapter 7

Theory of Fragmentation

A common theme in Chapters 4, 5, and 6 is how strong competition between different magnetic orders may lead to phenomena such as ObD and the realization of a spin-liquid phase. Moreover, in Chapter 5, we observed a cascade of reorientations of the total magnetization vector in the colinear ferromagnetic phase and hinted that this may be related to the adjacent spin-liquid phase, i.e. the spin-liquid realized in the $J_{\mathrm{DM}}/J = 2$ model. In fact, since a spin-liquid is the product of strong competition, we might expect signatures of such competition in the immediate vicinity of the spin-liquid. In fact, recent work on FeF_3 [75] and $Yb_2Ti_2O_7$ [142, 161] identified anisotropic features in the spin correlation functions similar to those observed in the adjacent spin-liquid phases[1] before falling into a magnetically ordered phase. On the other hand, there has been increasing attention in dipolar-octupolar Nd-based compounds where pinch point features in the *ordered* phase have been observed [102, 162–166], a phenomenon known as fragmentation [102, 162]. Although recent work has related the observation of such features in the correlation function observed in an ordered phase to the proximate spin-liquids [107, 167], there is still no general argument or procedure which can be used to unmistakably expose such connection. In this chapter, we provide a general procedure to illustrate how the proximity to a spin-liquid phase in the pyrochlore lattice results in the observation of remnant anisotropic correlation of the spin-liquid in the adjacent ordered phases at low temperatures. We demonstrate and present this general framework for the Coulomb spin-liquid realized in the Heisenberg antiferromagnetic model and simply elucidate how it can be generalized for other spin-liquids.

[1] This being the Coulomb spin-liquid in a Heisenberg antiferromagnet [43, 143] for FeF_3, and the pinch-line-singularity spin-liquid [107] for $Yb_2Ti_2O_7$.

7.1 The Coulomb Phase in the Heisenberg Antiferromagnet

In order to study how the proximity to the Coulomb phase realized in a Heisenberg antiferromagnet may affect the correlation functions observed in an adjacent ordered phase, we first have to provide a general description of the Coulomb phase realized in the Heisenberg antiferromagnet. As discussed in Subsection 2.3.3, the Hamiltonian in the Heisenberg antiferromagnet can be expressed in the follwing way

$$\mathcal{H}_{\text{Heis}} = J \sum_{\langle ij \rangle} \boldsymbol{S}_i^T \left(\mathcal{A}_{ij} \otimes \mathbb{1}_{3\times 3} \right) \boldsymbol{S}_j, \tag{7.1}$$

$$= \frac{J}{2} \sum_{\boxtimes} \left(\sum_{i \in \boxtimes} \boldsymbol{S}_i \right)^2 + \mathcal{E}_0, \tag{7.2}$$

where $\mathcal{E}_0$ is the ground state energy, $\boxtimes$ denotes both the up and down tetrahedra in the pyrochlore lattice,$J(\mathcal{A}_{ij} \otimes \mathbb{1}_{3\times 3})$ is the interaction matrix of the Heisenberg antiferromagnetic model, $\mathcal{A}$ is the pyrochlore adjacency matrix, and $\mathbb{1}_{3\times 3}$ is the identity in three dimensions. Clearly, spin configurations with vanishing magnetic moment in every tetrahedron minimize this Hamiltonian. In fact, an irrep analysis of this model identify four degenerate minimum energy irrep modes corresponding to the A_2, E, $T_{1\perp}$, and T_2, i.e. the antiferromagnetic irrep modes. Classically, the Hamiltonian in Eq. (7.2) exhibits an extensively degenerate ground-state manifold composed of all possible antiferromagnetic configurations [43]. This degeneracy is reflected in the spectrum of the interaction matrix where six low-energy degenerate flat bands are observed, see Fig. 7.1 and Appendix C for a description of the high-symmetry paths used in this chapter.

As shown in Subsection 2.3.3, performing a transformation from spins in a single tetrahedron to charges Q^α and fluxes $\boldsymbol{B}^\alpha$ degrees of freedom defined

$$Q^\alpha = \frac{1}{2} \sum_a S_a^\alpha, \tag{7.3}$$

$$\boldsymbol{B}^\alpha = \frac{\sqrt{3}}{2} \sum_a \boldsymbol{z}_a \, S_a^\alpha, \tag{7.4}$$

allows for the construction of an effective long-wavelength theory at low temperatures where $Q^\alpha = 0$ [42], yielding

$$\mathcal{H}_{\text{Heis}} = J \sum_{\boldsymbol{q}} \sum_{\alpha} |\boldsymbol{q} \cdot \boldsymbol{B}^\alpha(\boldsymbol{q})|^2 + O(\boldsymbol{q}^4). \tag{7.5}$$

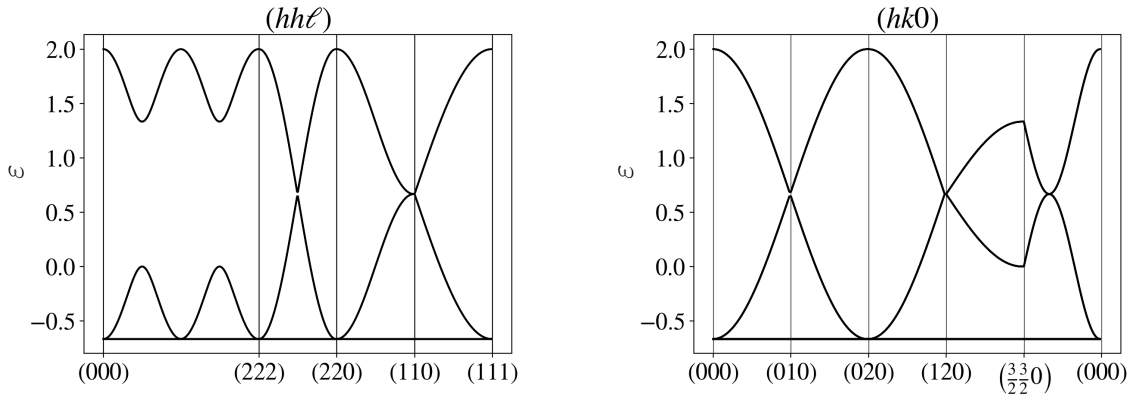


Figure 7.1: Energy bands of the interaction matrix of the Heisenberg antiferromagnet illustrated in two high-symmetry paths in the $(hh\ell)$ (a) and $(hk0)$ (b).

At low temperatures, the fluxes become transverse to $\boldsymbol{q}$, i.e. $\boldsymbol{q} \cdot \boldsymbol{B}^{\alpha} = 0$ which, in real space, translates into a divergence-free condition $\nabla \cdot \boldsymbol{B}^{\alpha} = 0$ [13, 44]. In terms of the interaction matrix, and as described in Section 2.2 and Subsection 2.3.3, the flat band modes corresponds to the fluxes which fulfill this divergence-free constraint, i.e. $\nabla \cdot \boldsymbol{B}^{\alpha} = 0$, the lowest dispersive bands correspond to the fluxes which violate this constraint, i.e. $\nabla \cdot \boldsymbol{B}^{\alpha} \neq 0$, while the dispersive upper bands to the states where magnetic charges are present, i.e. $Q^{\alpha} \neq 0$. The classification of the fluxes degrees of freedom according to the divergence-free constraint can be generally done by implementing the Helmholtz-Hodge decomposition [27, 102, 162], where a vector field $\boldsymbol{B}$ can be divided into three separate components

$$\boldsymbol{B} = \underbrace{\nabla\phi}_{\text{Irrotational}} + \underbrace{\nabla \times \boldsymbol{A}}_{\text{Rotational}} + \underbrace{\boldsymbol{H}}_{\text{Harmonic}} . \tag{7.6}$$

In the above equation, ϕ is a scalar field, and $\boldsymbol{A}$ and $\boldsymbol{H}$ are vector fields. In this decomposition, the rotational component is divergence-free, the irrotational component is curl-free and the harmonic component is both divergence- and curl-free [105]. Note that the harmonic component being both divergence- and curl-free can be though as a constant shift of the vector field $\boldsymbol{B}$. According to Eq. (7.5) and Eq. (7.6), the ground state manifold is uniquely composed of rotational fluxes which in turn result in the observation of sharp twofold pinch points in the correlation function at low temperatures [3, 42, 43], see Fig. 2.10. The Helmholtz-Hodge decomposition in Eq. (7.6) was first explicitly introduced

to pyrochlore magnetism in Ref. [27], where the spin degrees of freedom in an ordered phase are decomposed into ordered irrotational components and fluctuating rotational components. This decomposition results in the simultaneous presence of magnetic Bragg peaks and pinch point features in the neutron structure factor produced by the irrotational and rotational degrees of freedom, respectively.

Having identified the ground state manifold, we can now construct a projector into the ground state manifold, $\mathbb{P}_{\text{Rot}}$, and the excited states, $\mathbb{P}_{\text{Irrot}}$, using the eigen modes of the interaction matrix, $\{\phi_n(\boldsymbol{q})\}$[2]

$$\mathbb{P}_{\text{Rot}}(\boldsymbol{q}) \equiv \sum_{\substack{n \in \text{ flat band} \\ \boldsymbol{q}\neq 0}} \phi_n(\boldsymbol{q})\phi_n^T(\boldsymbol{q}), \tag{7.7}$$

$$\mathbb{P}_{\text{Irrot}}(\boldsymbol{q}) \equiv \sum_{\substack{n \notin \text{ flat band} \\ \boldsymbol{q}\neq 0}} \phi_n(\boldsymbol{q})\phi_n^T(\boldsymbol{q}) + \sum_{\substack{n \\ \boldsymbol{q}=0}} \phi_n(\boldsymbol{q})\phi_n^T(\boldsymbol{q}), \tag{7.8}$$

where we have chosen to include both the irrotational and harmonic space in the projection $\mathbb{P}_{\text{Irrot}}$. By construction, the addition of these projectors sums to the identity operator in spin configuration space. For a spin configuration $S_c(\boldsymbol{q}) = \frac{1}{N}\sum_i \boldsymbol{S}_i e^{i\boldsymbol{r}_i\cdot\boldsymbol{q}}$, we may construct a measure of how rotational or irrotational the configuration is by employing the rotational and irrotational projectors

$$P_{\text{Rot}} \equiv \frac{\left|\mathbb{P}_{\text{Rot}}(\boldsymbol{q})\boldsymbol{S}_c(\boldsymbol{q})\right|^2}{\left|\boldsymbol{S}_c(\boldsymbol{q})\right|^2}, \tag{7.9}$$

$$P_{\text{Irrot}} \equiv \frac{\left|\mathbb{P}_{\text{Irrot}}(\boldsymbol{q})\boldsymbol{S}_c(\boldsymbol{q})\right|^2}{\left|\boldsymbol{S}_c(\boldsymbol{q})\right|^2}, \tag{7.10}$$

where both P_{Rot} and P_{Irrot} are constrained to be positive, less than one, and the sum of the two projections is constrained to be 1, i.e. $0 \leq P_{\text{Rot}}, P_{\text{Irrot}} \leq 1$ and $P_{\text{Rot}} + P_{\text{Irrot}} = 1$. The quantity P_{Rot} (P_{Rot}) therefore measures how rotational (irrotational) a spin configuration is. As a proof of concept, we may apply these projectors to the eigen modes $\{\phi_n(\boldsymbol{q})\}$ of the interaction matrix of the Heisenberg antiferromagnetic in Eq. (7.2) and illustrate the projection by coloring the corresponding eigenvalues $\{\varepsilon_n(\boldsymbol{q})\}$, i.e. the energy bands of the interaction matrix. Figure 7.2 shows the bands of interaction matrix of the Heisenberg antiferromagnetic model colored by the irrotational projection P_{Irrot}. In this figure, a value of 1 (red) means that the eigenvector considered is fully irrotational while a value of 0 (blue) means that the eigenvector is fully rotational.

[2]Thanks to the spectral theorem, the interaction matrix of the Heisenberg antiferromagnet can be expressed as $J(\mathcal{A}_{ij} \otimes \mathbb{1}_{3\times 3}) = \sum_n \varepsilon_n \phi_n(\boldsymbol{q})\phi_n^T(\boldsymbol{q})$, where ε_n is the energy associated which each mode $\{\phi_n(\boldsymbol{q})\}$. Moreover, these modes are constructed using the eigen modes of the adjacency matrix.

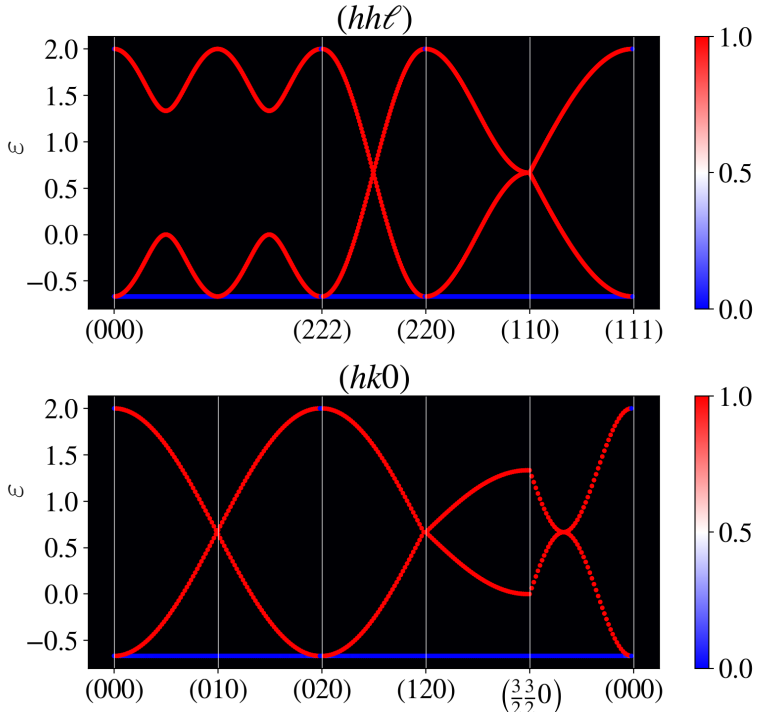


Figure 7.2: Bands of the Heisenberg antiferromagnetic model colored by the projection P_{Irrot} in a high-symmetry path in the $(hh\ell)$ (upper plot) and $(hk0)$ (lower plot) planes.

The projections P_{Irrot} can therefore be used to track the rotational modes (for which $P_{\text{Irrot}} = 0$) as the Heisenberg antiferromagnetic Hamiltonian is perturbed. In the next section, we show how the observation of twofold pinch points associated to the correlations produced by rotational modes can be exposed by the application of this projector.

7.2 The Single-Ion Anisotropy Model

In this section, we consider the Heisenberg antiferromagnetic model with a single-ion anisotropy term,

$$\mathcal{H} = J \sum_{\langle ij \rangle} \boldsymbol{S}_i \cdot \boldsymbol{S}_j + d \sum_i (\boldsymbol{z}_i \cdot \boldsymbol{S}_i)^2, \tag{7.11}$$

where we take $J > 0$, $d < 0$[3], and $|d| < J$. An irrep analysis of this model identifies the A_2 irrep, i.e. the AIAO configuration, as the lowest energy $\boldsymbol{q} = \mathbf{0}$ configuration, see Eq. (3.49)-(3.54) where $J_1 = J_2 = J$ and $J_3 = J_4 = 0$. The results presented in this section were obtained using $d/J = -0.25$. A MC study of this model for a system size $L = 10$ confirms the realization of a low-temperature ordered phase with an AIAO configuration. Moreover, a consequent study of the neutron structure factor of this model in the $(hh\ell)$ plane shows pinch-point-like features above T_c *and* below T_c underneath the magnetic Bragg peaks, as can be seen in Fig. 7.3, where some of the pinch points are marked by the white arrows.

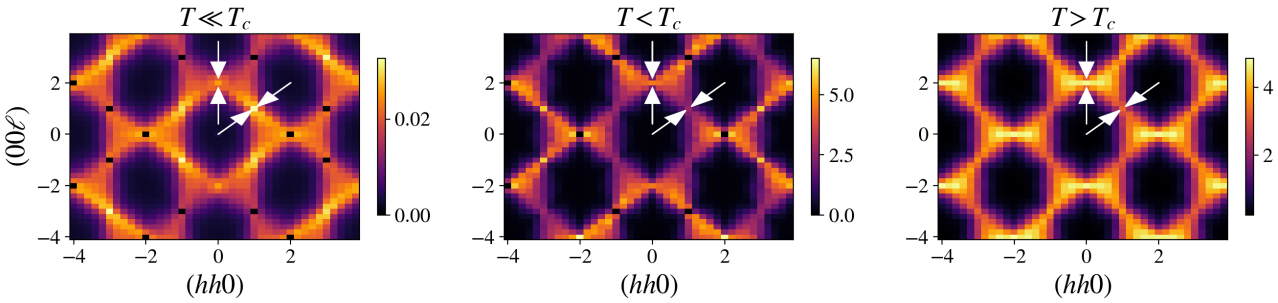


Figure 7.3: Neutron scattering in the $(hh\ell)$ plane obtained through MC simulations for a system size $L = 10$. The temperatures at which these correlation function were obtained are shown in the title of each panel. For both $T < T_c$ and $T \ll T_c$, we have removed the magnetic Bragg peaks to expose the diffuse scattering pattern.

Above T_c, the observation of these features is associated to the contribution of rotational modes before the AIAO modes become critical and the rotational modes become depopulated. In fact, a study of the interaction matrix bands of the single-ion anisotropy model illustrates how the rotational models corresponding to the flat bands observed in the Heisenberg antiferromagnetic model have been slightly shifted in energy or distorted, see Fig. 7.4 and compare it with Fig. 7.1[4].

On the other hand, the observation of the pinch-point-like features below T_c is related to the spin fluctuations about the ordered configuration. At low temperatures, these fluctuations can be described by a classical low-temperature expansion (CLTE), as discussed in

[3]The choice of this sign therefore identifies the single-ion anisotropy term in the Hamiltonian in Eq. (7.11) as an easy-axis term.

[4]This means that at temperatures above T_c, the contribution of the rotational modes is somewhat similar to what would be expected in the Heisenberg antiferromagnetic model which results in the observation of broadened pinch points.

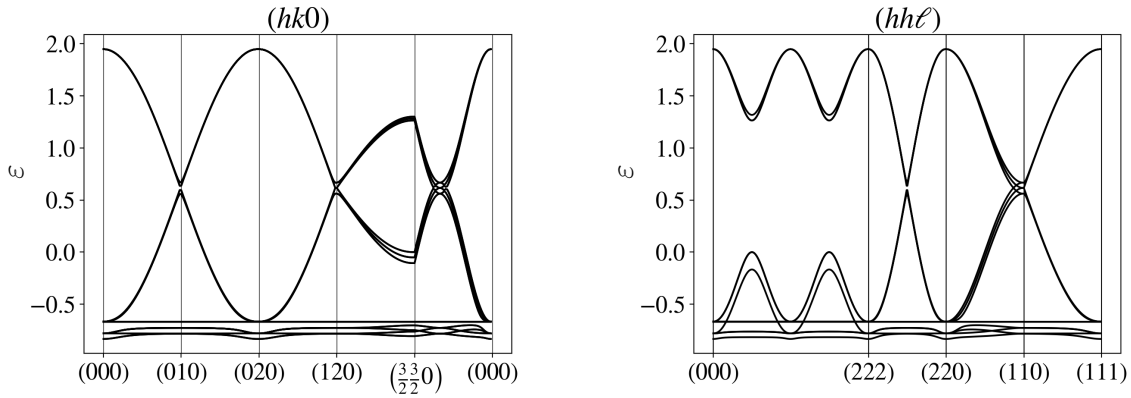


Figure 7.4: Energy bands of the interaction matrix of the single-ion-anisotropy model in Eq. (7.11) illustrated in two high-symmetry paths in the $(hh\ell)$ (a) and $(hk0)$ (b).

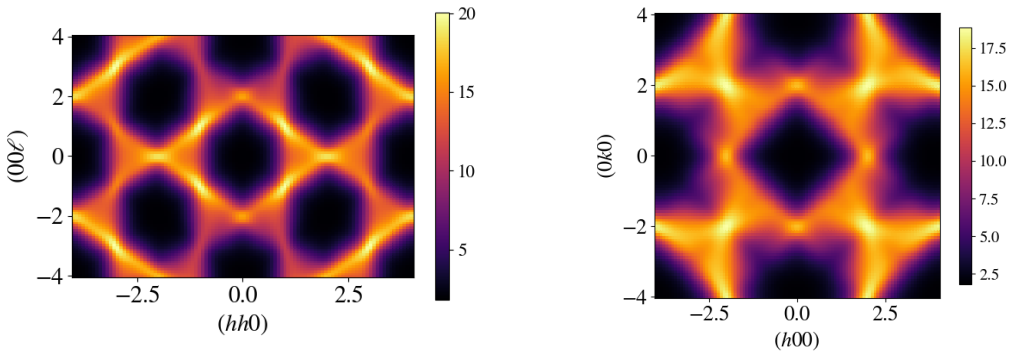
Section 3.2. The neutron structure factor produced by these fluctuations obtained through a CLTE is shown in Fig. 7.5[5]. A comparison between Fig. 7.5 and the structure factors measured in MC at low temperatures shows that the predictions provided by these two methods agree, which allows us to utilize in the CLTE approximation to expose the origin of the pinch-point-like features observed.

7.2.1 A Classical Low-Temperature Expansion

As discussed in Section 3.2, a CLTE is designed to describe the spin fluctuations about an ordered configuration. The description provided in Section 3.2 does not expose how the fluctuating components about the ground state lead to the observation of pinch-point-like features in the neutron structure factor. Therefore, in this subsection we provide an alternative description of the spin fluctuations to expose how these components lead to the observation of pinch-point-like features in the neutron structure factor in the ordered phase.

Assuming an ordered configuration at low temperatures, we may express the spin vari-

[5]Note that the expression for the correlation function given by CLTE has the temperatures T as a prefactor. Since this prefactor does not change the modulation of the correlation function, the results presented in this chapter omit this factor.



(a) $(hh\ell)$ (b) $(hk0)$

Figure 7.5: Neutron structure factor in the $(hh\ell)$ (a) and $(hk0)$ (b) planes obtained using a CLTE. These correlation functions were obtained using Eq. (3.13) where the temperature prefactor is not taken into account.

able in terms of ordering and fluctuating components

$$\mathbf{S}_i = \mathbf{S}_i^{\text{Ord}} + \mathbf{S}_i^{\delta}, \tag{7.12}$$

where $\mathbf{S}_i^{\text{Ord}}$ is the component of the spin at site i along the ordered configuration[6] and $\mathbf{S}_i^{\delta}$ is the fluctuating component which we assume $|\mathbf{S}_i^{\delta}| \ll 1$. Note that the fluctuating component $\mathbf{S}_i^{\delta}$ for spins ordering in an AIAO configuration are constrained to the local xy planes. Using Eq. (7.12), we may rewrite the Hamiltonian (7.11) keeping only quadratic terms in $\mathbf{S}_i^{\delta}$. The Heisenberg Hamiltonian can be expressed as

$$\begin{aligned}
\mathcal{H}_{\text{Heis}} &= J \sum_{\langle ia,jb\rangle} \mathbf{S}_{ia} \cdot \mathbf{S}_{jb} \\
&= \frac{J}{2} \sum_{\boxtimes} \left(\sum_{i \in \boxtimes} \mathbf{S}_i^{\text{Ord}} + \mathbf{S}_i^{\delta} \right)^2 + \mathcal{E}_0 \\
&= \frac{J}{2} \sum_{\boxtimes} \left[\left(\sum_{i \in \boxtimes} \mathbf{S}_i^{\text{Ord}} \right)^2 + \left(\sum_{i \in \boxtimes} \mathbf{S}_i^{\delta} \right)^2 + 2 \left(\sum_{i \in \boxtimes} \mathbf{S}_i^{\delta} \right) \left(\sum_{i \in \boxtimes} \mathbf{S}_i^{\text{Ord}} \right) \right] + \mathcal{E}_0,
\end{aligned} \tag{7.13}$$

where $\mathcal{E}_0$ is the ground state energy of the Heisenberg antiferromagnetic model. On the

[6] For the A_2 irrep these correspond to the local $\boldsymbol{z}$ directions.

other hand, the single-ion anisotropy Hamiltonian can be expressed as

$$\begin{aligned}\mathcal{H}_{\rm SIA} &= d\sum_i (\mathbf{S}_i\cdot\hat{\mathbf{z}}_i)^2 \\ &= d\sum_i (S_i^{\rm Ord})^2 \\ &= \frac{d}{2}\sum_{\boxtimes}\sum_{i\in\boxtimes}(S_i^{\rm Ord})^2,\end{aligned}$$

where we have used the fact that the ground state configuration is an AIAO configuration where the spins point along their local z directions. Altogether, up to the constant $\mathcal{E}_0$, the Hamiltonian in the ordered basis can be written as

$$\begin{aligned}\mathcal{H} &= \frac{J}{2}\sum_{\boxtimes}\left[\left(\sum_{i\in\boxtimes}\mathbf{S}_i^{\rm Ord}\right)^2+\left(\sum_{i\in\boxtimes}\mathbf{S}_i^{\delta}\right)^2+2\left(\sum_{i\in\boxtimes}\mathbf{S}_i^{\delta}\right)\left(\sum_{i\in\boxtimes}\mathbf{S}_i^{\rm Ord}\right)\right]+\frac{d}{2}\sum_{\boxtimes}\sum_{i\in\boxtimes}(S_i^{\rm Ord})^2 \\ &= \underbrace{\frac{d}{2}\sum_{\boxtimes}\sum_{i\in\boxtimes}(S_i^{\rm Ord})^2+\frac{J}{2}\sum_{\boxtimes}\left(\sum_{i\in\boxtimes}\mathbf{S}_i^{\rm Ord}\right)^2}_{\text{Ordered}}+\underbrace{\frac{J}{2}\sum_{\boxtimes}\left(\sum_{i\in\boxtimes}\mathbf{S}_i^{\delta}\right)^2}_{\text{Fluctuating}}+\underbrace{J\sum_{\boxtimes}\left(\sum_{i\in\boxtimes}\mathbf{S}_i^{\delta}\right)\left(\sum_{i\in\boxtimes}\mathbf{S}_i^{\rm Ord}\right)}_{\text{Coupling}} \\ &= \mathcal{H}_{\rm Ordered}+\mathcal{H}_{\rm Fluctuating}+\mathcal{H}_{\rm Coupling} \\ &= \frac{J}{2}\sum_{\boxtimes}\left(\sum_{i\in\boxtimes}\mathbf{S}_i^{\delta}\right)^2+\frac{d}{2}\sum_{\boxtimes}\sum_{i\in\boxtimes}\left(1-|\,\mathbf{S}_i^{\delta}\,|^2\right)+\mathcal{O}(|\,\mathbf{S}_i^{\delta}\,|^3),\end{aligned} \tag{7.14}$$

where the following approximations have been used

$$
\begin{aligned}
\frac{d}{2}\sum_{\boxtimes}\sum_{i\in\boxtimes}(S_i^{\mathrm{Ord}})^2 &= \frac{d}{2}\sum_{\boxtimes}\sum_{i\in\boxtimes}(1-\mid \mathbf{S}_i^{\delta}\mid^2)\\
\frac{J}{2}\sum_{\boxtimes}\left(\sum_{i\in\boxtimes}\mathbf{S}_i^{\mathrm{Ord}}\right)^2 &= \frac{J}{2}\sum_{\boxtimes}\left(\sum_{i\in\boxtimes}\left(1-\frac{1}{2}\mid \mathbf{S}_i^{\delta}\mid^2\right)\hat{\mathbf{S}}_i^{\mathrm{Ord}}\right)^2 + O(\mid \mathbf{S}_i^{\delta}\mid^4)\\
&= \frac{J}{2}\sum_{\boxtimes}\left(\underbrace{\sum_{i\in\boxtimes}\hat{\mathbf{S}}_i^{\mathrm{Ord}}}_{=0} - \frac{1}{2}\sum_{i\in\boxtimes}\mid \mathbf{S}_i^{\delta}\mid^2\hat{\mathbf{S}}_i^{\mathrm{Ord}}\right)^2 + O(\mid \mathbf{S}_i^{\delta}\mid^4)\\
&= \frac{J}{8}\sum_{\boxtimes}\left(\sum_{i\in\boxtimes}\mid \mathbf{S}_i^{\delta}\mid^2\hat{\mathbf{S}}_i^{\mathrm{Ord}}\right)^2 + O(\mid \mathbf{S}_i^{\delta}\mid^4)\\
&= O(\mid \mathbf{S}_i^{\delta}\mid^4).
\end{aligned}
$$

Note that the effective Hamiltonian describing the fluctuating components in Eq. (7.14) resembles the Heisenberg antiferromagnet Hamiltonian up to the term proportional to d[7][8], this term is however a constant shift in the overall energy. Therefore, as the low energy modes of the regular Heisenberg antiferromagnet are rotational, we would expect that the low energy modes of Eq. (7.14) to be rotational as well. To demonstrate this, we use the projector P_{Irrot} to characterize the modes of the effective interaction matrix between the fluctuating components, i.e. the Hessian matrix $H_{a,b}^{\alpha,\gamma}(\boldsymbol{q})$ derived in Section 3.2.

Figure 7.6 shows the eight eigen bands[9] of the Hessian colored by the irrotational projection P_{Irrot}. The band structure of the Hessian shows two flat low energy bands which, according to the irrotational projection, are fully rotational (blue), similar to what is observed in the Heisenberg antiferromagnetic model. In the Heisenberg antiferromagnet

[7]The linear term coming form the coupling vanishes as $\sum_{i\in\boxtimes}\hat{\mathbf{S}}^{\mathrm{Ord}} = 0$ as the ordered state is antiferromagnetic.

[8]In a CLTE, the expression describing the coupling between ordered and fluctuating components produce cubic terms in the fluctuating components, which in the notation of Section 3.2 would result in δn^{α}, $(\delta n^{\alpha})^2\,\delta n^{\beta}$ and $(\delta n^{\alpha})^3$ terms with $\alpha,\beta\in\{x,y\}$. These terms would be neglected in such an analysis, leaving behind the Coulomb phase like term, which in turn explains the pinch point features observed in the structure factor.

[9]In the full interaction matrix, we have twelve bands as there are three degrees of freedom per spin and four spins in a single tetrahedron ($3\times 4 = 12$). The Hessian however only considers fluctuations about an ordered state and therefore only possess two degrees of freedom per spin, $2\times 4 = 8$.

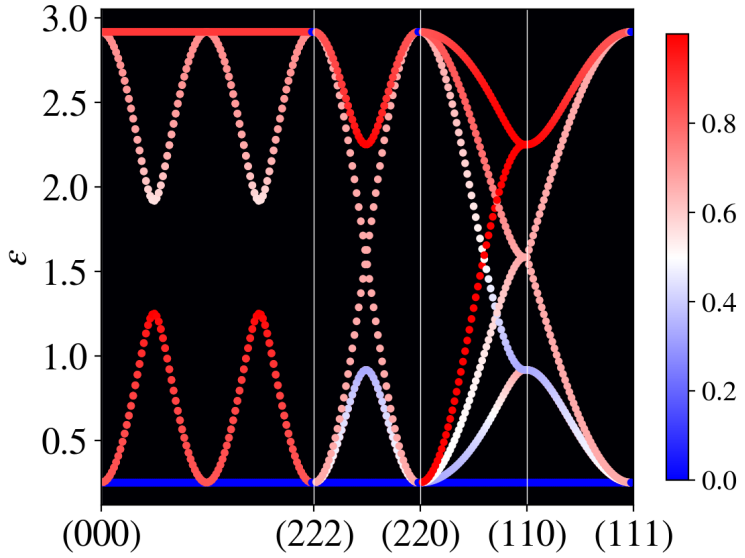
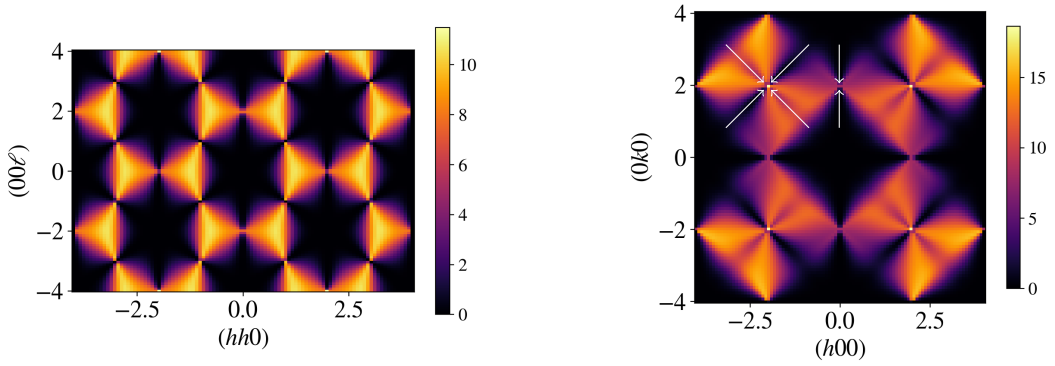


Figure 7.6: Energy bands of the Hessian along a high-symmetry path in the $(hh\ell)$ plane colored by the irrotational projection P_{Irrot}.

model, as the temperature is lowered, the excited bands, and therefore the irrotational modes, are rapidly depopulated as the temperature is decreased resulting in the observation of sharp pinch point features [43, 143]. In contrast, for the effective Hamiltonian in Eq. (7.14), the population of the eigen modes of the Hessian is proportional to $T/\varepsilon_n(\boldsymbol{q})$ (see Eq. (3.12)) as is its contribution to the neutron structure factor (see Eq. (3.13)). The non-vanishing contribution of the irrotational modes (red bands) results in widen pinch points, i.e. the pinch-point-like features, observed in Fig. 7.5[10].

Although the neutron structure factor predicted by CLTE results from the combined rotational and irrotational eigen modes of the Hessian, we can isolate the contribution resulting from the rotational eigen modes numerically to further study the origin of the pinch-point-like features. This is possible given that the correlation function obtained in the CLTE results from the separate contribution of each eigen mode, see Eq. (3.13). Fig. 7.7 shows the neutron structure factor in the $(hh\ell)$ and $(hk0)$ planes resulting from the contribution of the two lowest eigen modes.

[10]Note that if we take $d \to 0$ the contribution of the lower bands rapidly increases in comparison to the higher energy bands. For such case, the pinch points in Fig. 7.5 would become sharper



(a) $(hh\ell)$ (b) $(hk0)$

Figure 7.7: Neutron structure factor in the $(hh\ell)$ (a) and $(hk0)$ (b) obtained using a CLTE considering the contribution of only the two lowest bands. The white arrows in the $(hk0)$ plane illustrate the location of the twofold and fourfold pinch pints.

As expected, the neutron structure factor obtained from only considering the rotational contributions yields *sharp* pinch points in the $(hh\ell)$ plane. Perhaps more interesting is the observation of both twofold and fourfold pinch points in the $(hk0)$ plane. As discussed in Chapter 6, the observation of fourfold pinch points has been related to the realization of fractons and possibly the realization of a rank-2 effective theory [108, 145, 146]. In the next subsection, we explore the possibility of an effective rank-2 theory which can be used to understand the observation of fourfold pinch points.

7.2.2 Effective Low-Energy Theory

The derivation of a low-energy theory can be obtained by considering the irrep modes and how these are incorporated in the theory when performing a long-wavelength approximation. This procedure was followed by Refs. [107, 108] for the rank-2 $U(1)$, and pinch-line-singularity spin-liquids by considering the low-energy irreps of the corresponding models. In fact, an equivalent construction can be performed for the Coulomb spin-liquid observed in the Heisenberg antiferromagnetic model where the three flux variables defined in Eq. (7.4) can be re-expressed in terms of the low-energy irrep modes components. As mentioned before, for the Heisenberg antiferromagnet, the low-energy irrep modes are the A_2, E, $T_{1\perp}$, and T_2 irreps. This construction for the regular Heisenberg antiferromagnetic model is performed by considering the rank-2 tensor $\mathcal{M}$ whose column vectors are defined

by the fluxes in Eq. (7.4), namely

$$\mathcal{M}^{\alpha\gamma} = \frac{\sqrt{3}}{2}\sum_a z_a^\alpha S_a^\gamma, \tag{7.15}$$

which can be further divided into three contributions

$$\mathcal{M} = \sqrt{2}\left(\mathcal{M}_{\text{Sym}} + \mathcal{M}_{\text{Asym}} + \mathcal{M}_{\text{Tracefull}}\right), \tag{7.16}$$

where

$$\mathcal{M}_{\text{Tracefull}} = \sqrt{\frac{2}{3}} m_{A_2} \mathbb{1}, \tag{7.17}$$

$$\mathcal{M}_{\text{Sym}} = \begin{pmatrix} \frac{2}{\sqrt{3}}\psi_2 & m^{xy}_{T_1\perp} & m^{xz}_{T_1\perp} \\ m^{xy}_{T_1\perp} & -\frac{1}{\sqrt{3}}\psi_2 - \psi_3 & m^{yz}_{T_1\perp} \\ m^{xz}_{T_1\perp} & m^{yz}_{T_1\perp} & -\frac{1}{\sqrt{3}}\psi_2 + \psi_3 \end{pmatrix}, \tag{7.18}$$

$$\mathcal{M}_{\text{Asym}} = \begin{pmatrix} 0 & m^{xy}_{T_2} & -m^{xz}_{T_2} \\ -m^{xy}_{T_2} & 0 & m^{yz}_{T_2} \\ m^{xz}_{T_2} & -m^{yz}_{T_2} & 0 \end{pmatrix}. \tag{7.19}$$

In Eq. (7.17)-(7.19), the $m^{\alpha\gamma}_{T_1\perp}$ ($m^{\alpha\gamma}_{T_2}$) correspond to the $T_{1\perp}$ (T_2) irrep modes where the spins lie in the global $\alpha\gamma$ plane. The effective low-energy theory for the Heisenberg antiferromagnet in Eq. (7.5) therefore becomes

$$\mathcal{H}_{\text{Heis}} = J\sum_{\boldsymbol{q}} |\boldsymbol{q}\cdot\mathcal{M}|^2 + O(\boldsymbol{q}^4), \tag{7.20}$$

where now $\boldsymbol{q}\cdot\mathcal{M}$ results in a vector whose components are the dot product with the fluxes $\boldsymbol{q}\cdot\boldsymbol{B}^\alpha$.

Constructing a low-energy theory for the fluctuations of the single-ion anisotropy model in Eq. (7.14) first requires the identification of the irrep modes. Fortunately, since the spin fluctuations $\boldsymbol{S}^\delta$ are constrained to the local xy planes, only the xy irreps need to be considered, i.e. the E, T_1^{xy}, and T_2 irreps. Note that the T_1^{xy} irrep is ferromagnetic while the E, T_2 irreps are antiferromagnetic, this observation makes clear that the E and T_2 irreps correspond to the low energy irreps according to Eq. (7.14)[11]. Given the similarity

[11] When computed exactly, the IEP associated to the E and T_2 irreps is $-d/2$ while for the T_1^{xy} irrep is $\frac{1}{6}(8J-3d)$.

of the fluctuating Hamiltonian in Eq. (7.14) with the Hamiltonian in Eq. (7.2) we can use an adapted version of the charge and flux transformation in Eq. (7.4)

$$Q_\delta^\alpha = \frac{1}{2}\sum_a (S_a^\delta)^\alpha, \tag{7.21}$$

$$\mathcal{M}_\delta^{\alpha\gamma} = \frac{\sqrt{3}}{2}\sum_a z_a^\alpha (S_a^\delta)^\gamma, \tag{7.22}$$

where we have simply replaced the spins $\boldsymbol{S}_a$ in Eq. (7.4) and Eq. (7.15) by the corresponding fluctuating components $\boldsymbol{S}_a^\delta$.

As mentioned before, the next step to follow is to consider a long-wavelength approximation while only considering the low-energy irreps, which in our case are the E and the T_2 irreps. Doing this assumes that, at low temperatures, all other irreps are effectively depopulated, which is not true for the fluctuating components[12][13]. However, we may perform this approximation to rationalize the contribution of the lowest bands to the neutron structure factor. Therefore, performing a long-wavelength approximation by considering only the E and T_2 irrep results in the low-energy effective theory

$$\mathcal{H}_{\text{eff}} = \sum_{\boldsymbol{q}} \left[d\,\text{Tr}\left[\mathcal{M}^T\mathcal{M}\right] + \xi^2 |\boldsymbol{q}\cdot\mathcal{M}|^2 \right] + O(\boldsymbol{q}^4). \tag{7.23}$$

In the above equation, the first term corresponds to the constant shift in Eq. (7.14) while the second term is an emergent Gauss' law in the rank-2 tensor $\mathcal{M}$[14] where ξ is a function of the coupling J[15]. Reference [108] associated the realization of an emergent Gauss' law in a rank-2 tensor with the observation of fourfold pinch points in the rank-2 $U(1)$ spin-liquid. The same principle seems to be valid for the effective low-energy theory of the Hamiltonian (7.14) as both an emergent Gauss' law in a rank-2 tensor and the observation of fourfold pinch point in the correlation function are obtained.

[12] These depopulate as T/ε and therefore cannot be neglected.

[13] There is, however, a model that realize this low-temperature effective theory for the full spins $\boldsymbol{S}_i$. This model is the single-ion-anisotropy with *positive* d [168]. In such model, the E and T_2 are the low energy degenerate irreps and the SCGA produces the same patterns as in Fig. 7.7. Unfortunately, this model presents ObD selection towards the E irrep which prevents the spin-liquid and full low-energy theory to be realized.

[14] As noted in Section 2.2, in real space, this transforms into a $\nabla\cdot\mathcal{M}$.

[15] Here $\xi \propto J^{1/2}$ characterizes the dispersion of the quadratic dispersive modes.

7.3 The Magnon Bands

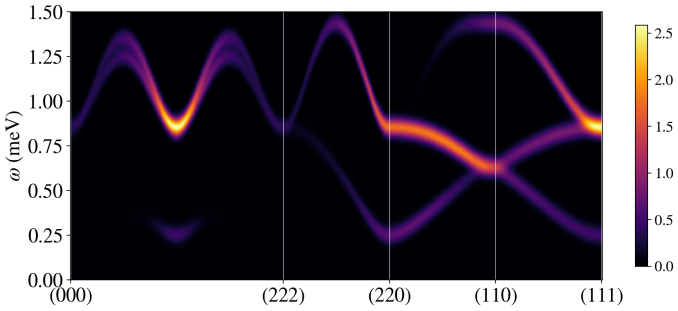
In the previous section we demonstrated that the physical origin of the pinch-point-like features observed in the ordered phase of the single-ion anisotropy model in Eq. (7.11) can be traced to the rotational fluctuations about the ordered spin configurations. A CLTE was used to expose the rotational nature of these modes (see Fig. 7.6) and numerically filter the contribution produced by those, i.e. the sharp pinch point correlations. Although this filtering can easily be performed numerically, we are interested in exposing how this could also be performed *experimentally*. This filtering, and therefore the observation of pinch points, has been performed in the magnon bands for dipolar-octupolar compounds [102, 162–165] and for a Heisenberg antiferromagnetic model in the kagomé lattice [167]. In these systems, a low-energy magnon flat band *uniquely* composed of rotational modes is observed, where its contribution of the magnon flat band to the neutron structure factor results in sharp pinch point features. We refer the reader to Appendix H for a derivation of the rotational modes describing these band in the dipolar-octupolar Hamiltonian. In this section, we demonstrate that a similar effect can be exposed in the magnon bands of the single-ion anisotropy Hamiltonian in Eq. (7.11).

Figure 7.8 shows the magnon bands obtained for the single-ion anisotropy model and the neutron structure factor resulting from energy integrating the contribution of all magnon bands in the $(hh\ell)$ plane, in other words

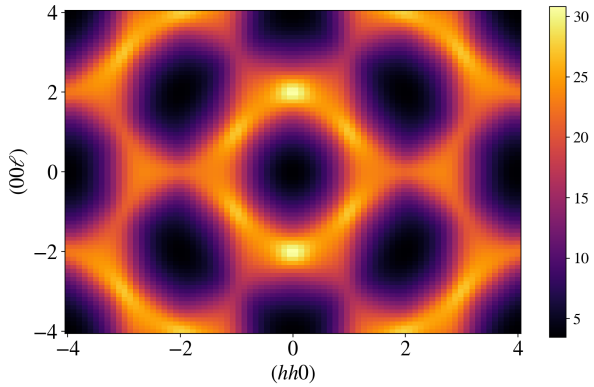
$$S(\boldsymbol{q}) = \int_0^\infty S(\boldsymbol{q}, \omega) d\omega. \tag{7.24}$$

The energy-integrated inelastic neutron structure factor considers the contribution of all four magnon bands. We refer the reader to Section 3.3 for more details in the derivation of these modes and the integration of its contribution. Similarly to what was observed in the neutron structure factor in Fig. 7.5, the integrated inelastic neutron scattering shows pinch-point-like features presumably related to the correlations produced by rotational modes. To expose the rotational nature of the magnon eigenvectors, we consider the projection P_{Irrot} and color the magnon bands accordingly as shown in Fig. 7.9. The irrotational projection in these bands reveal that the two lower magnon bands are strongly rotational, i.e. $P_{\text{Irrot}} \ll 1$, whereas the two upper magnon bands have a mixed rotational/irrotational nature.

To filter the contribution of the strongly rotational magnon bands to the neutron structure factor we may define an energy window of integration which isolates these modes and



(a) Magnon bands in a high-symmetry path in the $(hh\ell)$ plane.



(b) Integrated inelastic neutron scattering in the $(hh\ell)$ plane.

Figure 7.8: (a) Magnon bands of the single-ion anisotropy Hamiltonian in a high-symmetry path in the $(hh\ell)$ plane where we have considered $J = 1$ meV and $d = -0.25$ meV. Here we have used a Gaussian function to make the magnon bands wider to mimic what would be observed in an experiment. (b) Energy integrated inelastic neutron scattering obtained from integrating the contribution of the magnon bands shown in panel (a).

therefore their contribution. In other words, we consider

$$S(\boldsymbol{q}) = \int_0^{\omega_{\text{cut}}} S(\boldsymbol{q}, \omega) d\omega, \tag{7.25}$$

where ω_{cut} is an upper energy bound defined at the top of the second lowest excited band, this energy is illustrated by the white dashed line in Fig. 7.9. The integrated inelastic

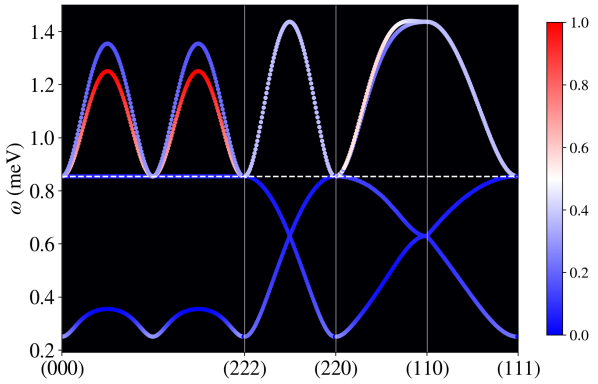


Figure 7.9: Magnon bands of the single-ion anisotropy Hamiltonian in a high-symmetry path in the $(hh\ell)$ plane where we have considered $J = 1$ meV and $d = -0.25$ meV. The coloring of the bands is obtained by using the P_{Irrot} projection where $P_{\text{Irrot}} = 0$ (blue) means that the corresponding mode is fully rotational, $P_{\text{Irrot}} = 1$ (red) means that the corresponding mode is fully irrotational, and $0 < P_{\text{Irrot}} < 1$ means that the corresponding mode has a mixed rotational-irrotational nature. Here the white dashed line represents ω_{cut}.

neutron structure factor over the energy window $[0, \omega_{\text{cut}}]$ is illustrated in Fig. 7.10 in both the $(hh\ell)$ and $(hk0)$ planes.

Similarly to what was observed in Fig. 7.7, the integrated inelastic neutron structure factor over the strongly rotational lower magnon bands in Fig. 7.10 illustrates sharp twofold pinch points. In contrast, the fourfold pinch points observed in Fig. 7.7 are not visible. The fourfold pinch points were related to the isolated contribution of the rotational bands and the effective long-wavelength theory constructed by considering the E and T_2 irreps. In the magnon bands, however, the lower two bands are not fully rotational which might be related to the lack of fourfold pinch points when integrating these bands. However, other anisotropic features in the inelastic neutron structure factor can be obtained by considering the contribution of higher magnon bands. Although we currently do not have a full understanding of what these correlations imply, for completeness, we nevertheless present these results in Fig. 7.11[16].

[16]Interestingly, the fourfold pinch points in the third excited band are observed at band touching points which suggest that these features might have a topological origin.

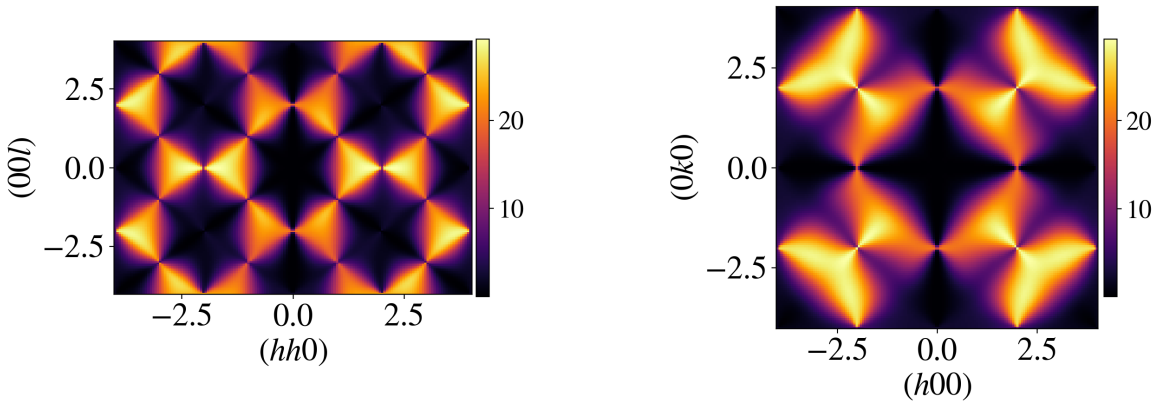


Figure 7.10: Energy integrated inelastic neutron scattering obtained from integrating the contribution of the two lower magnon bands in the $(hh\ell)$ (left) and $(hk0)$ (right) planes.

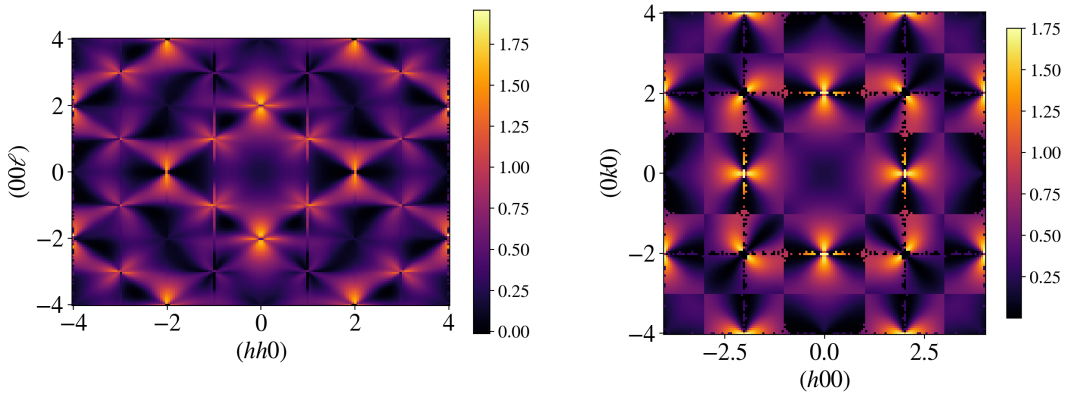


Figure 7.11: Energy integrated inelastic neutron scattering obtained from integrating the contribution of the third magnon band in the $(hh\ell)$ (left) and $(hk0)$ (right) planes. These figures present discontinuous and highly varying features (noise) in sections where two magnon bands cross, i.e. energy degeneracy lines in the magnon bands. In other words, these features are numerical artifacts resulting from separating the contribution of the modes at these degeneracy lines.

7.4 Pinch Points in FeF_3 and Proximity to Other Spin-Liquids

As was initially discussed at the beginning of this chapter, we chose the single-ion anisotropy as a starting point to demonstrate how sharp pinch point features associated to the proximate Coulomb spin liquid can be observed in an ordered phase. However, our results can be generalized to other systems which are proximate to the Coulomb spin-liquid realized in the Heisenberg antiferromagnet. For example, consider the compound FeF_3 [75] described by a Heisenberg and DM Hamiltonian with $J > 0$, $J_{\mathrm{DM}} > 0$, and $J_{\mathrm{DM}} \ll J$, see Eq. (4.1). Similarly to the single-ion anisotropy model, this Hamiltonian presents a low-temperature AIAO phase where, above T_c, pinch point features have been observed [75]. Applying an equivalent analysis to the magnon bands of this model reveals that the two lowest magnon bands are strongly rotational. Integrating over these bands in the $(hh\ell)$ and $(hk0)$ planes reveals twofold pinch points similar to the ones in Fig. 7.8. These results are summarized in Fig. 7.12.

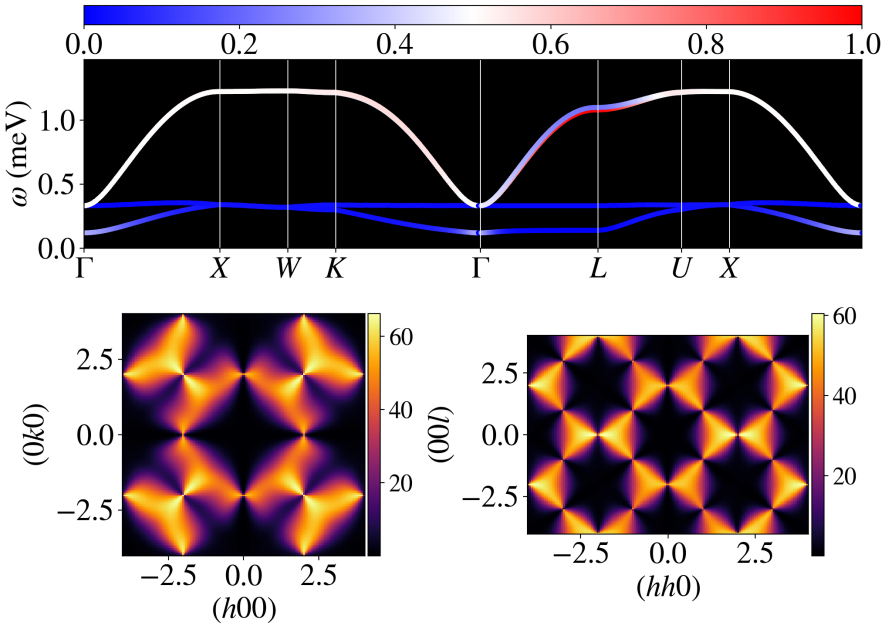


Figure 7.12: Magnon bands for the Heisenberg and DM Hamiltonian with $J = 1\mathrm{meV}$, $J_{\mathrm{DM}} = 0.02/\mathrm{meV}$ (upper plot).

Although the results presented so far assume an AIAO order as the low-temperature

phase, our analysis can be generalized to Hamiltonians proximate to the Heisenberg antiferromagnet Coulomb spin-liquid ultimately undergoing ordering to the low-temperature states. The motivation behind choosing the AIAO ordered, and in particular the single-ion anisotropy model, is that we can build a transparent interpretation, both numerically and analytically, which serves as a stepping stone when generalizing our results.

Although the work presented in this chapter focuses on the Coulomb spin-liquid realized in the Heisenberg antiferromagnet, we can generalize its application to other spin-liquids. To do so, we would have to define an equivalent projection capable of distinguishing the spin configurations composing the ground state manifold of the proximate spin-liquid. Numerically, this projection has the same form as $\mathbb{P}_{\text{Irrot}}$ in Eq. (7.8). However, to produce a meaningful interpretation, a long-wavelength theory of the proximate spin-liquids would be necessary.

7.5 Conclusion and Outlook

In this chapter, we studied how the proximity of a model to a spin-liquid phase results in the observation of remnant correlations of the spin-liquid in the near by ordered phases. To illustrate this, we considered the Coulomb spin-liquid and the single-ion anisotropy model where we used a classical low-temperature expansion and linear spin wave theory to expose how sharp pinch point features can be observed in the ordered phase. The observation of these correlations can be traced back to the rotational nature of the spin fluctuations about the ordered states, which we demonstrated numerically and analytically using the projector $\mathbb{P}_{\text{Irrot}}$. This projector was built by considering the rotational spin subspace which corresponds to the ground state manifold of the Coulomb spin-liquid. Therefore, the application of $\mathbb{P}_{\text{Irrot}}$ allowed us to track the rotational spin modes and consider their contribution to the different correlation functions considered. We speculate that a similar construction can be generalized to other spin-liquids. For example, the results presented in this chapter are of particular interest to study the compound $Yb_2Ti_2O_7$ [142] where rods of (neutron) scattering may be related to the continuous lines of intensity observed for the proximate spin-liquid, the pinch-line-singularity spin-liquid [107].

Chapter 8

General Conclusions and Broad Outlook

In this thesis we have studied symmetry breaking, classical and quantum order-by-disorder (ObD), a novel spin-liquid phase, and how the proximity to a spin-liquid affects the correlations function in an ordered phase in the pyrochlore lattice. In particular, these phenomena were exposed and carefully studied for the Heisenberg and Dzyaloshinskii-Moriya (DM) Hamiltonian,

$$\mathcal{H} = J\sum_{\langle ij\rangle}\boldsymbol{S}_i\cdot\boldsymbol{S}_j + J_{\rm DM}\sum_{\langle ij\rangle}\boldsymbol{D}_{ij}\cdot(\boldsymbol{S}_i\times\boldsymbol{S}_j), \tag{8.1}$$

where the interest in this model originates from the exact degeneracy between two symmetry breaking phases [110] for a range of parameters $\{J, J_{\rm DM}\}$ which we have demonstrated to be fruitful grounds for the identification of exotic phenomena.

In Chapter 4, we identified the $\boldsymbol{q}=\boldsymbol{0}$ magnetic phases for the Hamiltonian (8.1) in both classical and quantum models. Using a number of classical and quantum approaches, we identified three magnetically ordered phases (AIAO, Γ_5, and colinear ferromagnetic phase) in addition to two spin-liquid phases (the Heisenberg antiferromagnet Coulomb spin-liquid and the novel $J_{\rm DM}/J=2$ spin-liquid). Interestingly, our quantum phase diagram identified with a pseudo-fermion functional renormalization group (PFFRG) method finds that the two classical spin-liquid points extent for a finite region of ratios $J_{\rm DM}/J$. Additionally, we studied the ObD selection of the ψ_2 and ψ_3 states in the Γ_5 phase at T_c and $T\to 0$ where we found that the classical and quantum models roughly agree in the selection of these phases [1].

In Chapter 5, we studied the classical and quantum ObD selection of the total magnetization orientation in the colinear ferromagnetic phase identified in Chapter 4. In general terms, we found good agreement between the classical and quantum analytical predictions where two preferred total magnetization orientations were identified as $T \to 0$. Interestingly, both the classical and quantum models present a reorientation of the total magnetization vector when approaching the Γ_5 boundary. However, the quantum ObD was performed with linear spin-wave theory ignoring the paramagnetic region identified by PFFRG in Chapter 4. This paramagnetic region might be a result of an instability of the ferromagnetic phase close to the classical Γ_5 boundary which is not captured by the approximations we considered. This instability of the ferromagnetic phase might be captured using Holstein-Primakoff transformation and considering magnon-magnon interactions [141] that are ignored in the LSW theory which we leave to investigation in future work. The tools and approximations used in this chapter allowed us to study the classical ObD selection at all temperatures while quantum ObD selection was only performed for $T \to 0$. Additional work employing a high-temperature series expansions may therefore allow us to generalize our work and to further compare and contrast the ObD selection in both the classical and quantum models.

In Chapter 6, we studied the novel spin-liquid identified in Chapter 4. A classical Monte Carlo study allowed us to identify a transition temperature T^* which separates two distinct spin-liquid phases. The spin-liquid phase above T^* exhibits a correlation function where anisotropic features such as continuous intensity lines, twofold and fourfold pinch are observed. In contrast, the spin-liquid below T^* exhibits a correlation function similar to the one observed for a spin-ice system which lead us to identify this phase as a spin-ice spin-liquid built from Heisenberg spins. A posterior analysis using a self-consistent gaussian approximation and iterative minimization suggests that the low temperature spin-ice spin-liquid is selected by an entropic mechanism. Validating this observation would require the study of the entropic weight associated with the spin-ice states which we leave for future work. The Hamiltonian and spin-liquid studied in this chapter are of special relevance for the non-Kramers pyrochlores where we believe other novel low-temperature phases may be realized.

In Chapter 7 we studied how the correlation functions in ordered phases proximate to a spin-liquid may present remnant features characteristic of the spin-liquid. To demonstrate this, we considered the Coulomb spin-liquid and the Heisenberg antiferromagnetic model with a small additional single-ion anisotropy term. The remnant correlations in the low-temperature ordered phase were exposed by employing a classical low-temperature expansion and linear spin wave theory which unveil sharp twofold pinch points, characteristic of a Coulomb phase, in the ordered phase correlation functions. The observation of these

correlations was traced back to spin fluctuations about the ordered states which conserve some of the correlations characteristic of the Coulomb spin-liquid. This identification was done analytically and numerically using a projector $\mathbb{P}_{\text{Irrot}}$ capable of tracking the spin modes composing the Coulomb phase ground state manifold. We expect our results to be generalizable to any other spin liquid by identifying a pertinent projector $\mathbb{P}_{\text{Ground}-\text{State}}$.

In conclusion, in this thesis, we have presented a thorough analysis of the Heisenberg and DM model by dissecting the ordered and disordered phases identified and the mechanisms leading to these. Our work motivates the study of other magnetic Hamiltonians which may lie at phase boundaries between different ordered phases and resulting in the observation of new exotic phenomena. Moreover, our results can be used to spearhead the search for models in the interaction parameter space which may realize similar types of spin-liquids and even to motivate the search of these in other lattices.

References

[1] V. Noculak, D. Lozano-Gómez, J. Oitmaa, R. R. P. Singh, Y. Iqbal, M. J. P. Gingras, and J. Reuther, "Classical and quantum phases of the pyrochlore S=1/2 magnet with Heisenberg and Dzyaloshinskii-Moriya interactions," (2022), arXiv:2211.08823 .

[2] D. Lozano-Gómez, D. Pereira, and M. J. P. Gingras, "Unsupervised machine learning of quenched gauge symmetries: A proof-of-concept demonstration," Phys. Rev. Research **4**, 043118 (2022).

[3] K. T. K. Chung, J. S. K. Goh, A. Mukherjee, W. Jin, D. Lozano-Gómez, and M. J. P. Gingras, "Probing flat band physics in spin ice systems via polarized neutron scattering," Phys. Rev. Lett. **128**, 107201 (2022).

[4] M. Taillefumier, O. Benton, H. Yan, L. D. C. Jaubert, and N. Shannon, "Competing spin liquids and hidden spin-nematic order in spin ice with frustrated transverse exchange," Phys. Rev. X **7**, 041057 (2017).

[5] T. Vicsek, A. Czirók, E. Ben-Jacob, I. Cohen, and O. Shochet, "Novel type of phase transition in a system of self-driven particles," Phys. Rev. Lett. **75**, 1226–1229 (1995).

[6] H. Iyetomi, "Collective phenomena in economic systems," in *Complexity, Heterogeneity, and the Methods of Statistical Physics in Economics: Essays in Memory of Masanao Aoki*, edited by H. Aoyama, Y. Aruka, and H. Yoshikawa (Springer Singapore, Singapore, 2020) pp. 177–201.

[7] E. Ising, "Beitrag zur Theorie des Ferromagnetismus," Zeitschrift für Physik **31**, 253–258 (1925).

[8] L. Onsager, "Crystal Statistics. I. A Two-Dimensional Model with an Order-Disorder Transition," Phys. Rev. **65**, 117–149 (1944).

[9] G. H. Wannier, "Antiferromagnetism. The Triangular Ising Net," Phys. Rev. **79**, 357–364 (1950).

[10] P. Fazekas and P. W. Anderson, "On the ground state properties of the anisotropic triangular antiferromagnet," The Philosophical Magazine: A Journal of Theoretical Experimental and Applied Physics **30**, 423–440 (1974).

[11] P. Nikolić and T. Senthil, "Theory of the kagomé lattice Ising antiferromagnet in weak transverse fields," Phys. Rev. B **71**, 024401 (2005).

[12] R. Stübel and W. Janke, "Finite-size scaling of Monte Carlo simulations for the fcc Ising antiferromagnet: Effects of the low-temperature phase degeneracy," Phys. Rev. B **98**, 174413 (2018).

[13] C. Castelnovo, R. Moessner, and S. L. Sondhi, "Magnetic monopoles in spin ice," Nature **451**, 42–45 (2008).

[14] G. Chen and L. Balents, "Spin-orbit effects in $Na_4Ir_3O_8$: A hyper-kagomé lattice antiferromagnet," Phys. Rev. B **78**, 094403 (2008).

[15] J. M. Hopkinson and H.-Y. Kee, "Geometric frustration inherent to the trillium lattice, a sublattice of the B20 structure," Phys. Rev. B **74**, 224441 (2006).

[16] P. Anderson, "Resonating valence bonds: A new kind of insulator?" Materials Research Bulletin **8**, 153–160 (1973).

[17] P. W. Anderson, "The resonating valence bond state in La_2CuO_4 and superconductivity," Science **235**, 1196–1198 (1987).

[18] C. Broholm, R. J. Cava, S. A. Kivelson, D. G. Nocera, M. R. Norman, and T. Senthil, "Quantum spin liquids," Science **367**, 0668 (2020).

[19] J. S. Gardner, M. J. P. Gingras, and J. E. Greedan, "Magnetic pyrochlore oxides," Rev. Mod. Phys. **82**, 53–107 (2010).

[20] A. M. Hallas, J. Gaudet, and B. D. Gaulin, "Experimental insights into ground-state selection of quantum xy pyrochlores," Annual Review of Condensed Matter Physics **9**, 105–124 (2018).

[21] G. R. Lumpkin and R. D. Aughterson, "Perspectives on pyrochlores, defect fluorites, and related compounds: Building blocks for chemical diversity and functionality," Frontiers in Chemistry **9** (2021).

[22] A. F. Fuentes, K. Boulahya, M. Maczka, J. Hanuza, and U. Amador, "Synthesis of disordered pyrochlores, $A_2Ti_2O_7$ (A=Y, Gd and Dy), by mechanical milling of constituent oxides," Solid State Sciences **7**, 343–353 (2005).

[23] J. G. Rau and M. J. Gingras, "Frustrated quantum rare-earth pyrochlores," Annual Review of Condensed Matter Physics **10**, 357–386 (2019).

[24] G. Sim and S. Lee, "Discovery of a new type of magnetic order on pyrochlore spinels," Phys. Rev. B **98**, 014423 (2018).

[25] J. Villain, R. Bidaux, J.-P. Carton, and R. Conte, "Order as an effect of disorder," Journal de Physique **41**, 1263–1272 (1980).

[26] Y. Onose, T. Ideue, H. Katsura, Y. Shiomi, N. Nagaosa, and Y. Tokura, "Observation of the magnon hall effect," Science **329**, 297–299 (2010).

[27] M. E. Brooks-Bartlett, S. T. Banks, L. D. Jaubert, A. Harman-Clarke, and P. C. Holdsworth, "Magnetic-moment fragmentation and monopole crystallization," Physical Review X **4**, 1–16 (2014).

[28] S. T. Bramwell and M. J. P. Gingras, "Spin ice state in frustrated magnetic pyrochlore materials," Science **294**, 1495–1501 (2001).

[29] J. Gaudet, E. M. Smith, J. Dudemaine, J. Beare, C. R. C. Buhariwalla, N. P. Butch, M. B. Stone, A. I. Kolesnikov, G. Xu, D. R. Yahne, K. A. Ross, C. A. Marjerrison, J. D. Garrett, G. M. Luke, A. D. Bianchi, and B. D. Gaulin, "Quantum spin ice dynamics in the dipole-octupole pyrochlore magnet $Ce_2Zr_2O_7$," Phys. Rev. Lett. **122**, 187201 (2019).

[30] T. Fennell, P. P. Deen, A. R. Wildes, K. Schmalzl, D. Prabhakaran, A. T. Boothroyd, R. J. Aldus, D. F. McMorrow, and S. T. Bramwell, "Magnetic Coulomb Phase in the Spin Ice $Ho_2Ti_2O_7$," Science **326**, 415–417 (2009).

[31] T. Fennell, O. A. Petrenko, B. Fåk, S. T. Bramwell, M. Enjalran, T. Yavors'kii, M. J. P. Gingras, R. G. Melko, and G. Balakrishnan, "Neutron scattering investigation of the spin ice state in $Dy_2Ti_2O_7$," Phys. Rev. B **70**, 134408 (2004).

[32] Fennell, T., "Neutron scattering studies of spin ices and spin liquids," Collection SFN **13**, 04001 (2014).

[33] P. Fazekas, *Lecture Notes On Electron Correlation And Magnetism* (World Scientific Publishing Company, 1999).

[34] M. Hutchings, "Point-charge calculations of energy levels of magnetic ions in crystalline electric fields," (Academic Press, 1964) pp. 227–273.

[35] H. Tasaki, *Physics and Mathematics of Quantum Many-Body Systems* (Springer, 2020).

[36] M. Ruminy, E. Pomjakushina, K. Iida, K. Kamazawa, D. T. Adroja, U. Stuhr, and T. Fennell, "Crystal-field parameters of the rare-earth pyrochlores $R_2Ti_2O_7$ (R = Tb, Dy, and Ho)," Phys. Rev. B **94**, 024430 (2016).

[37] T. Takayama, J. Chaloupka, A. Smerald, G. Khaliullin, and H. Takagi, "Spin–orbit-entangled electronic phases in 4d and 5d transition-metal compounds," Journal of the Physical Society of Japan **90**, 062001 (2021), https://doi.org/10.7566/JPSJ.90.062001 .

[38] A. Bertin, Y. Chapuis, P. D. de Réotier, and A. Yaouanc, "Crystal electric field in the $R_2Ti_2O_7$ pyrochlore compounds," Journal of Physics: Condensed Matter **24**, 256003 (2012).

[39] Y.-P. Huang, G. Chen, and M. Hermele, "Quantum spin ices and topological phases from dipolar-octupolar doublets on the pyrochlore lattice," Phys. Rev. Lett. **112**, 167203 (2014).

[40] F. Desrochers, L. E. Chern, and Y. B. Kim, "Competing $U(1)$ and $\mathbb{Z}_2$ dipolar-octupolar quantum spin liquids on the pyrochlore lattice: Application to $Ce_2Zr_2O_7$," Phys. Rev. B **105**, 035149 (2022).

[41] L. Pauling, "The structure and entropy of ice and of other crystals with some randomness of atomic arrangement," Journal of the American Chemical Society **57**, 2680–2684 (1935).

[42] P. H. Conlon and J. T. Chalker, "Absent pinch points and emergent clusters: Further neighbor interactions in the pyrochlore Heisenberg antiferromagnet," Phys. Rev. B **81**, 224413 (2010).

[43] R. Moessner and J. T. Chalker, "Low-temperature properties of classical geometrically frustrated antiferromagnets," Phys. Rev. B **58**, 12049–12062 (1998).

[44] S. V. Isakov, K. Gregor, R. Moessner, and S. L. Sondhi, "Dipolar spin correlations in classical pyrochlore magnets," Phys. Rev. Lett. **93**, 167204 (2004).

[45] S. V. Isakov, R. Moessner, and S. L. Sondhi, "Why spin ice obeys the ice rules," Phys. Rev. Lett. **95**, 217201 (2005).

[46] S. Isakov, *Correlations in Frustrated Magnets: Classical and Quantum Aspects*, Ph.D. thesis, Stockhol University, (2004).

[47] C. Lacroix, P. Mendels, and F. Mila, *Introduction to Frustrated Magnetism* (Springer Series in Solid-State Sciences 164, 2010) p. 679.

[48] R. G. Melko and M. J. P. Gingras, "Monte carlo studies of the dipolar spin ice model," Journal of Physics: Condensed Matter **16**, R1277 (2004).

[49] L. D. C. Jaubert, M. J. Harris, T. Fennell, R. G. Melko, S. T. Bramwell, and P. C. W. Holdsworth, "Topological-sector fluctuations and curie-law crossover in spin ice," Phys. Rev. X **3**, 011014 (2013).

[50] L. D. C. Jaubert, M. Haque, and R. Moessner, "Analysis of a Fully Packed Loop Model Arising in a Magnetic Coulomb Phase," Phys. Rev. Lett. **107**, 177202 (2011).

[51] L. Savary and L. Balents, "Quantum spin liquids: a review," Reports on Progress in Physics **80**, 016502 (2016).

[52] L. D. C. Jaubert and P. C. W. Holdsworth, "Signature of magnetic monopole and Dirac string dynamics in spin ice," Nature Physics **5**, 258–261 (2009).

[53] L. D. C. Jaubert and P. C. W. Holdsworth, "Magnetic monopole dynamics in spin ice," Journal of Physics: Condensed Matter **23**, 164222 (2011).

[54] J. G. Rau and M. J. P. Gingras, "Spin slush in an extended spin ice model," Nature Publishing Group **7**, 1–7 (2016).

[55] T. Mizoguchi and M. Udagawa, "Flat-band engineering in tight-binding models: Beyond the nearest-neighbor hopping," **235118**, 1–12 (2019).

[56] M. Hermele, M. P. A. Fisher, and L. Balents, "Pyrochlore photons: The U(1) spin liquid in a S = $\frac{1}{2}$ three-dimensional frustrated magnet," Phys. Rev. B **69**, 064404 (2004).

[57] L. Savary and L. Balents, "Coulombic quantum liquids in spin-1/2 pyrochlores," Phys. Rev. Lett. **108**, 037202 (2012).

[58] S. Lee, S. Onoda, and L. Balents, "Generic quantum spin ice," Phys. Rev. B **86**, 104412 (2012).

[59] L. E. Chern, Y. B. Kim, and C. Castelnovo, "Competing quantum spin liquids, gauge fluctuations, and anisotropic interactions in a breathing pyrochlore lattice," Phys. Rev. B **106**, 134402 (2022).

[60] Y. Kato and S. Onoda, "Numerical evidence of quantum melting of spin ice: Quantum-to-classical crossover," Phys. Rev. Lett. **115**, 077202 (2015).

[61] J. Oitmaa, R. R. P. Singh, B. Javanparast, A. G. R. Day, B. V. Bagheri, and M. J. P. Gingras, "Phase transition and thermal order-by-disorder in the pyrochlore antiferromagnet $Er_2Ti_2O_7$: A high-temperature series expansion study," Phys. Rev. B **88**, 220404 (2013).

[62] L. D. C. Jaubert, O. Benton, J. G. Rau, J. Oitmaa, R. R. P. Singh, N. Shannon, and M. J. P. Gingras, "Are multiphase competition and order by disorder the keys to understanding $Yb_2Ti_2O_7$?" Phys. Rev. Lett. **115**, 267208 (2015).

[63] B. Tang, E. Khatami, and M. Rigol, "A short introduction to numerical linked-cluster expansions," Computer Physics Communications **184**, 557–564 (2013).

[64] N. R. Hayre, K. A. Ross, R. Applegate, T. Lin, R. R. P. Singh, B. D. Gaulin, and M. J. P. Gingras, "Thermodynamic properties of $Yb_2Ti_2O_7$ pyrochlore as a function of temperature and magnetic field: Validation of a quantum spin ice exchange hamiltonian," Phys. Rev. B **87**, 184423 (2013).

[65] Y. Iqbal, T. Müller, P. Ghosh, M. J. P. Gingras, H. O. Jeschke, S. Rachel, J. Reuther, and R. Thomale, "Quantum and Classical Phases of the Pyrochlore Heisenberg Model with Competing Interactions," Phys. Rev. X **9**, 011005 (2019).

[66] M. Hering, J. Sonnenschein, Y. Iqbal, and J. Reuther, "Characterization of quantum spin liquids and their spinon band structures via functional renormalization," Phys. Rev. B **99**, 100405 (2019).

[67] F. L. Buessen, V. Noculak, S. Trebst, and J. Reuther, "Functional renormalization group for frustrated magnets with nondiagonal spin interactions," Phys. Rev. B **100**, 125164 (2019).

[68] N. Niggemann, B. Sbierski, and J. Reuther, "Frustrated quantum spins at finite temperature: Pseudo-majorana functional renormalization group approach," Phys. Rev. B **103**, 104431 (2021).

[69] C. Feng, A. Wietek, E. M. Stoudenmire, and R. R. P. Singh, "Order, disorder, and monopole confinement in the spin-$\frac{1}{2}$ XXZ model on a pyrochlore tube," Phys. Rev. B **106**, 075135 (2022).

[70] K. A. Ross, L. Savary, B. D. Gaulin, and L. Balents, "Quantum excitations in quantum spin ice," Phys. Rev. X **1**, 021002 (2011).

[71] B. Javanparast, A. G. R. Day, Z. Hao, and M. J. P. Gingras, "Order-by-disorder near criticality in xy pyrochlore magnets," Phys. Rev. B **91**, 174424 (2015).

[72] T. Moriya, "Anisotropic Superexchange Interaction and Weak Ferromagnetism," Physical Review **120**, 91–98 (1960).

[73] M. Elhajal, B. Canals, R. Sunyer, and C. Lacroix, "Ordering in the pyrochlore antiferromagnet due to Dzyaloshinsky-Moriya interactions," Physical Review B **71**, 094420 (2005).

[74] H. Yan, O. Benton, L. Jaubert, and N. Shannon, "Theory of multiple-phase competition in pyrochlore magnets with anisotropic exchange with application to $Yb_2Ti_2O_7$, $Er_2Ti_2O_7$,and $Er_2Sn_2O_7$," Physical Review B **95**, 094422 (2017).

[75] A. Sadeghi, M. Alaei, F. Shahbazi, and M. J. P. Gingras, "Spin hamiltonian, order out of a coulomb phase, and pseudocriticality in the frustrated pyrochlore heisenberg antiferromagnet fef_3," Phys. Rev. B **91**, 140407 (2015).

[76] B. Canals, M. Elhajal, and C. Lacroix, "Ising-like order by disorder in the pyrochlore antiferromagnet with Dzyaloshinskii-Moriya interactions," Phys. Rev. B **78**, 214431 (2008).

[77] X. Zhang, H. Zhou, L. Yu, H. J. Gardner, S. von Molnár, C. Wiebe, and P. Xiong, "Electronic transport in the ferromagnetic pyrochlore $Lu_2V_2O_7$: Role of magnetization," Phys. Rev. B **91**, 205107 (2015).

[78] H. D. Zhou, E. S. Choi, J. A. Souza, J. Lu, Y. Xin, L. L. Lumata, B. S. Conner, L. Balicas, J. S. Brooks, J. J. Neumeier, and C. R. Wiebe, "Magnetic-polaron-driven magnetoresistance in the pyrochlore $Lu_2V_2O_7$," Phys. Rev. B **77**, 020411 (2008).

[79] K. Riedl, D. Guterding, H. O. Jeschke, M. J. P. Gingras, and R. Valentí, "Ab initio determination of spin hamiltonians with anisotropic exchange interactions: The case of the pyrochlore ferromagnet $Lu_2V_2O_7$," Phys. Rev. B **94**, 014410 (2016).

[80] M. Mena, R. S. Perry, T. G. Perring, M. D. Le, S. Guerrero, M. Storni, D. T. Adroja, C. Rüegg, and D. F. McMorrow, "Spin-wave spectrum of the quantum ferromagnet on the pyrochlore lattice $Lu_2V_2O_7$," Phys. Rev. Lett. **113**, 047202 (2014).

[81] D. V. Nazipov, A. E. Nikiforov, and V. A. Chernyshev, "Exchange interaction in pyrochlore vanadates $Lu_2V_2O_7$ and $Y_2V_2O_7$: Ab initio approach," Physics of the Solid State **58**, 1989–1994 (2016).

[82] D. R. Yahne, D. Pereira, L. D. C. Jaubert, L. D. Sanjeewa, M. Powell, J. W. Kolis, G. Xu, M. Enjalran, M. J. P. Gingras, and K. A. Ross, "Understanding reentrance in frustrated magnets: The case of the $Er_2Sn_2O_7$ pyrochlore," Phys. Rev. Lett. **127**, 277206 (2021).

[83] S. E. Palmer and J. T. Chalker, "Order induced by dipolar interactions in a geometrically frustrated antiferromagnet," Phys. Rev. B **62**, 488–492 (2000).

[84] P. G. Welch, J. A. M. Paddison, M. D. Le, J. S. Gardner, W.-T. Chen, A. R. Wildes, A. L. Goodwin, and J. R. Stewart, "Magnetic structure and exchange interactions in the heisenberg pyrochlore antiferromagnet $Gd_2Pt_2O_7$," Phys. Rev. B **105**, 094402 (2022).

[85] P. A. McClarty, J. N. Cosman, A. G. D. Maestro, and M. J. P. Gingras, "Calculation of the expected zero-field muon relaxation rate in the geometrically frustrated rare earth pyrochlore $Gd_2Sn_2O_7$ antiferromagnet," Journal of Physics: Condensed Matter **23**, 164216 (2011).

[86] M. E. Zhitomirsky, P. C. W. Holdsworth, and R. Moessner, "Nature of finite-temperature transition in anisotropic pyrochlore $Er_2Ti_2O_7$," Physical Review B **89**, 140403 (2014).

[87] M. E. Zhitomirsky, M. V. Gvozdikova, P. C. W. Holdsworth, and R. Moessner, "Quantum Order by Disorder and Accidental Soft Mode in $Er_2Ti_2O_7$," Phys. Rev. Lett. **109**, 077204 (2012).

[88] P. A. McClarty, S. H. Curnoe, and M. J. P. Gingras, "Energetic selection of ordered states in a model of the $Er_2Ti_2O_7$ frustrated pyrochlore xy antiferromagnet," Journal of Physics: Conference Series **145**, 012032 (2009).

[89] C. L. Sarkis, J. G. Rau, L. D. Sanjeewa, M. Powell, J. Kolis, J. Marbey, S. Hill, J. A. Rodriguez-Rivera, H. S. Nair, D. R. Yahne, S. Säubert, M. J. P. Gingras, and K. A. Ross, "Unravelling competing microscopic interactions at a phase boundary:

A single-crystal study of the metastable antiferromagnetic pyrochlore $Yb_2Ge_2O_7$," Phys. Rev. B **102**, 134418 (2020).

[90] P. A. McClarty, P. Stasiak, and M. J. P. Gingras, "Order-by-disorder in the xy pyrochlore antiferromagnet," Phys. Rev. B **89**, 024425 (2014).

[91] J. D. Thompson, P. A. McClarty, and M. J. P. Gingras, "Local susceptibility of the $Yb_2Ti_2O_7$ rare earth pyrochlore computed from a Hamiltonian with anisotropic exchange," Journal of Physics: Condensed Matter **23**, 164219 (2011).

[92] J. D. Thompson, P. A. McClarty, H. M. Rønnow, L. P. Regnault, A. Sorge, and M. J. Gingras, "Rods of neutron scattering intensity in $Yb_2Ti_2O_7$: Compelling evidence for significant anisotropic exchange in a magnetic pyrochlore oxide," Physical Review Letters **106**, 9–12 (2011).

[93] J. D. Thompson, P. A. McClarty, D. Prabhakaran, I. Cabrera, T. Guidi, and R. Coldea, "Quasiparticle Breakdown and Spin Hamiltonian of the Frustrated Quantum Pyrochlore $Yb_2Ti_2O_7$ in a Magnetic Field," Physical Review Letters **119**, 1–6 (2017).

[94] J. Robert, E. Lhotel, G. Remenyi, S. Sahling, I. Mirebeau, C. Decorse, B. Canals, and S. Petit, "Spin dynamics in the presence of competing ferromagnetic and antiferromagnetic correlations in $Yb_2Ti_2O_7$," Physical Review B - Condensed Matter and Materials Physics **92**, 1–15 (2015).

[95] A. Scheie, J. Kindervater, S. Zhang, H. J. Changlani, G. Sala, G. Ehlers, A. Heinemann, G. S. Tucker, S. M. Koohpayeh, and C. Broholm, "Multiphase magnetism in $Yb_2Ti_2O_7$," Proceedings of the National Academy of Sciences **117**, 27245–27254 (2020).

[96] B. Javanparast, Z. Hao, M. Enjalran, and M. J. P. Gingras, "Fluctuation-driven selection at criticality in a frustrated magnetic system: The case of multiple-**k** partial order on the pyrochlore lattice," Phys. Rev. Lett. **114**, 130601 (2015).

[97] J. Dorier, F. Becca, and F. Mila, "Quantum compass model on the square lattice," Phys. Rev. B **72**, 024448 (2005).

[98] A. Pires, "Two dimensional compass model with Heisenberg interactions," Journal of Magnetism and Magnetic Materials **452**, 326–330 (2018).

[99] P. Chandra, P. Coleman, and I. Ritchey, "The anisotropic kagomé antiferromagnet: a topological spin glass?" J. Phys. I France **3**, 591–610 (1993).

[100] R. Schick, T. Ziman, and M. E. Zhitomirsky, "Quantum versus thermal fluctuations in the fcc antiferromagnet: Alternative routes to order by disorder," Physical Review B **102**, 220405 (2020).

[101] J. N. Reimers, "Absence of long-range order in a three-dimensional geometrically frustrated antiferromagnet," Phys. Rev. B **45**, 7287–7294 (1992).

[102] O. Benton, "Quantum origins of moment fragmentation in $Nd_2Zr_2O_7$," Physical Review B **94**, 1–6 (2016).

[103] O. Benton, O. Sikora, and N. Shannon, "Seeing the light : Experimental signatures of emergent electromagnetism in a quantum spin ice," **075154**, 1–25 (2012).

[104] A. Bhardwaj, S. Zhang, H. Yan, R. Moessner, A. H. Nevidomskyy, and H. J. Changlani, "Sleuthing out exotic quantum spin liquidity in the pyrochlore magnet $Ce_2Zr_2O_7$," npj Quantum Materials **7**, 51 (2022).

[105] E. Lhotel, L. D. C. Jaubert, and P. C. W. Holdsworth, "Fragmentation in frustrated magnets: A review," Journal of Low Temperature Physics **201**, 710–737 (2020).

[106] R. Sibille, N. Gauthier, H. Yan, M. Ciomaga Hatnean, J. Ollivier, B. Winn, U. Filges, G. Balakrishnan, M. Kenzelmann, N. Shannon, and T. Fennell, "Experimental signatures of emergent quantum electrodynamics in $Pr_2Hf_2O_7$," Nature Physics **14**, 711–715 (2018).

[107] O. Benton, L. D. C. Jaubert, H. Yan, and N. Shannon, "A spin-liquid with pinch-line singularities on the pyrochlore lattice," Nature Communications **7**, 11572 (2016).

[108] H. Yan, O. Benton, L. D. C. Jaubert, and N. Shannon, "Rank–2 U(1) spin liquid on the breathing pyrochlore lattice," Phys. Rev. Lett. **124**, 127203 (2020).

[109] P. Ghosh, Y. Iqbal, T. Müller, R. T. Ponnaganti, R. Thomale, R. Narayanan, J. Reuther, M. J. P. Gingras, and H. O. Jeschke, "Breathing chromium spinels: a showcase for a variety of pyrochlore Heisenberg Hamiltonians," npj Quantum Materials **4**, 63 (2019).

[110] A. W. C. Wong, Z. Hao, and M. J. P. Gingras, "Ground state phase diagram of generic xy pyrochlore magnets with quantum fluctuations," Phys. Rev. B **88**, 144402 (2013).

[111] S. Zhang, H. J. Changlani, K. W. Plumb, O. Tchernyshyov, and R. Moessner, "Dynamical structure factor of the three-dimensional quantum spin liquid candidate $NaCaNi_2F_7$," Phys. Rev. Lett. **122**, 167203 (2019).

[112] G.-W. Chern, "Pyrochlore antiferromagnet with antisymmetric exchange interactions: critical behavior and order from disorder," (2010), arXiv:1008.3038 [cond-mat.str-el] .

[113] T. Coletta, M. E. Zhitomirsky, and F. Mila, "Quantum stabilization of classically unstable plateau structures," Phys. Rev. B **87**, 060407 (2013).

[114] L.-J. Chang, S. Onoda, Y. Su, Y.-J. Kao, K.-D. Tsuei, Y. Yasui, K. Kakurai, and M. R. Lees, "Higgs transition from a magnetic Coulomb liquid to a ferromagnet in $Yb_2Ti_2O_7$," Nature Communications **3**, 992 (2012).

[115] C. Castelnovo and R. Moessner, "Rod motifs in neutron scattering in spin ice," **121102**, 1–5 (2019).

[116] K. A. Ross, J. P. Ruff, C. P. Adams, J. S. Gardner, H. A. Dabkowska, Y. Qiu, J. R. Copley, and B. D. Gaulin, "Two-Dimensional Kagome Correlations and Field Induced Order in the Ferromagnetic XY Pyrochlore $Yb_2Ti_2O_7$," Physical Review Letters **103**, 1–4 (2009).

[117] J. F. Cornwell, *Group Theory in Physics* (Elsevier, 1997).

[118] O. V. Kovalev, *Representations of the Crystallographic Space Groups* (Gordon and Breach, 1993).

[119] O. Benton, "Classical and quantum spin liquids on the pyrochlore lattice," Ph.D. thesis, University of Bristol, (2014).

[120] J. D. Alzate-Cardona, D. Sabogal-Suárez, R. F. L. Evans, and E. Restrepo-Parra, "Optimal phase space sampling for Monte Carlo simulations of Heisenberg spin systems," Journal of Physics: Condensed Matter **31**, 095802 (2019).

[121] H. Dai, "A review on the exact monte carlo simulation," in *Bayesian Inference on Complicated Data*, edited by N. Tang (IntechOpen, Rijeka, 2019) Chap. 3.

[122] R. Nafise, A. Mojtaba, and A. Hadi, "Espins: A program for classical monte-carlo simulations of spin systems," (2019), arXiv:1912.00793 [cond-mat.str-el] .

[123] H. Suzuki, "Monte carlo simulation of classical spin models with chaotic billiards," Phys. Rev. E **88**, 052144 (2013).

[124] M. Creutz, "Overrelaxation and Monte Carlo simulation," Phys. Rev. D **36**, 515–519 (1987).

[125] P. Chandra, P. Coleman, and I. Ritchey, "The anisotropic kagomé antiferromagnet: a topological spin glass?" Journal de Physique I **3**, 591–610 (1993).

[126] S. M. A. Tabei, F. Vernay, and M. J. P. Gingras, "Effective spin-$\frac{1}{2}$ description of transverse-field-induced random fields in dipolar spin glasses with strong single-ion anisotropy," Phys. Rev. B **77**, 014432 (2008).

[127] S. M. A. Tabei, M. J. P. Gingras, Y.-J. Kao, P. Stasiak, and J.-Y. Fortin, "Induced Random Fields in the $LiHo_xY_{1-x}F_4$ Quantum Ising Magnet in a Transverse Magnetic Field," Phys. Rev. Lett. **97**, 237203 (2006).

[128] T. Moriya, "New mechanism of anisotropic superexchange interaction," Phys. Rev. Lett. **4**, 228–230 (1960).

[129] I. Dzyaloshinsky, "A thermodynamic theory of "weak" ferromagnetism of antiferromagnetics," Journal of Physics and Chemistry of Solids **4**, 241–255 (1958).

[130] J. N. Reimers, A. J. Berlinsky, and A. C. Shi, "Mean-field approach to magnetic ordering in highly frustrated pyrochlores," Physical Review B **43**, 865–878 (1991).

[131] M. Enjalran and M. J. P. Gingras, "Theory of paramagnetic scattering in highly frustrated magnets with long-range dipole-dipole interactions: The case of the $Tb_2Ti_2O_7$ pyrochlore antiferromagnet," Phys. Rev. B **70**, 174426 (2004).

[132] D. P. Landau and K. Binder, *A Guide to Monte Carlo Simulations in Statistical Physics*, 4th ed. (Cambridge University Press, 2014).

[133] E. C. Andrade, J. A. Hoyos, S. Rachel, and M. Vojta, "Cluster-glass phase in pyrochlore xy antiferromagnets with quenched disorder," Phys. Rev. Lett. **120**, 097204 (2018).

[134] J. Lou, A. W. Sandvik, and L. Balents, "Emergence of U(1) symmetry in the 3d xy model with Z_q anisotropy," Phys. Rev. Lett. **99**, 207203 (2007).

[135] J. R. Tessman, "Magnetic anisotropy at 0° k," Phys. Rev. **96**, 1192–1195 (1954).

[136] M. H. Cohen and F. Keffer, "Dipolar ferromagnetism at 0° k," Phys. Rev. **99**, 1135–1140 (1955).

[137] J. P. Bouchaud and P. G. Zérah, "Dipolar ferromagnetism: A Monte Carlo study," Phys. Rev. B **47**, 9095–9097 (1993).

[138] N. Su, F. Li, Y. Jiao, Z. Liu, J. Sun, B. Wang, Y. Sui, H. Zhou, G. Chen, and J. Cheng, "Asymmetric ferromagnetic criticality in pyrochlore ferromagnet $Lu_2V_2O_7$," Science Bulletin **64**, 1222–1227 (2019).

[139] A. Aharony, "Critical behavior of anisotropic cubic systems," Phys. Rev. B **8**, 4270–4273 (1973).

[140] Y. Sizyuk, N. B. Perkins, and P. Wölfle, "Lifting mean-field degeneracies in anisotropic classical spin systems," Phys. Rev. B **92**, 155131 (2015).

[141] J. G. Rau, R. Moessner, and P. A. McClarty, "Magnon interactions in the frustrated pyrochlore ferromagnet $yb_2ti_2o_7$," Phys. Rev. B **100**, 104423 (2019).

[142] A. Scheie, O. Benton, M. Taillefumier, L. D. C. Jaubert, G. Sala, N. Jalarvo, S. M. Koohpayeh, and N. Shannon, "Dynamical scaling as a signature of multiple phase competition in $Yb_2Ti_2O_7$," Phys. Rev. Lett. **129**, 217202 (2022).

[143] C. L. Henley, "The "Coulomb Phase" in Frustrated Systems," Annual Review of Condensed Matter Physics **1**, 179–210 (2010).

[144] H. Kadowaki, H. Takatsu, T. Taniguchi, B. Fåk, and J. Ollivier, "Composite spin and quadrupole wave in the ordered phase of $Tb_{2+x}Ti_{2-x}O_{7+y}$," SPIN **05**, 1540003 (2015).

[145] H. Yan and J. Reuther, "Low-energy structure of spiral spin liquids," Phys. Rev. Res. **4**, 023175 (2022).

[146] M. Pretko, "The fracton gauge principle," Phys. Rev. B **98**, 115134 (2018).

[147] E. Lake and M. Hermele, "Subdimensional criticality: Condensation of lineons and planons in the x-cube model," Phys. Rev. B **104**, 165121 (2021).

[148] J. T. Chalker, P. C. W. Holdsworth, and E. F. Shender, "Hidden order in a frustrated system: Properties of the heisenberg kagomé antiferromagnet," Phys. Rev. Lett. **68**, 855–858 (1992).

[149] J. Lee and J. M. Kosterlitz, "New numerical method to study phase transitions," Phys. Rev. Lett. **65**, 137–140 (1990).

[150] H. Shinaoka, Y. Tomita, and Y. Motome, "Spin-Glass Transition in Bond-Disordered Heisenberg Antiferromagnets Coupled with Local Lattice Distortions on a Pyrochlore Lattice," Phys. Rev. Lett. **107**, 047204 (2011).

[151] H. Shinaoka, Y. Tomita, and Y. Motome, "Loop algorithm for classical antiferromagnetic Heisenberg models with biquadratic interactions," Journal of Physics: Conference Series **320**, 012009 (2011).

[152] H. Shinaoka and Y. Motome, "Loop algorithm for classical heisenberg models with spin-ice type degeneracy," Phys. Rev. B **82**, 134420 (2010).

[153] S. Lee, S. Onoda, and L. Balents, "Generic quantum spin ice," Phys. Rev. B **86**, 104412 (2012).

[154] S. Onoda and Y. Tanaka, "Quantum fluctuations in the effective pseudospin-$\frac{1}{2}$ model for magnetic pyrochlore oxides," Phys. Rev. B **83**, 094411 (2011).

[155] H. Takatsu, S. Onoda, S. Kittaka, A. Kasahara, Y. Kono, T. Sakakibara, Y. Kato, B. Fåk, J. Ollivier, J. W. Lynn, T. Taniguchi, M. Wakita, and H. Kadowaki, "Order in the frustrated pyrochlore $Tb_{2+x}Ti_{2-x}O_{7+y}$," Phys. Rev. Lett. **116**, 217201 (2016).

[156] K. Kimura, S. Nakatsuji, J.-J. Wen, C. Broholm, M. B. Stone, E. Nishibori, and H. Sawa, "Quantum fluctuations in spin-ice-like $Pr_2Zr_2O_7$," Nature Communications **4**, 1934 (2013).

[157] P. Bonville, I. Mirebeau, A. Gukasov, S. Petit, and J. Robert, "Low temperature phase diagram for the pyrochlore compound $Tb_2Ti_2O_7$," Journal of Physics: Conference Series **320**, 012006 (2011).

[158] P. Bonville, I. Mirebeau, A. Gukasov, S. Petit, and J. Robert, "Tetragonal distortion yielding a two-singlet spin liquid in pyrochlore $Tb_2Ti_2O_7$," Phys. Rev. B **84**, 184409 (2011).

[159] S. Petit, P. Bonville, J. Robert, C. Decorse, and I. Mirebeau, "Spin liquid correlations, anisotropic exchange, and symmetry breaking in $Tb_2Ti_2O_7$," Phys. Rev. B **86**, 174403 (2012).

[160] A. M. Hallas, W. Jin, J. Gaudet, E. M. Tonita, D. Pomaranski, C. R. C. Buhariwalla, M. Tachibana, N. P. Butch, S. Calder, M. B. Stone, G. M. Luke, C. R. Wiebe, J. B. Kycia, M. J. P. Gingras, and B. D. Gaulin, "Intertwined magnetic dipolar and electric quadrupolar correlations in the pyrochlore $Tb_2Ge_2O_7$," (2020), arXiv:2009.05036 [cond-mat.str-el] .

[161] J. Xu, O. Benton, V. K. Anand, A. T. Islam, T. Guidi, G. Ehlers, E. Feng, Y. Su, A. Sakai, P. Gegenwart, and B. Lake, "Anisotropic exchange Hamiltonian, magnetic phase diagram, and domain inversion of $Nd_2Zr_2O_7$," Physical Review B **99**, 1–14 (2019).

[162] S. Petit, E. Lhotel, B. Canals, M. Ciomaga Hatnean, J. Ollivier, H. Mutka, E. Ressouche, A. R. Wildes, M. R. Lees, and G. Balakrishnan, "Observation of magnetic fragmentation in spin ice," Nature Physics **12**, 746–750 (2016).

[163] J. Xu, C. Balz, C. Baines, H. Luetkens, and B. Lake, "Spin dynamics of the ordered dipolar-octupolar pseudospin-$\frac{1}{2}$ pyrochlore $Nd_2Zr_2O_7$ probed by muon spin relaxation," Phys. Rev. B **94**, 064425 (2016).

[164] A. Samartzis, J. Xu, V. K. Anand, A. T. M. N. Islam, J. Ollivier, Y. Su, and B. Lake, "Pinch points and half-moons in dipolar-octupolar $Nd_2Hf_2O_7$," Phys. Rev. B **106**, L100401 (2022).

[165] S. J. Gomez, P. M. Sarte, M. Zelensky, A. M. Hallas, B. A. Gonzalez, K. H. Hong, E. J. Pace, S. Calder, M. B. Stone, Y. Su, E. Feng, M. D. Le, C. Stock, J. P. Attfield, S. D. Wilson, C. R. Wiebe, and A. A. Aczel, "Absence of moment fragmentation in the mixed B-site pyrochlore Nd_2GaSbO_7," Phys. Rev. B **103**, 214419 (2021).

[166] M. Léger, E. Lhotel, M. Ciomaga Hatnean, J. Ollivier, A. R. Wildes, S. Raymond, E. Ressouche, G. Balakrishnan, and S. Petit, "Spin dynamics and unconventional coulomb phase in $Nd_2Zr_2O_7$," Phys. Rev. Lett. **126**, 247201 (2021).

[167] H. Yan, R. Pohle, and N. Shannon, "Half moons are pinch points with dispersion," Phys. Rev. B **98**, 140402 (2018).

[168] J. D. M. Champion, S. T. Bramwell, P. C. Holdsworth, and M. J. Harris, "Competition Between Exchange and Anisotropy in a Pyrochlore Ferromagnet," EPL - Europhysics Letters **57**, 93–99 (2002).

[169] A. B. Harris, C. Kallin, and A. J. Berlinsky, "Possible Néel orderings of the Kagomé antiferromagnet," Phys. Rev. B **45**, 2899–2919 (1992).

[170] M. Kardar, *Statistical physics of fields* (Cambridge University Press, 2007).

[171] W. Schwalm, B. Moritz, M. Giona, and M. Schwalm, "Vector difference calculus for physical lattice models," Phys. Rev. E **59**, 1217–1233 (1999).

[172] S. M. A. Tabei, "Interplay of Disorder and Transverse-Field Induced Quantum Fluctuations in the $LiHo_xY_{1-x}F_4$ Ising Magnetic Material," Ph.D. thesis, University of Waterloo, (2008).

[173] B. Bauer, L. D. Carr, H. G. Evertz, A. Feiguin, J. Freire, S. Fuchs, L. Gamper, J. Gukelberger, E. Gull, S. Guertler, A. Hehn, R. Igarashi, S. V. Isakov, D. Koop, P. N. Ma, P. Mates, H. Matsuo, O. Parcollet, G. Pawłowski, J. D. Picon, L. Pollet, E. Santos, V. W. Scarola, U. Schollwöck, C. Silva, B. Surer, S. Todo, S. Trebst, M. Troyer, M. L. Wall, P. Werner, and S. Wessel, "The alps project release 2.0: open source software for strongly correlated systems," Journal of Statistical Mechanics: Theory and Experiment **2011**, P05001 (2011).

APPENDICES

Appendix A

Pyrochlore Lattice Vectors and Local Basis

The pyrochlore lattice can be described by a face-centered cubic (FCC) lattice with a four sublattice basis resulting in the corner sharing network of tetrahedra illustrated in Fig. 1.4. In the global frame, the FCC lattice vectors are given by

$$\boldsymbol{R}_1 = \frac{r_c}{2}\begin{pmatrix}1\\1\\0\end{pmatrix}, \quad \boldsymbol{R}_2 = \frac{r_c}{2}\begin{pmatrix}1\\0\\1\end{pmatrix}, \quad \boldsymbol{R}_3 = \frac{r_c}{2}\begin{pmatrix}0\\1\\1\end{pmatrix}, \tag{A.1}$$

where r_c is the length of the FCC unit cell[1], and $\boldsymbol{x}, \boldsymbol{y}, \boldsymbol{z}$ are the global Cartesian unit vectors. The four sublattices, labeled by $a = \{0, 1, 2, 3\}$, positions are given by

$$\boldsymbol{r}_0 = \boldsymbol{0}, \quad \boldsymbol{r}_1 = \boldsymbol{R}_1/2, \quad \boldsymbol{r}_2 = \boldsymbol{R}_2/2, \quad \boldsymbol{r}_3 = \boldsymbol{R}_3/2. \tag{A.2}$$

Fig. A.1 depicts the FCC and sublattice basis vectors in a single FCC unit cell where only the up tetrahedra are shown. With the above convention we define the *local* basis for the spin in the sublattice $a = 0$ as

$$\boldsymbol{x}_0 = \frac{1}{\sqrt{6}}\begin{pmatrix}-1\\-1\\2\end{pmatrix}, \quad \boldsymbol{y}_0 = \frac{1}{\sqrt{2}}\begin{pmatrix}1\\-1\\0\end{pmatrix}, \quad \boldsymbol{z}_0 = \frac{1}{\sqrt{3}}\begin{pmatrix}1\\1\\1\end{pmatrix}.$$

[1]Note that in the main text we set $r_c = 1$ for simplicity.

The basis vectors for all other sublattices can be obtained by applying transformations in T_d. For completeness, here we provide the local z direction of all sublattices.

$$\boldsymbol{z}_0 = \frac{1}{\sqrt{3}}\begin{pmatrix}1\\1\\1\end{pmatrix}, \quad \boldsymbol{z}_1 = \frac{1}{\sqrt{3}}\begin{pmatrix}-1\\-1\\1\end{pmatrix}, \quad \boldsymbol{z}_2 = \frac{1}{\sqrt{3}}\begin{pmatrix}-1\\1\\-1\end{pmatrix}, \quad \boldsymbol{z}_3 = \frac{1}{\sqrt{3}}\begin{pmatrix}1\\-1\\-1\end{pmatrix}. \tag{A.3}$$

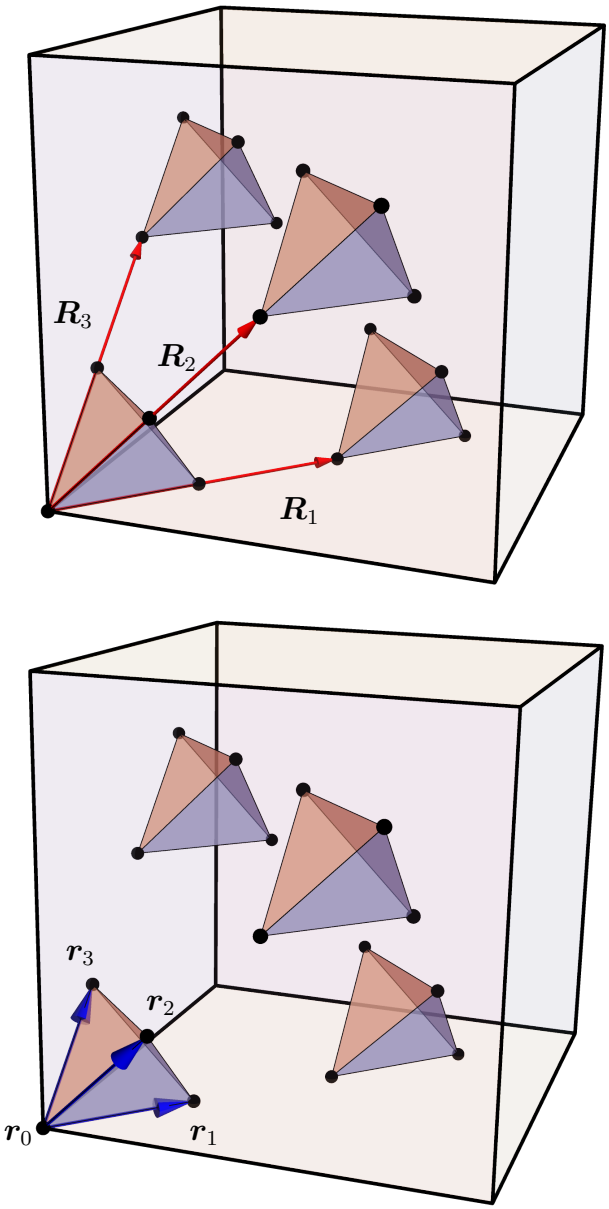


Figure A.1: Pyrochlore lattice for a single FCC unit cell where the FCC vectors $\{\boldsymbol{R}\}$ are illustrated in red and the sublattice vectors $\{\boldsymbol{r}\}$ are shown in blue. Here the size of the box, i.e. the cubic unit cell, is r_c.

Appendix B

Neutron Scattering

In this appendix, we provide the expressions used for the neutron scattering structure factors used in this thesis. We consider incident neutrons initially polarized along a fixed direction $\hat{z}_s$ which are then scattered in a direction defined by the wave vector $\boldsymbol{q}$. For each possible scattering wave vector $\boldsymbol{q}$ lying in a perpendicular plane to $\hat{z}_s$, we define a local basis $\{\hat{x}_s, \hat{y}_s, \hat{z}_s\}$, where $\hat{x}_s \parallel \boldsymbol{q}$ and $\hat{y}_s = \hat{z}_s \times \hat{x}_s$ as illustrated in Fig. B.1.

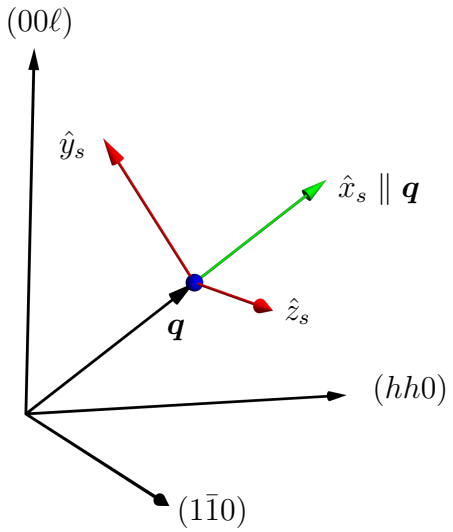


Figure B.1: An scattered neutron with wave vector $\boldsymbol{q}$ in the $(hh\ell)$ scattering plane where the incident neutron initial polarization axis is $\hat{z}_s \parallel (1\bar{1}0)$, and the local basis defined by the direction of wave vector $\boldsymbol{q}$ and the polarization axis $\hat{z}_s$ is shown.

To measure the correlation functions obtained through neutron scattering one must compute the correlation functions of the spin components which are transverse to the incident neutron wave vector $\boldsymbol{q}$ [32, 119]

$$S_\perp(\boldsymbol{q}) = \sum_\alpha \sum_{a,b} (S_a^\alpha)_\perp(-\boldsymbol{q})(S_b^\alpha)_\perp(\boldsymbol{q}).$$

This measurement can be expressed in terms of a projection of the full correlation function in the following way

$$\begin{aligned}
S_\perp(\boldsymbol{q}) &= \sum_{\alpha,\gamma} \delta_{\alpha,\gamma} \sum_{a,b} (S_a^\alpha)_\perp (S_b^\gamma)_\perp \\
&= \sum_{\alpha,\gamma} \delta_{\alpha,\gamma} \sum_{a,b} (S_a^\alpha - (\boldsymbol{S}_a \cdot \hat{\boldsymbol{q}})\hat{\boldsymbol{q}}^\alpha)(S_b^\gamma - (\boldsymbol{S}_b \cdot \hat{\boldsymbol{q}})\hat{\boldsymbol{q}}^\gamma) \\
&= \sum_{\alpha,\gamma} \delta_{\alpha,\gamma} \sum_{a,b} (S_a^\alpha S_b^\gamma - 2S_a^\alpha \hat{\boldsymbol{q}}^\gamma (\boldsymbol{S}_b \cdot \hat{\boldsymbol{q}}) + \hat{\boldsymbol{q}}^\alpha \hat{\boldsymbol{q}}^\gamma (\boldsymbol{S}_a \cdot \hat{\boldsymbol{q}})(\boldsymbol{S}_b \cdot \hat{\boldsymbol{q}})) \\
&= \sum_{\alpha,\gamma} \sum_{a,b} S_a^\alpha S_b^\gamma \delta_{\alpha,\gamma} - \sum_{\alpha} \sum_{a,b} S_a^\alpha \hat{\boldsymbol{q}}^\alpha (\boldsymbol{S}_b \cdot \hat{\boldsymbol{q}}) \\
&= \sum_{\alpha,\gamma} \sum_{a,b} S_a^\alpha S_b^\gamma \delta_{\alpha,\gamma} - \sum_{\alpha,\gamma} \sum_{a,b} S_a^\alpha \hat{\boldsymbol{q}}^\alpha S_b^\gamma \hat{\boldsymbol{q}}^\gamma \\
&= \sum_{\alpha,\gamma} \sum_{a,b} (S_a^\alpha S_b^\gamma) (\delta_{\alpha,\gamma} - \hat{\boldsymbol{q}}^\alpha \hat{\boldsymbol{q}}^\gamma), \qquad \text{(B.1)}
\end{aligned}$$

where a, b are the sublattice indices, α, γ label the Cartesian components, and $\delta_{\alpha,\gamma}$ is the Kronecker delta. The inclusion of the neutron projection results in the expression provided in Eq. (1.7) corresponding to the unpolarized neutron scattering

$$S_\perp(\boldsymbol{q}) = \sum_{\alpha,\gamma} \sum_{a,b} (\delta_{\alpha,\gamma} - \hat{\boldsymbol{q}}^\alpha \hat{\boldsymbol{q}}^\gamma) (S_a^\alpha(-\boldsymbol{q}) S_b^\gamma(\boldsymbol{q})). \qquad \text{(B.2)}$$

The unpolarized neutron scattering can be further divided depending on whether the scattered neutron has flipped its spin upon scattering or not. To perform this analysis we consider the incident neutron defined by a scattering wave vector $\boldsymbol{q}$ to be polarized along the $\hat{z}_s$ direction, see Fig. B.1. The case where the scattered neutron does not flip its spin is captured by the non-spin-flip (NSF) channel. The NSF channel is obtained by studying the correlations of the components of the $(\boldsymbol{S}_a^\alpha)_\perp$ which are parallel to the polarization vector

$\hat{z}_s$. In this case, one would obtain

$$\begin{aligned} S_{\perp}^{\mathrm{NSF}}(\boldsymbol{q}) &= \sum_{\alpha,\gamma} \hat{z}_s^{\alpha}\hat{z}_s^{\gamma} \sum_{a,b} (S_a^{\alpha})_{\perp}(S_b^{\gamma})_{\perp} \\ &= \sum_{\alpha,\gamma} \hat{z}_s^{\alpha}\hat{z}_s^{\gamma} \sum_{a,b} (S_a^{\alpha} - (\boldsymbol{S}_a \cdot \hat{\boldsymbol{q}})\hat{\boldsymbol{q}}^{\alpha})(S_b^{\gamma} - (\boldsymbol{S}_b \cdot \hat{\boldsymbol{q}})\hat{\boldsymbol{q}}^{\gamma}) \\ &= \sum_{\alpha,\gamma} \hat{z}_s{}^{\alpha}\hat{z}_s^{\gamma} \sum_{a,b} (S_a^{\alpha}S_b^{\gamma} - 2S_a^{\alpha}\hat{\boldsymbol{q}}^{\gamma}(\boldsymbol{S}_b \cdot \hat{\boldsymbol{q}}) + \hat{\boldsymbol{q}}^{\alpha}\hat{\boldsymbol{q}}^{\gamma}(\boldsymbol{S}_a \cdot \hat{\boldsymbol{q}})(\boldsymbol{S}_b \cdot \hat{\boldsymbol{q}})) \\ &= \sum_{\alpha,\gamma} \sum_{a,b} (S_a^{\alpha}S_b^{\gamma}) (\hat{z}_s^{\alpha}\hat{z}_s^{\gamma}), \end{aligned} \tag{B.3}$$

where, in the third line, the second and third term vanishes as the scattering vector $\boldsymbol{q}$ is perpendicular to $\hat{z}_s$. For completeness, we also provide the expression for the correlation function between two spins, i.e. the spin-spin correlation function, although it has not been explicitly used in this thesis,

$$S_{\perp}(\boldsymbol{q}) = \sum_{\alpha} \sum_{a,b} S_a^{\alpha}(-\boldsymbol{q}) S_b^{\alpha}(\boldsymbol{q}),$$

where $\boldsymbol{S}_a(\boldsymbol{q}) = \frac{1}{\sqrt{N}} \sum_i \boldsymbol{S}_{ia} e^{-i((\boldsymbol{R}_i + \boldsymbol{r}_a)\cdot \boldsymbol{q})}$.

In this thesis, we consider the spins $\boldsymbol{S}_i$ to describe the magnetic moments $\boldsymbol{\mu}_i$, i.e. $\boldsymbol{\mu}_i = \boldsymbol{S}_i$. However, for real materials [70], and as discussed in the introduction of Chapter 2, these two quantities are generally related by an anisotropic g-tensor

$$\mu_{ia}^{\alpha} = \sum_{\gamma} g_a^{\alpha,\gamma} S_{ia}^{\gamma}, \tag{B.4}$$

where $g_a^{\alpha,\gamma}$ is the g-tensor associated to the a sublattice.

Appendix C

High-Symmetry Paths in the Brillouin Zone

In this appendix, we provide the high-symmetry in the Brillouin zone used to present the interaction matrix bands, the Hessian bands, and the magnon bands in Chapter 6 in the $(hh\ell)$ and $(hk0)$ planes. The high-symmetry paths for both scattering planes are shown in Fig. C.1.

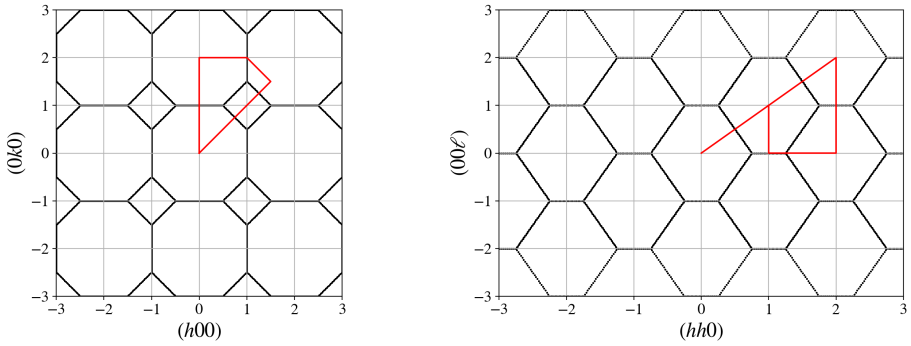


Figure C.1: High-symmetry paths demarked in red in the $(hk0)$ (left) and $(hh\ell)$ (right) planes. The black dots denote the boundary between different Brillouin zones.

These two paths in both scattering planes were chosen to include some of the high-symmetry points in the Brillouin zone. In Fig. C.2 we illustrate the high-symmetry paths and points in the reciprocal space where the labeling and exact value of the high-symmetry

points is provided in Tab. C.1. From Fig. C.2 it is therefore clear why the $(hh\ell)$ and the $(hk0)$ planes are chosen to illustrate the neutron scattering correlation functions: these planes contain some of the symmetry paths and points in reciprocal space.

	h	k	ℓ
Γ	0	0	0
X	0	2	0
U	1/2	2	1/2
W	1	2	0
K	3/2	3/2	0
L	1	1	1

Table C.1: High-symmetry points

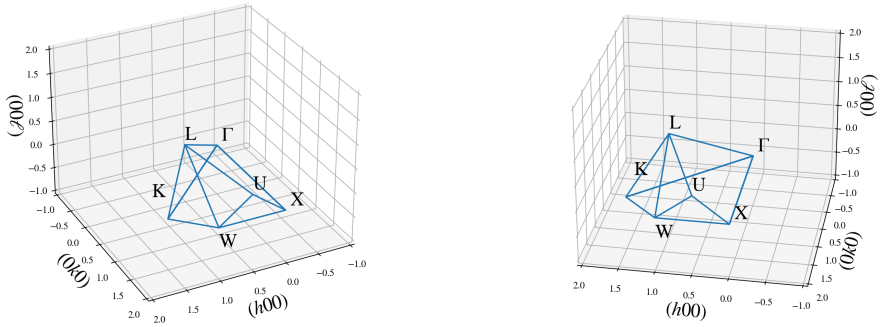


Figure C.2: 3D high-symmetry paths and points illustrated in different two perspectives.

Appendix D

Classical Low-Temperature Expansion in a Field

In this appendix we present an extension of the classical low-temperature expansion (CLTE) in a field. Starting from what was done in Section. 3.2, we now consider the application of a magnetic field $\boldsymbol{B}$ through a Zeeman coupling

$$\mathcal{H}_Z = -\mu_B \sum_{ia} \boldsymbol{B} \cdot \boldsymbol{\mu}_{ia} = -\mu_B \sum_{ia} \sum_{\alpha,\beta} B^{\alpha} g_a^{\alpha,\beta} S_{ia}^{\beta}, \tag{D.1}$$

where $g_a^{\alpha,\beta}$ is the g tensor of sublattice a. To introduce this term into the low temperature expansion, one has to consider the spins along the ordering direction as in Eq. (3.6). Since the magnetic field in Eq. (D.1) is defined in the global frame and the spins in the CLTE are taken in the local ordering frame, to take the dot product, we express the spin in the global frame as the rotated spins in the local frame

$$\begin{aligned} \mathbf{S}_a^{\text{global}} &= R_a^T \mathbf{S}_a^{\text{local}} \\ S_a^{\beta,\text{global}} &= \sum_{\gamma} (R_a^T)^{\beta,\gamma} S_a^{\gamma,\text{local}} \\ &= \sum_{\gamma} R_a^{\gamma,\beta} S_a^{\gamma,\text{local}}. \end{aligned}$$

Introducing this notation into Eq. (D.1) one obtains

$$\begin{aligned}\mathcal{H}_Z &= -\mu_B \sum_{ia} \sum_{\gamma} \left[\sum_{\alpha,\beta} H^{\alpha} \cdot g_a^{\alpha,\beta} R_a^{\gamma,\beta} \right] S_{ia}^{\gamma} \\ &= -\mu_B \sum_{ia} \sum_{\gamma} \tilde{H}_a^{\gamma} S_{ia}^{\gamma} \end{aligned} \tag{D.2}$$

where we have defined the effective local magnetic field $\tilde{H}_a$ as

$$\tilde{H}_a^{\gamma} = \sum_{\alpha,\beta} H^{\alpha} \cdot g_a^{\alpha,\beta} R_a^{\gamma,\beta}.$$

The expression above can be easily included into the low temperature expansion in Eq. (3.9) as it would only contain quadratic terms corresponding to the same sublattice. In other words,

$$\begin{aligned}\mathcal{H}_Z^{(2)} &= \frac{\mu_B}{2S} \sum_{ia} \tilde{H}_a^z \left((\delta n_{ia}^x)^2 + (\delta n_{ia}^y)^2 \right) \\ &= \frac{\mu_B}{2S} \sum_{ia} \sum_{\alpha} \tilde{H}_a^z (\delta n_{ia}^{\alpha})^2, \end{aligned} \tag{D.3}$$

while also including a correction to the classical ground state energy

$$\mathcal{H}_Z^{(0)} = -NS\mu_B \sum_a \tilde{H}_a^z.$$

Finally, by introducing a Fourier transform the Zeeman term becomes

$$\begin{aligned}\mathcal{H}_Z^{(2)} &= \frac{\mu_B}{2S} \sum_{ia} \sum_{\alpha} \tilde{H}_a^z (\delta n_{ia}^{\alpha})^2 \\ &= \frac{\mu_B}{2SN} \sum_{ia} \tilde{H}_a^z \sum_{\alpha} \sum_{\mathbf{q},\mathbf{k}} \delta n_a^{\alpha}(\mathbf{q}) \delta n_a^{\alpha}(\mathbf{k}) e^{i(\mathbf{q}+\mathbf{k})\cdot \mathbf{R}_{ia}} \\ &= \frac{\mu_B}{2S} \sum_{a} \tilde{H}_a^z \sum_{\alpha} \sum_{\mathbf{k}} \delta n_a^{\alpha}(-\mathbf{k}) \delta n_a^{\alpha}(\mathbf{k}). \end{aligned} \tag{D.4}$$

It is important to note that the application of a magnetic field will in general change the ground state configuration and therefore the ordered basis defined in Eq. (3.6) which is used in this approximation. For example, for the nearest-neighbor Hamiltonian in the pyrochlore lattice, the $\boldsymbol{q} = \mathbf{0}$ modes are generally expected to be modified and therefore will not be characterized by the irrep modes of T_d[1]. The ground state spin configurations can be obtained numerically by an iterative minimization approach described in Section 3.5.

[1]This is a consequence of breaking the tetrahedral symmetry when applying a field.

Appendix E

Interaction Parameters Basis

As mentioned in Chapters 2 and 3, there are multiple interaction parameter basis used in the literature to describe the most general nearest-neighbor Hamiltonian. Here we provide the transformation which relate the three basis discussed in this thesis, namely the local basis $\{J_{zz}, J_{\pm}, J_{\pm\pm}, J_{z\pm}\}$, $\{J_1, J_2, J_3, J_4\}$, $\{J, J_{\rm Pd}, J_{\rm Ising}, J_{\rm DM}\}$. These transformations can also be found in Refs. [70, 74]. $\{J, J_{\rm Pd}, J_{\rm Ising}, J_{\rm DM}\}$ to $\{J_1, J_2, J_3, J_4\}$.

$$J = J_1 - J_3, \tag{E.1}$$
$$J_{\rm Ising} = -3J_1 + 3J_2 + 3J_3, \tag{E.2}$$
$$J_{\rm Pd} = -2J_1 + 2J_2 + 4J_3, \tag{E.3}$$
$$J_{\rm DM} = -J_1 + J_2 + J_3 + J_4, \tag{E.4}$$

or equivalently

$$J_1 = J - \frac{1}{3}J_{\rm Ising} + \frac{1}{2}J_{\rm Pd}, \tag{E.5}$$
$$J_2 = J + \frac{1}{3}J_{\rm Ising}, \tag{E.6}$$
$$J_3 = -\frac{1}{3}J_{\rm Ising} + \frac{1}{2}J_{\rm Pd}, \tag{E.7}$$
$$J_4 = -\frac{1}{3}J_{\rm Ising} + J_{\rm DM}. \tag{E.8}$$

$\{J_1, J_2, J_3, J_4\}$ to $\{J_{zz}, J_{\pm}, J_{\pm\pm}, J_{z\pm}\}$

$$J_{zz} = -\frac{1}{3}\left(2J_1 - J_2 + 2J_3 + 4J_4\right), \tag{E.9}$$

$$J_{\pm} = \frac{1}{6}\left(2J_1 - J_2 - J_3 - 2J_4\right), \tag{E.10}$$

$$J_{\pm\pm} = \frac{1}{6}\left(J_1 + J_2 - 2J_3 + 2J_4\right), \tag{E.11}$$

$$J_{z\pm} = \frac{1}{3\sqrt{2}}\left(J_1 + J_2 + J_3 - J_4\right) \tag{E.12}$$

or equivalently

$$J_1 = \frac{1}{3}\left(-J_{zz} + 4J_{\pm} + 2J_{\pm\pm} + 2\sqrt{2}J_{z\pm}\right), \tag{E.13}$$

$$J_2 = \frac{1}{3}\left(J_{zz} - 4J_{\pm} + 4J_{\pm\pm} + 4\sqrt{2}J_{z\pm}\right), \tag{E.14}$$

$$J_3 = \frac{1}{3}\left(-J_{zz} - 2J_{\pm} - 4J_{\pm\pm} + 2\sqrt{2}J_{z\pm}\right), \tag{E.15}$$

$$J_4 = \frac{1}{3}\left(-J_{zz} - 2J_{\pm} + 2J_{\pm\pm} - \sqrt{2}J_{z\pm}\right). \tag{E.16}$$

$$\tag{E.17}$$

Appendix F

Linear Spin Wave Theory

Here we provide the full derivation of the inelastic neutron structure factor obtained through linear spin wave theory following the results presented in Section 3.3.

After having identified the quadratic Hamiltonian and the Bogoliubov transformation used to find its eigenvalues, one may be interested in obtaining the correlator associated with the transverse components. To define this correlator, it is useful to express the spin components in terms of the bosonic operators

$$\begin{aligned} \hat{S}_a^x(\boldsymbol{q}) &= \sqrt{\frac{S}{2}}\left(\hat{c}_a(\boldsymbol{q}) + \hat{c}_a^\dagger(-\boldsymbol{q})\right), \\ \hat{S}_a^y(\boldsymbol{q}) &= -i\sqrt{\frac{S}{2}}\left(\hat{c}_a(\boldsymbol{q}) - \hat{c}_a^\dagger(-\boldsymbol{q})\right), \end{aligned} \tag{F.1}$$

such that the correlation function can be written as

$$\langle \hat{S}_a^\alpha(-\boldsymbol{q})\hat{S}_b^\beta(\boldsymbol{q})\rangle = \frac{S}{2} I_\alpha I_\beta \left\langle \left(\hat{c}_a(-\boldsymbol{q}) + p_\alpha \hat{c}_a^\dagger(\boldsymbol{q})\right)\left(\hat{c}_b(\boldsymbol{q}) + p_\beta \hat{c}_b^\dagger(-\boldsymbol{q})\right)\right\rangle,$$

where $I_x = 1$, $I_y = -i$, $p_x = 1$ and $p_y = -1$. Based on this correlation function, one can compute different quantities of interest. For example, we are interested in obtaining the inelastic neutron scattering which describe the possible excitations observed in the system. This quantity can be obtained by computing

$$S(\boldsymbol{q},\omega) = \sum_{a,b}\sum_{\alpha,\beta}\sum_{\gamma,\phi} \underbrace{\left(\delta_{\alpha,\beta} - \frac{q_\alpha q_\beta}{\boldsymbol{q}^2}\right)}_{\text{projection factor}} R_a^{\alpha,\gamma} R_b^{\beta,\phi} \langle \hat{S}_a^\gamma(-\boldsymbol{q},-\omega)\hat{S}_b^\phi(\boldsymbol{q},\omega)\rangle,$$

where we have added the neutron projection discussed in Appendix B and the rotation matrices to take the correlation function in the lab frame[1]. All together, the expression for the inelastic neutron scattering can be written

$$
\begin{aligned}
S(\boldsymbol{q},\omega) &= \sum_{a,b}\sum_{\alpha,\beta}\sum_{\gamma,\phi}\left(\delta_{\alpha,\beta}-\frac{q_\alpha q_\beta}{\boldsymbol{q}^2}\right)R_a^{\alpha,\gamma}R_b^{\beta,\phi} \\
&\quad\times\frac{S}{2}I_\gamma I_\phi\left\langle\left(\hat{c}_a(-\boldsymbol{q},-\omega)+p_\gamma\hat{c}_a^\dagger(\boldsymbol{q},\omega)\right)\left(\hat{c}_b(\boldsymbol{q},\omega)+p_\phi\hat{c}_b^\dagger(-\boldsymbol{q},-\omega)\right)\right\rangle \\
&= \sum_{a,b}\sum_{\alpha,\beta}\left(\delta_{\alpha,\beta}-\frac{q_\alpha q_\beta}{\boldsymbol{q}^2}\right) \\
&\quad\times\frac{S}{2}\left\langle\begin{pmatrix}\hat{c}_a^\dagger(\boldsymbol{q},\omega) & \hat{c}_a(-\boldsymbol{q},-\omega)\end{pmatrix}\underbrace{\sum_{\gamma,\phi}I_\gamma I_\phi\begin{pmatrix}p_\gamma R_a^{\alpha,\gamma}R_b^{\beta,\phi} & p_\gamma p_\phi R_a^{\alpha,\gamma}R_b^{\beta,\phi}\\ R_a^{\alpha,\gamma}R_b^{\beta,\phi} & p_\phi R_a^{\alpha,\gamma}R_b^{\beta,\phi}\end{pmatrix}}_{M_{a,b}^{\alpha,\beta}}\begin{pmatrix}\hat{c}_b(\boldsymbol{q},\omega)\\ \hat{c}_b^\dagger(-\boldsymbol{q},-\omega)\end{pmatrix}\right\rangle \\
&= \frac{S}{2}\sum_{a,b}\sum_{\alpha,\beta}\left(\delta_{\alpha,\beta}-\frac{q_\alpha q_\beta}{\boldsymbol{q}^2}\right)\left\langle\begin{pmatrix}\hat{c}_a^\dagger(\boldsymbol{q},\omega) & \hat{c}_a(-\boldsymbol{q},-\omega)\end{pmatrix}M_{a,b}^{\alpha,\beta}\begin{pmatrix}\hat{c}_b(\boldsymbol{q},\omega)\\ \hat{c}_b^\dagger(-\boldsymbol{q},-\omega)\end{pmatrix}\right\rangle.
\end{aligned}
$$

Note that $M_{a,b}^{\alpha,\beta}$ are the components of an 8×8 matrix dependent of the parameters α and β. Therefore, using this identification, one can write the above expression as

$$
\begin{aligned}
S(\boldsymbol{q},\omega) &= \frac{S}{2}\sum_{a,b}\sum_{\alpha,\beta}\left(\delta_{\alpha,\beta}-\frac{q_\alpha q_\beta}{\boldsymbol{q}^2}\right)\left\langle\begin{pmatrix}\hat{c}_a^\dagger(\boldsymbol{q},\omega) & \hat{c}_a(-\boldsymbol{q},-\omega)\end{pmatrix}M_{a,b}^{\alpha,\beta}\begin{pmatrix}\hat{c}_b(\boldsymbol{q},\omega)\\ \hat{c}_b^\dagger(-\boldsymbol{q},-\omega)\end{pmatrix}\right\rangle \\
&= \frac{S}{2}\sum_{\alpha,\beta}\left(\delta_{\alpha,\beta}-\frac{q_\alpha q_\beta}{\boldsymbol{q}^2}\right)\left\langle X^\dagger(\boldsymbol{q},\omega)\mathbf{M}^{\alpha,\beta}X(\boldsymbol{q},\omega)\right\rangle \\
&= \frac{S}{2}\sum_{\alpha,\beta}\left(\delta_{\alpha,\beta}-\frac{q_\alpha q_\beta}{\boldsymbol{q}^2}\right)\left\langle Y^\dagger(\boldsymbol{q},\omega)\left[\sigma U^{-1}\sigma\mathbf{M}^{\alpha,\beta}U\right]Y(\boldsymbol{q},\omega)\right\rangle.
\end{aligned}
$$

where we have used the Bogoliubov transformation to express the vector X in terms of the magnon bosons Y [70, 74] recalling that

$$
\begin{aligned}
X(\boldsymbol{q}) &= UY(\boldsymbol{q}) \\
X^\dagger(\boldsymbol{q}) &= Y^\dagger(\boldsymbol{q})U^\dagger \\
&= Y^\dagger(\boldsymbol{q})\sigma U^{-1}\sigma,
\end{aligned}
$$

[1]This rotation is necessary as the spins are defined along their local ordering direction.

as is discussed in detail in Section 3.3. Note that, since the Hamiltonian described is diagonal in the basis defined by $Y(\boldsymbol{q})$, the system can effectively be described as a harmonic oscillator with decoupled eigenvectors; therefore, the only non vanishing quadratic terms are the ones involving the same sublattice operators, *i.e.* terms describing the same boson

$$\begin{aligned}\langle Y_{a+s}(-\boldsymbol{q},-\omega)Y_a(\boldsymbol{q},\omega)\rangle &= \langle \hat{d}_a^\dagger(\boldsymbol{q},\omega)\hat{d}_a(\boldsymbol{q},\omega)\rangle \simeq n_{\mathrm{BE}}(\epsilon_a)\delta(\omega-\epsilon_a)\\ \langle Y_a(-\boldsymbol{q},-\omega)Y_{a+s}(\boldsymbol{q},\omega)\rangle &= \langle \hat{d}_a(\boldsymbol{q},\omega)\hat{d}_a^\dagger(\boldsymbol{q},\omega)\rangle \simeq (1+n_{\mathrm{BE}}(\epsilon_a))\delta(\omega-\epsilon_a),\end{aligned} \tag{F.2}$$

where $n_{\mathrm{BE}}(\epsilon_a)$ is the Bose-Einstein distribution evaluated at the energy ϵ_a. Given the average above, it is clear that only the diagonal components of the resulting matrix contribute to the overall result as all other terms will have a vanishing expectation value. In other words, if we define

$$\tilde{\mathbf{M}}^{\alpha,\beta} = \sigma U^{-1}\sigma \mathbf{M}^{\alpha,\beta} U$$

the inelastic neutron scattering can be written

$$\begin{aligned}S(\boldsymbol{q},\omega) &= \frac{S}{2}\sum_{\alpha,\beta}\left(\delta_{\alpha,\beta}-\frac{q_\alpha q_\beta}{\boldsymbol{q}^2}\right)\left\langle Y^\dagger(\boldsymbol{q},\omega)\left[\tilde{\mathbf{M}}^{\alpha,\beta}\right]Y(\boldsymbol{q},\omega)\right\rangle\\ &= \frac{S}{2}\sum_{\alpha,\beta}\left(\delta_{\alpha,\beta}-\frac{q_\alpha q_\beta}{\boldsymbol{q}^2}\right)\sum_a\left[n_{\mathrm{BE}}(\epsilon_a)\delta(\omega-\epsilon_a)\tilde{\mathbf{M}}^{\alpha,\beta}_{a,a}+(1+n_{\mathrm{BE}}(\epsilon_a))\delta(\omega-\epsilon_a)\tilde{\mathbf{M}}^{\alpha,\beta}_{a+s,a+s}\right].\end{aligned}$$

In other words, the intensity of each band can be described by contributions given by each magnon mode weighted by the Bose-Einstein distribution. After having an expression for the inelastic neutron scattering, one can compute the equal-time neutron scattering as an energy integrated inelastic neutron scattering. In other words,

$$\begin{aligned}S(\boldsymbol{q}) &= S(\boldsymbol{q},0)\\ &= \int_0^\infty S(\boldsymbol{q},\omega)e^{i\omega\cdot 0}d\omega = \int_0^\infty S(\boldsymbol{q},\omega)d\omega.\end{aligned} \tag{F.3}$$

Appendix G

High Temperature Series Expansion

In this appendix we provide a high-temperature series expansion calculation for order parameter susceptibility. The results shown here are referred to in Ref. [1]. Broadly speaking, this approach is based on a Taylor series of the exponential function. Consider the Heisenberg and Dzyaloshinskii-Moriya (DM) Hamiltonian

$$\begin{aligned}\mathcal{H} &= \underbrace{J\sum_{\langle i,j\rangle}\boldsymbol{S}_i\cdot\boldsymbol{S}_j}_{\mathbb{J}} + \underbrace{J_{\mathrm{DM}}\sum_{\langle i,j\rangle}\boldsymbol{D}_{ij}\left(\boldsymbol{S}_i\times\boldsymbol{S}_j\right)}_{\mathbb{D}} + \underbrace{\sum_t h_t M_t}_{\mathbb{M}} \\ &\equiv \mathbb{J}+\mathbb{D}+\mathbb{M}, \end{aligned} \tag{G.1}$$

and the expansion for the free energy (divided by $-k_{\mathrm{B}}T$)

$$\begin{aligned}\ln(\mathcal{Z}) &= \ln\left(\mathrm{Tr}\left\{\mathrm{e}^{-\beta(\mathbb{J}+\mathbb{D}+\mathbb{M})}\right\}\right) \\ &= \ln\left(\mathrm{Tr}\left\{1+\sum_{\mathrm{n}\geq 1}\frac{(-\beta)^{\mathrm{n}}}{\mathrm{n!}}(\mathbb{J}+\mathbb{D}+\mathbb{M})^{\mathrm{n}}\right\}\right) \\ &= \ln\left((2S+1)^N\left(1+\sum_{n\geq 1}\frac{(-\beta)^n}{n!}\mathrm{Tr}\left\{\frac{(\mathbb{J}+\mathbb{D}+\mathbb{M})^{\mathrm{n}}}{(2\mathrm{S}+1)^{\mathrm{N}}}\right\}\right)\right) \\ &= N\ln(2S+1)+\ln\left(1+\sum_{n\geq 1}\frac{(-\beta)^n}{n!}\mu_n\right) \\ &= N\ln(2S+1)+\sum_{n\geq 1}\frac{(-\beta)^n}{n!}\lambda_n, \end{aligned} \tag{G.2}$$

where λ_n are the cumulants related to μ_n. For example, the first cumulants [169] are

$$\begin{aligned}\lambda_1 &= \mu_1,\\ \lambda_2 &= \mu_2 - \mu_1^2,\\ \lambda_3 &= \mu_3 - 3\mu_1\mu_2 + 2\mu_1^3,\\ \vdots &= \vdots.\end{aligned}$$

In the above expressions, the third term in Eq. (G.1) is added according to the method of sources [170] to measure the susceptibility associated with M[1],

$$\chi_M = \frac{\langle M^2\rangle - \langle M\rangle^2}{k_{\rm B}T}, \tag{G.3}$$

which may be obtained by computing

$$\begin{aligned}\chi_M &= \frac{1}{\beta}\frac{\partial^2}{\partial h^2}\ln(\mathcal{Z})\Big|_{h=0}\\ &= \frac{1}{\beta}\left[\sum_{n\geq 1}\frac{(-\beta)^n}{n!}\frac{\partial^2}{\partial h^2}\lambda_n\right]\Big|_{h=0}\\ &= -\frac{\partial^2}{\partial h^2}\lambda_1 + \frac{\beta}{2}\frac{\partial^2}{\partial h^2}\lambda_2 - \frac{\beta^2}{6}\frac{\partial^2}{\partial h^2}\lambda_3 + \mathcal{O}(\beta^3)\Big|_{h=0}.\end{aligned} \tag{G.4}$$

Note that the first cumulant vanishes as the dependence in h is linear

$$\frac{\partial^2}{\partial h^2}\lambda_1 = \frac{\partial^2}{\partial h^2}\mu_1 = \frac{1}{(2S+1)^N}\frac{\partial^2}{\partial h^2}\mathrm{Tr}\left(\underbrace{\mathbb{J}+\mathbb{D}+\mathbb{M}}_{\mathcal{O}(\mathrm{h})}\right) = 0. \tag{G.5}$$

On the other hand, for the second cummulant we have

$$\frac{\partial^2}{\partial h^2}\lambda_2 = \frac{\partial^2}{\partial h^2}(\mu_2 - \mu_1^2), \tag{G.6}$$

[1]In practice, this means adding a fictitious field along the direction of the vector M with which we can take derivatives to obtain its correlation functions. Note that we have dropped the label t denoting the parameter in a single tetrahedron such that $M = \sum_t M_t$.

with

$$\begin{aligned}\mu_2 &= \frac{1}{(2S+1)^N}\mathrm{Tr}\left(\mathbb{J}+\mathbb{D}+\mathbb{M}\right)^2 \\ &= \frac{1}{(2S+1)^N}\left(\mathrm{Tr}(\mathbb{M}^2+\mathbb{J}\mathbb{M}+\mathbb{D}\mathbb{M}++\mathbb{M}\mathbb{J}+\mathbb{M}\mathbb{D}+\mathcal{O}(1))\right) \\ &= \frac{1}{(2S+1)^N}\left(\mathrm{Tr}(\mathbb{M}^2)+\mathcal{O}(\mathrm{h})+\mathcal{O}(1)\right). \end{aligned} \tag{G.7}$$

Note, however, that a second derivative with respect to h will make all terms which are not quadratic in h vanish (as the subsequent step would be to evaluate at $h=0$). Finally, and by a similar argument, we compute

$$\mu_1^2 = \frac{1}{(2S+1)^{2N}}\mathrm{Tr}(\mathbb{M})^2+\mathcal{O}(\mathrm{h})+\mathcal{O}(1). \tag{G.8}$$

Equipped with the above results we may express the susceptibility related to the spin configuration M_t, to order β, as

$$\chi_M = \frac{\beta}{2}\left[\frac{1}{(2S+1)^N}\frac{\partial^2}{\partial h^2}\mathrm{Tr}(\mathbb{M}^2)-\frac{1}{(2\mathrm{S}+1)^{2\mathrm{N}}}\underbrace{\frac{\partial^2}{\partial h^2}\mathrm{Tr}(\mathbb{M})^2}_{=0}\right]+\mathcal{O}(\beta), \tag{G.9}$$

where the second term in the expression vanishes as M is assumed to be linear in the spin variables. The next order term in the series is given by λ_3 which due to the fact that $\mu_1=0$, simplifies to

$$\begin{aligned}\lambda_3=\mu_3 &= \frac{1}{(2S+1)^N}\mathrm{Tr}\left(\underbrace{\{(\mathbb{J}+\mathbb{D})\mathbb{M},\mathbb{M}\}}_{\mathrm{Anti-commutator}}\right) \\ &= \frac{1}{(2S+1)^N}\mathrm{Tr}\left((\mathbb{J}+\mathbb{D})\mathbb{M}\mathbb{M}+\mathbb{M}(\mathbb{J}+\mathbb{D})\mathbb{M}\right) \\ &= \frac{2}{(2S+1)^N}\mathrm{Tr}\left((\mathbb{J}+\mathbb{D})\mathbb{M}\mathbb{M}\right). \end{aligned} \tag{G.10}$$

Therefore, to order β^3 the susceptibility is

$$\begin{aligned}\chi_M &= \frac{\beta}{2}\frac{1}{(2S+1)^N}\frac{\partial^2}{\partial h^2}\mathrm{Tr}(\mathbb{M}^2)-\frac{\beta^2}{3}\frac{1}{(2\mathrm{S}+1)^{\mathrm{N}}}\frac{\partial^2}{\partial \mathrm{h}^2}\mathrm{Tr}\left((\mathbb{J}+\mathbb{D})\mathbb{M}\mathbb{M}\right)+\mathcal{O}(\beta^3) \\ &= \frac{1}{(2S+1)^N}\left[\frac{\beta}{2}\frac{\partial^2}{\partial h^2}\mathrm{Tr}(\mathbb{M}^2)-\frac{\beta^2}{3}\frac{\partial^2}{\partial \mathrm{h}^2}\mathrm{Tr}\left((\mathbb{J}+\mathbb{D})\mathbb{M}\mathbb{M}\right)\right]+\mathcal{O}(\beta^3). \end{aligned} \tag{G.11}$$

Before proceeding with the calculation for a specific order parameter, or field, M we may note the following useful properties of the trace for a spin-1/2 system

$$\mathrm{Tr}(S_i^\alpha) = 0,$$

for $\alpha \in \{x, y, z\}$ and i any lattice point. Moreover, and recalling that the square of any Pauli operator is equal to the identity matrix, we have

$$\mathrm{Tr}(S_i^\alpha S_j^\beta) = \frac{\hbar^2}{2}\delta_{ij}\delta^{\alpha\beta}. \tag{G.12}$$

As a consequence, we note that, for the first in Eq. (G.11), only terms as $M \cdot M$ contribute as all other terms have mixed site indices and therefore vanish, see Eq. (G.12). A similar case is observed for the second term of Eq. (G.11): provided that M is a linear combination of the spin operators in a single tetrahedron, only the terms proportional to $\mathrm{Tr}(S_i^\alpha \mathcal{H}_{ij}^{\alpha\beta} S_j^\beta S_i^\alpha S_j^\beta)$ do not vanish. In fact, this expression can be readily evaluated by noting

$$\begin{aligned}
\mathrm{Tr}(S_i^\alpha \mathcal{H}_{ij}^{\alpha\beta} S_j^\beta S_i^\alpha S_j^\beta) &= \mathcal{H}_{ij}^{\alpha\beta}\mathrm{Tr}(S_i^\alpha S_i^\alpha S_j^\beta S_j^\beta) \\
&= \mathcal{H}_{ij}^{\alpha\beta}\mathrm{Tr}_i(S_i^\alpha S_i^\alpha)\mathrm{Tr}_j(S_j^\beta S_j^\beta) \\
&= \mathcal{H}_{ij}^{\alpha\beta}\frac{\hbar^4}{4}.
\end{aligned} \tag{G.13}$$

From these results we can see that (i) the first term of Eq. (G.11) produces a "norm" or normalization of the order parameter or field and (ii) the computation of the trace is equivalent to the sum of the different spin-spin interaction terms produced by the combination of the spin operators and the M order parameter. For instance, consider the order parameter related to one of the T_1 co-planar states

$$m_{xy}^{T_1} = \frac{1}{\sqrt{2}}\left(-S_0^x + S_1^x - S_2^x + S_3^x - S_0^y + S_1^y + S_2^y - S_3^y\right). \tag{G.14}$$

From the above observations, we see that the trace of the square of the above order parameter is equivalent to

$$\begin{aligned}
\mathrm{Tr}\left((m_{xy}^{T_1})^2\right) &= \frac{1}{2}\mathrm{Tr}\left(\sum_a (S_a^x)^2 + \sum_a (S_a^y)^2\right) \\
&= \sum_a \mathrm{Tr}\left((S_a^x)^2\right) \\
&= 4\frac{\hbar^2}{2} = 2\hbar^2,
\end{aligned} \tag{G.15}$$

where a, b denote the sublattice indices. On the other hand, and recalling that there are no self-interactions, i.e. $\mathcal{H}_{aa}^{\alpha\beta} = 0$, we only have to calculate the different contributions from the diagonal contributions. For the Heisenberg and Dzyaloshinskii Hamiltonian, we have $\mathcal{H}_{ab}^{\alpha\alpha} = J$. A trick for counting all the contributions from these type of terms is to consider the sign product matrix

$$\text{sign}(S_a^x, S_b^x) = \begin{pmatrix} 0 & -1 & +1 & -1 \\ -1 & 0 & -1 & +1 \\ +1 & -1 & 0 & -1 \\ -1 & +1 & -1 & 0 \end{pmatrix} \tag{G.16}$$

and sum the components of this matrix. This matrix is constructed by assigning the sign of a component by the sign of the term in the product $S_a^x H_{ab}^{\alpha,\beta} S_b^x S_a^x S_b^x$ resulting from the product $S_a^x H_{ab}^{\alpha,\beta} S_b^x m_{xy}^{T_1} m_{xy}^{T_1}$. Note that the diagonal vanishes from our previous observation where no on-site (diagonal) terms exist. For this case, the sum of the components of the sign product matrix gives a total of -4. In other words,

$$2 \times \text{Tr} \left(\sum_{ab} S_a^x H_{ab}^{x,x} S_b^x m_{xy}^{T_1} m_{xy}^{T_1} \right) = -4J \frac{\hbar^4}{4}, \tag{G.17}$$

where the factor 2 on the left hand side is included as we have not included the factor $1/\sqrt{2}$ in Eq. (G.14). An equivalent argument can be used to calculate the contribution from the y components of the spin, producing an analogous result. Therefore, we have

$$2 \times \text{Tr} \left(\sum_{\alpha} \sum_{ab} S_a^\alpha H_{ab}^{\alpha,\alpha} S_b^\alpha m_{xy}^{T_1} m_{xy}^{T_1} \right) = -2J\hbar^4. \tag{G.18}$$

Lastly, we consider the mixed terms which couple the x and y components of the field by considering the sign product matrix

$$\text{sign}(S_a^x, S_b^y) = \begin{pmatrix} 0 & -1 & +1 & -1 \\ -1 & 0 & -1 & +1 \\ -1 & +1 & 0 & +1 \\ +1 & -1 & +1 & 0 \end{pmatrix} = \underbrace{\begin{pmatrix} 0 & 0 & +1 & -1 \\ 0 & 0 & -1 & +1 \\ -1 & +1 & 0 & 0 \\ +1 & -1 & 0 & 0 \end{pmatrix}}_{\text{antisymmetric}} + \underbrace{\begin{pmatrix} 0 & -1 & 0 & 0 \\ -1 & 0 & 0 & 0 \\ 0 & 0 & 0 & +1 \\ 0 & 0 & +1 & 0 \end{pmatrix}}_{\text{symmetric}}. \tag{G.19}$$

Note that the mixed coupling stemming from the DM interaction are antisymmetric in the spin components for a given spin-spin interaction term $a - b$, i.e. $H_{ab}^{x,y} = -H_{ba}^{x,y}$.

Therefore, the *symmetric* contribution from the above matrix vanish when considering the corresponding coupling. On the other hand, by considering the couplings, we have

$$\begin{aligned} H^{x,y}_{0,2} &= -J_{\rm DM} \\ H^{x,y}_{0,3} &= J_{\rm DM} \\ H^{x,y}_{1,2} &= J_{\rm DM} \\ H^{x,y}_{1,3} &= -J_{\rm DM}. \end{aligned}$$

Therefore, we find that

$$2 \times {\rm Tr} \left(\sum_{\substack{\alpha,\beta \\ \alpha \neq \beta}} \sum_{ab} S^{\alpha}_{a} H^{\alpha,\beta}_{ab} S^{\beta}_{b} m^{T_1}_{xy} m^{T_1}_{xy} \right) = -(4 \times 2 \times 2) J_{\rm DM} \frac{\hbar^4}{4} = -4 J_{\rm DM} \hbar^4, \quad \text{(G.20)}$$

where the factor 4 comes from the contribution of the upper triangular terms in the sign matrix, the first factor 2 comes from the equivalent contribution from the lower triangular terms, and the second factor 2 in the parenthesis comes from considering an equivalent contributions from $S^{y}_{a} S^{x}_{b}$.

From these results, Eq. (G.15), Eq. (G.18) and Eq. (G.20), allow to rewrite the susceptibility for the $m^{T_1}_{xy}$ order parameter as[2]

$$\chi_{m^{T_1}_{xy}} = \frac{N_{\boxtimes}}{(2S+1)^N} \left[\frac{\beta}{2} 2\hbar^2 + \frac{\beta^2}{3} (J + 2J_{\rm DM}) \hbar^4 \right] + \mathcal{O}(\beta^3)., \quad \text{(G.21)}$$

where $N_{\boxtimes}$ is the number of tetrahedra in the pyrochlore lattice.

After having derived an expression for the susceptibility for *one* of the possible orders of the co-planar state, it is natural to seek an the extension to the other possible orders. For example,

$$m^{T_1}_{yz} = \frac{1}{\sqrt{2}} \left(-S^{y}_{0} - S^{y}_{1} + S^{y}_{2} + S^{y}_{3} - S^{z}_{0} + S^{z}_{1} - S^{z}_{2} + S^{z}_{3} \right). \quad \text{(G.22)}$$

It is easy to note that the square of the trace of this field will produce an equivalent contribution as for the previous case. Moreover, the only difference for this field is the

[2]Note that in this expression the normalization factor $1/\sqrt{2}$ in expression Eq. (G.14) has already been included.

fact that the terms $H_{ab}^{y,z}$ in the Hamiltonian may produce a different contribution. This difference would in turn lead us to the same counting procedure as illustrated above. In fact, note that

$$\text{sign}(S_a^y, S_b^z) = \begin{pmatrix} 0 & +1 & -1 & -1 \\ -1 & 0 & +1 & +1 \\ +1 & +1 & 0 & -1 \\ -1 & -1 & +1 & 0 \end{pmatrix} = \underbrace{\begin{pmatrix} 0 & +1 & -1 & 0 \\ -1 & 0 & 0 & +1 \\ +1 & 0 & 0 & -1 \\ 0 & -1 & +1 & 0 \end{pmatrix}}_{\text{antisymmetric}} + \underbrace{\begin{pmatrix} 0 & 0 & 0 & -1 \\ 0 & 0 & +1 & 0 \\ 0 & +1 & 0 & 0 \\ -1 & 0 & 0 & 0 \end{pmatrix}}_{\text{symmetric}}. \tag{G.23}$$

The above decomposition into the symmetric and antisymmetric part of the sign matrix is useful as the interaction $H_{ab}^{y,z}$ considering only the DM interactions is antisymmetric itself, i.e. $H_{ab}^{y,z} = -H_{ab}^{z,y}$, as a consequence, the symmetric contribution will vanish. Moreover, a peculiar result is obtained if the specific sublattice contributions are considered: since

$$\begin{aligned} H_{0,1}^{y,z} &= -J_{\text{DM}} \\ H_{0,2}^{y,z} &= J_{\text{DM}} \\ H_{1,3}^{y,z} &= -J_{\text{DM}} \\ H_{2,3}^{y,z} &= J_{\text{DM}} \end{aligned}$$

This expression produces the same type of contribution as the one computed for the order parameter $m_{xy}^{T_1}$. Therefore, we conclude

$$\chi_{m_{yz}^{T_1}} = \chi_{m_{xy}^{T_1}} = \frac{N_{\boxtimes}}{(2S+1)^N}\left[\frac{\beta}{2}2\hbar^2 + \frac{\beta^2}{3}(J+2J_{\text{DM}})\hbar^4\right] + \mathcal{O}(\beta^3). \tag{G.24}$$

Let us now consider the same quantity, but for an order parameter describing a ψ_3 order given by

$$m_{\psi_3}^E = \frac{1}{\sqrt{2}}\left(S_0^x - S_1^x - S_2^x + S_3^x - S_0^y + S_1^y - S_2^y + S_3^y\right). \tag{G.25}$$

Note that the form of this order parameter closely resembles that of the $m_{xy}^{T_1}$ order parameter. In fact, every argument used to calculate the susceptibility for this parameter is

equivalent with the exception of the cross terms where the sign product matrix is given by

$$\operatorname{sign}(S_a^x, S_b^y) = \begin{pmatrix} 0 & +1 & +1 & -1 \\ +1 & 0 & -1 & +1 \\ -1 & +1 & 0 & -1 \\ +1 & -1 & -1 & 0 \end{pmatrix} = \underbrace{\begin{pmatrix} 0 & 0 & +1 & -1 \\ 0 & 0 & -1 & +1 \\ -1 & +1 & 0 & 0 \\ +1 & -1 & 0 & 0 \end{pmatrix}}_{\text{antisymmetric}} + \underbrace{\begin{pmatrix} 0 & +1 & 0 & 0 \\ +1 & 0 & 0 & 0 \\ 0 & 0 & 0 & -1 \\ 0 & 0 & -1 & 0 \end{pmatrix}}_{\text{symmetric}}. \tag{G.26}$$

The resulting sign product matrix closely resembles the one calculated for the $m_{xy}^{T_1}$. In fact, carrying out this calculation yields

$$\chi_{m_{xy}^{T_1}} = \chi_{m_{\psi_3}^{E}}, \tag{G.27}$$

which implies that, to order β^2, the susceptibilities for both irrep modes in the Heisenberg and Dzyaloshinskii-Moriya model are exactly the same.

Appendix H

Dipolar-Octupolar Fragmentation Derivation

In this appendix, we present an analysis of the Helmholtz-Hodge decomposition similar to what was presented by Ref. [102]. Consider the Hamiltonian

$$\mathcal{H} = J \sum_{\langle ia,jb \rangle} \boldsymbol{S}_{ia} \cdot \boldsymbol{S}_{jb} + d \sum_{ia} (\boldsymbol{S}_{ia} \cdot \boldsymbol{z})^2,$$

where the indices i, j label the FCC lattice position and the indices a, b label the sublattice basis. To gain some intuition into the equations of motion for the fluctuating degrees of freedom, first, consider that the ion anisotropy term is directed along the *global* z-direction such that the ground state configuration consists on spins pointing along these directions. Lets now study the evolution of the S^x component produced by the equation of motion

$$\begin{aligned}
\partial_t S^x_{\ell c} &= i \left[\mathcal{H}, S^x_{\ell c} \right], \\
&= i \left[J \sum_{\langle ia,jb \rangle} S^y_{ia} \cdot S^y_{jb} + S^z_{ia} \cdot S^z_{jb} + d \sum_{ia} (S^z_{ia})^2, S^x_{\ell c} \right], \\
&= iJ \sum_{\langle ia,jb \rangle} \left[S^y_{ia} \cdot S^y_{jb}, S^x_{\ell c} \right] + \left[S^z_{ia} \cdot S^z_{jb}, S^x_{\ell c} \right] + id \sum_{ia} \left[(S^z_{ia})^2, S^x_{\ell c} \right].
\end{aligned}$$

To proceed, we use the following two identities

$$[AB, C] = A [B, C] + [A, C] B, \tag{H.1}$$

$$\left[S^\alpha_i, S^\beta_j \right] = i \epsilon_{\alpha\beta\gamma} S^\gamma_i \delta_{i,j}, \tag{H.2}$$

where $\hbar = 1$ is considered throughout the following calculations. Applying the identifies in Eq. (H.1)-(H.2) simplify the equations of motion to

$$\begin{aligned}
\partial_t S^x_{\ell c} &= -J \sum_{\langle ia,jb\rangle} \left(-S^y_{ia}\cdot\delta_{\ell c,jb}S^z_{\ell c} - \delta_{\ell c,ia}S^z_{\ell c}\cdot S^y_{jb} + S^z_{ia}\cdot S^y_{\ell c}\delta_{\ell c,jb} + S^z_{jb}\cdot S^y_{\ell c}\delta_{\ell c,ia}\right), \\
&\quad -d\sum_{ia}\left(S^z_{ia}S^y_{\ell c}\delta_{ia,\ell,c} + S^y_{\ell c}\delta_{ia,\ell,c}S^z_{ia}\right), \\
&= J\sum_{ia@\ell c} S^y_{ia}\cdot S^z_{\ell c} - J\sum_{ia@\ell c} S^z_{ia}\cdot S^y_{\ell c} - d(S^z_{\ell c}S^y_{\ell c} + S^y_{\ell c}S^z_{\ell c}),
\end{aligned}$$

where the $ia@\ell c$ denotes the sum of all ia neighbours of ℓc. Before continuing any further, we note that if we had only considered the Heisenberg exchange term of the Hamiltonian, the equations of motion would yield

$$\begin{aligned}
\partial_t S^x_{\ell c} &= J\left(\sum_{ia@\ell c} S^y_{ia}\cdot S^z_{\ell c} - S^z_{ia}\cdot S^y_{\ell c}\right), \\
\partial_t S^y_{\ell c} &= -J\left(\sum_{ia@\ell c} S^x_{ia}\cdot S^z_{\ell c} - S^z_{ia}\cdot S^x_{\ell c}\right).
\end{aligned}$$

Furthermore, in the ordered state and to first order in the fluctuations of the spins[1], we may assume $S^z_{ia} \sim S$, simplifying the above equation to

$$\begin{aligned}
\partial_t S^x_{\ell c} &= JS\left(\sum_{ia@\ell c} S^y_{ia} - S^y_{\ell c}\right), \\
\partial_t S^y_{\ell c} &= -JS\left(\sum_{ia@\ell c} S^x_{ia} - S^x_{\ell c}\right).
\end{aligned}$$

Moreover, since the above computation is done by considering the ordering direction along the z-direction, all other components will only produce infinitesimal contributions. In addition to the simplifications considered above, we may simplify the expressions in terms of lattice vector calculus: the first term of this sum can be taken as the "outgoing flux" at site ℓc. In fact, this term can be expressed in terms of a lattice gradient and divergence in the following way

$$\sum_{ia@\ell c}\left(S^y_{ia} - S^y_{\ell c}\right) = \nabla\cdot(\nabla S^y_{\ell c}) = \nabla^2 S^y_{\ell c}. \tag{H.3}$$

[1]This argument is similar to the one presented in Section 3.3

Further details of this vector calculus can be found in Ref. [171]. Note that this representation is especially useful when considering spin-ice and its representation in gauge fields[2]. Using the lattice calculus representation, the equation of motion for the S^x spin components can be expressed in the following way

$$\partial_t S^x_{\ell c} = JS\nabla\cdot(\nabla S^y_{\ell c}) - 2SdS^y_{\ell c}, \tag{H.4}$$

Similarly, the equation of motion for the S^y spin components is obtained

$$\partial_t S^y_{\ell c} = -JS\nabla\cdot(\nabla S^x_{\ell c}) + 2SdS^x_{\ell c}. \tag{H.5}$$

Note that the effect of adding the single-ion anisotropy term into the above equation is to introduce an extra term $\propto S^{x,y}$, which does not produce any extra $\boldsymbol{q}$-dependence when applying a Fourier transform. This procedure is further exemplified in Ref. [167] where a Heisenberg model with an applied field along the global z-direction is applied.

Now, let us introduce the Helmholtz-Hodge decomposition where a vector field $\boldsymbol{M}_t$ can be written in the following way

$$\boldsymbol{M}_t = \nabla\psi + \nabla\times\boldsymbol{A} + \boldsymbol{W}, \tag{H.6}$$

where the first term is divergence-full, the second is divergence-free and the last term refers to the *harmonic* contribution. If the harmonic part is neglected, when applying this identity to the spin degrees of freedom, one can independently find a solution for ψ and $\boldsymbol{A}$. Furthermore, it has been established that the existence of the $\boldsymbol{A}$ field is related to the observation of Coulomb-like correlations [102]. We are interested in applying the Helmholtz-Hodge decomposition to the above models in the diamond lattice, the parent lattice of the pyrochlore lattice. To do so, we consider the magnetization on every tetrahedron $\boldsymbol{M}$ defined as

$$\boldsymbol{M}_t = \sum_{i\in t}\boldsymbol{S}_i, \tag{H.7}$$

where t label a tetrahedron surrounding one site of the diamond lattice. Here, we simplify the notation by considering $ia \to i$ to avoid a clutter of variables. Before continuing,

[2]This identification can be made as the pyrochlore lattice is the dual of the diamond lattice where the spins in the pyrochlore lattice are located on the bonds defining the diamond lattice. In other words, the 0-simplexes in the pyrochlore lattice are taken as 1-simplexes on the diamond lattice [171]. As such, the gradient defined above is taken in the diamond lattice.

consider the following expression related to the Laplacian of such degrees of freedom

$$\begin{aligned}
\sum_{t'@t}(\boldsymbol{M}_{t'}-\boldsymbol{M}_t) &= \sum_{t'@t}\boldsymbol{M}_{t'}-z^{\text{Diamond}}\sum_{i\in t}\boldsymbol{S}_i,\\
&= \sum_{i\in t}\sum_{j@i}\boldsymbol{S}_j-(z^{\text{Diamond}}-2)\sum_{i\in t}\boldsymbol{S}_i-z^{\text{Diamond}}\sum_{i\in t}\boldsymbol{S}_i,\\
&= \sum_{i\in t}\sum_{j@i}\boldsymbol{S}_j-(2z^{\text{Diamond}}-2)\sum_{i\in t}\boldsymbol{S}_i,\\
&= \sum_{i\in t}\sum_{j@i}\boldsymbol{S}_j-z^{\text{Pyrochlore}}\sum_{i\in t}\boldsymbol{S}_i,\\
&= \sum_{i\in t}\sum_{j@i}(\boldsymbol{S}_j-\boldsymbol{S}_i),
\end{aligned}\tag{H.8}$$

where $z^{\text{Diamond}}=4$ and $z^{\text{Pyrochlore}}=6$ are the coordination numbers of the corresponding lattices. Using the above equation, one can define the equations of motion for the magnetization as

$$\begin{aligned}
\partial_t M_t^x &= JS\nabla\cdot(\nabla M_t^y)-S(2d)M_t^y,\\
\partial_t M_t^y &= -JS\nabla\cdot(\nabla M_t^x)+S(2d)M_t^x.
\end{aligned}$$

Applying the Helmholtz-Hodge decomposition to these equations, and, in particular, by considering the Heisenberg equation for the M^x component, the effective equations of motions yield

$$\begin{aligned}
\partial_t\psi^x &= S\left(J\nabla^2\psi^y-2d\psi^y\right),\\
\partial_t\boldsymbol{A}^x &= -2Sd\boldsymbol{A}^y,
\end{aligned}\tag{H.9}$$

explicitly decoupling the divergence-free and divergence-full components of the spin. This however only considers the Helmholtz-Hodge decomposition of the field $\boldsymbol{M}_t$.

The above case was considered to get familiarized with the calculations done to explicitly demonstrate how the divergence-full and divergence-free degrees of freedom are separated. As in Ref. [167], this case is a very simple example where the ordered state is considered along the *global* z-direction. Motivated by this analysis we can now study the general bilinear Hamiltonians presented in Chapter 2 which may host ordered ground state configurations at low temperatures. In particular, we are interested in the AIAO ground state which has the property of being defined along the local z direction of each sublattice

of the pyrochlore lattice. We consider the general bilinear Hamiltonian

$$\begin{aligned}\mathcal{H} &= \sum_{\langle ij\rangle}\big\{J_{zz}S_i^zS_j^z - J_{\pm}(S_i^+S_j^- + S_i^-S_j^+) + J_{\pm\pm}(\gamma_{ij}S_i^+S_j^+ + \gamma_{ij}^*S_i^-S_j^-) \\ &\quad + J_{z\pm}(\zeta_{ij}S_i^zS_j^+ + \zeta_{ij}^*S_i^zS_j^- + i\leftrightarrow j)\big\}, \end{aligned} \tag{H.10}$$

where symmetric phase factors γ_{ij} and ζ_{ij} are introduced, the ladder operators are defined as

$$\begin{aligned} S_k^+ &= S_k^x + iS_k^y, \\ S_k^- &= S_k^x - iS_k^y, \\ S_k^x &= \frac{1}{2}(S_k^+ + S_k^-), \\ S_k^y &= \frac{1}{2i}(S_k^+ - S_k^-),, \end{aligned}$$

and the ground state configuration requires $\langle S^z\rangle \sim S$ and $\langle S^\pm\rangle \ll S$. To continue, we consider the equations of motion for $S^\pm$. To do so, the following commutators are needed

$$\begin{aligned} \left[S_i^z, S_j^\pm\right] &= \pm S_i^\pm\delta_{ij}, \\ \left[S_i^+, S_j^-\right] &= 2S_i^z\delta_{ij}, \\ \left[S_i^\pm, S_j^\pm\right] &= 0. \end{aligned}$$

First, consider the J_{zz} term

$$\begin{aligned} \sum_{\langle i,j\rangle}[S_i^zS_j^z, S_k^\pm] &= \sum_{\langle i,j\rangle}\left(S_i^z[S_j^z, S_k^\pm] + [S_i^z, S_k^\pm]S_j^z\right), \\ &= \pm\sum_{\langle i,j\rangle}\left(S_i^zS_k^\pm\delta_{jk} + S_j^zS_k^\pm\delta_{ik}\right), \\ &= \pm\sum_{i@k}S_i^zS_k^\pm. \end{aligned} \tag{H.11}$$

Next, consider the $J_\pm$ term for the S^+ operator

$$\begin{aligned} \sum_{\langle i,j\rangle}[S_i^+S_j^- + S_i^-S_j^+, S_k^+] &= \sum_{\langle i,j\rangle}\left(S_i^+[S_j^-, S_k^+] + [S_i^-, S_k^+]S_j^+\right), \\ &= -2\sum_{\langle i,j\rangle}\left(S_i^+S_k^z\delta_{jk} + S_k^zS_j^+\delta_{ik}\right), \\ &= -2\sum_{i@k}S_i^+S_k^z, \end{aligned} \tag{H.12}$$

and similarly for the S^- operator

$$\begin{aligned}\sum_{\langle i,j\rangle}[S_i^+S_j^- + S_i^-S_j^+, S_k^-] &= \sum_{\langle i,j\rangle}\left([S_i^+, S_k^-]S_j^- + S_i^-[S_j^+, S_k^-]\right), \\ &= 2\sum_{\langle i,j\rangle}\left(S_k^zS_j^-\delta_{ik} + S_i^-S_k^z\delta_{jk}\right), \\ &= 2\sum_{i@k} S_i^-S_k^z. \end{aligned} \tag{H.13}$$

Now, for the $J_{\pm\pm}$ term we have to take into account that fact that a phase factor, γ_{ij}, must be considered as part of the commutators. First, take the equation of motion for S^+

$$\begin{aligned}\sum_{\langle i,j\rangle}[\gamma_{ij}S_i^+S_j^+ + \gamma_{ij}^*S_i^-S_j^-, S_k^+] &= \sum_{\langle i,j\rangle}\gamma_{ij}^*[S_i^-S_j^-, S_k^+], \\ &= \sum_{\langle i,j\rangle}\gamma_{ij}^*\left(S_i^-[S_j^-, S_k^+] + [S_i^-, S_k^+]S_j^-\right), \\ &= -2\sum_{\langle i,j\rangle}\gamma_{ij}^*\left(S_i^-S_k^z\delta_{jk} + S_k^zS_j^-\delta_{ik}\right), \\ &= -2\sum_{i@k}\gamma_{ik}^*S_i^-S_k^z, \end{aligned} \tag{H.14}$$

and for the S^- operator

$$\begin{aligned}\sum_{\langle i,j\rangle}[\gamma_{ij}S_i^+S_j^+ + \gamma_{ij}^*S_i^-S_j^-, S_k^-] &= \sum_{\langle i,j\rangle}\gamma_{ij}[S_i^+S_j^+, S_k^-], \\ &= \sum_{\langle i,j\rangle}\gamma_{ij}\left(S_i^+[S_j^+, S_k^-] + [S_i^+, S_k^-]S_j^+\right), \\ &= 2\sum_{\langle i,j\rangle}\gamma_{ij}\left(S_i^+S_k^z\delta_{jk} + S_k^zS_j^+\delta_{ik}\right), \\ &= 2\sum_{i@k}\gamma_{ik}S_i^+S_k^z. \end{aligned} \tag{H.15}$$

Finally, for the term $J_{z\pm}$, the commutator for the operator S^+ is given by

$$\begin{aligned}
\sum_{\langle i,j\rangle}[\zeta_{ij}S_i^zS_j^+ + \zeta_{ij}^*S_i^zS_j^-, S_k^+] &= \sum_{\langle i,j\rangle}\zeta_{ij}[S_i^zS_j^+, S_k^+] + \zeta_{ij}^*[S_i^zS_j^-, S_k^+], \\
&= \sum_{\langle i,j\rangle}\zeta_{ij}[S_i^z, S_k^+]S_j^+ + \zeta_{ij}^*(S_i^z[S_j^-, S_k^+] + [S_i^z, S_k^+]S_j^-), \\
&= \sum_{\langle i,j\rangle}\zeta_{ij}S_k^+S_j^+\delta_{ik} + \zeta_{ij}^*(-2S_i^zS_k^z\delta_{jk} + S_k^+S_j^-\delta_{ik}), \\
&= -2\sum_{\langle i,j\rangle}\zeta_{ij}^*S_i^zS_k^z\delta_{jk} + \sum_{\langle i,j\rangle}\zeta_{ij}S_k^+S_j^+\delta_{ik} + \zeta_{ij}^*S_k^+S_j^-\delta_{ik}, \\
&= -\sum_{i@k}\zeta_{ik}^*S_i^zS_k^z + \sum_{\langle i,j\rangle}\zeta_{ij}S_k^+S_j^+\delta_{ik} + \zeta_{ij}^*S_k^+S_j^-\delta_{ik}, \quad \text{(H.16)}
\end{aligned}$$

the remaining term containing a $J_{z\pm}$ interaction term are easily obtained by exchanging the labels $i \leftrightarrow j$. Lastly, for the S^- operator one has

$$\begin{aligned}
\sum_{\langle i,j\rangle}[\zeta_{ij}S_i^zS_j^+ + \zeta_{ij}^*S_i^zS_j^-, S_k^-] &= \sum_{\langle i,j\rangle}\zeta_{ij}[S_i^zS_j^+, S_k^-] + \zeta_{ij}^*[S_i^zS_j^-, S_k^-], \\
&= \sum_{\langle i,j\rangle}\zeta_{ij}(S_i^z[S_j^+, S_k^-] + [S_i^z, S_k^-]S_j^+) + \zeta_{ij}^*[S_i^z, S_k^-]S_j^-, \\
&= \sum_{\langle i,j\rangle}\zeta_{ij}(2S_i^zS_k^z\delta_{jk} - S_k^-S_j^+\delta_{ik}) - \zeta_{ij}^*S_k^-S_j^-\delta_{ik}, \\
&= 2\sum_{\langle i,j\rangle}\zeta_{ij}S_i^zS_k^z\delta_{jk} - \sum_{\langle i,j\rangle}\zeta_{ij}S_k^-S_j^+\delta_{ik} + \zeta_{ij}^*S_k^-S_j^-\delta_{ik}, \\
&= \sum_{i@k}\zeta_{ik}S_i^zS_k^z - \sum_{\langle i,j\rangle}\zeta_{ij}S_k^-S_j^+\delta_{ik} + \zeta_{ij}^*S_k^-S_j^-\delta_{ik}. \quad \text{(H.17)}
\end{aligned}$$

Note that in the last two commutators, only the first term is considered as all other terms are of order $\langle S^+S^-\rangle$ which, to first order, are ignored. Taking all the above contributions

into account yields

$$\begin{aligned}
-i\frac{\partial}{\partial t}S_k^+ &= \left[\mathcal{H}, S_k^+\right] \\
&= \sum_{i@k} J_{zz}S_i^zS_k^+ + 2J_\pm S_i^+S_k^z - 2J_{\pm\pm}\gamma_{ik}^*S_i^-S_k^z - 2J_{z\pm}\zeta_{ik}^*S_i^zS_k^z + O(S^+S^-), \\
&\simeq S\sum_{i@k} J_{zz}S_k^+ + 2J_\pm S_i^+ - 2J_{\pm\pm}\gamma_{ik}^*S_i^- - 2J_{z\pm}\zeta_{ik}^*S + O(S^+S^-), \\
-i\frac{\partial}{\partial t}S_k^- &= \left[\mathcal{H}, S_k^-\right] \\
&= \sum_{i@k} -J_{zz}S_i^zS_k^- - 2J_\pm S_i^-S_k^z + 2J_{\pm\pm}\gamma_{ik}S_i^+S_k^z + 2J_{z\pm}\zeta_{ik}S_i^zS_k^z + O(S^+S^-), \\
&\simeq S\sum_{i@k} -J_{zz}S_k^- - 2J_\pm S_i^- + 2J_{\pm\pm}\gamma_{ik}S_i^+ + 2J_{z\pm}\zeta_{ik}S + O(S^+S^-). \qquad \text{(H.18)}
\end{aligned}$$

With the above expressions, the equations of motion for the transverse components of the spin result in the expression

$$\begin{aligned}
-i\frac{\partial}{\partial t}S_k^x &\simeq S\frac{1}{2}\sum_{j@k} J_{zz}(S_k^+ - S_k^-) + 2J_\pm(S_j^+ - S_j^-) + 2J_{\pm\pm}(\gamma_{jk}S_j^+ - \gamma_{jk}^*S_j^-) + 2J_{z\pm}(\zeta_{jk} - \zeta_{jk}^*)S \\
&\quad + O(S^+S^-), \\
&= S\sum_{j@k} J_{zz}(iS_k^y) + 2J_\pm(iS_j^y) + J_{\pm\pm}(\gamma_{jk}S_j^+ - \gamma_{jk}^*S_j^-) + 2J_{z\pm}(\zeta_{jk} - \zeta_{jk}^*)S + O(S^+S^-),
\end{aligned}$$

where the last term can be rewritten by separating the real and complex components of the phase factor γ_{jk} as

$$\left(\mathrm{Re}(\gamma_{jk}) + i\,\mathrm{Im}(\gamma_{jk})\right)\left(S_j^x + iS_j^y\right) - \left(\mathrm{Re}(\gamma_{jk}) - i\,\mathrm{Im}(\gamma_{jk})\right)\left(S_j^x - iS_j^y\right) = 2i\,\mathrm{Re}(\gamma_{jk})S_j^y + 2i\,\mathrm{Im}(\gamma_{jk})S_j^x,$$

finally obtaining

$$\begin{aligned}
\frac{\partial}{\partial t}S_k^x &\simeq -S\sum_{j@k} J_{zz}S_k^y + 2J_\pm S_j^y + 2J_{\pm\pm}(\mathrm{Re}(\gamma_{jk})S_j^y + \mathrm{Im}(\gamma_{jk})S_j^x) + 4J_{z\pm}\,\mathrm{Im}(\zeta_{jk})S + O(S^+S^-), \\
&= -S\sum_{j@k} J_{zz}S_k^y + (2J_\pm + 2J_{\pm\pm}\,\mathrm{Re}(\gamma_{jk}))S_j^y + 2\,\mathrm{Im}(\gamma_{jk})J_{\pm\pm}S_j^x + 4J_{z\pm}\,\mathrm{Im}(\zeta_{jk})S \\
&\quad + O(S^+S^-), \qquad \text{(H.19)}
\end{aligned}$$

and for S^y

$$\begin{aligned}
-i\frac{\partial}{\partial t}S_k^y &\simeq S\frac{1}{2i}\sum_{j@k} J_{zz}(S_k^+ + S_k^-) + 2J_{\pm}(S_j^+ + S_j^-) - 2J_{\pm\pm}(\gamma_{jk}S_j^+ + \gamma_{jk}^* S_j^-) - 2J_{z\pm}(\zeta_{jk} + \zeta_{jk}^*)S \\
&\quad + O(S^+S^-), \\
\frac{\partial}{\partial t}S_k^y &= S\sum_{j@k} J_{zz}S_k^x + (2J_{\pm} - 2\,\mathrm{Re}(\gamma_{jk})J_{\pm\pm})S_j^x + 2\,\mathrm{Im}(\gamma_{jk})J_{\pm\pm}S_j^y - 4SJ_{z\pm}\,\mathrm{Re}(\zeta_{jk}) \\
&\quad + O(S^+S^-).
\end{aligned} \tag{H.20}$$

Note that, for both equations of motion, there is only one term proportional to $\mathrm{Im}(\gamma_{jk})$ which contains the same spin component corresponding to the derivative in the left-hand side of the equation. This particular term can be neglected if the phase factors are taken to be real, see Chapter 2. This scenario can be realized in the Dipolar-Octupolar (DO) Hamiltonian[3] for which $J_{z\pm} = 0$ [102] resulting in the following simplified equations

$$\begin{aligned}
\frac{\partial}{\partial t}S_k^x &= -S\sum_{j@k} J_{zz}S_k^y + 2(J_{\pm} + J_{\pm\pm})S_j^y + O(S^+S^-), \\
\frac{\partial}{\partial t}S_k^y &= S\sum_{j@k} J_{zz}S_k^x + 2(J_{\pm} - J_{\pm\pm})S_j^x + O(S^+S^-).
\end{aligned} \tag{H.21}$$

Taking the interactions variables $J_{xx} = 2(J_{\pm\pm} - J_{\pm})$ and $J_{yy} = -2(J_{\pm\pm} + J_{\pm})$ [23] the equations of motion become

$$\begin{aligned}
\frac{\partial}{\partial t}S_k^x &= -S\sum_{j@k} J_{zz}S_k^y - J_{yy}(S_j^y - S_k^y) - J_{yy}S_k^y + O(S^+S^-) \\
\frac{\partial}{\partial t}S_k^y &= S\sum_{j@k} J_{zz}S_k^x - J_{xx}(S_j^x - S_k^x) - J_{xx}S_k^x + O(S^+S^-).
\end{aligned} \tag{H.22}$$

Using the resulting equations of motion for the DO Hamiltonian we may now obtain the equations of motion for the magnetization, given by Eq. (H.7), in each tetrahedron

$$\begin{aligned}
\frac{\partial}{\partial t}M_t^x &= (-6SJ_{zz} + 6SJ_{yy})M_t^y + SJ_{yy}\nabla^2 M_t^y + O(S^+S^-), \\
\frac{\partial}{\partial t}M_t^y &= (6SJ_{zz} - 6SJ_{xx})M_t^x - SJ_{xx}\nabla^2 M_t^x + O(S^+S^-).
\end{aligned} \tag{H.23}$$

[3] In general, $J_{z\pm} \neq 0$ for the DO Hamiltonian. However, we may produce a rotation in the spin components to a basis in which this coupling vanishes.

The expressions obtained are equivalent to those found by Ref. [102]. Moreover, the application of the Helmholtz-Hodge decomposition to the above expressions effectively decouples the rotational and irrotational degrees of freedom. In the general bilinear Hamiltonian, where the phase factors are complex and $J_{z\pm} \neq 0$, the equations of motion mix the magnetization components. Moreover, note that the complex phase factors produce a constant term in both equations which can be expressed as either the gradient or curl of a certain function, making the separation between the rotational and irrotational degrees of freedom less intuitive.

Appendix I

Perturbative Monte Carlo

In this last appendix, we present a perturbative Monte Carlo technique. This technique can be used to perturbatively introduce the effect of quantum terms starting from a classical theory and was used by Refs. [126, 127, 172] in the study of $LiHo_xY_{1-x}F_4$ upon the introduction of disorder. Here we extend this approach to an XXZ Hamiltonian in the pyrochlore lattice. Consider the spin 1/2 XXZ model on the pyrochlore lattice

$$\mathcal{H} = \sum_{\langle ij \rangle} \left[J\sigma_i^z\sigma_j^z + J_\perp(\sigma_i^x\sigma_j^x + \sigma_i^y\sigma_j^y) \right], \tag{I.1}$$

where $J > 0$, and $J_\perp$ will be taken as a perturbation. To study this model, a cumulant expansion method can be performed. Through this procedure, a quantum Hamiltonian can be expressed in a perturbative series as a classical Hamiltonian such that the partition function can be written in the following way

$$Z = \langle e^{-\beta\mathcal{H}} \rangle = \sum_i e^{-\beta\mathcal{H}_{\text{eff}}[\psi_i]}, \tag{I.2}$$

where ψ_i represents a classical product state. To continue with this derivation, the Hamiltonian can be divided into a "classical", $\mathcal{H}_0$, and "quantum", $\mathcal{H}_1$, terms:

$$\mathcal{H} = \underbrace{J\sum_{\langle ij \rangle} \sigma_i^z\sigma_j^z}_{\mathcal{H}_0} + \underbrace{J_\perp \sum_{\langle ij \rangle} (\sigma_i^x\sigma_j^x + \sigma_i^y\sigma_j^y)}_{\mathcal{H}_1}.$$

Prior to applying this definition, a perturbation series of the partition function can be obtained in the following way

$$\begin{aligned}
Z &= e^{-\beta\langle\mathcal{H}\rangle}\langle e^{-\beta(\mathcal{H}-\langle\mathcal{H}\rangle)}\rangle, \\
\ln Z &= -\beta\langle\mathcal{H}\rangle + \ln\langle e^{-\beta(\mathcal{H}-\langle\mathcal{H}\rangle)}\rangle, \\
&= -\beta\langle\mathcal{H}\rangle + \ln\left\langle 1 + \sum_{n=1}^{\infty}\frac{1}{n!}\left(-\beta(\mathcal{H}-\langle\mathcal{H}\rangle)\right)^n\right\rangle, \\
&= -\beta\langle\mathcal{H}\rangle + \ln\left(1 + \underbrace{\left\langle \sum_{n=1}^{\infty}\frac{1}{n!}\left(-\beta(\mathcal{H}-\langle\mathcal{H}\rangle)\right)^n\right\rangle}_{x}\right), \\
&= -\beta\langle\mathcal{H}\rangle + x - \frac{x^2}{2} + \frac{x^3}{3} + \cdots \\
\langle e^{-\beta\mathcal{H}}\rangle &= \exp\left\{-\beta\langle\mathcal{H}\rangle + x - \frac{x^2}{2} + \frac{x^3}{3} + \cdots\right\}.
\end{aligned}$$

Finally, we choose a basis conformed by product states $\left\{ \mid \psi\rangle \;\middle|\; \mid \psi\rangle = \bigotimes_i \mid \sigma_i^z\rangle \right\}$. It is easy to note that the expectation value of a spin-flip operator for any state in this basis vanishes. Therefore, the previous expression can be written in the following way

$$\begin{aligned}
\langle e^{-\beta\mathcal{H}}\rangle &= \exp\left\{-\beta\langle\mathcal{H}_0\rangle + x - \frac{x^2}{2} + \frac{x^3}{3} + \cdots\right\}, \\
\mathcal{H}_{\text{eff}} &= \langle\mathcal{H}_0\rangle - \frac{1}{\beta}\left(x - \frac{x^2}{2} + \frac{x^3}{3} + \cdots\right).
\end{aligned}$$

Moreover, we note that the first term of the series in x now vanishes as a consequence of the product basis chosen. The expression above is exact; however, it is obvious that such a series will not be used as it involves an infinite number of terms. Instead, we may consider a perturbation series given by considering the case $J_\perp \ll J$, where the first term in the series is of order $J_\perp^2$. Therefore, the lowest order in the perturbation series, the effective Hamiltonian can be written as

$$\begin{aligned}
\mathcal{H}_{\text{eff}} &= \langle\mathcal{H}_0\rangle - \frac{1}{\beta}\sum_{n=2}^{\infty}\frac{(-\beta)^n}{n!}\Big\langle\left(\mathcal{H}-\langle\mathcal{H}_0\rangle\right)^n\Big\rangle + O(J_\perp^4), \\
&= \langle\mathcal{H}_0\rangle - \frac{1}{\beta}\sum_{n=2}^{\infty}\frac{(-\beta)^n}{n!}\Big\langle\mathcal{H}_1\left(\mathcal{H}_0 - E_0[\psi]\right)^{n-2}\mathcal{H}_1\Big\rangle + O(J_\perp^4),
\end{aligned}$$

where only the first term in x is used. The expression above is further simplified by the fact that the basis chosen is a classical product state basis. To continue and obtain an effective Hamiltonian, the trace over the n power operator must be performed. In this process, the following identities are used

$$\begin{aligned}\sigma_i^x\sigma_j^x|\psi\rangle &= |f_i f_j\psi\rangle,\\ \sigma_i^y\sigma_j^y|\psi\rangle &= -\sigma_i^z\sigma_j^z|f_i f_j\psi\rangle,\end{aligned}$$

where, $|f_i f_j\psi\rangle$ is represented as the state $\mid \psi\rangle$ with the spins i and j flipped, and σ_i^z is the value of the spin in site i prior to being flipped. By using the classical product states and the identities previously stated the following operator, the following operation can be calculated

$$\begin{aligned}\mathcal{H}_1 \mid \psi\rangle &= J_\perp \sum_{\langle ij\rangle}(1-\sigma_i^z\sigma_j^z) \mid f_i f_j\psi\rangle,\\ (\mathcal{H}_0 - E_0[\psi])^{n-2}\,\mathcal{H}_1 \mid \psi\rangle &= J_\perp \sum_{\langle ij\rangle}(1-\sigma_i^z\sigma_j^z)\,(E_0[f_i f_j\psi]-E_0[\psi])^{n-2} \mid f_i f_j\psi\rangle,\\ \mathcal{H}_1\,(\mathcal{H}_0 - E_0[\psi])^{n-2}\,\mathcal{H}_1 \mid \psi\rangle &= J_\perp^2 \sum_{\langle lk\rangle}\sum_{\langle ij\rangle}(1-\sigma_l^z\sigma_k^z)(1-\sigma_i^z\sigma_j^z)\,(E_0[f_i f_j\psi]-E_0[\psi])^{n-2} \mid f_i f_j f_l f_k\psi\rangle.\end{aligned}$$

Finally, this state is going to be projected into the original state $|\psi\rangle$. Hence, to have a non-zero contribution the flips obtained must cancel out. This will only happen when $(i,j) = (k,l)$ and $(i,j) = (l,k)$; however, only one of the cases is included to avoid overcounting. To include this constraint, two delta functions can be added such that

$$\begin{aligned}\mathcal{H}_1\,(\mathcal{H}_0 - E_0[\psi])^{n-2}\,\mathcal{H}_1 \mid \psi\rangle &= J_\perp^2 \sum_{\langle lk\rangle}\sum_{\langle ij\rangle}(1-\sigma_l^z\sigma_k^z)(1-\sigma_i^z\sigma_j^z)\,(E_0[f_i f_j\psi]-E_0[\psi])^{n-2}\,(\delta_{i,k}\delta_{j,l}) \mid \psi\rangle,\\ &= J_\perp^2 \sum_{\langle ij\rangle}(1-\sigma_i^z\sigma_j^z)^2\,(E_0[f_i f_j\psi]-E_0[\psi])^{n-2} \mid \psi\rangle,\\ &= J_\perp^2 \sum_{\langle ij\rangle}(1-2\sigma_i^z\sigma_j^z+(\sigma_i^z\sigma_j^z)^2)\,(E_0[f_i f_j\psi]-E_0[\psi])^{n-2} \mid \psi\rangle,\\ &= 2J_\perp^2 \sum_{\langle ij\rangle}(1-\sigma_i^z\sigma_j^z)\,(\Delta E_0[f_i f_j\psi])^{n-2} \mid \psi\rangle.\end{aligned}$$

In this way, the effective Hamiltonian is found to be

$$\begin{aligned}
\mathcal{H}_{\text{eff}} &= J\sum_{\langle ij\rangle}\sigma_i^z\sigma_j^z - \frac{1}{\beta}2J_\perp^2\sum_{\langle ij\rangle}(1-\sigma_i^z\sigma_j^z)\frac{1}{\Delta E_0[f_if_j\psi]^2}\left(\sum_{n=2}^{\infty}\frac{(-\beta\Delta E_0[f_if_j\psi])^n}{n!}\right)+O(J_\perp^4),\\
&= J\sum_{\langle ij\rangle}\sigma_i^z\sigma_j^z - \frac{1}{\beta}2J_\perp^2\sum_{\langle ij\rangle}(1-\sigma_i^z\sigma_j^z)\frac{1}{\Delta E_0[f_if_j\psi]^2}\left(\sum_{n=2}^{\infty}\frac{(-\beta\Delta E_0[f_if_j\psi])^n}{n!}\right)+O(J_\perp^4),\\
&= J\sum_{\langle ij\rangle}\sigma_i^z\sigma_j^z - 2J_\perp^2\beta\sum_{\langle ij\rangle}(1-\sigma_i^z\sigma_j^z)\frac{1}{\beta^2\Delta E_0[f_if_j\psi]^2}\left(\sum_{n=2}^{\infty}\frac{\left(\overbrace{-\beta\Delta E_0[f_if_j\psi]}^{x}\right)^n}{n!}\right)+O(J_\perp^4),\\
&= J\sum_{\langle ij\rangle}\sigma_i^z\sigma_j^z - 2J_\perp^2\beta\sum_{\langle ij\rangle}(1-\sigma_i^z\sigma_j^z)\frac{1}{x^2}\left(\sum_{n=2}^{\infty}\frac{x^n}{n!}\right)+O(J_\perp^4),\\
&= J\sum_{\langle ij\rangle}\sigma_i^z\sigma_j^z - 2J_\perp^2\beta\sum_{\langle ij\rangle}(1-\sigma_i^z\sigma_j^z)\left(\frac{e^x-x-1}{x^2}\right)+O(J_\perp^4),\\
&= J\sum_{\langle ij\rangle}\sigma_i^z\sigma_j^z - 2J_\perp^2\beta\sum_{\langle ij\rangle}(1-\sigma_i^z\sigma_j^z)F_{ij}(x)+O(J_\perp^4),
\end{aligned}$$

where the sub-indices i, j in the function F are added to label the site dependence of the variable x. Lastly, we need to obtain an expression for the energy change in the classical Hamiltonian given by two distinct, but neighboring spins to obtain an expression for x in Eq. (I.3). This energy change is produced by every neighboring spin of the site i and j without taking into account the pair (i, j):

$$\begin{aligned}
\Delta E[f_if_j] &= -2J\left(\sigma_i^z\sum_{l\in NN(i)}\sigma_l^z+\sigma_j^z\sum_{l\in NN(j)}\sigma_l^z\right)+4J\sigma_i^z\sigma_j^z,\\
&= -2J\left(\sigma_i^z\sum_{\substack{l\in NN(i)\\ l\neq j}}\sigma_l^z+\sigma_j^z\sum_{\substack{l\in NN(j)\\ l\neq i}}\sigma_l^z\right). \qquad \text{(I.3)}
\end{aligned}$$

Using the above expression for x, the effective Hamiltonian can be expressed as

$$\mathcal{H}_{\rm eff}[\psi] = J\sum_{\langle ij\rangle}\sigma_i^z\sigma_j^z - 2J_\perp^2\beta\sum_{\langle ij\rangle}(1-\sigma_i^z\sigma_j^z)F\left[2\beta J\left(\sigma_i^z\sum_{\substack{l\in NN(i)\\ l\neq j}}\sigma_l^z + \sigma_j^z\sum_{\substack{l\in NN(j)\\ l\neq i}}\sigma_l^z\right)\right] + O(J_\perp^4). \tag{I.4}$$

I.1 High temperature-$J_\perp$ expansion

As a consequence of this derivation, the effective Hamiltonian has a temperature dependence that is encoded in the explicit β term in the perturbation term, as well as in the function $F(x)$. Therefore, through this simple recognition, a high-temperature expansion can be obtained for the Hamiltonian by using the Taylor expansion of the function $F(x)$:

$$\begin{aligned} F(x) &= \frac{e^x - x - 1}{x^2}, \\ &= \sum_{n=2}^{\infty}\frac{x^{n-2}}{n!} = \frac{1}{2} + \frac{x}{6} + \cdots, \end{aligned}$$

where the variable x is proportional to β. Hence, by only using the first two terms of the series the effective Hamiltonian is further simplified to

$$\begin{aligned} \mathcal{H}_{\rm eff}[\psi] &= J\sum_{\langle ij\rangle}\sigma_i^z\sigma_j^z - 2J_\perp^2\beta\sum_{\langle ij\rangle}(1-\sigma_i^z\sigma_j^z)\left[\frac{1}{2} + \frac{J\beta}{3}\left(\sigma_i^z\sum_{\substack{l\in NN(i)\\ l\neq j}}\sigma_l^z + \sigma_j^z\sum_{\substack{l\in NN(j)\\ l\neq i}}\sigma_l^z\right)\right] \\ &\quad + O(J_\perp^2\beta^3) + O(J_\perp^4), \\ &= J\sum_{\langle ij\rangle}\sigma_i^z\sigma_j^z - J_\perp^2\beta\sum_{\langle ij\rangle}(1-\sigma_i^z\sigma_j^z) - \frac{2JJ_\perp^2\beta^2}{3}\sum_{\langle ij\rangle}(1-\sigma_i^z\sigma_j^z)\left(\sigma_i^z\sum_{\substack{l\in NN(i)\\ l\neq j}}\sigma_l^z + \sigma_j^z\sum_{\substack{l\in NN(j)\\ l\neq i}}\sigma_l^z\right) \\ &\quad + O(J_\perp^2\beta^3) + O(J_\perp^4). \end{aligned}$$

As can be seen, the previous expression redefines the Ising interaction by a small parameter and adds a small perturbative term to the Hamiltonian at this order. Therefore, the Hamiltonian is

$$\mathcal{H}_{\text{eff}}[\psi] = \overbrace{-J_\perp^2\beta\left(\frac{N\times z}{2}\right)}^{-J_\perp^2\beta\sum_{\langle ij\rangle}1} + (J+J_\perp^2\beta)\sum_{\langle ij\rangle}\sigma_i^z\sigma_j^z - \frac{2JJ_\perp^2\beta^2}{3}\sum_{\langle ij\rangle}\left(\sigma_i^z\sum_{\substack{l\in NN(i)\\ l\neq j}}\sigma_l^z + \sigma_j^z\sum_{\substack{l\in NN(j)\\ l\neq i}}\sigma_l^z\right),$$

$$+\frac{2JJ_\perp^2\beta^2}{3}\sum_{\langle ij\rangle}\left(\sigma_j^z\sum_{\substack{l\in NN(i)\\ l\neq j}}\sigma_l^z + \sigma_i^z\sum_{\substack{l\in NN(j)\\ l\neq i}}\sigma_l^z\right) + O(J_\perp^2\beta^3) + O(J_\perp^4),$$

where z is the number of first nearest neighbors for every site. This expression can be identified with terms of first, second and third nearest neighbor. To do so, consider the following case: say that for every site i, its nearest neighbors are labeled i_1, i_2, i_3, i_4, i_5 and i_6. Therefore, the second term involving the l-th nearest neighbor that is not the j-th neighbor can be expressed as an explicit sum over each sum that does not contain a specific neighbor of the i-th spin:

$$\sum_{\langle ij\rangle}\sigma_i^z\sum_{\substack{l\in NN(i)\\ l\neq j}}\sigma_l^z = \sum_i\sigma_i^z\begin{pmatrix} 0 & +\sigma_{i_2}^z & +\sigma_{i_3}^z & +\sigma_{i_4}^z & +\sigma_{i_5}^z & +\sigma_{i_6}^z\\ +\sigma_{i_1}^z & +0 & +\sigma_{i_3}^z & +\sigma_{i_4}^z & +\sigma_{i_5}^z & +\sigma_{i_6}^z\\ +\sigma_{i_1}^z & +\sigma_{i_2}^z & +0 & +\sigma_{i_4}^z & +\sigma_{i_5}^z & +\sigma_{i_6}^z\\ +\sigma_{i_1}^z & +\sigma_{i_2}^z & +\sigma_{i_3}^z & +0 & +\sigma_{i_5}^z & +\sigma_{i_6}^z\\ +\sigma_{i_1}^z & +\sigma_{i_2}^z & +\sigma_{i_3}^z & +\sigma_{i_4}^z & +0 & +\sigma_{i_6}^z\\ +\sigma_{i_1}^z & +\sigma_{i_2}^z & +\sigma_{i_3}^z & +\sigma_{i_4}^z & +\sigma_{i_5}^z & +0 \end{pmatrix}$$

$$= 5\sum_{\langle ij\rangle}\sigma_i^z\sigma_j^z = (z-1)\sum_{\langle ij\rangle}\sigma_i^z\sigma_j^z,$$

where $z=6$ is the coordination number of the pyrochlore lattice. Therefore, it is easy to notice that the second term of the effective Hamiltonian is a nearest-neighbor term with a factor $10\frac{2JJ_\perp^2\beta^2}{3} = 2(z-1)\frac{2JJ_\perp^2\beta^2}{3}$. The third term of the Hamiltonian provides a different kind of interaction as it is a term between the i-th site and the neighbors of its j-th neighbor (without taking into account the $i-j$ interaction). This term can be regarded as every possible connection between site i and any other site that requires exactly 2 links. With this idea in mind, it is easy to check that, for the pyrochlore lattice, every first nearest neighbor is still contributes as it can be reached by 2 different paths (this result is lattice dependent, in the case of the pyrochlore it is true, however, in the case of the square lattice this term does not appear). In the same way, every second nearest neighbor and third

nearest neighbor, type a [54][1], is connected to the site i. Hence, this term can be written as

$$\begin{aligned}\sum_{\langle ij\rangle}\sigma_i^z\sum_{\substack{l\in NN(j)\\ l\neq i}}\sigma_l^z &= n_1\sum_{\langle ij\rangle}\sigma_i^z\sigma_j^z+n_2\sum_{\langle\langle ij\rangle\rangle}\sigma_i^z\sigma_j^z+n_3\sum_{\langle\langle\langle ij\rangle\rangle\rangle_a}\sigma_i^z\sigma_j^z,\\ &= 2\sum_{\langle ij\rangle}\sigma_i^z\sigma_j^z+\sum_{\langle\langle ij\rangle\rangle}\sigma_i^z\sigma_j^z+\sum_{\langle\langle\langle ij\rangle\rangle\rangle_a}\sigma_i^z\sigma_j^z. \qquad \text{(I.5)}\end{aligned}$$

In the equation above, the constants n_i, with $i\in\{1,2,3\}$, denote the number of possible 2-bond paths through which a specific 1st, 2nd or 3rd nearest neighbor can be reached; thus, lattice dependent. For the pyrochlore lattice, the values are 2, 1 and 1 respectively. An interesting side effect of this "double link" connection is that the third nearest neighbor of type "b" is not present in this approximation. These constants can change depending the lattice considered. For example, for the square lattice, there is no contribution from the first nearest-neighbors to Eq. (I.5). However, for the square lattice, there are two ways of getting to a second neighbor.

For the pyrochlore lattice, the third term in the Hamiltonian produces a first nearest-neighbor term with a factor $-4\frac{4JJ_\perp^2\beta^2}{3}$, and farther nearest-neighbors terms:

$$\begin{aligned}\mathcal{H}_{\text{eff}}[\psi] &= -J_\perp^2\beta\left(\frac{N\times z}{2}\right)+(J+J_\perp^2\beta)\sum_{\langle ij\rangle}\sigma_i^z\sigma_j^z-2(z-1)\frac{2JJ_\perp^2\beta^2}{3}\sum_{\langle ij\rangle}\sigma_i^z\sigma_j^z\\ &\quad+2\frac{2JJ_\perp^2\beta^2}{3}\left(2\sum_{\langle ij\rangle}\sigma_i^z\sigma_j^z+\sum_{\langle\langle ij\rangle\rangle}\sigma_i^z\sigma_j^z+\sum_{\langle\langle\langle ij\rangle\rangle\rangle_a}\sigma_i^z\sigma_j^z\right)+O(J_\perp^2\beta^3)+O(J_\perp^4),\\ \mathcal{H}_{\text{eff}}[\psi] &= -J_\perp^2\beta\left(\frac{N\times z}{2}\right)+(J+J_\perp^2\beta)\sum_{\langle ij\rangle}\sigma_i^z\sigma_j^z-2(z-1)\frac{2JJ_\perp^2\beta^2}{3}\sum_{\langle ij\rangle}\sigma_i^z\sigma_j^z+4\frac{2JJ_\perp^2\beta^2}{3}\sum_{\langle ij\rangle}\sigma_i^z\sigma_j^z\\ &\quad+\frac{4JJ_\perp^2\beta^2}{3}\left(\sum_{\langle\langle ij\rangle\rangle}\sigma_i^z\sigma_j^z+\sum_{\langle\langle\langle ij\rangle\rangle\rangle_a}\sigma_i^z\sigma_j^z\right)+O(J_\perp^2\beta^3)+O(J_\perp^4).\end{aligned}$$

[1]The pyrochlore lattice has two types of third nearest-neighbors, type a and b where both neighbors are equally distant, but are connected by a different number of bonds.

Therefore, the Hamiltonian can be written as a first, second and third-nearest neighbors

$$\begin{aligned}\mathcal{H}_{\text{eff}}[\psi] &= -J_\perp^2\beta\left(\frac{N\times z}{2}\right)+(J+J_\perp^2\beta-\frac{2}{3}(2z-6)JJ_\perp^2\beta^2)\sum_{\langle ij\rangle}\sigma_i^z\sigma_j^z \\ &\quad +\frac{4JJ_\perp^2\beta^2}{3}\left(\sum_{\langle\langle ij\rangle\rangle}\sigma_i^z\sigma_j^z+\sum_{\langle\langle\langle ij\rangle\rangle\rangle_a}\sigma_i^z\sigma_j^z\right)+O(J_\perp^2\beta^3)+O(J_\perp^4).\end{aligned}$$

In this way, the effective Hamiltonian can be rewritten in terms of the coefficients J_1, J_2 and J_{3a} defined as

$$\begin{aligned}J_1 &= (J+J_\perp^2\beta-\frac{2}{3}(2z-6)JJ_\perp^2\beta^2), \\ J_2 &= \frac{4JJ_\perp^2\beta^2}{3}, \\ J_{3a} &= \frac{4JJ_\perp^2\beta^2}{3},\end{aligned}$$

such that the total Hamiltonian is

$$\begin{aligned}\mathcal{H}_{\text{eff}}[\psi] &= -J_\perp^2\beta\left(\frac{N\times z}{2}\right)+J_1\sum_{\langle ij\rangle}\sigma_i^z\sigma_j^z+J_2\sum_{\langle\langle ij\rangle\rangle}\sigma_i^z\sigma_j^z+J_{3a}\sum_{\langle\langle\langle ij\rangle\rangle\rangle_a}\sigma_i^z\sigma_j^z+O(J_\perp^2\beta^3) \\ &\quad +O(J_\perp^4).\end{aligned} \tag{I.6}$$

As may have been expected, the effective Hamiltonian obtained is an extended Ising model with farther nearest-neighbor interactions. However, this new expression has an extra dependence on temperature, given by its coefficients. Consequently, this dependence will modify the way the thermodynamics quantities are obtained whenever a temperature dependence is involved. For this reason, the derivative with respect to β will be needed:

$$\begin{aligned}\frac{\partial}{\partial\beta}\left(\mathcal{H}_{\text{eff}}[\psi]\right) &= -J_\perp^2\left(\frac{N\times z}{2}\right)+(J_\perp^2-\frac{4}{3}(2z-6)JJ_\perp^2\beta)\sum_{\langle ij\rangle}\sigma_i^z\sigma_j^z+\frac{8JJ_\perp^2\beta}{3}\sum_{\langle\langle ij\rangle\rangle}\sigma_i^z\sigma_j^z \\ &\quad +\frac{8JJ_\perp^2\beta}{3}\sum_{\langle\langle\langle ij\rangle\rangle\rangle_a}\sigma_i^z\sigma_j^z+O(J_\perp^2\beta^2)+O(J_\perp^4), \\ \frac{\partial^2}{\partial\beta^2}\left(\mathcal{H}_{\text{eff}}[\psi]\right) &= -\frac{4}{3}(2z-6)JJ_\perp^2\sum_{\langle ij\rangle}\sigma_i^z\sigma_j^z+\frac{8JJ_\perp^2}{3}\sum_{\langle\langle ij\rangle\rangle}\sigma_i^z\sigma_j^z+\frac{8JJ_\perp^2}{3}\sum_{\langle\langle\langle ij\rangle\rangle\rangle_a}\sigma_i^z\sigma_j^z+O(J_\perp^2\beta) \\ &\quad +O(J_\perp^4).\end{aligned}$$

Using this expression, the average energy can be obtained

$$\begin{aligned}
\langle E\rangle &= -\frac{1}{Z}\frac{\partial Z}{\partial\beta},\\
&= -\frac{1}{Z}\frac{\partial}{\partial\beta}\left(\sum_{\psi} e^{-\beta\mathcal{H}_{\text{eff}}[\psi]}\right),\\
&= -\frac{1}{Z}\sum_{\psi} e^{-\beta\mathcal{H}_{\text{eff}}[\psi]}\left(-\mathcal{H}_{\text{eff}}-\beta\frac{\partial\mathcal{H}_{\text{eff}}}{\partial\beta}\right),\\
&= \left\langle \mathcal{H}_{\text{eff}}+\beta\frac{\partial\mathcal{H}_{\text{eff}}}{\partial\beta}\right\rangle + O(J_\perp^2\beta^3) + O(J_\perp^4),\\
&= \langle E_{\text{eff}}\rangle + O(J_\perp^2\beta^3) + \ O(J_\perp^4).
\end{aligned}$$

As well as the heat capacity defined as

$$\begin{aligned}
\frac{\partial}{\partial T}\langle E\rangle &= -k_{\text{B}}\beta^2\frac{\partial}{\partial\beta}\langle E\rangle,\\
&= k_{\text{B}}\beta^2\frac{\partial}{\partial\beta}\left(\frac{1}{Z}\frac{\partial Z}{\partial\beta}\right),\\
&= k_{\text{B}}\beta^2\left(\frac{1}{Z}\frac{\partial^2 Z}{\partial\beta^2}-\frac{1}{Z^2}\left(\frac{\partial Z}{\partial\beta}\right)^2\right),\\
&= k_{\text{B}}\beta^2\left(\frac{1}{Z}\frac{\partial}{\partial\beta}\left(\sum_{\psi} e^{-\beta\mathcal{H}_{\text{eff}}[\psi]}\left(-\mathcal{H}_{\text{eff}}-\beta\frac{\partial\mathcal{H}_{\text{eff}}}{\partial\beta}\right)\right)-\langle E_{\text{eff}}\rangle^2\right),\\
&= k_{\text{B}}\beta^2\left(\left\langle E_{\text{eff}}^2\right\rangle-\langle E_{\text{eff}}\rangle^2-\left\langle 2\frac{\partial\mathcal{H}_{\text{eff}}}{\partial\beta}+\beta\frac{\partial^2\mathcal{H}_{\text{eff}}}{\partial\beta^2}\right\rangle\right),\\
C_v &= k_{\text{B}}\beta^2\left(\left\langle\Delta E_{\text{eff}}^2\right\rangle-\left\langle 2\frac{\partial\mathcal{H}_{\text{eff}}}{\partial\beta}+\beta\frac{\partial^2\mathcal{H}_{\text{eff}}}{\partial\beta^2}\right\rangle\right).
\end{aligned} \tag{I.7}$$

I.2 Magnetization

To obtain the magnetization the source method can be used. To do so, a longitudinal field term should be added to the Hamiltonian. The quantities of interest, magnetization, and susceptibility are derived through this dependence. Finally, the field is set to zero.

Following this argument, the new Hamiltonian is defined as

$$\mathcal{H} = \underbrace{J\sum_{\langle ij\rangle}\sigma_i^z\sigma_j^z + h\sum_i s_i^z}_{\mathcal{H}_0} + \underbrace{J_\perp\sum_{\langle ij\rangle}(\sigma_i^x\sigma_j^x + \sigma_i^y\sigma_j^y)}_{\mathcal{H}_1}.$$

With this Hamiltonian, the derivation above is still valid; however, the classical term and the energy shift should include the field term. Therefore, an extra change in the energy term due to two neighboring spin flips is require:

$$\Delta E_h(i,j) = -2h\left(\sigma_i^z + \sigma_j^z\right).$$

As could have been expected, when both neighboring spins are pointing in different directions the energy of the system does not change. However, because of the geometric frustration, it is guaranteed that a finite energy shift will happen for some pair (i,j). Altogether, the total Hamiltonian for the system is

$$\begin{aligned}\mathcal{H}_{\text{eff}}[\psi] &= J\sum_{\langle ij\rangle}\sigma_i^z\sigma_j^z + h\sum_i\sigma_i^z - 2J_\perp^2\beta\sum_{\langle ij\rangle}(1-\sigma_i^z\sigma_j^z)\\ &\quad\times F\left[2\beta J\left(\sigma_i^z\sum_{\substack{l\in NN(i)\\ l\neq j}}\sigma_l^z + \sigma_j^z\sum_{\substack{l\in NN(j)\\ l\neq i}}\sigma_l^z\right) + 2\beta h\left(\sigma_i^z+\sigma_j^z\right)\right] + O(J_\perp^4).\end{aligned}$$

With this new effective Hamiltonian, the magnetization is defined in the following way

$$\begin{aligned}
\langle M_z \rangle &= -\frac{1}{\beta}\left(\frac{1}{Z}\frac{\partial Z}{\partial h}\right)_{h=0}, \\
&= -\frac{1}{\beta}\left(\frac{1}{Z}\frac{\partial}{\partial h}\sum_{\psi} e^{-\beta\mathcal{H}_{\text{eff}}[\psi]}\right)_{h=0}, \\
&= \left[\frac{1}{Z}\sum_{\psi} e^{-\beta\mathcal{H}_{\text{eff}}[\psi]}\left(\frac{\partial\mathcal{H}_{\text{eff}}}{\partial h}\right)\right]_{h=0}, \\
&= \left[\frac{1}{Z}\sum_{\psi} e^{-\beta\mathcal{H}_{\text{eff}}[\psi]}\left(\sum_i \sigma_i^z - 4J_\perp^2\beta^2\sum_{\langle ij\rangle}(1-\sigma_i^z\sigma_j^z)(\sigma_i^z+\sigma_j^z)\frac{\partial}{\partial x}F(x)\right)\right]_{h=0}, \\
&= \left[\frac{1}{Z}\sum_{\psi} e^{-\beta\mathcal{H}_{\text{eff}}[\psi]}\left(\sum_i \sigma_i^z - 4J_\perp^2\beta^2\sum_{\langle ij\rangle}(\sigma_i^z+\sigma_j^z-\sigma_i^z-\sigma_j^z)\frac{\partial}{\partial x}F(x)\right)\right]_{h=0}, \\
&= \left[\frac{1}{Z}\sum_{\psi} e^{-\beta\mathcal{H}_{\text{eff}}[\psi]}\left(\sum_i \sigma_i^z\right)\right]_{h=0}.
\end{aligned}$$

Therefore, the magnetization term ends up being described by the usual expression even with the effective Hamiltonian. As a consequence, the powers of the magnetization are described in the usual way[2]

$$\langle M_z^n \rangle = \left[\frac{1}{Z}\sum_{\psi} e^{-\beta\mathcal{H}_{\text{eff}}[\psi]}\left(\sum_i \sigma_i^z\right)^n\right]_{h=0}.$$

I.3 Structure factor

After having derived some of the most relevant and simple thermodynamic quantities, we want to study the effect of this perturbative procedure on the expression of the structure factor, see Appendix B. To obtain this expression we can start with the modified Hamiltonian (I.8) with an on-site field h_i;

$$\mathcal{H} = \underbrace{J\sum_{\langle ij\rangle}\sigma_i^z\sigma_j^z + \sum_i h_i s_i^z}_{\mathcal{H}_0} + \underbrace{J_\perp\sum_{\langle ij\rangle}(\sigma_i^x\sigma_j^x + \sigma_i^y\sigma_j^y)}_{\mathcal{H}_1}.$$

[2]This result might not agree with what was found by Ref. [172] for a different system.

As before, the energy change produced by flipping two neighboring spins is

$$\Delta E_h(i,j) = -2\left(h_i\sigma_i^z + h_j\sigma_j^z\right),$$

which in turn would produces an effective Hamiltonian of the form

$$\begin{aligned}
\mathcal{H}_{\rm eff}[\psi] &= J\sum_{\langle ij\rangle}\sigma_i^z\sigma_j^z + \sum_i h_i\sigma_i^z, \\
&\quad -2J_\perp^2\beta\sum_{\langle ij\rangle}(1-\sigma_i^z\sigma_j^z)F\left[2\beta J\left(\sigma_i^z\sum_{\substack{l\in NN(i)\\ l\neq j}}\sigma_l^z + \sigma_j^z\sum_{\substack{l\in NN(j)\\ l\neq i}}\sigma_l^z\right) + 2\beta\left(h_i\sigma_i^z + h_j\sigma_j^z\right)\right] \\
&\quad + O(J_\perp^4).
\end{aligned}$$

To obtain the factor $\sigma_i^z\sigma_j^z$ needed to describe the structure factor, we can derive the partition function with respect to the onsite field variables h_i and h_j

$$\begin{aligned}
\langle\sigma_i^z\sigma_j^z\rangle &= \frac{1}{\beta^2}\left(\frac{1}{Z}\frac{\partial^2 Z}{\partial h_i\partial h_j}\right)_{h=0}, \\
&= \frac{1}{\beta^2}\left(\frac{1}{Z}\frac{\partial^2}{\partial h_i\partial h_j}\sum_\psi e^{-\beta\mathcal{H}_{\rm eff}[\psi]}\right)_{h=0}, \\
&= -\frac{1}{\beta}\left[\frac{1}{Z}\frac{\partial}{\partial h_i}\sum_\psi e^{-\beta\mathcal{H}_{\rm eff}[\psi]}\left(\frac{\partial\mathcal{H}_{\rm eff}}{\partial h_j}\right)\right]_{h=0}, \\
&= -\frac{1}{\beta}\left[\frac{1}{Z}\frac{\partial}{\partial h_i}\sum_\psi e^{-\beta\mathcal{H}_{\rm eff}[\psi]}\left(\sigma_j^z - 4J_\perp^2\beta^2\sum_{i\in NN(j)}(1-\sigma_i^z\sigma_j^z)(\sigma_j^z)\frac{\partial}{\partial x}F(x)\right)\right]_{h=0}, \\
\langle\sigma_i^z\sigma_j^z\rangle &= -\frac{1}{\beta}\Big[\frac{1}{Z}\sum_\psi e^{-\beta\mathcal{H}_{\rm eff}[\psi]}\left(\frac{\partial\mathcal{H}_{\rm eff}}{\partial h_i}\big(\sigma_j^z - 4J_\perp^2\beta^2\sum_{i\in NN(j)}(\sigma_j^z-\sigma_i^z)\frac{\partial}{\partial x}F(x)\right) \\
&\quad -8J_\perp^2\beta^3\sum_{i\in NN(j)}(\sigma_j^z-\sigma_i^z)\sigma_i^z\frac{\partial^2}{\partial x^2}F(x)\big)\Big]_{h=0}. \qquad \text{(I.8)}
\end{aligned}$$

I.4 Application to the XXZ model on the square lattice

To benchmark the result obtained for the XXZ model through the PMC approach, we study the effective Hamiltonian derived by performing a high-temperature expansion of the function F,

$$F(y) = \sum_{n=2}^{\infty} \frac{y^{n-2}}{n!} = \frac{1}{2} + \frac{y}{6} + O(y^2),$$

where $y \propto \beta$. This expansion produces interaction terms between sites that are connected by two Manhattan distances of the form

$$n_1 \sum_{\langle ij \rangle} \sigma_i^z \sigma_j^z + n_2 \sum_{\langle\langle ij \rangle\rangle} \sigma_i^z \sigma_j^z + n_3 \sum_{\langle\langle\langle ij \rangle\rangle\rangle} \sigma_i^z \sigma_j^z,$$

where the sums run over the first, second, and third nearest neighbors pairs, respectively. In this expression, the constants n_1, n_2 and n_3 describe the number of paths composed by two bond distances that connect a pair of neighbors of a given kind. For the pyrochlore lattice, there are two paths connecting the first nearest neighbors and only one path connecting the second and third type a [54] nearest-neighbors. Therefore, by introducing these terms into the Hamiltonian, the effective high-temperature expression is obtained

$$\begin{aligned} \mathcal{H}_{\text{eff}}[\psi] &= -J_\perp^2 \beta \left(\frac{N \times z}{2} \right) + J_1 \sum_{\langle ij \rangle} \sigma_i^z \sigma_j^z + J_2 \sum_{\langle\langle ij \rangle\rangle} \sigma_i^z \sigma_j^z \\ &\quad + J_{3a} \sum_{\langle\langle\langle ij \rangle\rangle\rangle_a} \sigma_i^z \sigma_j^z + O(J_\perp^2 \beta^3) + O(J_\perp^4), \end{aligned} \tag{I.9}$$

where the coupling constants J_1, J_2 and J_{3a} are defined as

$$\begin{aligned} J_1 &= (J + J_\perp^2 \beta - \frac{2}{3}(2z - 6) J J_\perp^2 \beta^2), \\ J_2 &= \frac{4 J J_\perp^2 \beta^2}{3}, \\ J_{3a} &= \frac{4 J J_\perp^2 \beta^2}{3}. \end{aligned}$$

This derivation provides equal weights for both second and third type a nearest neighbors. As such, and by following the results reported in Ref. [54], the two-in-two-out manifold is still considered the ground state of the system.

To study the performance of the PMC method, we study the square lattice with ferromagnetic couplings and compare our results with QMC simulations. To perform these simulations, we use a single spin flip update algorithm (SSF) and the effective thermodynamic quantities described above. For the square lattice, the effective energy possesses a term that depends on the first, second, and third nearest neighbors of the spin in question, this dependence is depicted in Figure I.1. To benchmark this technique, we first study the

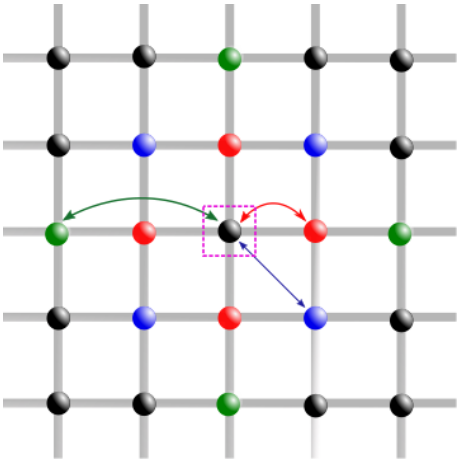


Figure I.1: Nearest neighbors diagram for a square lattice. The center site in black is the base site, red sites as the first neighbors, blue sites as the second nearest neighbors, and green sites as the third nearest neighbors.

moments of the magnetization. In particular, we focus on the second and fourth moment as these two functions are used in the binder cumulant to extract the transition temperature. The results for the moments of the magnetization for $J_\perp = -0.07$ are presented in Figure I.3.

As can be seen, the behavior of the curves found through the PMC simulations agrees well with the QMC results obtained using the ALPS package [173]. Furthermore, we compute the Binder radio,

$$G = \frac{1}{2}\left(3 - \frac{\langle M^4 \rangle}{\langle M^2 \rangle^2}\right),$$

and extract the transition temperatures provided by both QMC and PMC (see Figure I.4). To further test the validity of the method, we extract the transition temperature for several values of $J_\perp$. We construct a function by means of the L-dependent Binder ratio function G_L,

$$F_{J_\perp} = G_{10} + G_{12} - 2G_{15} \tag{I.10}$$

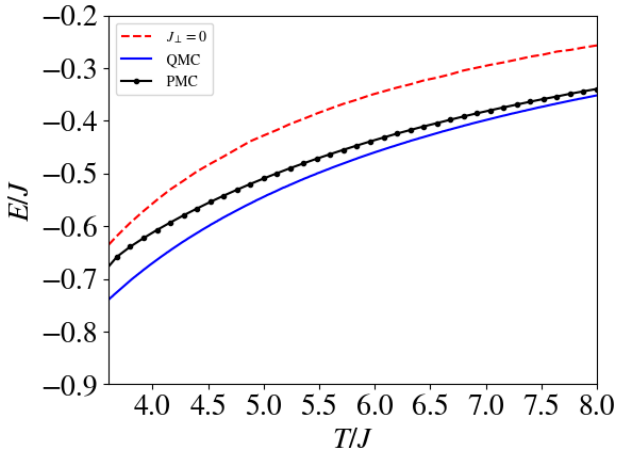
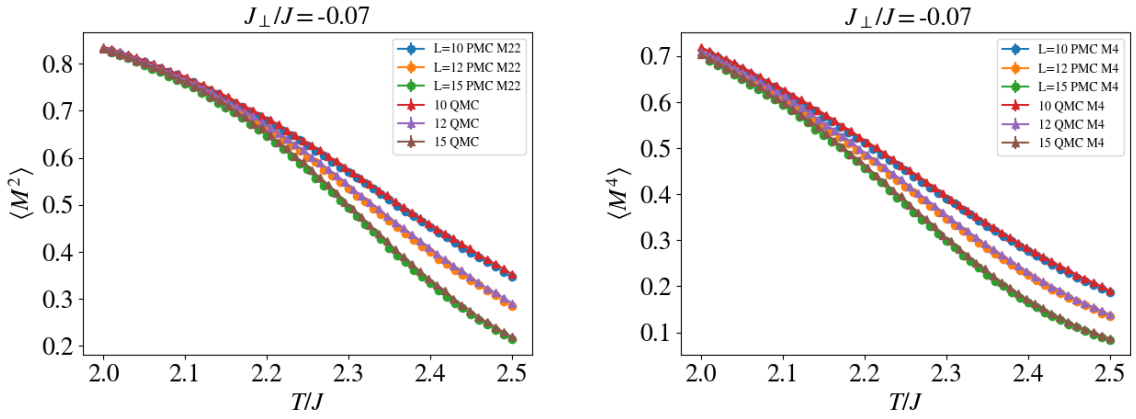


Figure I.2: Energy curves for $J_\perp = -0.5J$.



(a) (b)

Figure I.3: Moments of the magnetization obtained through PMC and QMC simulations for $J_\perp = -0.07J$ (a) $\langle M^2 \rangle$, (b) $\langle M^4 \rangle$.

to obtain the critical temperature as the point where $F_{J_\perp} = 0$. Applying this procedure to both sets of data the phase diagram in Figure I.5 is obtained. The results obtained show a good agreement between the critical values found for both methods. In fact, the percentage error between the critical temperatures found is less than 1% for the values of $J_\perp$ considered.

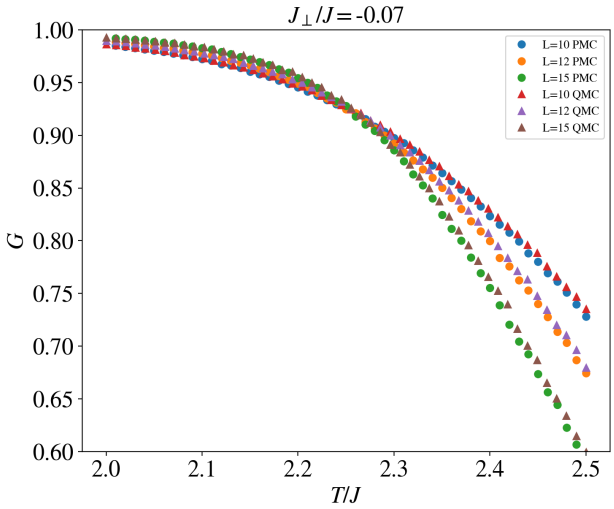


Figure I.4: Binder ratio obtained by QMC and PMC for $J_\perp = -0.07J$.

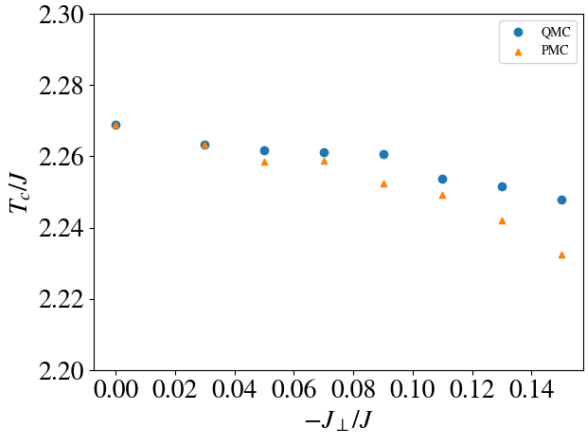


Figure I.5: Phase diagram for the XXZ model with ferromagnetic interactions obtained through QMC and PMC simulations.

I.5 Conclusions

In this appendix, we presented a perturbative approach known as PMC to study the XXZ model (I.1). The calculations presented in this appendix were largely based on previously work [126, 127, 172] where PMC was used to study a different Hamiltonian. To

demonstrate the validity of this approach, we studied the XXZ model on a square lattice and compared the thermodynamic quantities obtained by PMC and QMC where we found good agreement between the two methods. Although we used QMC to benchmark this perturbative approach, it is worth noting that, in contrast to QMC, PMC does not present a sign problem and can therefore be used to study the XXZ model for both positive and negative values of $J_\perp$. Consequently, this method could be used to study the XXZ model on the pyrochlore lattice for both signs of $J_\perp$ where QMC has been used to study the case $J_\perp < 0$ [60], but presents a sign problem for $J_\perp > 0$. For $J_\perp < 0$, Ref. [60] found a modulation in the in the neutron scattering NSF channel [60] which is not present when $J_\perp = 0$ [3]. The application of PMC to the XXZ model may provide key insights regarding the origin of this modulation. Furthermore, we believe that this perturbative approach can be applied to other Hamiltonians which may represent an invaluable tool when studying quantum systems.